

# **Geologic and kinematic model of a complex landslide in crystalline rock (Randa, Switzerland)**

A dissertation submitted to the  
SWISS FEDERAL INSTITUTE OF TECHNOLOGY ZURICH

for the degree of  
DOCTOR OF NATURAL SCIENCES

presented by

HEIKE WILLENBERG

Dipl.-Geol., Rheinisch Westfälische Technische Hochschule Aachen, Germany

born 20.12.1972

citizen of Germany

accepted on the recommendation of

Prof. Dr. Simon Loew, examiner

Prof. Dr. Erik Eberhardt, co-examiner

Dr. Keith F. Evans, co-examiner

Prof. Dr. Herbert H. Einstein, co-examiner

2004



*Wir verstehen so manches nicht,  
nicht nur was das Gemüt betrifft,  
ich nicht, Du nicht, wir nicht.  
- Oder irre ich mich ?*

(Frank Spilker, Die Sterne)





# Contents

<b>1</b>	<b>Introduction.....</b>	<b>1</b>
1.1	Study motivation .....	2
1.2	Thesis objectives.....	2
1.3	Structure of the thesis.....	3
1.4	Investigation site.....	4
1.4.1	<i>Selection of the study site.....</i>	4
1.4.2	<i>Geological setting.....</i>	6
1.4.3	<i>Rockslides in the study area and previous studies .....</i>	10
1.4.3.1	<i>The 1991 Randa rockslides .....</i>	10
1.4.3.2	<i>Other slope instabilities in the Matter valley.....</i>	13
1.4.4	<i>Monitoring of the current instability 1991-2000.....</i>	14
1.4.5	<i>Investigations in the study area Randa 2000-2004.....</i>	16
1.4.5.1	<i>Research boreholes .....</i>	16
1.4.5.2	<i>Borehole logging .....</i>	16
1.4.5.3	<i>Geotechnical and microseismic network.....</i>	16
1.4.5.4	<i>Geological mapping .....</i>	18
1.4.5.5	<i>Laboratory testing .....</i>	18
1.4.6	<i>Geophysical investigations.....</i>	19
<b>2</b>	<b>Integrating geological and geophysical investigations towards a 3-D engineering geological model of an unstable slope in crystalline rock.....</b>	<b>21</b>
2.1	Introduction.....	22
2.1.1	<i>Preface.....</i>	22
2.1.2	<i>Considered rockslide scenarios .....</i>	23
2.1.3	<i>Structural terminology for discontinuity mapping .....</i>	23
2.2	Lithology.....	24
2.3	Discontinuity network of the study area.....	26
2.3.1	<i>Fault network.....</i>	26
2.3.2	<i>Small-scale fracture network and structural compartments.....</i>	27
2.3.3	<i>Fracture properties .....</i>	28
2.3.4	<i>Summary.....</i>	29

---

2.4	Constraining the extent of major fractures and faults with georadar and seismic investigation data .....	30
2.4.1	<i>Interpretation of single-hole georadar reflection profile results .....</i>	<i>31</i>
2.4.2	<i>Interpretation of 3-D surface georadar results.....</i>	<i>33</i>
2.4.3	<i>Interpretation of surface seismic refraction tomography results.....</i>	<i>33</i>
2.4.4	<i>Summary.....</i>	<i>35</i>
2.5	Rock mechanical testing .....	35
2.6	Engineering geological model for the study area.....	36
2.7	Figures.....	38
<b>3</b>	<b>Establishing a block kinematic model for the study site using a multi-component geotechnical monitoring system.....</b>	<b>55</b>
3.1	Introduction.....	56
3.2	Design and implementation of the monitoring network .....	56
3.2.1	<i>Geological model of the study site .....</i>	<i>57</i>
3.2.2	<i>Installation of the monitoring network components .....</i>	<i>58</i>
3.2.3	<i>Data acquisition system .....</i>	<i>59</i>
3.3	Methodology and results of surface displacement measurements.....	59
3.3.1	<i>Geodetic survey.....</i>	<i>60</i>
3.3.2	<i>Simple benchmark line surveys.....</i>	<i>61</i>
3.3.3	<i>Crackmeters.....</i>	<i>61</i>
3.3.4	<i>Benchmark quadrilaterals.....</i>	<i>62</i>
3.3.4.1	<i>Method and results.....</i>	<i>62</i>
3.3.4.2	<i>Comparison with simple benchmark arrays and crackmeter monitoring .....</i>	<i>64</i>
3.3.5	<i>Displacement fields at the surface .....</i>	<i>65</i>
3.4	Methodology and results of displacement measurements at depth.....	66
3.4.1	<i>Methodology of inclinometer/extensometer surveys .....</i>	<i>66</i>
3.4.2	<i>Inclinometer raw data .....</i>	<i>68</i>
3.4.3	<i>Standard reduction of inclinometer data from a repeat survey.....</i>	<i>69</i>
3.4.4	<i>Error sources and correction schemes for inclinometer survey data.....</i>	<i>70</i>
3.4.5	<i>Calculation of the 3-D displacement vector along the boreholes .....</i>	<i>74</i>
3.4.6	<i>Results: displacement fields measured in the deep boreholes .....</i>	<i>75</i>
3.5	Integration of monitoring results to a block kinematic model .....	78

---

3.6	Analysis of the continuous measurements .....	79
3.7	Implication for the analysis of the acting rockslide processes.....	82
3.8	Figures.....	83
<b>4</b>	<b>Modelling the internal kinematics and deformation of a complex rockslide based on field data constraints obtained at the study site .....</b>	<b>109</b>
4.1	Introduction.....	110
4.2	Site description.....	111
4.3	Previous modelling studies of the 1991 Randa rockslide events .....	112
4.4	Modelling internal deformation of an unstable slope in dependence on the geometry of the basal sliding surface(s) .....	114
4.4.1	<i>Modelling task.....</i>	<i>114</i>
4.4.2	<i>Theoretical background .....</i>	<i>115</i>
4.4.3	<i>Modelling inclinometer/extensometer in UDEC .....</i>	<i>115</i>
4.4.4	<i>Modelling methodology and considered scenarios .....</i>	<i>116</i>
4.4.5	<i>Model properties.....</i>	<i>118</i>
4.4.5.1	<i>Rock joint properties.....</i>	<i>118</i>
4.4.5.2	<i>Rock block properties .....</i>	<i>119</i>
4.4.6	<i>Results and comparison with measured displacement fields.....</i>	<i>121</i>
4.4.6.1	<i>Case I - Planar sliding surface.....</i>	<i>121</i>
4.4.6.2	<i>Case II - Circular sliding surface.....</i>	<i>123</i>
4.4.6.3	<i>Case III - Bilinear sliding surface .....</i>	<i>124</i>
4.4.6.4	<i>Case IV - Stepped sliding surface .....</i>	<i>126</i>
4.4.7	<i>Discussion.....</i>	<i>127</i>
4.4.7.1	<i>Implications of the modelling results for the investigated slope instability.....</i>	<i>127</i>
4.4.7.2	<i>Implications for modelling complex rockslides .....</i>	<i>129</i>
4.5	Figures.....	130
<b>5</b>	<b>Conclusions and perspectives.....</b>	<b>149</b>
5.1	Conclusions .....	150
5.1.1	<i>Integrating geological and geophysical investigations towards a 3-D engineering geological model of an unstable slope in crystalline rock .....</i>	<i>150</i>
5.1.2	<i>Establishing a block kinematic model for the study site using a multi-component geotechnical monitoring system.....</i>	<i>151</i>

---

5.1.3	<i>Modelling the internal kinematics and deformation of a complex rockslide based on field data constraints</i> .....	152
5.1.4	<i>Implications for the slope stability assessment of the present day instability</i> .....	153
5.2	Perspectives and recommendations for further studies.....	153
<b>References</b> .....		<b>155</b>
<b>A-1</b>	<b>Appendix</b> .....	<b>163</b>
A-1.1	Borehole logging.....	164
A- 1.1.1	<i>SB 120</i> .....	164
A- 1.1.2	<i>SB 50N</i> .....	171
A- 1.1.3	<i>SB 50S</i> .....	174
A-1.2	Scanline mapping.....	177
A-1.3	Rock mechanical testing .....	182
A- 1.3.1	<i>Uniaxial tests</i> .....	183
A- 1.3.2	<i>Triaxial tests</i> .....	184
<b>Acknowledgements</b>		
<b>Curriculum vitae</b>		

## List of figures

- Figure 1-1: Tectonic map of Switzerland with sites of the investigations to select the main study site. Sites where temporary seismic monitoring was performed are denoted with stars, the other sites with filled circles..... 4
- Figure 1-2: Location of Randa in Switzerland and photo of the scarp of the 1991 Randa rockslide. Above the scarp the project area for the monitoring of the current instability is situated..... 6
- Figure 1-3: Geological map of the Matter valley (modified after Bearth 1964). The scarp of the 1991 rockslides is marked in black, the blue dotted line indicates the bypass gallery for the river Vispa built in 1992..... 7
- Figure 1-4: Tectonic map (top) and profile (bottom) of the Matter valley. Tectonic map modified after Steck et al. 1999; tectonic profile modified after Steck et al. 1997. .... 8
- Figure 1-5: Back-shearing model for basement nappes (modified after Epard & Escher 1996). By the formation of a shear zone the normal limbs of the evolving fold nappe are sheared backwards (i.e. to the left) and only weakly deformed. The investigated slope is situated within one of these weakly deformed limbs..... 8
- Figure 1-6: View along the Matter valley from S to N. The western slope of the valley (left) has been affected by the 1991 Randa rockslide. The eastern, foliation-parallel slope is characterised by slides parallel to foliation or involving debris and moraines..... 9
- Figure 1-7: Topographic map of the project area before the 1991 rockslide. The scarps of the two main rockslide events of the April 18 and May 09 1991 are indicated. Black lines mark the position of surface fractures that were active between the first and second rockslide event. .... 11
- Figure 1-8: Cross-section for the 1991 rockslide showing the suggested instability promoting fractures (Wagner 1991)..... 12
- Figure 1-9: Climate record for the five year period prior the 1991 rockslide (modified after Eberhardt et al. 2001). The climate data was recorded in the Matter valley at Zermatt (1638 m altitude) by METEOSCHWEIZ..... 12
- Figure 1-10: Geotechnical monitoring 1991-2000. Locations of open fractures at surface and retro-reflectors belonging to the geodetic survey are shown and specified according to their displacement information. The grey area delineates the assumed extent of the current instability; blue arrows denote the direction of surface displacements..... 15
- Figure 1-11: Results of the geodetic monitoring 1996-2000. Displacement magnitudes include error bars. Data and results provided by Crealp. .... 15
- Figure 1-12: Geotechnical and microseismic monitoring network designed and implemented for the research project. .... 17
- Figure 1-13: Geological and geophysical investigations performed for the research project. .... 18
- Figure 2-1: Possible instability scenarios for the investigated slope instability. The nomenclature of the rockslide types relates to Cruden & Varnes (1996) and Hungr & Evans (2004)..... 38
- Figure 2-2: Overview of the study area around the 1991 rockslide scarp. The mapped area is highlighted in green, the scarp region of the 1991 rockslide and other steep rock faces were

- analysed using aerial photographs. Topography taken from Landestopographie, sheet Mischabel 1:50 000..... 39
- Figure 2-3: Lithological units and subunits in the study area with dip direction of the foliation fractures plotted in blue. Digital elevation model provided by CREALP..... 40
- Figure 2-4: a) Aerial photograph of the study area around the scarp of the 1991 rockslides. (photo provided by Landestopographie) with the traces of faults and fracture zones. b) Stereonet of faults and fracture zones mapped at the surface. The set F1 is parallel to foliation and contains brittle-ductile shear zones. c) Stereonet of major fractures intersected by the borehole; pure phyllonites parallel to foliation (i.e. without fracture) are not plotted. The stereonet for the surface and borehole data show a good agreement of preferred fault and fracture zone orientation. .... 41
- Figure 2-5: Examples of faults mapped. a-b) Outcrop photograph and expanded sketch of the fault core of a F1 fault. The lithology above and below the fault are comparable; below the fault a large fracture is exposed c) Outcrop sketch of a F2 fault. d-e) Outcrop photograph and sketch of a F3 fault..... 42
- Figure 2-6: Thin sections of fault cores. a) Thin section taken from a foliation parallel fault F1. The thin section is oriented perpendicular to the foliation. In the phyllonitic fault core oxidated mylonitic bands (brown) surround rounded feldspar-rich lenses . b) Thin section taken from a steep N-S striking F3 fault (see Figure 2-5 d-e). A fine-grained fault gouge is shown in the enlarged view..... 43
- Figure 2-7: Traces, dip direction and dip of faults and fracture zones (mapped and estimated from aerial photographs). Digital elevation model provided by CREALP..... 44
- Figure 2-8: Structural compartments of the study area. For each compartment stereonet are given for the fractures, foliation fractures and faults (equal area, lower hemisphere, weighted). ..... 45
- Figure 2-9: Stereonets showing fracture sets within the three structural compartments (equal area, lower hemisphere, weighted). Foliation fractures are not shown. .... 46
- Figure 2-10: Properties of the fracture sets in structural compartment I, II & III. a) Mean normal set spacing calculated using negative exponential distribution parameters derived by maximum likelihood method and nonlinear least square fitting. For small sample numbers no reliable fit could be obtained. b) Mean trace length calculated using lognormal distribution fitted in least square sense and the Laslett estimation. c) Percentage of fractures with both ends connected to other fractures wrt number of fractures with both ends observable. d) Mean JRC values for the fracture sets in all structural compartments. .... 47
- Figure 2-11: Geophysical surface and subsurface investigations. On the surface 3-D georadar (grey area) and surface seismic profiles (blue lines) were measured. In the boreholes georadar single-hole and cross-hole test (light blue line) were performed. The extent of the current instability is indicated by yellow shading; active segments that show opening are highlighted in red. .... 48
- Figure 2-12: Principle of the single-hole georadar reflection method. a) Fracture plane reflecting the georadar signal. b) The characteristic reflection pattern generated by a planar reflector. .... 48
- Figure 2-13: Fracture mapping in SB 120 (modified after Willenberg et al. 2004). a) Incremental displacement magnitude along the hole and azimuth,  $\theta$  and dip,  $\phi$ , of the relative displacement

vectors. The stars at 5 and 103 m denote zones where casing deformation is related to ungrouted sections. b) Number of fractures per inclinometer interval (0.61m) derived from the optical televiewer image. c) Digitised fracture traces on the optical televiewer image. Major fractures are highlighted in orange and dip-direction and dip supplied. d) Georadar reflection image with predicted (solid) and picked (dashed) reflections. The six predictions shown could be associated with georadar reflections. .... 49

Figure 2-14: Fracture mapping in SB 50S. a) Incremental displacement magnitude along the hole and azimuth of the relative displacement vectors. b) Number of fractures per inclinometer interval (0.61m) derived from the optical televiewer image. c) Digitised fracture traces on the optical televiewer image. Major fractures are highlighted and dip-direction and dip supplied. d) Georadar reflection image with predicted (solid) reflections. .... 50

Figure 2-15: Fracture mapping in SB 50N. a) Incremental displacement magnitude along the hole and azimuth of the relative displacement vectors. b) Number of fractures per inclinometer interval (0.61m) derived from the optical televiewer image. c) Digitised fracture traces on the optical televiewer image. Major fractures are highlighted and dip-direction and dip supplied. d) Georadar reflection image with predicted (solid) reflection and reflection with corrected (dashed) dip. .... 51

Figure 2-16: Comparison of 3-D surface georadar and mapped faults and fracture zones. a) Map of the investigation area showing the three georadar fields, the plotted two upper fields are highlighted. b) Picked reflectors and diffractors in the investigation volume for the fields I and II c) Vertical cross-section through the georadar volume; the picked reflections and diffractors are denoted A-G. b) and c) were modified after Heincke et al. (2004). .... 52

Figure 2-17: Grid of surface seismic line. Plotted are P-wave velocities derived by refraction tomography at 15m below surface together with the faults and fracture zones extrapolated to 15 m depth. .... 53

Figure 2-18: Profile of calculated p-wave velocities in SB 120 for the seismic lines H1 (north-south direction, green) and Q2 (east-west profile, red) in comparison to the lithological and fracture records derived from optical televiewer images. For each cell (2.6 m) two velocity values are plotted with red and green dots. Major fractures are indicated in red on the digitised fracture intersections at the borehole wall. The histogram to the right shows the number of fractures per meter. .... 53

Figure 2-19: Analysis of uniaxial and triaxial laboratory testing applying Coulomb and Hoek-Brown failure criteria. .... 54

Figure 3-1: 5-m contour map of the study area showing the faults and fracture zones and instrumentation locations. The extent of the unstable rock mass is shown shaded. Active fractures and the location of monitoring devices for surface fracture opening are shown in Figure 3-2. .... 83

Figure 3-2: Location of retro-reflectors and benchmark arrays across fractures. Open fractures at the surface are shown as solid lines on the network of faults and fracture zones (dashed lines). Major open fractures are labelled. Fractures equipped with a benchmark quadrilateral are highlighted. .... 84

- Figure 3-3: Orientation of the fractures in the study area shown in lower hemisphere, equal area stereographic projection. Isolines follow 5,10,15,20% densities. Foliation fractures are not plotted. a) Small-scale fracture network mapped at the surface. Six fracture sets were identified. b) Minor fractures mapped within the boreholes SB 120, SB 50S and SB 50N. c) Faults and fracture zones mapped at the surface. d) Major fractures mapped within the boreholes. Three dominating families of faults and fracture zones were accounted for (F1-F3). ..... 85
- Figure 3-4: Composition of the casing installed in the boreholes showing the various integrated modules. .... 86
- Figure 3-5: On-site data acquisition system and wireless radio link to the station in the valley. The seismometers in the shallow boreholes are not shown. .... 86
- Figure 3-6: Surface displacements 1996-2003 derived from geodetic survey (results provided by CREALP). The locations of the retro-reflectors are shown in Figure 3-1. a) Magnitude of displacement vectors with error bars. b) Mean azimuth and dip of the displacement vector for reflectors between 2300 and 2400 m altitude. The shaded area denotes the error estimate. c) Mean azimuth and dip of the displacement vector for reflectors between 1900 and 2200 m altitude. .... 87
- Figure 3-7: Horizontal component of the surface displacement vectors plotted on a map of the site which shows active fractures (dashed lines) and the likely extent of the unstable part of the rock mass (shaded). The displacement vectors of the retro-reflectors of the geodetic survey (blue) and the borehole tops (green) are absolute since they are referenced to an external coordinate system. The displacement vectors across active fractures (red) indicate the relative displacements of the southern or eastern side with respect to the northern or western side. .... 88
- Figure 3-8: Results of all resurveys of the simple benchmark pairs during the period 2001-2003. The benchmark pairs at q2, o and x are equipped with wire-spring assemblies: the others are rock bolt pairs. Black dots denote measurements taken. .... 89
- Figure 3-9: Fracture-opening and temperature recorded by the crackmeters North (x2) and South (q2). The length-change curve is shown unfiltered after outlier-removal whereas the temperature curve was filtered using a 2-days low-pass filter. An expanded view of the data between August and September 2003 is shown in the Figure 3-10. The arrow indicates a sudden offset in q2 followed 5 days later by a gradual offset in x2. The latter is possibly of thermo-elastic origin. .... 90
- Figure 3-10: Expanded view of Figure 3-9 showing four weeks unfiltered records of crackmeter length-change (with outliers removed) and temperature. The diurnal length change fluctuations of  $\pm 0.1\text{mm}$  correlate with the daily temperature variations of  $\pm 7^\circ\text{C}$ . .... 90
- Figure 3-11: a) Illustration of the benchmark quadrilateral measurement and analysis principle. The initial quadrilateral geometry, ABCD, is delineated in grey and the deformed quadrilateral, ABC'D', in black. b) A pair of benchmark quadrilaterals in different planes across fracture 'r' (horizontal and vertical). .... 91
- Figure 3-12: a) The benchmark quadrilateral tool and benchmarks developed for the project. In operation, blocks A and B are clamped to their rails and block C slides until the pins below blocks A and C locate in the benchmarks. Block C is then clamped and the distance between



- the outer edges of blocks B and C measured with a caliper. b) Illustration of benchmark and locating-pin seating. The benchmarks are rockbolts which have a hemispherical recess milled into their heads into which the ball of the locating pin seats c) Technical details of the tool. (design Solexperts, Schwerzenbach, Switzerland; sketch modified after Peter Giger)..... 91
- Figure 3-13: Displacement magnitude and direction estimates derived from two different analysis procedures applied to the benchmark quadrilateral measurements at the fractures r, q2 and x2. The geometry of the arrays are shown at right and are essentially horizontal, except for the quadrilateral r-vertical (see Figure 3-11b). The direction of the displacement vectors are measured anticlockwise from the baseline AB looking down. Error bars were estimated by taking an error of 0.15 mm per length measurement. .... 92
- Figure 3-14: Comparison of displacement magnitude estimates from quadrilateral arrays, simple benchmark pairs and crackmeters at three active fractures where multiple measurements were made. The quadrilateral results are from Figure 3-13.: a) results for fracture r; b) results for fracture q2 and c) results for fracture x2. .... 93
- Figure 3-15: a) Photograph of the inclinometer probe which is 61 cm long. b) Photograph of the 2 m long INCREX extensometer probe being lowered into a casing. (Photographs by E. Eberhardt) ..... 94
- Figure 3-16: Coordinate systems used in the inclinometer/extensometer measurements. a) Top view of vertical inclinometer casing showing the groove pairs. A and B are the groove pairs at the surface and X and Y are the same groove pairs at depth. b) Series of inclinometer measurements which yield the inclination profile along the borehole. c) Illustration of the conversion of inclination change to inferred horizontal displacement vector. An angle change,  $\Delta\beta$ , in the x-direction implies a x-displacement of  $d_{x1}-d_{x0}$ . d) Conventions for deriving the 3-D displacement vector. .... 94
- Figure 3-17: a) Raw inclination data (X and Y-axes) of the initial survey of SB 120 expressed in degrees from vertical. b) Torsion profile measured with the spiral probe. c) Borehole trajectory (azimuth and dip) derived from the borehole geometry and optical televiewer logs. The trajectories derived from the raw inclination profiles in (a) are also shown for several different torsion corrections (see legend)..... 95
- Figure 3-18.: SB 50S and SB 50N raw data. a) Inclination profile of X- and Y-axes in SB 50S. b) Torsion measured with the spiral probe in SB 50S. c) Inclination profile of X- and Y-axes in SB 50N. d) Torsion measured with the spiral probe in SB 50N..... 95
- Figure 3-19: Illustration of standard method of inclinometer data reduction for S B120 using first repeat survey. a) Inclination profiles along the local X- and Y axes of the initial survey expressed in terms of deviation from vertical. b) Incremental displacements along the X- and Y-axes developed between the initial and first repeat survey. c) Incremental displacements along the A- and B-axes after rotation using the standard torsion correction (dashed lines). The corresponding cumulative horizontal displacement profiles,  $V_A$  and  $V_B$ , obtained by integration are shown in solid lines..... 96
- Figure 3-20: Conventions used for the analysis of cumulative horizontal displacement profiles. Steps in the cumulative inclination change curve indicate localised displacements. In

- crystalline rock, the slope between the steps depends on the presence of constant incremental inclination changes due to different block rotations. .... 97
- Figure 3-21: Illustration of the depth offset error and its correction for the first repeat survey in SB 120 a) Inclination profiles along the local X- and Y axes of the initial survey b-c) Effects of depth offsets on the cumulative A-and B-axis horizontal displacement change profile. The uncorrected form is shown in black. The grey lines denote the profiles after applying a uniform stretch to the depth scale of the first repeat profile with a range of extensions at the bottom to  $\pm 5$  cm in steps of 1 cm. The profile which best-matches the profile of initial survey was determined by cross-correlation and is shown in red. .... 98
- Figure 3-22: Illustration of the sensor rotation error and its correction for the third repeat survey in SB 120. a) Cumulative horizontal displacement profiles in the A- and B-directions for the first (green), second (red) and third repeat surveys after depth offset and empirical torsion correction. b) Effects of sensor rotation on the cumulative A- and B-axis cumulative displacement profiles obtained for the third repeat survey. The uncorrected profiles are shown in black whereas corrected profiles for various rotation angles are in grey. A sensor rotation of  $-0.08^\circ$  (light blue curve) gives a profile that is more in accord with the profiles of displacements obtained in the first (red) and second (green) repeat surveys. .... 99
- Figure 3-23: Derivation of 3-D displacement vector profiles from the combination of inclinometer and extensometer profiles for SB 120 a) Cumulative horizontal displacement profiles for the three repeat surveys after applying depth offset, sensor rotation and empirical torsion corrections (see Table 1-4). b) Cumulative axial displacement obtained by the INCRESX surveys. c) Incremental displacement magnitude. d-f) magnitude, dip and azimuth of the 3-D dislocation vector. .... 100
- Figure 3-24: Comparison of the 3-D displacement data from the fourth repeat survey of SB 120 with geological data from the optical televiewer images a) Magnitude of the 3-D dislocation vectors across localised displacement zones. b) Orientation of the 3-D dislocation vectors. c) Fracture traces from the optical televiewer images. Major fractures are highlighted and the dip vector given. d) Lithology (see legend for colour key). e) Fracture intensity f) Cumulative horizontal displacement. g) Cumulative axial displacement. .... 101
- Figure 3-25: Displacement data for SB 50S (top row). a) Cumulative horizontal displacements for the repeat surveys, with empirical torsion correction and application of depth offset. b) Incremental 2-D displacement vector. c) Magnitude of 2-D dislocation vector. d) Azimuth of 2-D dislocation vector. Displacement data for SB 50N (bottom row). e) Cumulative horizontal displacements for the repeat surveys, with empirical torsion correction and depth matching. f) Incremental 2-D displacement vector. g) Magnitude of 2-D dislocation vector. h) Azimuth of 2-D dislocation vector. .... 102
- Figure 3-26: Comparison of the 2-D displacement data from the fourth repeat survey of SB 50S with geological data from the optical televiewer images. a) Magnitude of the 2-D dislocation vectors across localised displacement zones. b) Orientation of the 2-D dislocation vectors. c) Fracture traces from the optical televiewer images. Major fractures are highlighted. d) Lithology (see legend for colour key). e) Fracture intensity. f) Cumulative horizontal displacement with empirical torsion correction and depth matching. .... 103

- Figure 3-27: Comparison of the 2-D displacement data from the fourth repeat survey of SB 50N with geological data from the optical televiewer images a) Magnitude of the 2-D dislocation vectors across localised displacement zones. b) Orientation of the 2-D dislocation vectors. c) Fracture traces from the optical televiewer images. Major fractures are highlighted. Shaded zones are open fractures. d) Lithology (see legend for colour key). e) Fracture intensity. f) Cumulative horizontal displacement with empirical torsion correction and depth matching. .... 104
- Figure 3-28: Orientation of active fractures mapped on the surface and at depth in the three deep boreholes. Lower-hemisphere, equal-area projection. .... 104
- Figure 3-29: 2-D block kinematic model of the investigated rock mass along the profile shown in the inset. a) Relative displacement vectors across dislocation zones, denoting the movement of the lower block wrt the upper. b) Absolute displacement vectors (i.e. expressed with respect to an external reference frame) for points along SB 120 Blue arrows denote surface displacement vectors, green arrows denote toppling of the blocks, light blue arrows translational sliding and brown arrows rotation as determined from the cumulative horizontal displacement profiles. For the two 50 m boreholes neither the surface displacement vector nor the inclination of the borehole displacement vectors are known. .... 105
- Figure 3-30: Continuous monitoring time series. a) Crackmeter record of surface fracture opening at fractures q2 and x2. b) Water pressure in SB 120 and SB 50S. c) Meteorological data provided by METEOSCHWEIZ: Precipitation (daily and cumulative annual) and snow height measured at Zermatt (station elevation 1638 m), both filtered with a 2-day lowpass filter. d) Temperature at the study site calculated from meteorological data from the valley using a linear temperature lapse of 0.51°C/100m and temperature record of the thermistor of the crackmeter x2. Atmospheric pressure extrapolated to the study site using a pressure lapse of 11.3 mbar/100m. .... 106
- Figure 3-31: a) Piezometer pressure measurements in SB 120 (blue) and SB 50S (red) with atmospheric pressure measured in the valley (data provided by METEOSCHWEIZ) and extrapolated to the study site. b) Expanded view I for SB 50S. c) Expanded view II for SB 50S. d) Expanded view I for SB 120. e) Expanded view II for SB 120. b-e show water pressures (not corrected for atmospheric pressure) from the left (red and blue) and atmospheric pressures from the right (light blue). .... 107
- Figure 4-1: a) Geological map of the study area showing the mapped lithologies, the fault and fracture zone network and the assumed extent of the unstable rock mass. The lithological units are labelled A and B according to their mechanical behaviour. b) Stereonets for the fractures, foliation fractures and faults for elevations 2000-2350 m. .... 130
- Figure 4-2: a) Horizontal surface displacement vectors (relative, i.e. one side of the active fracture with respect to the other: fracture opening in cyan; absolute, i.e. with respect to external reference frame: geodetic survey of reflectors and borehole tops in blue and green). Red segments of the fault and fracture zone network represent active opening surface fractures. b) Stereoplot showing the orientation of active fractures at the surface and at depth. The chosen direction for the modelling profile is approximately parallel to both the orientation of the active fractures and the direction of displacement. .... 131

- Figure 4-3: a) Profile of cumulative inclination changes for a two year period in SB 120 and inferred block rotations. b) Profile of cumulative vertical displacements showing two zones of shortening. c) Derived incremental displacement vector with incremental magnitude, azimuth and dip across dislocation zones are plotted to the right. The reference frame is bottom of the borehole with respect to the top..... 132
- Figure 4-4: Block model along the boreholes showing displacements at the borehole tops; also shown are absolute displacements along SB 120 obtained by the integration of the borehole displacements with geodetic displacement vectors. In the upper part (green arrows) inclinometer surveys indicate toppling, in the middle part (light blue arrows) sliding without block rotations was inferred and in the lowermost part (orange arrows) the bottom of the blocks is rotated towards the valley wrt the top..... 133
- Figure 4-5: Map showing the pre-rockslide topography before 1991 with orientations of active fractures before the second phase of the 1991 rockslide (after Schindler et al. 1993) and active fractures of the current instability. Also plotted are the inferred directions of sections for numerical modeling..... 134
- Figure 4-6: a) Discontinuum model used in Eberhardt et al. (2004). b) Discontinuum model used in Segalini & Giani (2004). Both models involve moderately inclined, through-going fractures dipping towards the valley as well as steep fractures dipping towards the valley..... 134
- Figure 4-7: General model geometry with lithological units of the two gneiss-types A and B together with the active fractures intersected by the boreholes. The model height zero refers to 970 m altitude..... 135
- Figure 4-8: Model geometries for the four kinematic models considered in the parametric study.. 135
- Figure 4-9: Conventions for the interpretation of measured and predicted cumulative horizontal displacement profiles in SB 120. Note that displacements are expressed with respect to the borehole top (positive displacements on the A axis indicate movements to the SSE). Steps in the cumulative displacement profile are interpreted as localised displacements on active fractures. In the upper part of the curves, constantly decreasing (A) and increasing (B) cumulative displacements indicate that the lower part of the blocks between the active fractures is rotated to NW which is identical with a toppling movement to the SW. In the middle part both cumulative displacement profiles are vertical which is interpreted as a sign for the absence of block rotations. In the lowermost section increasing (A) and decreasing (B) cumulative displacements indicate that the lower part of the blocks rotates towards SW..... 136
- Figure 4-10: a) Model I a - planar sliding surface with elastic blocks (a). Three areas A-C with different displacement patterns were distinguished. The \* highlights a block with small displacements intersected by the borehole. Predicted borehole displacement profiles are given in Figure 4-12. b) Model I b - planar sliding surface with elastic blocks with foliation fractures. Only two areas A-B with different displacement patterns were distinguished. .... 137
- Figure 4-11: Model I c - planar sliding surface with elasto-plastic blocks. Grey circles indicate that internal damage by tensile failure occurs mainly in the large blocks of area A; in area B only some blocks show internal damage..... 138
- Figure 4-12: Comparison of measured displacement profiles from SB 120 (a,c) and predicted displacement profiles for model I a - planar sliding surface with elastic blocks (b,d). The

displacements are expressed with respect to the borehole top and cannot be directly compared against the absolute block displacements shown in Figure 4-10a. ....	139
Figure 4-13: Model II a and II b - circular sliding surface with elastic blocks (a) and circular sliding surface with elastic blocks with foliation fractures (b). Next to the circular sliding surface steep fractures dipping away from the valley were added to the model. Predicted borehole displacement profiles for case II b are given in Figure 4-15. ....	140
Figure 4-14: Model II c - circular sliding surface with elasto-plastic blocks. ....	141
Figure 4-15: Comparison of measured displacement profiles from SB 120 (a,c) and predicted displacement profiles for model II b circular sliding surface with elastic blocks and foliation fractures (b,d). The displacements are expressed with respect to the borehole top and cannot be directly compared against the absolute block displacements shown in Figure 4-13b. ....	142
Figure 4-16: a) Model III a and III b - bilinear sliding surface with elastic blocks. In area A the displacement vectors are parallel to the lower sliding surface, in area B parallel to the steep back limitation of the unstable rock mass b) Model III b - bilinear sliding surface with elastic blocks with foliation fractures. Two fractures (1-2) accommodate the internal deformation of the block assembly. Predicted borehole displacement profiles are shown in Figure 4-18. ....	143
Figure 4-17: Model III c - bilinear sliding surface with elasto-plastic blocks. ....	144
Figure 4-18: Comparison of measured displacement profiles from SB 120 (a,c) and predicted displacement profiles for model III b - bilinear sliding surface with elastic blocks with foliation fractures (b,d). The displacements are expressed with respect to the borehole top and cannot be directly compared against the absolute block displacements shown in Figure 4-16. ....	145
Figure 4-19: a) Model IV a and IV b - stepped sliding surface with elastic blocks. Foliation fractures were only added below the investigated part of the rock mass. b) Model IV b - stepped sliding surface with elastic blocks with foliation fractures. Predicted borehole displacement profiles are given in Figure 4-21. ....	146
Figure 4-20: Model IV c - stepped sliding surface with elasto-plastic blocks with foliation fractures. Internal damage by tensile failure and yielding connects the intermittent fractures dipping towards the valley. In the lower part of the figure (<1100 m model height), internal damage is controlled by yielding. ....	147
Figure 4-21: Comparison of measured displacement profiles from SB 120 (a,c) and predicted displacement profiles for model IV b - stepped sliding surface with elastic blocks with foliation fractures (b,d). The displacements are expressed with respect to the borehole top and cannot be directly compared against the absolute block displacements shown in Figure 4-19b. ....	148
Figure A- 1: SB 120 optical televiewer log 0-30m showing digitised fractures, calculated dip directions and dip and lithological descriptions. ....	164
Figure A- 2: SB 120 optical televiewer log 30-55 m showing digitised fractures, calculated dip directions and dip and lithological descriptions. ....	165
Figure A- 3: SB 120 optical televiewer log 55-80 m showing digitised fractures, calculated dip directions and dip and lithological descriptions. ....	166

Figure A- 4: SB 120 optical televiewer log 80-105 m showing digitised fractures, calculated dip directions and dip and lithological descriptions.....	167
Figure A- 5: SB 120 optical televiewer log 105-118 m showing digitised fractures, calculated dip directions and dip and lithological descriptions.....	168
Figure A- 6: SB 120 well logs 0-60 m: Lithology, major fractures, fractures per meter, 4-arm caliper, borehole and inclinometer casing inclination, borehole azimuth, spectral gamma (gross gamma), K-U-Th content derived from spectral gamma log and observations during drilling. ....	169
Figure A- 7: SB 120 well logs 60-120 m: Lithology, major fractures, fractures per meter, 4-arm caliper, borehole and inclinometer casing inclination, borehole azimuth, spectral gamma (gross gamma), K-U-The content derived from spectral gamma log and observations during drilling. ....	170
Figure A- 8: SB 50N optical televiewer log 0-30m showing digitised fractures, calculated dip directions and dip and lithological descriptions.....	171
Figure A- 9: SB 50N optical televiewer log 30-51 m showing digitised fractures, calculated dip directions and dip and lithological descriptions.....	172
Figure A- 10: SB 50N well logs: Lithology, major fractures, fractures per meter, 4-arm caliper, borehole and inclinometer casing inclination, borehole azimuth, spectral gamma (gross gamma), K-U-Th content derived from spectral gamma log and observations during drilling. ....	173
Figure A- 11: SB 50S optical televiewer log 0-30m showing digitised fractures, calculated dip directions and dip and lithological descriptions.....	174
Figure A- 12: SB 50S optical televiewer log 30-52.5m showing digitised fractures, calculated dip directions and dip and lithological descriptions.....	175
Figure A- 13: SB 50S well logs: Lithology, major fractures, fractures per meter, 4-arm caliper, borehole and inclinometer casing inclination, borehole azimuth, spectral gamma (gross gamma), K-U-Th content derived from spectral gamma log and observations during drilling. ....	176
Figure A- 14: Histograms of normal-set spacing (left) and trace length (right) with fitted distributions and distribution means for fracture sets of the structural compartment I. Part1. ....	177
Figure A- 15: Histograms of normal-set spacing (left) and trace length (right) with fitted distributions and distribution means for fracture sets of the structural compartment I. Part2. ....	178
Figure A- 16: Histograms of normal-set spacing (left) and trace length (right) with fitted distributions and distribution means for fracture sets of the structural compartment II & III. Part1. ....	179
Figure A- 17: Histograms of normal-set spacing (left) and trace length (right) with fitted distributions and distribution means for fracture sets of the structural compartment II & III. Part2. ....	180

---

Figure A- 18: Histograms of normal-set spacing (left) and trace length (right) with fitted distributions and distribution means for fracture sets of the structural compartment II & III. Part3. ....	181
Figure A- 19: Stress-strain curves of uniaxial tests. ....	183
Figure A- 20: Stress-strain curves of triaxial tests. Confining pressures are plotted at the end of stress-strain curves. ....	184

## List of tables

Table 1-1: Sites and characteristics of slope instabilities of the preliminary investigations.....	5
Table 1-2: Dip direction and dip of the fracture sets defined by Wagner (1991), fault sets defined by Girod (1999) and description and structural classification. ....	11
Table 2-1: Overview of mapped lithologies. Description on mineral content is based on field mapping,*values taken from Girod (1999).....	25
Table 2-2: Mean orientation of fracture sets, foliation and faults in the study area.....	28
Table 3-1: Specifications of monitoring network components at surface and at depth.....	59
Table 3-2: Specifications for the crackmeters.....	61
Table 3-3: Specifications for the inclinometer/extensometer and spiral probes. ....	67
Table 3-4: Corrections and resulting displacements of the borehole bottom wrt top for the repeat surveys in SB 120. ....	74
Table 3-5: Correlation of dislocation zones, 3-D displacement vectors and fracture data for SB 120. The rake angle is the direction of slip in the plane of the fracture measured anticlockwise from the dip direction looking down. Most dislocations above 100 m imply predominantly shear movement with the footwall moving up-dip with respect to the hanging wall. ....	76
Table 3-6: Corrections and resulting displacements of the borehole bottom wrt top for the repeat surveys in SB 50S. ....	77
Table 3-7: Correlation of dislocation zones, 3-D displacement vectors and fracture data for SB 50S.	78
Table 3-8: Corrections and resulting displacements of the borehole bottom with respect to (wrt) top for the repeat surveys in SB 50N. ....	78
Table 3-9: Correlation of dislocation zones, 3-D displacement vectors and fracture data for SB 50N. ....	78
Table 3-10: Specifications for the piezometers. ....	81
Table 4-1: Modelled instability scenarios.....	117
Table 4-2: Overview of joint parameters for modelling.....	118
Table 4-3: Measured intact rock properties and rock mass properties based on GSI.....	119
Table 4-4: Overview of block parameters for modelling. ....	120
Table 4-5: Parameters for the presented models. ....	120
Table 4-6: Model result matrix.....	128
Table A- 1: Rock mechanical testing results. a) Results of the uniaxial tests. b) Results of the triaxial tests; the friction angle and cohesion were derived using the Coulomb-failure criterion. ....	182



## Summary

Rock slope instabilities in fractured crystalline rock tend to be complex. In many cases, planes of weakness like those associated with foliation, large faults or highly persistent fractures may dip away from the valley or may not be present. In such cases the failure surface has to develop by stepping through various fracture sets involving the failure of intact rock bridges and strength degradation along the sliding surface by means of progressive failure. To improve the understanding of the mechanisms leading to the development of such failure surfaces and the geological conditions under which these processes occur, a multidisciplinary project was initiated focussing on an unstable rock slope above the village of Randa (VS) in the Swiss Alps. The slope is situated in gneissic rocks with good to average rock mass quality. The foliation dips away from the valley which is in general favourable for slope stability. Nevertheless, the moving rock mass sits above the scarp of a multiple-event rockslide that occurred in 1991, involving 30 mio m<sup>3</sup>. To date, the unstable rock mass is slowly moving at surface displacement rates of up to 2 cm/year. In summer 2001, a multi-component geotechnical and microseismic monitoring network was installed at the surface and within three deep boreholes drilled into the unstable rock mass to depths of 50, 50 and 120 m. The installation campaign was accompanied by extensive field mapping and geophysical surface and borehole experiments. Within the framework of this project the focus of this thesis involves: i) the reconnaissance of the 3-D geological structure of the slope, ii) assessing the displacement fields at the surface and in boreholes using data from the geotechnical monitoring network, and iii) modelling the internal deformation of the unstable rock mass.

The displacements of the unstable rock mass were found to be distributed on a network of fault and fracture zones. Field mapping revealed that this large-scale discontinuity network should be regarded separately from the small-scale fracture network with mean trace lengths and normal set spacing in the range of 1-3 m. For the large-scale fault and fracture zone network two fault sets dipping NW and E and one fault set parallel to foliation were accounted for. The persistent nature of these features (i.e. minimum extent > 30 m) was confirmed by a joint analysis of single-hole georadar reflections and fracture data from optical televiewer images. Large, persistent faults or dominant fracture sets dipping towards the valley (i.e. to SE) which may serve as through-going sliding surfaces could not be identified either at the surface or in the boreholes.

Opening rates of surface fractures were measured with simple benchmark line surveys, continuously recording crackmeters and within benchmark quadrilateral arrays. The latter allow the orientation of the displacement vectors across the opening fractures as well as the magnitudes to be estimated. A special benchmark measurement tool was constructed for the readings in the benchmark quadrilateral arrays that was capable of measuring the small displacements encountered. The measurements revealed opening rates of several millimetres per year with a fluctuating signal overprinting a steady fracture opening rate. The fluctuations are probably of thermo-elastic origin. The direction of displacement vectors across different active fractures was found to lie within  $\pm 30^\circ$  from the normal to the strike of the fracture.

The analysis of inclinometer-/extensometer surveys from the deep boreholes brought to light deficiencies in the standard analysis procedure when applied in inclined boreholes with contorted

casings. After carefully eliminating systematic errors in the inclinometer measurements, profiles of horizontal displacements along the boreholes were obtained. For the 120 m borehole, these could be combined with profiles of axial strain to obtain the profiles of 3-D displacement vectors. The latter revealed that most of the active fractures belong to the set of NW-dipping faults with moderate to steep dip angles. The major active zones showed dislocations of up to 5 mm/year, which largely involve shear movement in a normal faulting sense (i.e. footwall moves up-dip with respect to hanging wall). In all cases, in-plane slip directions were within 30° of alignment with the fracture dip directions. The distribution of displacements on the fault and fracture zone network, which was measured at the surface and in the boreholes, suggested that the rock mass is dissected into various blocks of 10-20 m dimensions. In addition, the interpretation of the inclinometer surveys revealed that these blocks exhibit either toppling, translational sliding or rotational movements on a deeper sliding surface that was not intersected by the boreholes.

In order to investigate the instability processes, consideration had to be given to the fact that the location and geometry of the basal sliding surface(s) could be identified neither by surface- nor borehole observations. As such, numerical simulations involving the 2-D distinct element code (UDEC) were run to test and validate different instability scenarios that produce similar internal deformation patterns as those measured. Based on the four model geometries tested, fairly good agreement between modelled and measured displacement patterns were achieved for models involving either stepped or persistent planar sliding surfaces. The agreement with other model geometries (i.e. circular and bilinear sliding surfaces) was not as good. The step-path model gave especially promising results with respect to the geological model and indicators pointing to progressive failure through tensile yielding leading to a through-going failure plane that is not of tectonic origin. New insights into how displacement patterns within a fractured rock mass relate to the geometry of possible sliding surface(s) have been developed that provide valuable input into better understanding rockslide processes in crystalline rock.

Due to the multidisciplinary approach of the research project, the results presented in this thesis could be constrained and verified by comparing the results obtained using different investigation techniques, as applied to the mapping of faults and major fractures in crystalline rock, the geotechnical measurements of fracture opening at the surface or the interpretation of borehole displacement data. Similarly, the combination of geological mapping, the analysis of monitoring data and numerical modelling, such that the results constrained each other, proved to be necessary to better understand the processes acting on the investigated complex rockslide.

## Zusammenfassung

Felsrutschungen im geklüfteten Fels neigen zu Komplexität und häufig fehlen Trennflächen mit herabgesetzter Scherfestigkeit, wie zum Beispiel Schieferungsflächen, Störungen oder durchgängige Trennflächen, oder fallen gegen den Hang ein. In solchen Fällen muss sich ein getreppter Scherhorizont entwickeln, der zum einen durch bestehende Kluftsysteme verläuft und zum anderen durch den Bruch intakter Gesteinsbrücken durch progressive Bruchfortpflanzung gebildet wird. Um die Prozesse besser zu verstehen, die zu der Bildung eines solchen Scherhorizontes führen, und auch die geologischen Rahmenbedingungen, unter denen dies auftritt, wurde ein multidisziplinäres Forschungsprojekt gestartet; Ort der Untersuchungen ist ein instabiler Felshang oberhalb der Ortschaft Randa (Wallis) in den Schweizer Alpen. Dieser Felshang besteht vorwiegend aus Gneisen, deren Gebirgsqualität als mittel bis gut klassiert werden kann. Die Schieferung fällt in den Hang ein, was generell einen günstigen Einfluss auf die Hangstabilität haben sollte. Trotzdem gehört das Untersuchungsgebiet zu einer instabilen Felsmasse, deren Volumen auf 2.5-9 mio m<sup>3</sup> geschätzt wird und Oberflächenverschiebungen von bis zu 2 cm/Jahr aufweist. Es schliesst sich zudem an die Anrissnische eines mehrphasigen Bergsturzes mit einem Volumen von 30 mio m<sup>3</sup> aus dem Jahr 1991 an. Im Sommer 2001 wurde an der Oberfläche und in drei tiefen Bohrungen ein Multikomponenten-Messsystem für geotechnische und mikroseismische Messungen eingerichtet; dafür wurden Bohrungen 50, 50 und 120 m tief in die instabile Felsmasse abgeteuft. Zeitgleich wurden eine geologische Kartierung und geophysikalische Experimente in den Bohrlöchern und von der Oberfläche aus durchgeführt. Im Rahmen dieses Forschungsprojektes konzentriert sich diese Arbeit auf folgende Aspekte: i) die Erkundung der geologischen Struktur des Hanges in 3-D, ii) die Bewertung der Verschiebungsfelder an der Oberfläche und in der Tiefe, und iii) die Modellierung interner Deformationen in instabilen Hängen.

Es zeigte sich, dass die Verschiebungen der instabilen Felsmasse auf ein Netzwerk von Störungen und Kluftzonen verteilt sind. Dieses weiträumige Netzwerk liess sich anhand der Kartierungen von dem klein-massstäblichen Kluftnetzwerk abgrenzen, das durchschnittliche Kluftlängen und -abstände von 1-3 m aufweist. Das Netzwerk aus Störungen und Kluftzonen umfasst zwei Sets mit mittlerem bis steilen Einfallen nach Nordwest und Ost und ein Set parallel zur Schieferung. Die weiträumige Erstreckung dieser Trennflächen (>30 m) konnte durch eine gemeinsame Auswertung von Inloch-Radar-Reflexionen und Bohrlochkamera-Bildern bestätigt werden. Allerdings konnten keine grossen durchgängigen Trennflächen kartiert werden - weder an der Oberfläche noch in den Bohrlöchern-, die mittelsteil aus dem Hang einfallen und daher als durchgängige Gleithorizonte dienen könnten.

Kluftöffnungsraten an der Oberfläche wurden mit einfachen Messbolzen-Paaren, kontinuierlich messenden Rissmetern und Messbolzen-Vierecken erfasst; die Messung der Abstände in den Messbolzen-Vierecken erlaubte zudem die Bestimmung des Kluftöffnungsvektors. In Hinblick auf die geringen Verschiebungsraten wurde für die Abstandsmessungen in den Messbolzen-Vierecken ein spezielles Messgerät entwickelt. Die Messungen brachten Kluftöffnungsraten von einigen Millimetern pro Jahr, deren konstanter Trend von einem fluktuierenden Signal überprägt wird, das thermo-elastischen Effekten zugeschrieben wurde. Die Richtung der Kluftverschiebungen weicht  $\pm 30^\circ$  von der Senkrechten zum Kluftstreichen ab. Die Auswertung von Inklinometer-/Extensometermessungen brachte Defizite bei den Standardauswerteverfahren zu Tage, sobald

diese für geneigte Bohrungen mit verdrillten Messrohren angewendet werden. Erst nachdem systematische Fehler in den Inklinometermessungen sorgfältig korrigiert waren, konnten die erhaltenen horizontalen Verschiebungsprofile mit denen vertikaler Verschiebungen kombiniert werden. Die so erhaltenen 3-D Verschiebungsvektoren zeigten auf, dass die meisten aktiven Trennflächen dem Set mittelsteil bis steil nach Nordwesten einfallender Störungen angehören. Die Hauptverschiebungszonen weisen Verschiebungen von bis zu 5mm/Jahr auf, wobei die hauptsächlich Scher-Bewegungen auftreten, bei denen sich der liegende gegenüber dem hangenden Block nach oben verschiebt. Die Schervektoren auf den Flächen weichen  $\pm 30^\circ$  vom Trennflächeneinfallen ab. Dass die Verschiebungen an der Oberfläche und in der Tiefe auf dem Störungsnetzwerk stattfinden, legte nahe, dass die Felsmasse in Blöcke von 10-20m Grösse zerlegt ist. Diese Blöcke weisen zudem unterschiedliche Kipp-, Rutsch- und Rotationsbewegungen auf, wie aus den Resultaten der Inklinometermessungen geschlossen werden konnte.

Um die Prozesse der Hanginstabilität genauer zu untersuchen, musste besonders berücksichtigt werden, dass die Lage und Geometrie des Gleithorizontes weder durch die Untersuchungen an der Oberfläche noch in den Bohrungen bestimmt werden konnte. Daher wurde eine Reihe von numerischen Simulationen beruhend auf 2-D Diskontinuum Ansätzen (UDEEC) durchgeführt, um bei verschiedenen Instabilitätsszenarien zu testen, ob sich ähnliche interne Verformungen wie die gemessenen modellieren lassen. Von den vier getesteten Modellgeometrien konnte besonders für getreppte und ebene Gleitflächen eine gute Übereinstimmung von gemessenen und modellierten Verformungsfeldern erreicht werden. Weniger gute Übereinstimmung zeigten Modelle mit einer runden oder bi-linearen Gleitfläche. Als viel versprechend wurde besonders Modell „getreppte Gleitfläche“ angesehen, da es dem geologischen Modell des Hanges entspricht und auch Anzeichen dafür aufweist, dass sich durch progressive Bruchfortpflanzung mit Zugversagen durchgängige Scherflächen bilden können, die von nicht tektonischem Ursprung sind. Die gewonnen Erkenntnisse, wie interne Verformungsmuster mit der Geometrie sich entwickelnde Gleitflächen zusammenhängen, ergeben einen weiteren Schritt, die Prozesse von Felsrutschungen in geklüftetem Gebirge zu verstehen.

Augrund des multidisziplinären Projektansatzes beruhen die Ergebnisse, die in dieser Arbeit präsentiert werden, auf der gegenseitigen Verifizierung der Resultate verschiedener angewandter Erkundungsmethoden; so die Kartierung von Störungen und Kluftzonen im kristallinen Gebirge, die geotechnische Kluftöffnungsmessungen und die Interpretation von Verformungsmessungen in Bohrlöchern. Gleichzeitig zeigt diese Arbeit auch, dass zum Verstehen von komplexen Felsrutschungen eben diese Kombination verschiedener Untersuchungsmethoden und Ansätze nötig ist; in diesem Fall die Kombination von geologischer Kartierung, geotechnischem Monitoring und numerischen Simulationen.

# 1 Introduction

## 1.1 Study motivation

Large instabilities in natural rock slopes require extensive technical and economic efforts with respect to their recognition, prediction and/or mitigation, and the development of early warning systems. Considerable advances have been made concerning the risk management with early warning systems and improved mitigation techniques; for example surface velocities can be used to predict failure (Voight 1989, Crosta & Agliardi 2002). In the Swiss Alps, examples of effective early warning systems and mitigation measures for rock slope instabilities have been reported (Eyer et al. 1998, Brassler & Gruner 2002, Keusen 2002). However, to increase the effectiveness of early warning systems and risk management, more insight into the underlying mechanisms leading to slope failure is needed.

The need of to better understand the instability mechanisms applies especially to slope instabilities in fractured crystalline rock masses where the potential failure plane does not follow obvious large-scale planar structures like bedding-/ foliation planes or faults. Under such conditions, the potential failure surface may develop by stepping through several fracture sets or by failure of intact rock bridges (Einstein et al. 1983, Eberhardt et al. 2004). These so called progressive failure processes have been studied intensely in laboratory tests (Reyes & Einstein 1991, Einstein & Stephansson 2000, Gehle & Kutter 2003) and in fracture mechanics theory (e.g. Ingraffea 1987, Kemeny 1993). In slope stability analysis, several approaches have been tested for incorporating progressive failure in numerical modelling methods (e.g. Kawamoto & Takeda 1979, Chowdhury 1992, Einstein & Lee 1995, Tanaka 1998, Eberhardt et al. 2004). Most of these studies however have focussed on the back analysis of natural and engineered (e.g. open pit mine) rock slope failures.

Even though some famous large rockslides are known to have occurred in fractured rock masses without pre-existing failure surfaces (Huber 1992, Schindler et al. 1993), field studies on the manifestation of progressive failure mechanisms in rock slopes prior to catastrophic failure are scarce. Most field studies relate to monitoring progressive failure processes in deep mines and underground rock laboratories for nuclear waste disposal. To address these deficiencies, the research project "*Rockslide processes and mechanisms: Progressive development of shear/slide surfaces in rock slopes*" was initiated in 2000. This multidisciplinary research project of the groups of Engineering Geology (EG) and of Applied and Environmental Geophysics (AUG) of ETH Zürich comprises the geological and geophysical investigation of the unstable rock mass, geotechnical monitoring, microseismic monitoring and numerical modelling on the basis of the results obtained at the study site.

## 1.2 Thesis objectives

This thesis represents one of three parts of the research activities within the aforementioned multidisciplinary project. The primary objective of the thesis is to develop a 3-D engineering geological and kinematic model of an unstable slope in fractured crystalline rock, which can serve as a basis for analysing the processes leading to a potential failure. With respect to analysing possible progressive failure mechanisms at the study site, the construction of a three-dimensional lithological and discontinuity model on the basis of geological mapping and geophysical investigations is crucial. In this context the issues of discontinuity persistence sub-parallel to the potential failure surface and the

interconnectivity of the fracture network must be addressed. Furthermore, the quality of the intact rock plays an important role, as not only sliding along pre-existing, connected discontinuities must be considered but the possibility of intact rock failure as well.

Pursuant to the primary objective, a second task is the design and implementation of a monitoring network at the study site and the analysis of the resulting data in order to constrain the three-dimensional displacement fields. An objective is to distinguish whether the displacements within the rock mass are localised along large discontinuities or whether the small scale fracture network or intact rock accommodate much of the distributed rock mass deformation.

The third key objective of this thesis is to constrain the location of slide surfaces in crystalline rock based on numerical modelling methods. The approach is to integrate the geological model with the measured displacement field data so as to obtain a kinematic description of the slope instability. With respect to the multidisciplinary nature of the research project, these results offer the possibility of better constraining and interpreting the active geophysical experiments conducted at the study site and the processing of microseismic data.

### **1.3 Structure of the thesis**

The thesis is divided into three main chapters. Basic information about the study site and the work performed for the thesis is presented in the introduction. This includes the geological setting of the selected study site Randa, the documentation of an earlier rockslide event (30 mio m<sup>3</sup>) at the site that occurred in 1991, a review of the previous studies relating to the slope instability, a summary of the information available at the beginning of the study and the descriptions of field investigation techniques.

Chapter 2 presents a detailed study of a fractured crystalline rock mass and provides the main constraints for the engineering geological model for the current instability with an estimated volume of 2.7-9.2 mio m<sup>3</sup> (Ischi et al. 1991). This model attempts to identify which rock types and discontinuities promote slope instability. The chapter includes the description of representative rock types on the basis of lithological mapping and rock mechanical laboratory tests. Special attention is directed towards the analysis of the discontinuity network at the study site and on how geophysical surface and borehole experiments made it possible to compare mapping and experimental results.

Chapter 3 focuses on the geotechnical monitoring network, the displacement measurements and their analysis. As displacements relating to the slowly moving rockslide with maximum annual surface displacements of 1.5-2 cm had to be analysed with a high degree of precision, the improvement of standard correction schemes for the displacement measurements became necessary. To conclude this chapter, a block kinematic model of the investigated slope section is presented that includes the discontinuities accommodating the rock mass deformation and the resulting displacement fields.

The subsequent numerical slope stability modelling is described in Chapter 4. Different instability scenarios and their displacement patterns are modelled using the distinct element code UDEC (ITASCA 2000). The findings of the modelling study are used to constrain which basal sliding plane can cause the measured complex internal deformation of the unstable rock mass. The discussion interprets the results with respect to the failure mechanisms to be inferred for the study site.

Chapter 5 summarises the findings and concludes with several implications relating to the research project and the progressive development of shear/slide surfaces in massive brittle rock.

## 1.4 Investigation site

### 1.4.1 Selection of the study site

At the start of the project, preliminary investigations at seven rockslide and rockfall sites in Switzerland (Figure 1-1 and Table 1-1) were conducted to find a research site with the appropriate conditions to meet the study objectives, namely one involving a massive, unstable fractured rock slope. The evaluation focussed on the key instability mechanism of interest to the project which is the progressive development of a sliding plane. Thus sites without known pre-existing sliding planes, where the formation of a failure surface through non-persistent fractures may be required for failure, were favoured. Accessibility of the site for drilling and instrumentation installation was also a factor as was the ambient seismic noise level (i.e. traffic on roads or railways) for the microseismic monitoring. For each of the seven sites, information on the estimated volumes of the unstable rock mass, mean annual displacements, preliminary geological models, available infrastructure and expected noise was gathered (Table 1-1). At three sites (Randa, Val del Infern and Schynige Platte) temporary seismic stations were installed for several weeks in order to measure the noise level at the sites.

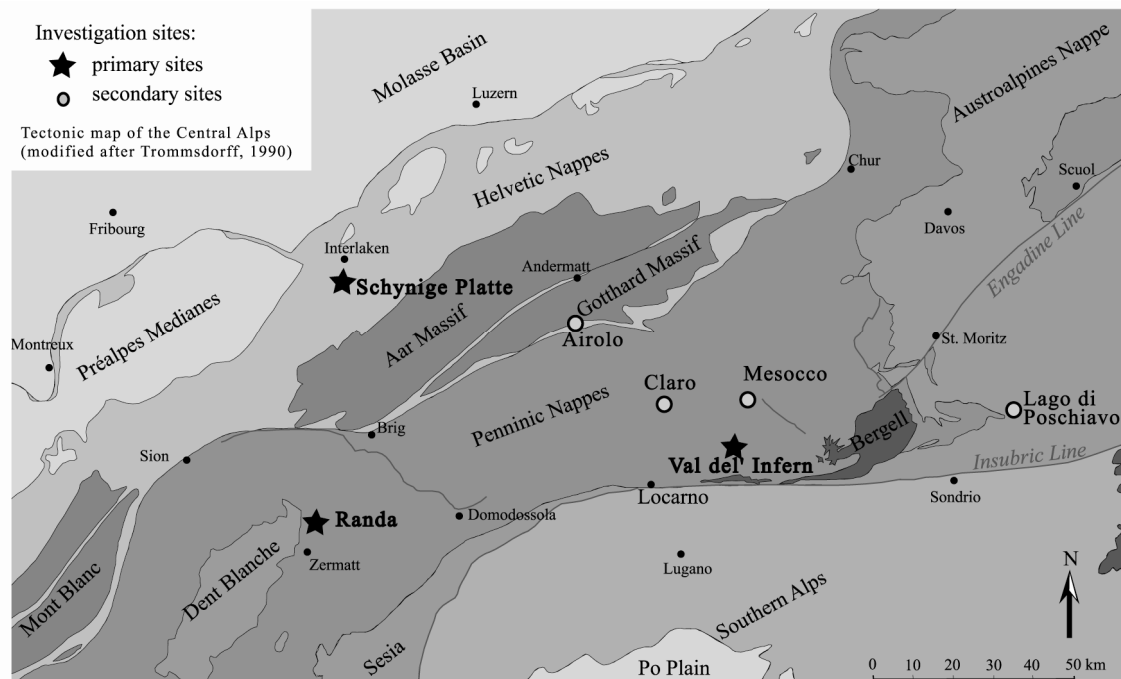


Figure 1-1: Tectonic map of Switzerland with sites of the investigations to select the main study site. Sites where temporary seismic monitoring was performed are denoted with stars, the other sites with filled circles.



Table 1-1: Sites and characteristics of slope instabilities of the preliminary investigations.

Site	Randa	Schynige Platte	Val del Infern	Airolo	Claro/ Alpe di roscioro	Mesocco	Lago di Poschiato
Tectonic position	Penninic nappes	Helvetic nappes	Penninic nappes	Penninic nappes	Penninic nappes	Penninic nappes	Austroalpine nappes
Rock type	Gneisses	Limestones and marls	Gneisses	Schists and gneisses	Gneisses and amphibolites	Schists and gneisses	Gneisses
Direction of foliation / bedding w.r.t orientation of the slope	Foliation dipping away from the valley	Bedding dipping gently towards the valley	Foliation dipping away from the valley	Foliation dipping away from the valley	Foliation dipping away from the valley	Foliation dipping away from the valley	Foliation dipping away from the valley
Estimated volumes	2.7-9.2 mio m <sup>3</sup>	350.000 m <sup>3</sup>	5.000 - 100.000 m <sup>3</sup>	50.000 m <sup>3</sup>	100.000 – 750.000 m <sup>3</sup>	100 m <sup>3</sup>	400 m <sup>3</sup>
Measured displacements	1-2 cm/a	3-4 cm/a	0.5-1 cm/a	0.3-10 cm/a	4-5 cm/a (rockfall 150.000 m <sup>3</sup> 2002)	1-5 cm/a (rockfall in 2001)	1 mm/week (remediation in 2001)
Inferred instability mechanism	sliding on fractures	Sliding on marl layer	Sliding on fractures	Chevron topple (Cruden & Varnes 1996)	Sliding on fractures	Sliding and toppling	Sliding on fractures
Existing geotechnical measurements	Geodetic survey, crackmeter	Extensometers, inclinometer, crackmeters	Geodetic survey	Geodetic survey, inclinometers	C	Geodetic survey, inclinometer, crackmeters, anchor load cells	Crackmeters
Infrastructure	None	Train	Road	None	None	Road	Road, train
Noise level	Low	High	High	Low	Low	High	high
References for reports and related studies	Ischi et al. 1991, Schindler et al. 1993	Keusen 2000, Senn 2002	Krähenbühl 2004, Zvanen 1999, Keusen 2002	Oppizzi 1995	Seno 1996	Müller & Bonanomi 1996, Spillmann 2001	Keusen & Graf 2000, Agliardi et al. 2001, Fraefel 2002

After evaluating the characteristics of the seven candidate sites, the Randa site was selected. The site is situated in the western Swiss Alps, canton Wallis, in the N-S trending Matter valley (Figure 1-2). On the western slope of the valley, above the village of Randa, an unstable rock mass is situated adjacent to the scarp of a large multi-event rockslide that occurred in 1991. As shown on the geological map of the Matter valley around Randa (Figure 1-3) the study area is situated within a gneiss series. The foliation of the gneisses dips away from the valley and thus favours slope stability; hence sliding along non-persistent fractures was assumed to be the governing instability mechanism. As such the site was considered as excellent for monitoring complex rockslide kinematics and progressive failure processes. In addition, the site is remote, being situated approximately 1 km above the valley floor and thus lower seismic noise levels were expected. Furthermore, the occurrence of a relatively well-documented rockslide in 1991 provided valuable background information on the type of instability likely to be acting in the slope.

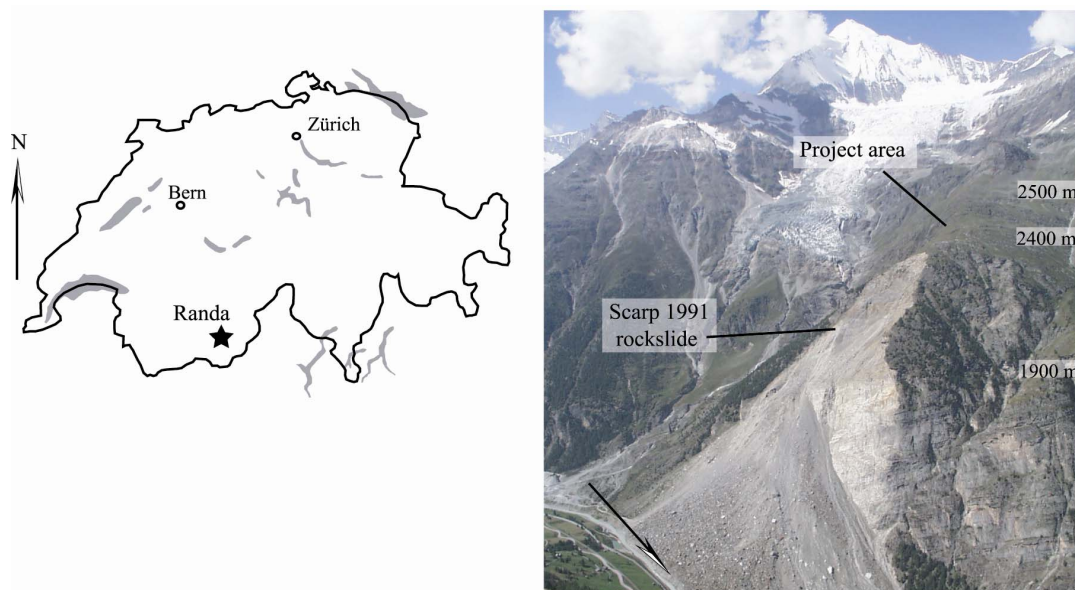


Figure 1-2: Location of Randa in Switzerland and photo of the scarp of the 1991 Randa rockslide. Above the scarp the project area for the monitoring of the current instability is situated.

## 1.4.2 Geological setting

The study area belongs to the Penninic Siviez-Mischabel nappe, one of four independent units of the Grand St-Bernard nappe. Figure 1-4 shows the tectonic structure of the Siviez-Mischabel nappe and the surrounding nappe pile in a map view and a profile along the river Vispa. Generally, the structure of the Siviez-Mischabel nappe is referred to as a large recumbent fold (going back to Aargand 1916). The core of the Siviez-Mischabel nappe is the so-called 'Randa-Augengneiss', a metamorphosed Permian porphyritic alkaline to subalkaline granitic intrusion. The intrusion is located within polycyclic palaeozoic gneisses, schists and amphibolites. These are overlain by a cover unit that consists of a metamorphic Permo-Carboniferous volcano-sedimentary sequence belonging as well to the Siviez-Mischabel nappe. The tectonic unit in the hanging wall of the Siviez-Mischabel includes a thick Triassic metasedimentary sequence referred to as nappe de Cimes Blanches. The overlying nappe du Tsaté comprises calcareous schists, serpentinites and metagabbros (Bearth 1964, Markley et al. 1999).

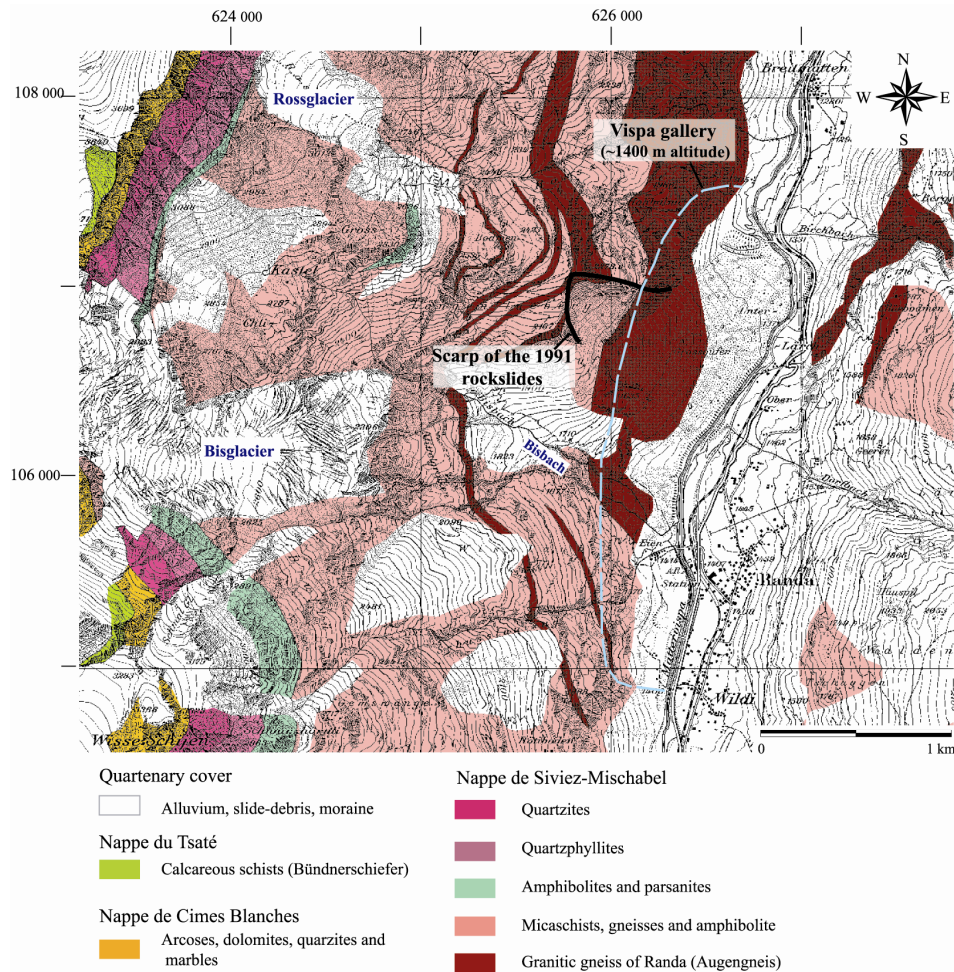


Figure 1-3: Geological map of the Matter valley (modified after Bearth 1964). The scarp of the 1991 rockslides in marked in black, the blue dotted line indicates the bypass gallery for the river Vispa built in 1992.

Crystallisation and deformation of the Siviez-Mischabel nappe took place in four Alpine deformation phases (Milnes et al. 1981, Müller 1983, Bussy et al. 1996, Markley et al. 1998). The beginning of Alpine deformation (thrusting) is dated in the Upper Cretaceous and Palaeocene, followed by isoclinal folding in Eocene. During this time span recrystallisation under upper greenschist facies conditions took place. The shape of a large recumbent fold is assumed to have developed in two back-folding phases (Oligocene-Eocene).

The identification of the overturned limbs of this large fold structure is only possible for a limited number of regions (Müller 1983, Escher 1988, Ellis et al. 1989, Markley et al. 1999). To explain the absence of overturned limbs, recent studies suggest an alternative back-shearing of the basement nappes instead of a classical back-folding model. This model is based on the formation of a shear zone that acts as a ductile ramp for back-shearing (Figure 1-5); thus the normal limbs are displaced backwards but only weakly deformed (Epard & Escher 1996, Müller 1983).

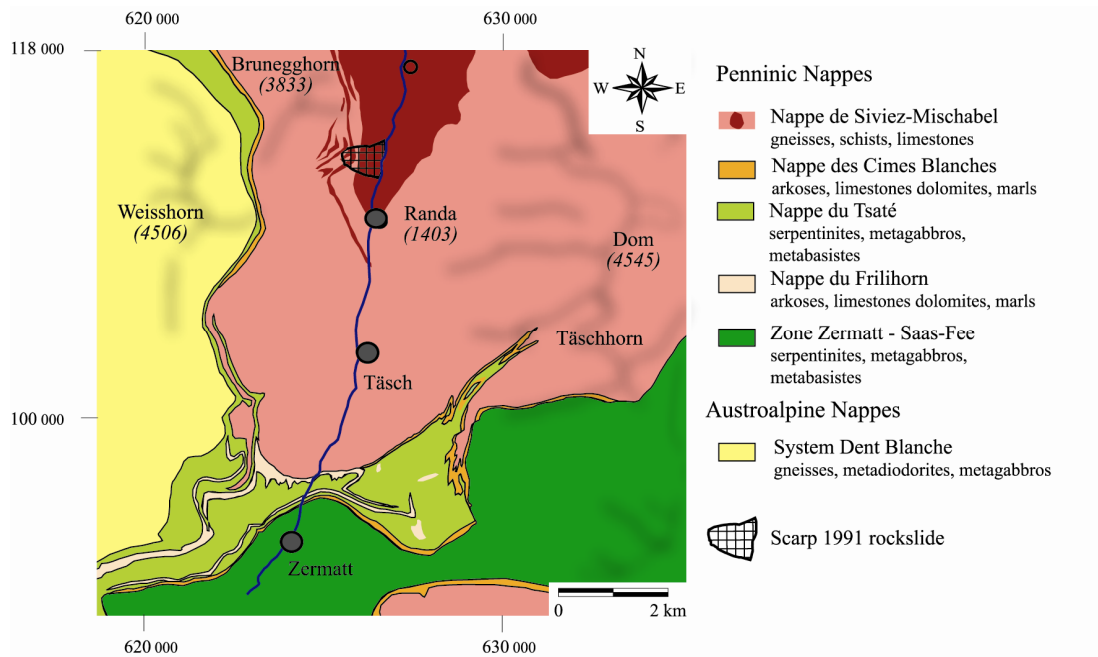


Figure 1-4: Tectonic map (top) and profile (bottom) of the Matter valley. Tectonic map modified after Steck et al. 1999; tectonic profile modified after Steck et al. 1997.

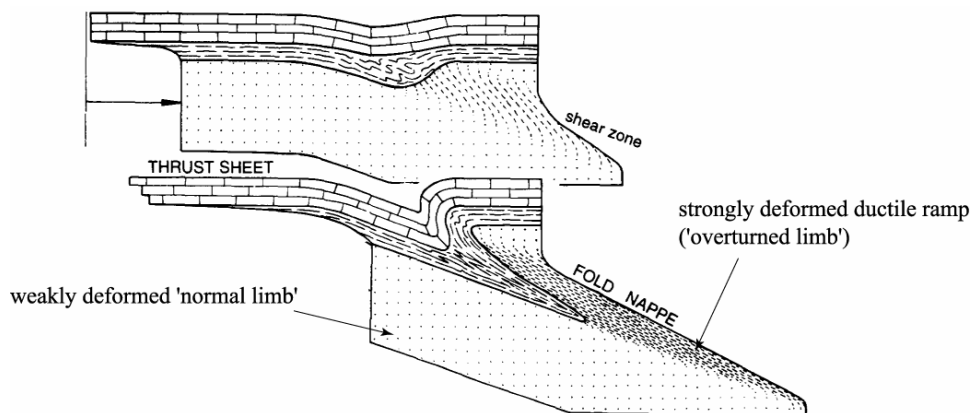


Figure 1-5: Back-shearing model for basement nappes (modified after Epard & Escher 1996). By the formation of a shear zone the normal limbs of the evolving fold nappe are sheared backwards (i.e. to the left) and only weakly deformed. The investigated slope is situated within one of these weakly deformed limbs.



The area of Randa is located within one of the above mentioned weakly deformed normal limbs, where the gneissic series of the Siviez-Mischabel nappe are dipping gently to the SW. The deformation structures related to the back-folding/-shearing exhibit different characteristics within the Randa augengneiss and the polymetamorphic paragneisses in the hanging wall (Müller 1983). The polycyclic paragneisses show only minor recrystallisation and heterogeneous deformation structures, i.e. undeformed sections alternate with regions of small kink-folds with flat axes. In contrast, the Randa augengneiss exhibits more intensive ductile deformation fabrics and recrystallisation.

The gneisses of the Siviez Mischabel nappe show the effects of physical and chemical weathering processes (Girod & Thélin 1998). At ground surface these include superficial disaggregation of phyllosilicates. Within the bypass gallery for the river Vispa (Figure 1-39) geochemical analyses proved that 200 m below surface percolating water within the macro- and mesoscale fracture system and micro cracks lead to the oxidation of pyrite, the alteration of chlorite and dissolution of calcite and feldspars (Girod 1999).

During glaciation the glaciers in the Matter valley reached a maximum elevation of approximately 2550-2700 m, i.e. 1300 m above valley ground (Jäckli 1962, Bearth 1964). Complete glacial release following melting is estimated to have occurred by 10000 y.b.p. (Winistorfer 1978). The climatic conditions in the upper Matter valley today are characterised as continental with high radiation and low precipitation (Gruber & Hoelzle 2001). Mean annual precipitation values in the valley are 600-700 mm, increasing towards 2000-2500 mm in the surrounding mountains (Landeshydrologie (Bundesaamt für Wasser und Geologie) 1992). The present-day geomorphology mirrors the inclination of the units to the southwest and the glacial overprint of the area which led to the formation of a U-shaped valley overprinted by postglacial erosional and depositional features (Figure 1-6). The western face of the valley is characterised by steep rock cliffs. On the other side of the valley moderately inclined, foliation-parallel slopes dominate. These are covered with glacial deposits, debris and rockslide material (Schindler & Eisenlohr 1992).



Figure 1-6: View along the Matter valley from S to N. The western slope of the valley (left) has been affected by the 1991 Randa rockslide. The eastern, foliation-parallel slope is characterised by slides parallel to foliation or involving debris and moraines.

### 1.4.3 Rockslides in the study area and previous studies

#### 1.4.3.1 *The 1991 Randa rockslides*

The 1991 rockslide occurred as a succession of two large rockslide events on April 18<sup>th</sup> and May 09<sup>th</sup>, 1991. They involved a total volume of ca. 30 mio m<sup>3</sup> of rock and affected the steep western flank of the valley, where foliation dips away from the valley. Both events were themselves multiphase events lasting several hours (Schindler et al. 1993). Before the first event precursors were noticed including increased rockfall activity during the winter. Larger rockfalls and intense water flow from daylighting fractures visible at the steep rock face occurred weeks-days before the first rockslide (Schindler & Eisenlohr 1992). Still, the first rockslide was unexpected and no geotechnical monitoring data was collected that could later be used to constrain the displacement directions of the slide mass and geological structures accommodating them. Monitoring began after the first rockslide with geodetic surveys, the measurement of opening cracks and simple seismic monitoring. Geodetic surveys performed before the second major rockslide revealed SE displacements (Ischi et al. 1991). At the surface opening fractures (Figure 1-7) were oriented NE-SW, N-S or W-E and showed opening directions perpendicular to their strike (Schindler et al. 1993).

The questions referring to the geological controls, kinematics, mechanisms and triggers of the 1991 rockslides are the subject of ongoing investigations. The 1991 rockslides affected the Randa Augengneiss and the overlying paragneisses of the Siviez-Mischabel nappe. Fracture mapping after the rockslide occurrence was performed across the entire slope (Wagner 1991, Schindler et al. 1993), with one study focussing on the fracture network of the Randa augengneisses as encountered during the construction of a bypass gallery for the river Vispa behind the 1991 rockslide debris (Girod 1999). Different structural compartments with different fracture sets and geometries of the blocks resulting from their intersection were accounted for. According to Wagner (1991) there are two compartments adjacent to the scarp; the rockslide scarp is treated as a separate third compartment. Within these three regions, ten fracture sets were defined (Table 1-2) and used for kinematical slope stability considerations. Figure 1-7 shows the scarps of the 1991 rockslides with the borders of the structural compartments defined by Wagner (1991) (denoted 3 and 4) and by Schindler et al. (1993) (denoted A and B). Instead of separating structural compartments by faults, Schindler et al. (1993) interpreted the fracture network based on the two main lithological compartments of the Randa Augengneiss and the paragneiss-series in the hanging wall. They concluded that, whereas the Randa Augengneiss was dissected into cubic blocks, the fracture network in the paragneisses showed a high variability in orientation and the blocks are smaller and flatter.

A large fault close to the valley floor with dip to the NE (plotted in Figure 1-7) is suggested as the basal shear plane for the first phase of the rockslide with subsequent sliding of adjacent blocks in SE direction along fractures dipping 40-50° to the SE (mean orientation 110°/45°) (Wagner 1991, Sartori et al. 2003). For the second major rockslide event, sliding is supposed to have occurred on the same SE dipping fracture set. Two steep fracture sets dipping to the N and E and a moderately inclined fracture set dipping to the NW (i.e. the fracture sets W1, W2 and W10 according to Wagner (1991)) are characterised as subsidiary fractures promoting the instability. The resulting fracture model of Wagner (1991) for the slope is shown in Figure 1-8.

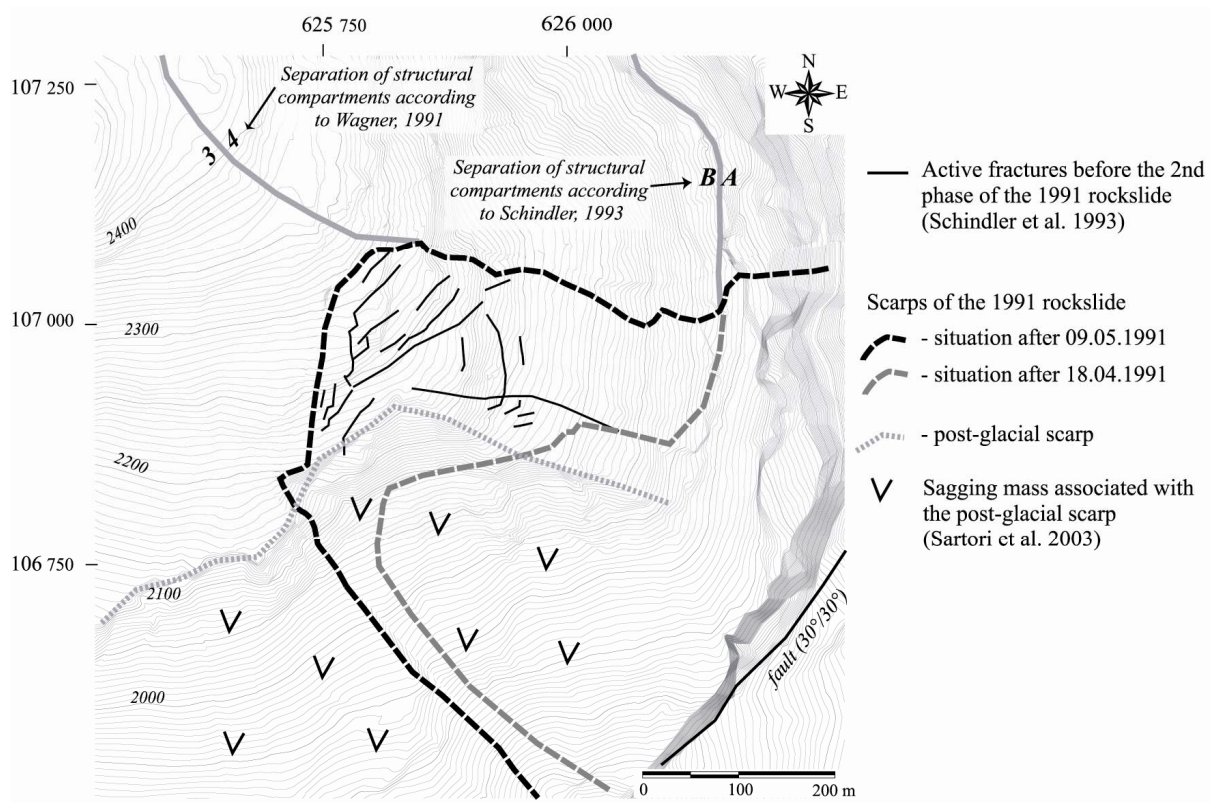


Figure 1-7: Topographic map of the project area before the 1991 rockslide. The scarps of the two main rockslide events of the April 18 and May 09 1991 are indicated. Black lines mark the position of surface fractures that were active between the first and second rockslide event.

Table 1-2: Dip direction and dip of the fracture sets defined by Wagner (1991), fault sets defined by Girod (1999) and description and structural classification.

Fracture set	Scarp of the 1991 rockslide	Compartment 3	Compartment 4	Description and structural classification (Wagner (1991) & Girod (1999))
W 1	02°/50°	34°/76°	25°/76°	open
W 2	70°/66°	64°/66°	75°/70°	open, high persistence, hybrid fractures (tension and shear)
W 3		58°/45°		
W 4	112°/46°		99°/67°	open, conductive, clay-infilling
W 5		134°/84°	117°/84°	
W 6	160°/85°		152°/59°	closed
W 7				not mapped
W 8	190°/35°	168°/85°		rare
W 9	254°/32°	236°/64°	204°/58°	
W 10	320°/35°	314°/56°	312°/58°	open, related to displacements on W4
S 1	260°/22°	228°/22°	240°/24°	closed
Faults FW 1	30°/50°			faults with gouge
Faults FW 2	260°/20°			mylonitic faults, type phyllonite
Faults FW 3	30°/50-90°			fracture zones due to diaclasis

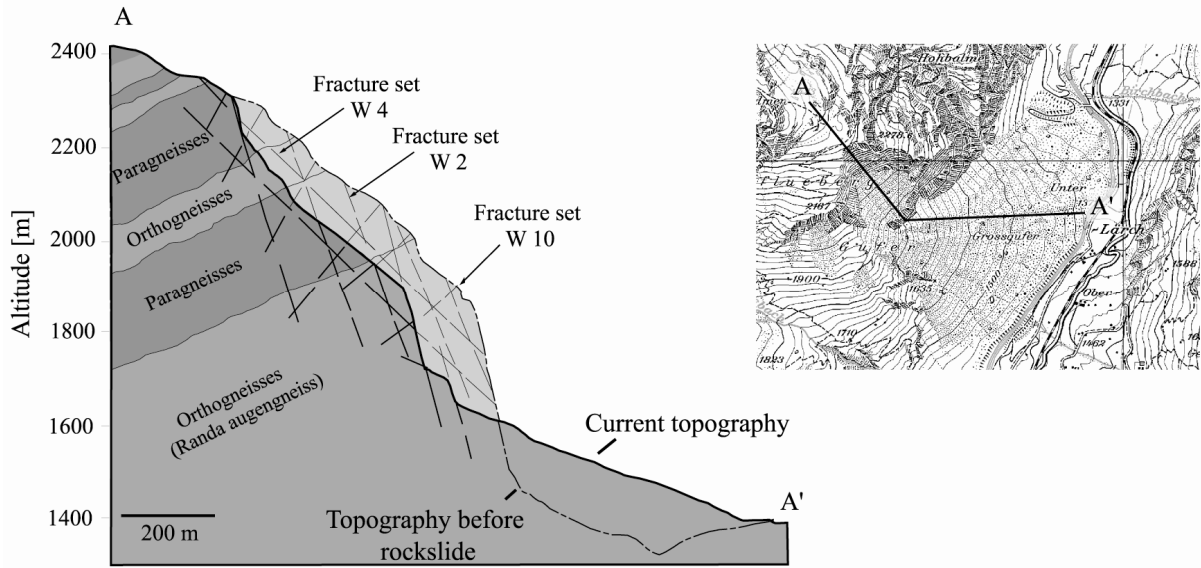


Figure 1-8: Cross-section for the 1991 rockslide showing the suggested instability promoting fractures (Wagner 1991).

Special focus has been directed to the mechanisms and the triggering of the 1991 rockslide events. In Figure 1-9 the climatic record for a five-year period before the rockslide event is plotted for a meteorological station in the Matter valley. No extreme environmental conditions (e.g. intensive precipitation or snow melt) could be identified before the rock slides. Likewise, the seismographic records show no earthquake before the rockslides and the melting of permafrost within the failed rock mass could be excluded as a triggering factor. Statistical permafrost modelling for the upper Matter valley revealed that no permafrost should be expected for the project area; the likelihood of permafrost increases for elevations above 2600-2800 m altitude (Gruber & Hoelzle 2001).

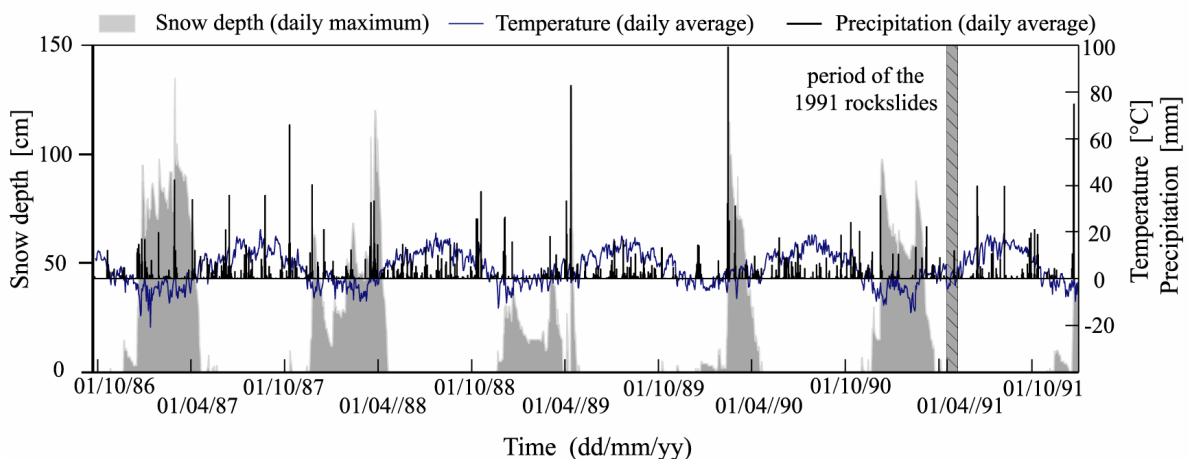


Figure 1-9: Climate record for the five year period prior the 1991 rockslide (modified after Eberhardt et al. 2001). The climate data was recorded in the Matter valley at Zermatt (1638 m altitude) by METEOSCHWEIZ.



One direction several hypotheses relating to the failure have taken is how the interaction of clay coated fractures and water pressures promoted rock mass destabilisation. Schindler & Eisenlohr (1992) concluded from examining the rockslide scarp that the upper 200 m of the paragneissic series were subjected to disaggregation and to the sedimentation of allochthonous clay and sand within the opening fractures. As such the presence of water in the fracture system could have led to a significant decrease in the frictional strength along the sediment coated fractures. The hypothesis of sediment coated fractures was not supported for the orthogneisses, based on geochemical analyses performed in the bypass gallery for the river Vispa in the metamorphosed granitic body. These analyses suggest neoformation of clay minerals by tectonic processes and precipitation of dissolved material in narrow fractures (Girod 1999). According to Girod (1999) clay minerals were only sparsely encountered in the bypass gallery and the low primary and secondary porosity at depth was insufficient. These observations point against the above-mentioned effect of decreasing the friction on the fractures significantly.

More recent studies focus on the long term destabilisation of the rock mass due to progressive failure through rock mass strength degradation mechanisms leading to the catastrophic failure of the rock slope (Eberhardt et al. 2001, Sartori et al. 2003, Eberhardt et al. 2004). Already Schindler et al. (1993) deduced from the long duration of the rockslide events that sliding occurred parallel to non-persistent fractures. Sartori et al. (2003) used mapping of fracture properties in the scarp to infer progressive fracturing leading to the failure of a key block on a basal sliding plane dipping with 30° NE. Eberhardt et al. (2004) analysed the influence of progressive failure in terms of the development of a failure surface by fracturing of intact rock bridges between non-persistent fractures and/or the generation of stress-release fractures after deglaciation favouring slope instability.

These previous studies concluded with differing instability models for the rock slope that include i) a persistent, pre-existing failure plane on which sliding occurred after a phase of progressively reduced shearing resistance (Sartori et al. 2003, to ii) a failure plane stepping through non-persistent fractures dipping towards the valley (Eberhardt et al. 2001) and iii) the progressive development of a failure plane by intact rock failure in tension (Eberhardt et al. 2004). Subsequent to these models, contradictory statements concerning the nature of the discontinuities dipping towards the valley have been made: Schindler et al. (1993) suggested the fracture network being of tectonic origin with mostly the steep fractures having opened due to stress-release after deglaciation, whereas Eberhardt et al. (2004) proposed propagation of stress-induced fractures dipping towards the valley on the basis numerical modelling. These open questions are closely linked to understanding the processes contributing to the current instability. As such, the volume of the current instability, its internal structure and the acting processes cannot be deduced a-priori from the information provided in the previous work. On the contrary, a thorough analysis of the current instability can provide new insights into the 1991 rockslide events, their precursors and evolution of failure. In addition, previous studies tended to focus on the metamorphosed intrusive rock body of the Randa augengneiss. However, the current instability is situated largely in the gneissic series in the hanging wall, for which detailed descriptions of the petrography or structural maps on a km scale are not available.

### **1.4.3.2 Other slope instabilities in the Matter valley**

Most post-glacial rock slope instabilities reported occurred on the eastern slope of the Matter valley, where foliation within the gneisses of the Siviez Mischabel nappe is dipping towards the valley (Joris 1995, Bloetzer & Stoffel 1998, Sartori et al. 2003). Slope instabilities that affected the western

slope of the valley, where foliation dips away from the valley, are scarce. In addition to the rockslides at Randa (1991), a second rockfall site is situated in the gneisses of the Siviez-Mischabel at St. Niklaus on the western side of the valley (rockfall Medji, Ladner et al. 2004).

Other slope instabilities found on the western side of the valley are sagging rock slopes associated with W-E cuts in the slope. For example the SW directed, pre-rockslide scarp at Randa is interpreted as a post-glacial geomorphologic feature (Figure 1-7), attributed to sagging with slope movement parallel to the dip of the foliation (Schindler & Eisenlohr 1992, Sartori et al. 2003).

#### **1.4.4 Monitoring of the current instability 1991-2000**

Following the 1991 rockslides, an early warning system for the remaining unstable rock mass was set up consisting of surface crackmeters, retro-reflectors for geodetic survey using an electronic distometer (1-D geodetic survey) and a climate station. In 1996 the network of reflectors for the geodetic survey was augmented by new reflectors for triangulation (3-D geodetic survey) (Ornstein et al. 2001, Jaboyedoff et al. 2004). Figure 1-10 shows the location of the network components and the estimated extent of the current instability at the surface. The components of the present monitoring network are clustered in two small areas of the instability-affected area, where most reflectors lie within the unstable rock mass; as such the transition from the unstable to the stable rock mass remains largely unconstrained. This applies especially to the lower part of the slope and the scarp of the 1991 rockslide, where the border between stable to unstable rock is unknown.

Although the geodetic system is restricted to surface observations, it supplied valuable information on the distribution of movements of the sliding rock body. Surface displacement data collected between 1996 and 2000 are plotted in Figure 1-11; these data and results were provided by Crealp (Centre de Recherche sur l'Environnement Alpin). With respect to the displacement rates two groups of reflectors were accounted for: the first group consisting of the reflectors 006,007 and 153 is situated between 2350 and 2250 m and exhibits annual surface displacements of 0.7-1.5 cm for the plotted time span. The second group of reflectors (150, 1551 and 152) with annual surface displacements of <1 cm is situated at 2150-1900 m altitude. Maximum displacement rates were seen to occur along the block closest to the 1991 rockslide scarp, decreasing to the NW with increasing distance away from the scarp. The measured displacement vectors are oriented to the SE (indicated in Figure 1-10) with dips varying between 5 and 55°. As such the surface displacement vectors are parallel to the dip direction of the failure plane of the second 1991 rockslide event, agreeing with the displacement direction measured before this event. As illustrated in Figure 1-10, several open surface fractures could be observed within the unstable rock mass. Periodic manual surface fracture opening surveys performed by Yann Dupertuis (mountain guide of Randa) suggested that the unstable rock mass was dissected into blocks, each separated from the other by opening fractures. Between autumn 1991 and spring 2001 surface fracture opening rates of up to 4 mm/year were measured.

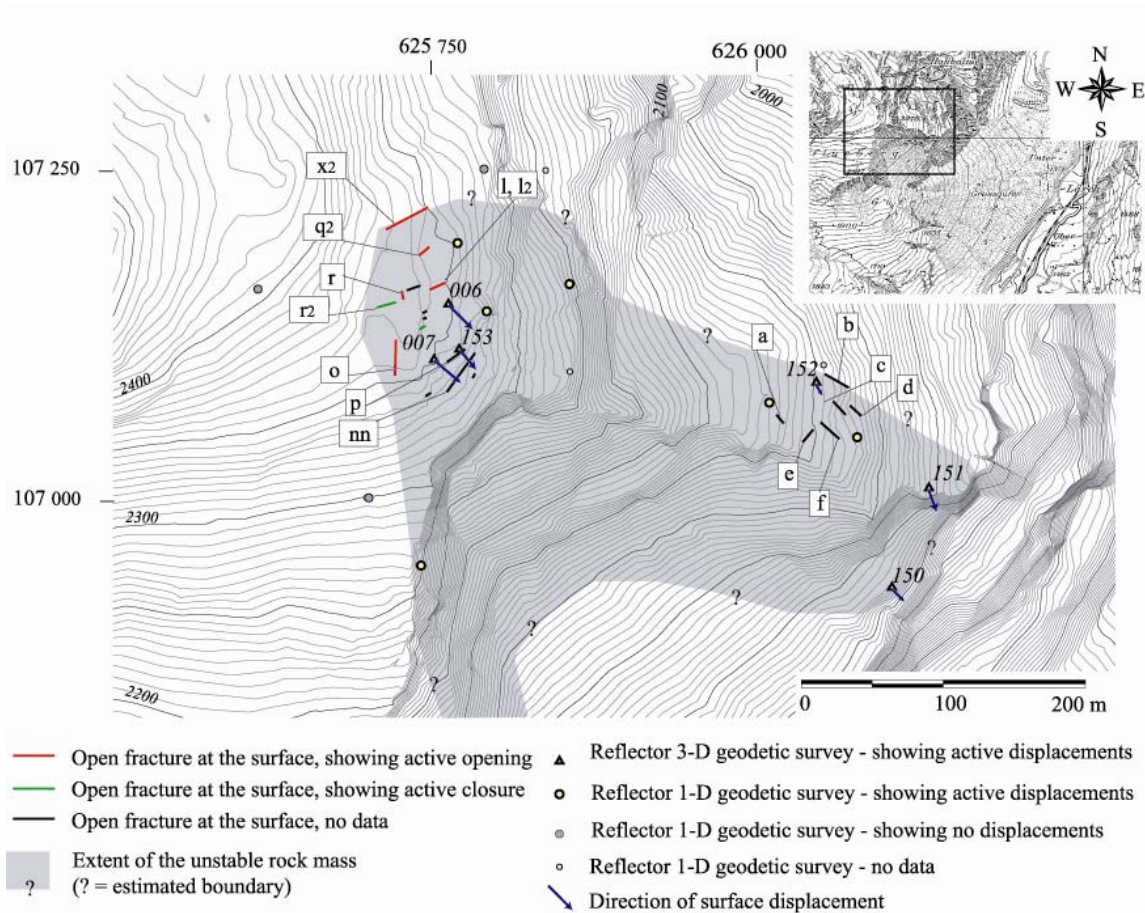


Figure 1-10: Geotechnical monitoring 1991-2000. Locations of open fractures at surface and retro-reflectors belonging to the geodetic survey are shown and specified according to their displacement information. The grey area delineates the assumed extent of the current instability; blue arrows denote the direction of surface displacements.

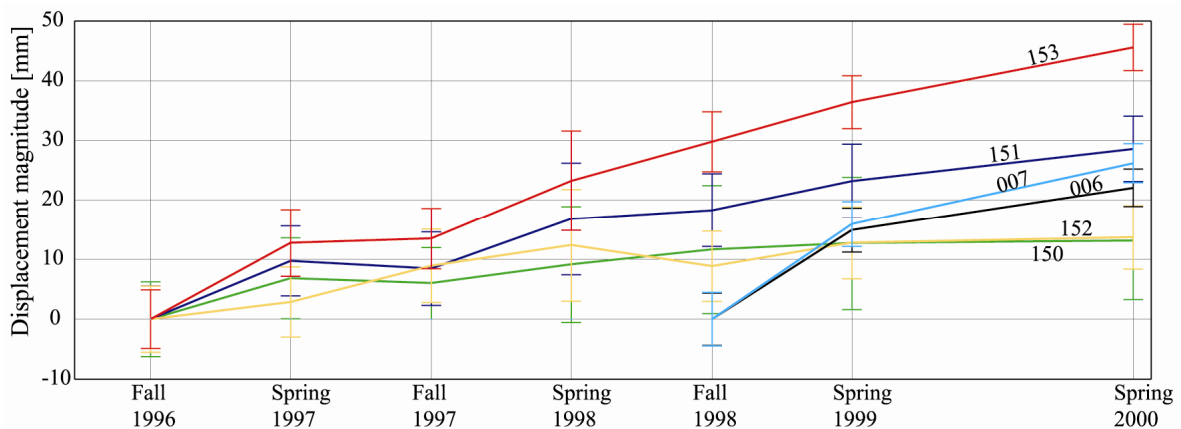


Figure 1-11: Results of the geodetic monitoring 1996-2000. Displacement magnitudes include error bars. Data and results provided by Crealp.

## 1.4.5 Investigations in the study area Randa 2000-2004

### 1.4.5.1 *Research boreholes*

Three research boreholes were drilled in summer 2001 with depths of 50, 50 and 120 m using destructive drilling. For the planning of the drilling campaign a preliminary geological model was used. The model was based on the spatial distribution of surface displacements, the location of open cracks and the analysis of discontinuity orientations and persistence as well as assumptions on potential shear/sliding zone depths. These assumptions were based on steeply dipping fractures that define the unstable blocks at surface. To obtain an estimate of the depth of the potential shear/sliding zone the large, debris-covered failure surface of the second 1991 rockslide event was extrapolated to the location of the planned boreholes and thus a maximum borehole depth derived.

The locations of the three boreholes (Figure 1-12) were constrained by the results of the geological model, as well as by drilling logistics, surface topography, geomorphology and spatial requirements for active crosshole seismic and radar experiments. Borehole SB 120 (i.e. 120 m deep) was located in the area where the greatest surface displacements were recorded. Its length corresponds to the assumed maximum depth of instability. Boreholes SB 50N and SB 50S (i.e. 50 m deep) were located within 30 m of each other and are separated by a steep opening fracture. The limited distance facilitated active crosshole testing, which was supposed to provide close spatial measurements of deformation, pore pressure and microseismic activity near a fracture. To complement the network of deep boreholes, a larger network of shallow boreholes (5 m deep) was drilled at suitable locations for the installation of additional geophones (Figure 1-12).

### 1.4.5.2 *Borehole logging*

The three deep boreholes were drilled with air and remained dry except for the lowermost 10 m of SB 120. After drilling caliper/borehole-trajectory and spectral gamma wireline logs were run along with an optical televiewer to provide oriented images of the borehole walls. The borehole trajectory (azimuth and inclination) and location of spalling along the borehole wall were measured by 4-arm caliper logs. All boreholes were found to deviate significantly from vertical, by up to 14° in SB 120 and up to 8° in the 50 m deep boreholes. The deviations are directed towards E-SE, which is perpendicular to the foliation. Larger breakout zones indicated by the borehole logs usually coincided with loss of air circulation during drilling. This observation pointed to the presence of open fractures that intersected the boreholes, which was later confirmed by optical televiewer images. The images of fractures that intersected the boreholes were digitised and their dip and dip-direction calculated according to the form of their sinusoid trace on the image of the borehole wall. Prior to combining the logs for interpretation, they were depth-matched using cable-stretch tests, correlations with the natural gamma logs of the sondes and with observations made during drilling. The logs and televiewer-derived fracture traces are provided in the appendix.

### 1.4.5.3 *Geotechnical and microseismic network*

After completion of the borehole tests, a geotechnical and microseismic network was established (Figure 1-12). The boreholes were cased with grooved PVC inclinometer casings which were cemented in place. The installations were made with the holes dry. The SB 120 casing also had outer steel rings for an induction coil transducer extensometer system (Interfels 'Increx' system) attached

every meter. These casings were surveyed every spring and autumn. Coaxial cables for time domain reflectometry (TDR) measurements were also cemented in place on the outside of the casings to compare against the inclinometer measurements. To determine the detailed time-history of the displacements on active fractures during the inter-survey period, two in-place biaxial inclinometers (Geokon vibrating wire in-place inclinometer; 2m baselength) were installed across prominent fractures in the 120m borehole. The biaxial inclination and temperature outputs from these instruments are sampled every six minutes by a data logger. Pressure sensors (Geokon vibrating wire piezometer), which are also sampled every 6 minutes, were installed at the bottoms of the holes. The borehole instrumentation was complemented by 3-component geophones installed at the borehole bottoms for monitoring microseismic activity associated with the rock mass movements. Additional geophones in nine of the ten shallow boreholes were added to the microseismic monitoring array (Figure 1-12).

At the surface the existing early warning system, which was established before 2000, was augmented by two automatic recording surface crackmeters (Geokon vibrating wire crackmeter); new surface benchmark arrays were installed over opening fractures to determine the vector of surface fracture opening (Figure 1-12).

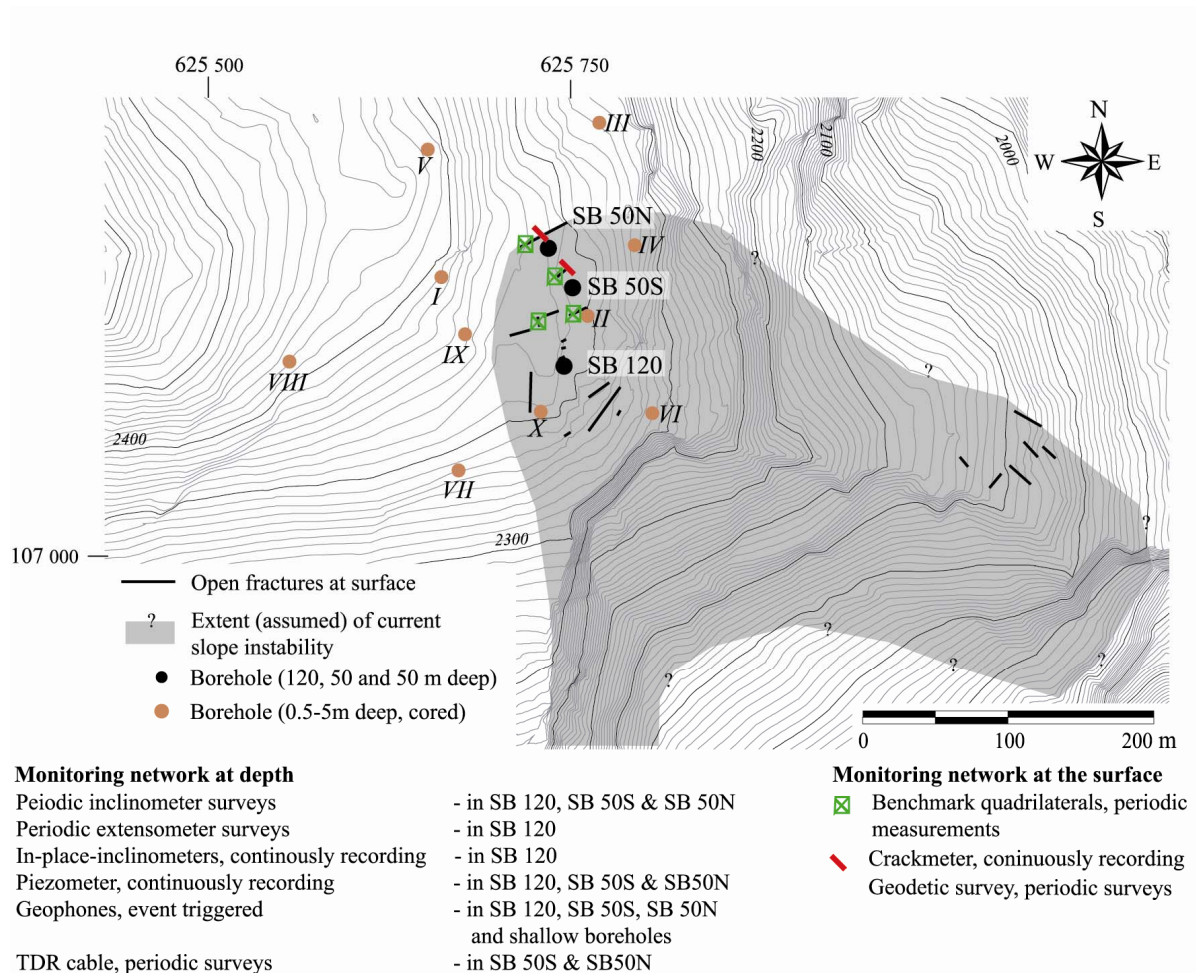


Figure 1-12: Geotechnical and microseismic monitoring network designed and implemented for the research project.



#### 1.4.5.4 Geological mapping

Field mapping focussed on the area surrounding the 1991 rockslide scarp (Figure 1-13). Outcrop mapping, surface scanlines for fracture mapping and retrieval of geological information from the optical televiewer images was possible for elevations between 2300 and 2500 m. Due to the limited accessibility of the area north of the scarp, areas below 2300 m altitude could only be mapped using a coarser surface outcrop grid.

The fracture mapping using scanlines followed the recommended procedures by Priest (1993). The obtained data were analysed with respect to orientation, fracture densities (i.e. fractures per meter along the scanline), mean normal set spacing and mean trace length.

#### 1.4.5.5 Laboratory testing

The intact rock properties were measured using samples retrieved from coring the shallow boreholes ( $\varnothing=9$  cm). The laboratory rock tests performed included uniaxial and triaxial compression tests. Analysis of the recorded stress-strain curves provided the elastic constants, Young's Modulus (E) and Poisson's ratio ( $\nu$ ), the uniaxial compressive strength ( $\sigma_{UCS}$ ) and the Coulomb shear strength parameters, friction angle ( $\phi$ ) and cohesion (c) of the intact rock. Rock densities were determined as well.

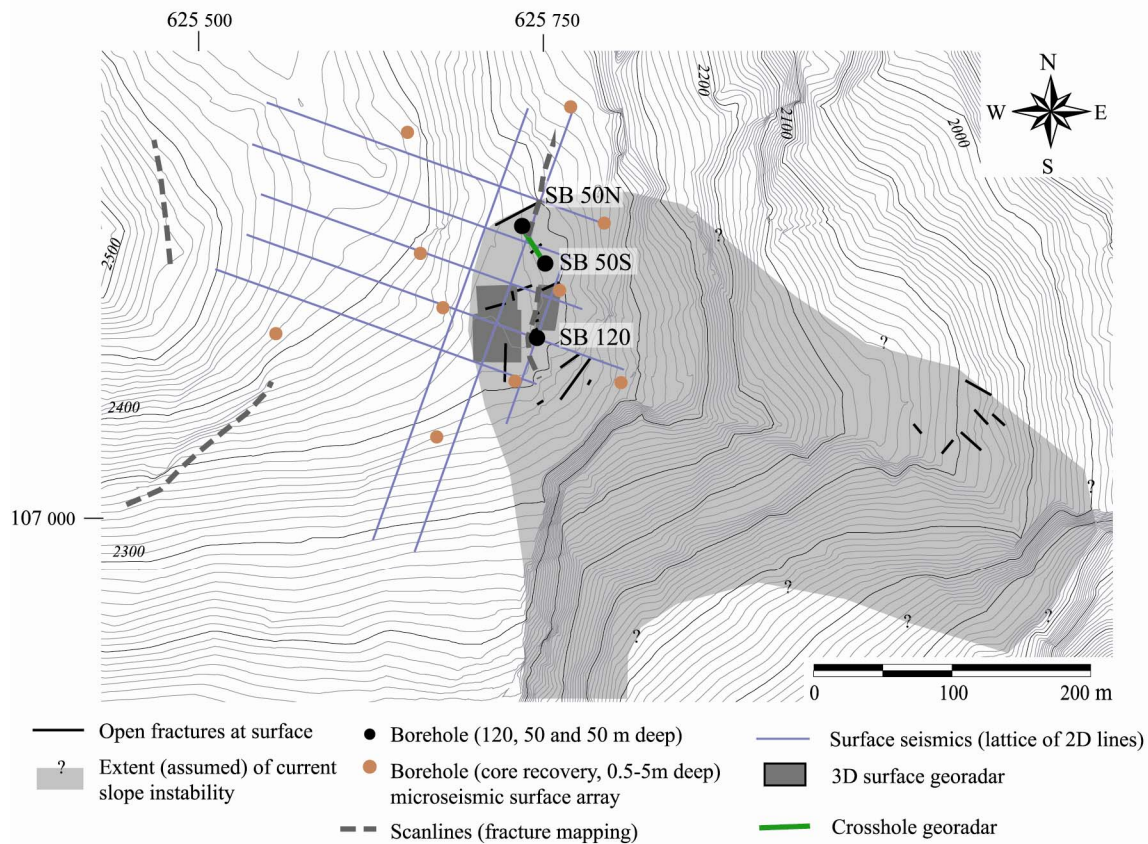


Figure 1-13: Geological and geophysical investigations performed for the research project.

## 1.4.6 Geophysical investigations

The mapping data is supported by geophysical investigations at surface and in boreholes. The borehole experiments include single-hole, borehole-to-surface and cross-hole georadar experiments. At the surface a 3-D surface georadar survey for three areas of 480-850 m<sup>3</sup> size was conducted (dark grey shaded areas in Figure 1-13); an active surface seismic experiment along eight lines was conducted to derive the subsurface velocity fields by means of refraction tomography. These investigations were performed and are analysed by Tom Spillmann and Björn Heincke (Applied and Environmental Geophysics, ETH Zürich) and will be presented as a part of their theses. Within the framework of this thesis the results of these investigations will be used to constrain the internal structure of the unstable rock mass.





## **2 Integrating geological and geophysical investigations towards a 3-D engineering geological model of an unstable slope in crystalline rock**

---

## 2.1 Introduction

### 2.1.1 Preface

This chapter presents the engineering geological reconnaissance of the study site, an unstable slope in crystalline gneissic rocks (i.e. Randa, Swiss Alps). This investigation aimed at providing a 3-dimensional (3-D) engineering-geological model of the slope. To this end a discrete model of the major fractures and faults is needed. With respect to slope stability considerations, the presence of instability-promoting fracture sets, and the interconnectivity of the small- and large-scale fracture networks are important parameters to be quantified (Einstein et al. 1983). This type of engineering geological investigation of fractured crystalline rock can resort to a large number of studies performed in mining, tunnelling, hydropower generation, and nuclear waste repository projects (e.g. Martel & Peterson 1991, Karasaki et al. 2000, Cosma et al. 2001, Schepers et al. 2001, Kilburn & Petley 2003). Yet, only a few studies have been published focussing on the detailed reconnaissance of the internal structure of unstable crystalline rock slopes (e.g. Sorriso-Valvo et al. 1999, Agliardi et al. 2001).

The assessment of this internal structure is crucial for predicting the location and extent of the failure surface(s), the volume of the unstable rock mass, the kinematics and the hazard related to catastrophic failure. The identification of a failure surface (sliding plane), however, becomes difficult, if highly persistent planar features like bedding planes, foliation planes or faults are absent or dip favourably away from the valley. Thus, the assessment of the discontinuity network within the unstable rock mass is required to provide kinematic constraints and to discriminate between different types of rock mass behaviour. For example, whether displacements are localised and accommodated on a few, extensive through-going planar features or whether they are distributed throughout the rock mass, perhaps stepping through the various steep and inclined fracture sets belonging to a small-scale fracture network.

In order to evaluate the geologic conditions underlying possible rockslide scenarios at the study site, detailed geological investigations were performed. The study site, a currently unstable rock mass at the so called Längenfluhberg (Figure 2-2) is situated above the scarp of a large, multiphase rockslide that occurred in 1991. The geological investigations at the site included the integrated application of detailed geological and fracture mapping at the surface and in boreholes, constrained by means of results obtained through geophysical surface and borehole experiments.

The first part of this chapter describes the assessment of the lithology and the discontinuity network within the study area. The focus of these investigations is related to defining the geometric constraints of a kinematic model for the unstable slope and the zonation of rock mass strength. In the second part the results obtained are compared against results of geophysical surface and borehole experiments. These results are used to extend surface mapping results into depth and to aid in the extrapolation of major structures intersected by the borehole into the surrounding host rock. The derived models will serve as a basis to assign a geological probability to the possible instability scenarios and to provide the geological constraints for a block kinematic model (Chapter 3) and numerical modelling of the internal deformation of the complex rockslide mass (Chapter 4).

## 2.1.2 Considered rockslide scenarios

The internal structure of a rock mass, together with the intact rock strength, is a key parameter to constrain potential instability mechanisms. Figure 2-1 shows six instability scenarios for fractured rock masses where the foliation/bedding planes are dipping away from the valley. The nomenclature for these six scenarios refers to Cruden & Varnes (1996) and Hungr & Evans (2004). The first three models, a) translational rockslide, b) translational rockslide on a stepped sliding surface and c) translational rockslide after the progressive development of the slide surface, represent instability scenarios proposed for the 1991 rockslides by several previous studies. Sartori et al. (2003) proposed translational sliding along either a pre-existing large fault or along a stepped sliding surface as the mechanism of the second 1991 rockslide and the present day instability. Schindler et al. (1993), based on the long duration of the 1991 rockslide, deduced that no through-going sliding surface pre-existed but that the failure surface followed fractures dipping moderately towards the valley and sub-vertically. Similarly, Eberhardt et al. (2004) concluded that progressive failure must be considered to account for the evolution of the failure surface through non-persistent fractures. As the sliding surface of the present-day instability does not necessarily have to follow the extension of the failure plane of the 1991 rockslide, the fourth model d) 'compound rockslide on a bi-linear sliding surface' is considered. Little attention has been paid to possible strength variations within the paragneisses, where the second 1991 rockslide and the present-day instability are situated. Hence the list of possible rockslide scenarios includes as well e) rotational rockslides, where the curved failure surface forms through weaker rocks and f) chevron toppling leading to a complex rock-topple/ -slide. In order to identify the relevant instability scenario for the investigated rock slope, the geological model has to provide information on the persistence of possible sliding surfaces and the strength properties of the intact rock and the rock mass.

## 2.1.3 Structural terminology for discontinuity mapping

The term *fracture* is used for discrete breaks in a rock mass where cohesion is lost through brittle rock failure (Ramsay & Huber 1987) but where only minor tectonic displacements have been accommodated. A tectonic structure was mapped as a *fault*, if indicators of significant differential displacement by brittle failure were found (Ramsay & Huber 1987). As the amount of differential displacement is difficult to quantify in polycyclic gneisses, faults were identified through the presence of brittle shear indicators like slickensides, Riedel fractures or cataclastic and gouge-type fabrics. According to these criteria, the intermediate brittle-ductile shear zones with brittle shear indicators were mapped as well as faults. The mapping criteria also accounted for ductile *shear zones* in the form of phyllonites (i.e. mm to cm thick, densely foliated, schistous gneisses). *Fracture zones* are defined herein as involving intense fracturing over dm-wide zones, where only minor differential displacement has been accommodated. The term foliation fracture in this text is used for cohesionless breaks in the rock mass that follow the penetrative, preferred orientation of minerals and other fabrics that developed under ductile deformation (Passchier & Trouw 1996).

The representation of structural mapping data is given on two scales: the *small-scale* discontinuity mapping focussed on decimetre- to metre-scale fractures, whereas the *large-scale* fracture network model comprises discontinuities with persistences greater than 10 m.

## 2.2 Lithology

The study area is located on the so-called “Längenfluhberg” around the scarp of the 1991 rock-slides as shown on the topographical map in Figure 2-2. The mapping area includes accessible outcrop regions above 2200 m elevation. In this area the lithology could be constrained by surface outcrop mapping; in contrast, the southern slope below was mostly covered with debris and the steep north-eastern slope was widely inaccessible.

The study area is situated within the gneisses of the Penninic Siviez-Mischabel nappe. The geological map for this area distinguishes ortho- and paragneisses on the basis of mapped parageneses (Bearth 1964). For the presented mapping study other criteria were chosen to delineate different lithologies. These include: i) quartz-feldspar content, ii) grain size, iii) mica content and distribution of mica within the rock, iv) petrographical heterogeneity on dm- and m-scale, and v) presence of small-scale deformation structures like micro-folds. These criteria were chosen to facilitate the correlation of rock lithologies to rock mass strength parameters (Shea et al. 1993, Hoek & Brown 1997). Lithological mapping of the mapping area accounted for seven lithological rock types; Table 2-1 lists these types and their characteristics.

The *Augengneisses* lithologically are made up of the metamorphosed Permian granitic intrusions. These gneisses form the steep rock faces extending from the valley floor up to elevations of 1800 m; above this elevation they appear as lenses of meter- to tens of meters thickness in the surrounding gneisses. According to Girod 1999 the augengneisses can be described as albite-quartz-biotite-muscovite gneisses with different size microcline-albite-plagioclase porphyroblasts and mylonitic gneisses with lepidoblastic mica-bands. Phyllonites of mm-cm thickness are frequent.

The second orthogneiss-type rocks in the study area are the *striped gneisses with feldspar-bands*. These surround the augengneisses between 2250 and 2350 m elevation. The feldspar-rich, medium grained gneisses contain cm- to dm thick feldspar-/quartz rich aplite-lenses.

The next type of gneisses involves heterogeneous, either chlorite- or quartz dominated gneisses that can be attributed to the series of paragneisses accounted for by Bearth 1964. The separation of these paragneissic series into different lithologies was made based on apparent strength differences. Hard gneisses with quartz in the matrix and typical feldspar-quartz porphyroblasts are the *dark gneisses with feldspar-bands and small feldspar-quartz porphyroblasts* and the *bright gneisses with feldspar-quartz porphyroblasts*. The two lithologies of the *striped gneisses with elongated quartz-lenses* and the fine grained *chloritic gneisses with small feldspar porphyroblasts* have lower hardnesses; they often exhibit small-scale folding and crenulation. The *chloritic schists with gneissic bands* represent the weakest rocks mapped in the mapping area.

The outcrop regions for these different lithologies are plotted in Figure 2-3 in combination with representative orientations of the foliation fractures. The lithological boundaries were found to follow the foliation, which is comparable to the results of previous studies (Bearth 1964, Müller 1983).

Table 2-1: Overview of mapped lithologies. Description on mineral content is based on field mapping,\*values taken from Girod (1999).

Lithological rock type	Grain size	Feldspar content and form	Quartz content and hardness	Mica content / distribution	Petrographic heterogeneity	Ductile deformation structures
Augengneisses	medium	high (50-70% *) in porphyroblasts	medium (30% *) in matrix	medium (10% *)	low (10m)	phylloinites
Striped gneisses with elongate quartz lenses	fine	medium in thin bands	medium in lenses	medium in lepidoblastic bands	medium (5m)	folds (dm-m scale)
Dark gneisses with feldspar-bands and small feldspar- and quartz porphyroblasts	fine-medium	medium-high homogeneous or in small porphyroblasts	high in matrix and porphyroblasts	medium in lepidoblastic bands	medium (5m)	crenulation
Striped gneisses with feldspar bands	medium	high homogeneous, in bands or porphyroblasts	medium in matrix	medium in lepidoblastic bands	medium-high (1m)	phylloinites
Chloritic gneisses with small feldspar porphyroblasts	fine-medium	medium in bands or small porphyroblasts	medium-low in matrix	medium in matrix	high (0.5m)	few phylloinites
Cloritic schists with gneisses	fine	medium-low in bands	low in matrix	high in matrix	medium	folds (dm scale) and crenulation
Bright gneisses with feldspar- and quartz porphyroblasts	medium	medium-high in matrix, bands and porphyroblasts	medium in matrix	medium in matrix	medium-high	-

## 2.3 Discontinuity network of the study area

The discontinuity network of the study area (i.e. large-scale fault and fracture zones and small-scale fracture network) was assessed by surface outcrop mapping, scanline mapping and analysis of aerial photographs. The outcrop conditions, which are characterised by long rock faces of limited height (i.e. <10 m height), allowed the spatial characteristics of the small-scale fracture network to be determined through scanline mapping. The large-scale network was inferred by tracing observed faults and fracture zones on aerial photographs with scales of 1:10000 and 1:6000 (provided by the Swiss Bundesamt für Landestopographie). Significant morphological depressions without outcrops were interpreted as fracture zones.

Surface-based outcrop mapping was extended over the complete mapping area; the scanlines measurements were performed along large rock faces in various lithologies and situated in the unstable as well as the stable part of the investigated rock mass (Figure 2-3). Surface data were augmented by borehole data from the three deep boreholes (denoted SB 120, SB 50S & SB 50N in Figure 2-3) drilled into the unstable rock mass. After drilling, the boreholes were logged using an optical televiewer that provided digital images of the borehole wall. Fracture dip and dip direction could be calculated from the resulting fracture traces on the borehole wall (digitised fracture traces for the boreholes are provided in the Appendix). In the boreholes minor and major fractures could be distinguished from the thickness of their traces in the optical televiewer images. Thus, schistose bands of > 2 mm thickness were identified as major fractures. As neither the presence of shear indicators nor the extent of a fracture could be determined on the optical televiewer images, the term major fracture was used instead of fault.

### 2.3.1 Fault network

A network of steep to moderately inclined fault and fracture zones and foliation-parallel faults was found in the study area. The location of these faults and fracture zones at the surface is associated with morphologic lineaments as the trace map on the aerial photograph (Figure 2-4a) illustrates. The orientations of all faults and fracture zones mapped on the surface are plotted in Figure 2-4b; likewise Figure 2-4c shows the orientations of major fractures intersected by the borehole. The stereoplots of faults and major fractures reveal the presence of three major fault sets.

The first fault set, denoted F1, comprises mostly brittle-ductile shear zones that are oriented parallel to foliation. They are characterised by two fractures at either side of a phyllonitic, partly weakened, band with rotated blasts indicating ductile shear. The fractures however exhibit slickensides and are accompanied by Riedel fractures. A typical outcrop situation is shown in Figure 2-5a/b; as indicated by the large fracture plane below the fault, F1-faults are often associated with auxiliary fractures dipping with 40-50° to the SE and hence towards the valley. The fractured phyllonitic fault core of an F1 fault is shown in Figure 2-6a. The mylonitic bands show strong alteration and weathering along the fractures which led to weakening of the gneisses along these faults. Faults of the F1 set are usually not associated with morphological structures and hence are not plotted in Figure 2-4a.

The second set (F2) includes brittle faults, brittle-ductile shear zones and fracture zones and exhibits fairly scattered orientations, dipping mainly to the N or NW. An example of such an E-W striking fault is shown in Figure 2-5c. Like the F1 faults, brittle shear indicators can be found in association

with a ductile shear zone characterised by the bending of the foliation. The fault shows anastomosing fractures dissecting the shear zone into small lentil-shaped bodies. In most cases the fault core is accompanied by intense fracturing. In contrast, the SE-NW striking faults of this set are not accompanied by a large damage zone. These SE-NW striking faults coincide with discrete open cracks at the surface.

The third set of faults and fracture zones (F3) strikes N-S, i.e. parallel to the valley. Usually morphological depressions are associated with these structures and outcrops are scarce. Large fracture zones with or without a fault core are typical for this set. Figure 2-5d-e shows an outcrop of a fault accompanied by a large fracture zone. Similar to Figure 2-5c the anastomosing fractures form lentil-shaped bodies within this fault. Thin sections of these rocks between the fractures show brittle shearing fabrics in form of cataclastic fault cores which consist of a fine grained gouge (Figure 2-6b), these; fissures within this gouge are filled with zeolithes.

The resulting fault map of the study area shows the traces of the steep fault sets F2 and F3 (Figure 2-7). A concentration of faults and fracture zones can be noted within the projected boundaries of the current slope instability. Here, the larger scale fault network provides two steep sets of through-going discontinuities in the rock mass that may form or contribute towards the development of lateral release planes in association with the unstable rock mass. The faults parallel to foliation are dipping away from the valley and hence are less critical with respect to slope stability considerations. The map also shows that projection of the extent of the fault and fracture zone segments required the use of aerial photographs, as they are hidden under slope debris and moraine deposits and could only be identified as lineaments.

### **2.3.2 Small-scale fracture network and structural compartments**

Unlike the fault orientation data, the fracture data for the entire mapping area were found to be highly scattered. This wide scattering of fracture orientation data suggested that the mapping area incorporates several structural compartments with different preferred fracture orientations. The amount of scattering could be reasonably minimised by accounting for three structural compartments (SC) (Figure 2-8). Their boundaries follow the boundaries of the lithological units. Along the northern scarp of the 19991 rockslides, the compartments extend from 1900 to 2380 m altitude (SC I), from 2380 to 2450 m (SC II) and from 2380 m to the upper border of the mapping area (SC III). This separation produced better results with respect to limiting the scatter and number of observed fracture sets per compartment than by separating stable and unstable areas.

The stereonet for the structural compartments show that the orientation patterns of the fracture network are different, whereas the orientation of the foliation fractures is almost constant for the entire mapping area (Figure 2-8). The above mentioned concentration of faults and fracture zones within SC I, which includes the unstable area, is shown as well.

Mean orientations of fracture sets were determined using cluster analysis of fracture orientations for each compartment and involved weighting to correct for the orientation bias associated with linear sampling techniques (Priest 1993). Even though the fracture density plots for the structural compartments still show scattering, reasonable clustering results could be obtained by accounting for eight mean cluster orientations (Figure 2-9). Foliation fractures were not considered in the clustering

procedure. In the following text the term ‘set’ is used for these derived clusters of preferred orientation (following Priest 1993). Table 2-2 shows that the individual structural compartments include six to seven of these eight fracture sets; the correlation with the fracture sets defined by Wagner (1991) is difficult.

The fracture network dominating each of the structural compartments consists mainly of the steep fracture sets 1-5. Set 1, with dip directions to the NE includes fractures normal to foliation and the axis of the large recumbent fold of the Siviez Mischabel nappe; similarly, the steep fracture sets 2-5 include tectonic fractures relating to the nappe structure. The wide scatter of these sets is likely to be related to the presence of steep stress release fractures that are oriented parallel to the valley which changes gradually with topography from strikes of N-S to E-W.

The clustering analysis revealed the presence of three moderately inclined fracture sets (6-8). The NE dipping fractures of set 6 could only be mapped in SC II and III; in contrast the fracture sets 7-8 primarily appear in SC I; fracture set 8 involves fractures that are oriented slightly oblique to the foliation fractures. More important is the more frequent occurrence of fractures belonging to set 7 in SC I, and thus within the unstable part of the rock mass. Dipping 30-60° NW, these fractures dip in the opposite direction than the measured direction of surface displacements (i.e. to the SE).

Table 2-2: Mean orientation of fracture sets, foliation and faults in the study area.

<i>Fracture set</i>	<i>Structural compartment</i>		<i>Structural compartment 3</i>
	<i>1</i>	<i>2</i>	
<i>1</i>	69°/68°	74°/68°	68°/68°
<i>2</i>	345°/72°	351°/70°	358°/70°
<i>3</i>	197°/71°	225°/75°	229°/75°
<i>4</i>		159°/72°	158°/77°
<i>5</i>	98°/70°	127°/68°	125°/62°
<i>6</i>		28°/25°	64°/39°
<i>7</i>	328°/39°		302°/46°
<i>8</i>	209°/29°		
<i>Foliation</i>	251°/22°	254°/27°	265°/29°
<i>Faults F 1</i>	242°/21°	236°/22°	
<i>Faults F 2</i>	335°/41°		339°/70°
<i>Faults F 3</i>	88°/65°		50°/76°

Of special interest is the frequency and extent of fractures dipping with 40-50° to SE and hence parallel to the observed surface displacements and the basal failure surface of the second 1991 rock-slide event. Even though some fractures with this orientation could be identified in the scarp of the 1991 rockslides, they were scarce in surface outcrops and borehole images. Their appearance in surface outcrops was found to be coupled to the presence of foliation-parallel brittle-ductile shear zones (F1). This observation suggests that these fractures are more likely of tectonic origin related to the fault formation as opposed to stress release fractures as hypothesised by Eberhardt et al. (2004) on the basis of numerical modelling.

### 2.3.3 Fracture properties

Mean normal-set spacings, mean trace length, termination characteristics and roughness estimations for the fracture sets are given in Figure 2-10. As the determination of most parameters involved



analysing the distribution characteristics, large sample numbers were required. Therefore SC II and III were combined, since they show fairly similar fracture orientation characteristics.

The mean spacing was calculated by fitting negative exponential distributions to the observed normal-set spacings. These normal-set spacings were obtained by calculating the spacing normal to the set's mean determined for a given scanline as a function of mean orientation of the set and the orientation of the scanline (Priest 1993). One method of deriving the distribution parameters applied a maximum likelihood estimation, alternatively nonlinear least-square fitting to the observed spacings was performed in order to obtain the parameters of the spacing distribution (see Appendix). The results are plotted in Figure 2-10a and show discrepancies in the mean spacing values of up to 1.5 m depending on the method applied. Nevertheless the results suggested relatively small mean normal set spacing values for all sets, ranging between 0.5 and 2.5 m.

Mean trace length values are plotted in Figure 2-10b. These values were derived by fitting log-normal distributions (as recommended by Mathab et al. 1995) to the observed trace lengths. The fit was applied to all observed trace length independent of the visibility of their termination points (see Appendix). In addition, mean trace length values were estimated according to Laslett (described in Priest 1993), who correlated mean trace length to the numbers of traces with both/ one/ no ends observable. The calculated mean trace lengths of 0.5 - 3.3 m, or more usually 1 - 2 m suggest a limited persistence for the small-scale fractures.

The connectivity ratio was defined as the number of fractures traces with both ends connected to other traces divided by the number of fractures with both ends observable. This ratio was chosen to provide a simple estimate of the fracture sets influence on the interconnectivity of the fracture network. The results indicated that the ratio varies with the structural compartments (Figure 2-10c); e.g. fracture set 7 (moderately inclined, dipping to NW) with an intermediate value of 50% in SC I and low value of 37% in SC II and III. Fractures of set 8 in SC 1 were found to be well interconnected with a ratio of 68% (inclined, dipping S-SE).

Outcrop mapping and analysis of the borehole televiewer data revealed that the steeply dipping fracture sets 1, 2 and 4 and the foliation fractures mostly show oxidation despite their rather low connectivity-ratio. This observation suggests that the connectivity ratio is apparently not related to the oxidation within the rock mass.

The joint roughness coefficients (JRC) as estimated in the field were analysed for the complete study area. Values of 8-9 could be attributed to the steep fracture sets 1 and 4 and the foliation fractures (Figure 2-10d). These values can be attributed to the assumed formation of the fractures through shearing deformation. Higher JRC values were observed for the moderately inclined fracture sets suggesting a more tensile origin.

### **2.3.4 Summary**

The study of the discontinuity network substantiated the initial differentiation between a small- and a large-scale network based on a threshold trace length of 5-10m. The small-scale fracture network was found to have lower mean normal-set spacing, ranging between 0.5 and 2.5 m, and mean trace lengths of 0.5-3.3 m. The geometry of this network was found to exhibit different patterns in the three structural compartments recognised in the mapping area.

The large-scale network includes fracture zones, brittle faults and/or brittle-ductile shear zones that dip either parallel to foliation to the W or steeply inclined to the E and NW. Similar to the small-scale fracture network, no faults and fracture zones dipping at 40-50° towards the valley could be identified during outcrop mapping or in the borehole data analysis. The generation of a stochastic fault network was considered impossible because, in contrast to the small-scale fracture network, no reliable observations could be made on the stochastic properties of the fault network, even though 50-120 m long scanlines were used. Thus, the 3-D engineering geological model had to be constructed by means of a discrete model, explicitly incorporating the major fractures, faults and fracture zones.

The small trace lengths and the low connectivity ratio of the small-scale fracture network suggest that the role of these small-scale fractures in the development of a larger scale failure surface is less important than those of the large-scale discontinuity network. With respect to the investigated slope instability mechanisms, the absence of either large-scale faults and fracture zones or a well developed fracture set with dip and dip-direction parallel to the measured surface displacement vectors has to be noted. This is important as fractures and faults of this orientation would serve as potential sliding surfaces. Nevertheless, a fracture set dipping in the opposite direction (i.e. NW) of the displacement vector could be identified predominantly in the lithological unit that is affected by the instability.

## **2.4 Constraining the extent of major fractures and faults with georadar and seismic investigation data**

The construction of the geological model requires the extrapolation of the mapped structures from the surface into depth and from the borehole wall into the rock mass. The following interpretation of geophysical surface and borehole experiments is intended to constrain this extrapolation using the preliminary results of a surface 2-D seismic refraction survey, a 3-D surface georadar survey and single-hole radar reflection profiles. Figure 2-11 shows the location of the investigated areas at the study site. The focus of the following sections is the verification of whether these applied investigation techniques were capable of providing information on the location and extent of major fractures, faults and fracture zones. Therefore, the interpretation included the calibration of the preliminary geophysical results with geological data to constrain the extrapolation of the geological structures observed at the surface and in the boreholes.

The geophysical data presented in the next section were recorded and analysed within the framework of two separate theses: Seismic and georadar borehole and borehole-to-surface experiments were conducted and analysed by Tom Spillmann (Applied and Environmental Geophysics, ETH Zürich); the section treating the analysis of single-hole radar reflection profiles is based on a collaborative work on integrating the geophysical data with geological and geotechnical data which was presented in Willenberg et al. (2004). Seismic and georadar surface investigations were performed by Björn Heincke (Applied and Environmental Geophysics, ETH Zürich). The interpretation of the surface georadar measurements is based on results published in Heincke et al. (2002) and Heincke et al. (2004). The tomograms used for the interpretation of the seismic survey were presented in Leahey (2003) and Heincke et al. (2003).

### 2.4.1 Interpretation of single-hole georadar reflection profile results

The borehole radar reflection survey is an electromagnetic surveying method, where the reflections relate to changes in the dielectrical properties and the water content in the investigated rock mass. Several previous case studies demonstrated that the georadar surveying method is applicable to map discrete fractures and faults within a rock mass (Holloway & Mugford 1990, Lane et al. 1994, Grasmück 1996, Green et al. 2003, Serzu et al. 2004). The principle of the single-hole radar method is shown in Figure 2-12a. The aim is to record reflections of emitted high frequency electromagnetic (EM) waves. By moving the transmitter and receiver antennae at constant offset along the borehole, an image of reflecting objects is acquired. In case of a planar fracture intersecting the borehole, the reflected signals form a hyperbolic pattern (Figure 2-12b). The travel time  $t$  of such reflections is governed by the equation

$$t = \frac{2}{v} \sqrt{z^2 \sin^2 \Theta + c^2 \cos^2 \Theta} \quad (\text{equ. 2.1})$$

in which  $v$  = velocity,  $\Theta$  = angle between the borehole and the fracture plane,  $2c$  = antenna offset and  $z$  = antenna midpoint distance from intersection point (Olsson et al. 1992).

For the survey at the study site a 100 MHz antenna was deployed. Georadar data acquired in borehole SB 120 revealed 6 hyperbolic features that could be associated with planar fractures (dashed lines in Figure 2-13). No signal energy was recorded close to the hyperbola apexes. Here, transmitter and receiver were on opposite sides of the fracture and thus no reflection could occur. Using a constant velocity  $v=0.12$  m/ns that was obtained from a cross-hole experiment between boreholes SB 50N and SB 50S, the reflection travel times corresponding to the major fractures delineated in the televiwer log were predicted (Figure 2-13c). Six out of the twenty predictions could be associated with the hyperbolic reflection patterns observed in the georadar section (orange shaded areas denoted A to F in Figure 2-13d). A reasonably good fit can be observed with the exception of prediction D. The small deviations found for predictions A to F are likely to be caused by curvatures of the reflectors, but the assumption of planar fractures seems to be generally well justified. The discrepancy observed for prediction D could be related to a step-like fracture offset occurring exactly at the borehole intersection. In general, as the prediction procedure provided a reasonable fit with the observed reflections, the assumptions of planar reflectors could be justified. This reflects as well the inaccuracies of deriving dip values of fractures by their trace on an optical televiwer image, which increase with irregularity of the borehole diameter.

An important feature of the georadar data is their capability to trace the fractures away from the boreholes. In particular, the extensions of the hyperbolic reflection patterns allow minimum fracture lengths to be determined. Applying basic migration principles (Yilmaz 2001) to pattern end points, minimum extensions between 7.8 and 49 m were determined. The effective persistences of these fractures may be longer, but strong reflections, possibly caused by more distant fractures that did not intersect the borehole (denoted X and Y in Figure 2-13d), obscure the hyperbolic patterns.

The minimum length estimates indicate that all fractures observed in the georadar data must be significant. However, only a limited number of major fractures identified on the televiwer images give rise to a clearly distinguishable reflection pattern. In order to better characterise the imaged major fractures, the georadar and televiwer data were combined with the displacement profile obtained

from inclinometer/extensometer surveys. Figure 2-13a shows the displacement profile along SB 120; the profile depicts the magnitude of the 3-D displacement vector per unit measurement interval (0.61 m). The peaks denote active zones between blocks where relative displacement has occurred within a one year period (for explanation of the analysis procedure see Chapter 3.4). Most peaks are contained within one measurement interval, indicating that the deformation is highly localised. In all cases, the peaks can be correlated with distinct major fractures. In contrast, if compared to fracture densities per inclinometer interval plotted in Figure 2-13b, regions of high fracture density (i.e. more than 3 fractures per 0.61 m) generally do not exhibit distributed displacement. It could be thus concluded that active zones coincide with the location of major fractures in the boreholes and that some of these can be identified in the radar single hole reflection analysis.

In addition to the analysis of fractures intersecting the borehole, information concerning the rock mass several meters below the borehole could be deduced. Hardly any major fractures dipping parallel to the dip of the surface displacement vector could be identified in the boreholes. To check whether such major fractures are located in the area below the borehole, the reflections of fractures without an intersection in the borehole were analysed. Below 110 m borehole depth, three reflectors can be recognised in the data (labelled Z1-Z3). However the apparent (i.e. unmigrated) dip of these reflectors corresponds to the dip of the fracture F at 110 m which has a dip of  $66^\circ$ . In consequence the reflectors Z1 and Z3 will have corresponding dips and are most likely oriented parallel to the other mapped major fractures that dip to the NW and hence not potential sliding surfaces.

Single-hole georadar reflection profiles were obtained as well in the two 50 m deep boreholes SB 50S and SB 50N (Figure 2-14 and Figure 2-15). In SB 50S a good fit of predicted and measured reflections could be obtained for prediction A, a NE dipping major fracture that accommodates only minor displacements; for this fracture, a minimum extent of 38 m could be derived. For the predictions related to several open fractures intersected between 15 and 22m borehole depth, however, only weak correlations were found. This may be reflect that too many major fractures are located in this section and that the major open fracture (denoted C) is sub-vertical and hence unfavourably oriented for being imaged in the reflection data. The predicted reflections of the major fractures at 34 and 47 m depth (denoted D and E) could not be associated with measured reflections as well. However, at least three reflectors (denoted X, Y and Z on the reflection data) were identified without an intersection in the borehole.

The georadar data measured in SB 50N are plotted in Figure 2-15. Only one prediction (A) could be associated with a major fracture intersecting the borehole at 21 m depth, and a minimum extent of 42 m was derived. The actual reflection indicates that the dip of the major fracture was overestimated by  $6^\circ$  in the borehole televiewer images, which is within the error margins for steep fractures. Prediction A corresponds to the only active fracture in SB 50N as indicated by the peak in the displacement profile shown in Figure 2-15a. At the bottom of the borehole another major fractured is intersected, but here no evidence of a reflection could be found.

In conclusion, the single-hole georadar proved to be a useful tool for identifying major, active fractures and attributing a minimum extent from the borehole wall into the rock mass. The derived persistence data for the active fractures intersected by the borehole will be used to constrain the kinematic block model of the investigated slope in Chapter 3.5.

## 2.4.2 Interpretation of 3-D surface georadar results

Like the georadar single-hole method, surface georadar experiments can be used to map major fractures in the subsurface. The surface topography around the boreholes is characterised by flattenings covered with moraine and slope debris and by steps over small rock cliffs. A 3-D surface ground penetration radar (GPR) survey was conducted at the study site on three 480 - 850 m<sup>2</sup> large fields located on these flattenings (denoted I-III in Figure 2-16). For the survey, two unshielded 100 MHz antennae were used. These were mounted on a sledge together with a target prism for a self-tracking theodolite with automatic target recognition capabilities. While the sledge was moved across the investigation area along parallel, densely spaced lines, the georadar data and the corresponding positions were collected simultaneously. The data acquisition is described in further detail in Heincke et al. (2002) and Heincke et al. (2004).

To date, processed and migrated georadar data sets are available for the two upper investigation fields I and II which were combined for analysis (Heincke et al. 2004). This study focussed on the processing of the 3-D data set and the identification of reflectors. In Figure 2-16b the 3-D volume is shown with the identified reflectors; Figure 2-16c provides an E-W vertical cross-section through the 3-D data. Reflectors could be identified to a depth of about 35m. Most identified larger reflectors (denoted C -G) dip gently in SW directions, only reflector A dips moderately to the east. Observations of soil and moraine thickness at the surface suggest that the reflector E is likely to coincide with the bedrock surface. The deeper reflectors C, F and G are dipping parallel to the foliation. Unfortunately the outcrop conditions and the lack of boreholes restrict any correlation of the prominent reflector C to a discrete fracture or fault. The location of the moderately dipping reflector A can be compared against the fault map derived by surface outcrop mapping and analysis of aerial photographs plotted in Figure 2-16 a. This comparison revealed that reflector A more or less coincides with the extrapolation of the fault denoted A on the fault trace map in Figure 2-16a.

The GPR method generally has difficulties in imaging steep reflectors. Several of such steep fractures are contained within the investigated rock volume (denoted r2 and B in Figure 2-16a). With the applied processing techniques these fractures either are not imaged at all (r2) or are associated with vertically aligned point-like diffractors. Figure 2-16c shows such diffractors (denoted B) that align along an almost vertical line. The line through the diffractors is contained in the plane of the large fault extrapolated from the rockslide scarp, denoted B in Figure 2-16a. To further enhance the analysis of the 3-D GPR data set, a separate analysis of vertically aligned diffractors has been initiated (Heincke et al., in prep).

The data available to date could be used to constrain the extent of fault A. As in the previous borehole georadar study no indicators for major discontinuities moderately dipping to the SE and hence towards the valley could be found.

## 2.4.3 Interpretation of surface seismic refraction tomography results

The seismic refraction tomography method provides a velocity distribution for the investigated rock volume and has been applied in several previous case studies (Martel & Peterson 1991, Schepers et al. 2001, Escuder Viruete et al. 2003). The survey at the study site was performed along five E-W oriented and three N-S oriented lines covering an area of approximately 250 x 250 m (Figure 2-11).

Small explosive charges of 5-50g were used to generate the seismic signals in shot intervals of 4 m along the lines. The signals were recorded by geophones at surface with a spacing of 2 m and at depth using the geophones in the microseismic array (three deep and nine shallow boreholes). According to the frequency content of the recorded signals, the predominant transmitted wavelength of p-waves was about 30 m and the resolution approximately 8 m. For every profile, a 2-D inversion algorithm of the first-arrival times of the p-waves was applied by Leahey (2003). An extension of the tomographic analysis in 3 dimensions is currently performed.

For an interpretation of the tomograms, the obtained p-wave velocities have to be related to rock mass properties. Marti et al. (2002) summarise density, shear and bulk modulus, porosity, pore content, fluid saturation and fracture occurrence as factors influencing seismic velocities. As the rock mass at the study site was found to be mostly dry, the interpretation of the seismic velocity focussed on how the seismic velocities relate to the lithology, the fracture density and the occurrence of major fractures (i.e. faults and fracture zones).

Figure 2-17 shows the seismic velocities 15 m below surface for the 2-D lines overlain on the map of faults and fracture zones extrapolated to 15 m below surface. Low velocities of 1000 m/s dominate on both the N-S directed and the E-W directed profiles in the middle of the investigated area. No clear correlation of this large low velocity zone with the fault and fracture zone data or with lithological changes can be deduced at this point of the analysis. Higher velocities between 2000 and 3000 m/s were calculated for the other regions. Within these regions small zones of lower velocities partially correspond to the locations where the profiles intersect faults and fracture zones striking normal to the profile (e.g. southern part of the profiles H1 and H2). At the intersection points of the seismic lines different seismic velocities can be observed. This difference probably relates to the 2-D representation of anisotropies within the rock mass that can be related either to the foliation of the gneisses or reduced seismic velocities across large faults that are either filled with soft material or include a large damage zone.

In order to better illustrate the relation between seismic velocities and the lithological and fracture data, vertical seismic velocity profiles were extracted from the two tomograms H1 (north-south directed) and Q2 (east-west directed) at the location borehole SB 120. In Figure 2-18 the velocity data are plotted against the lithological record, the location of major fractures and the fracture density derived from the optical televiewer images. Both p-wave velocity profiles show low velocities < 1000 m/s for the upper seven meters; below this depth the velocity increase to values between 1500 and 4000 m/s. This low velocity layer is thicker than the mapped moraine and slope debris cover, as the transition into bedrock was detected at 4.2 m depth and the optical televiewer images document fairly massive rock below 5 m. Whereas the velocities derived for the N-S directed profile are rather constant between 7 and 25 m with 1500 m/s and increase gradually to 2500 m/s at 40 m depth, the velocity profile for the E-W directed profile shows a band of higher velocities of 2000-4000 m/s between 8 and 15 m depth. The origin of this high velocity zone is unclear as lithological changes should affect the velocities on both profiles.

Both velocity profiles were found to be independent of the small scale fracture density; this observation corresponds to findings of comparing seismic velocities measured with sonic logging against fracture densities in granitic rocks (Moos & Zoback 1983). Likewise velocity variations at

major fractures could not be observed, even if focussing on the profile that is oriented normal to the strike of the major fractures.

To summarise, the results of the refraction tomography are difficult to use for constraining the geological model, as to date no clear correlation between the patterns of seismic velocity changes in the tomograms and lithological and fracture information could be recognised.

#### 2.4.4 Summary

For the described study key information on the location and extent of large discontinuities in the rock mass (i.e. faults and fracture zones of higher persistence) was required. The focus was directed towards moderately inclined to steeply dipping faults within the rock mass, as these had the more significant bearing with respect to slope instability. The results of the interpretation of the geophysical investigations suggest that the applied surface and borehole georadar experiments were able to image these major fractures except from cases where they were sub-vertical. Very useful results were obtained from the georadar single-hole reflection survey that placed constraints on the minimum extent of active major fractures. This parameter was impossible to constrain from surface outcrop mapping due to limited outcrop height. 3-D surface georadar data imaged faults and fracture zones identified through field mapping and the analysis of aerial photographs and thus validated the mapping results. Both surface and borehole georadar methods provided important input in a sense that they also showed the absence of large discontinuities dipping moderately towards the valley and hence parallel to the measured surface displacement vectors. The surface seismic refraction tomography data, in contrast, was found to be difficult to interpret at this point of the analysis, as the direct correlation of velocity variations and discrete major fractures was not possible.

### 2.5 Rock mechanical testing

For the construction of the engineering geological model of the slope information relating to the intact rock and rock mass strength was needed. The geotechnical properties of the stronger augengneiss-type rocks (called group B) and the intermediate fine grained chloritic and striped gneisses (group A) were determined by means of laboratory testing of intact rock samples performed at the University of Saskatchewan's Rock Mechanics Lab. Testing was performed using 9 cm diameter core samples obtained from depths of 0.5–5 m during the drilling of the shallow boreholes used in the microseismic monitoring network (Figure 2-3).

Laboratory testing involved uniaxial and triaxial tests. The analysis of the recorded stress-strain curves provided the elastic constants Young's Modulus (E) and Poisson's ratio ( $\nu$ ), the uniaxial compressive strength ( $\sigma_{UCS}$ ) and the Coulomb strength parameters: internal friction angle ( $\varphi$ ) and cohesion (c). Rock densities were also determined.

The results of the uniaxial and triaxial tests are plotted in Figure 2-19 in principle stress diagrams. The measured stress strain curves and detailed test results are given in the Appendix. The rock strength parameters were calculated using the linear Coulomb failure criterion:

$$\sigma_1 = \frac{2c \cdot \cos \varphi + \sigma_3 (1 + \sin \varphi)}{1 - \sin \varphi} \quad (\text{equ. 2.2}).$$

The simplified non-linear Hoek-Brown failure criterion for intact rock samples (i.e.  $s=1$ ; Hoek & Brown 1997) was also used:

$$\sigma_1 = \sigma_3 + \sigma_{ucs} \left( m_i \frac{\sigma_3}{\sigma_{ci}} + 1 \right)^{0.5} \quad (\text{equ. 2.3}),$$

where  $m_i$  = Hoek-Brown constant relating to rock strength.

Figure 2-19 shows that the best fitting curves calculated using the Coulomb and Hoek-Brown failure criterion exhibit only small differences. Therefore, intact rock strength parameters were obtained from the analysis with the Coulomb failure criterion.

The medium grain size, Augengneiss-type rocks of group B were found to have a mean uniaxial compressive strength  $\sigma_{ucs}=97$  MPa, a mean Young's modulus  $E=32$  GPa, an internal friction angle  $\phi=55^\circ$  and a cohesion  $c=16$  MPa. The Poisson's ratio for this gneiss type was calculated as  $\nu=0.21$  from the axial and lateral strains recorded during the uniaxial tests. The density was measured to be  $2640$  kg/m<sup>3</sup>. The values of uniaxial compressive strength and Young's modulus correlate well with other published determinations for the Randa Augengneiss of  $\sigma_{ucs} = 110$  MPa and  $E = 28$  GPa (Girod 1999). In contrast the fine grained gneisses of group A which had microfolds and higher mica content have lower strength values of  $\sigma_{ucs}=69$  MPa, a mean Young's modulus  $E=21$  GPa, an internal friction  $\phi=32^\circ$  and a cohesion  $c=19$  MPa. The Poisson's ratio is also smaller with  $\nu=0.14$ , whereas the density is slightly larger with  $2700$  kg/m<sup>3</sup>.

In summary, the results show that the lithological subunits exhibit a systematic contrast in intact rock strength parameters and thus indicate variations of rock strength within the slope. The derived values will be used to estimate the rock mass strength parameters that are needed for numerical slope stability modelling using the GSI (Geological strength index) rating in Chapter 4.

## 2.6 Engineering geological model for the study area

The aforementioned results can be used to constrain the most likely instability scenario for the investigated slope. To this end, the following aspects were focussed on: i) whether major discontinuities which can act as possible basal sliding planes are present within the rock mass, ii) whether a sliding plane might have developed through intact rock failure in weaker rocks, iii) which geological features form the lateral release planes of the unstable rock mass and iv) whether the unstable rock mass is a massive block or dissected into various blocks. These issues were addressed by the analysis of the fault and fracture network data and the lithological variations.

An important step towards the identification of possible basal sliding planes in the study area was the mapping of instability-promoting fractures and faults dipping towards the valley. In the study area, discontinuity mapping revealed the limited presence of fractures dipping towards the valley and thus parallel to the measured SE displacement direction. The occurrence of these instability-promoting fractures seems to be restricted to secondary fractures associated with foliation-parallel faults in the more competent, augengneiss-type units. These fractures are frequent in the Randa Augengneiss (mapped as well by Sartori et al. 2003). However, in the gneissic series in the hanging wall, they are rare. An important question is whether the large inclined failure plane of the second 1991 rockslide that is covered with debris above 1900 m extends underneath the area of the present-



day instability. An extrapolation test with different dips for this plane and the measured borehole geometry was performed to test the likelihood of an unlimited planar fault intersecting borehole SB 120. The results indicate that for dips above  $41^\circ$  the feature should intersect the borehole, whereas if the feature undulates or is inclined less than  $41^\circ$ , it would not. Regardless, neither fracture mapping nor the single-hole radar reflection analysis in SB 120 provided evidence for such a persistent fault, even though the analysis of the single-hole georadar reflections should have been able to resolve the presence of a prominent reflectors with such a dip for some tens of meters below the borehole.

Lithological mapping and rock mechanical testing performed allowed the direct characterisation of the different gneissic lithologies in the hanging wall of the massive Randa Augengneiss body. The different lithologies had systematically different intact rock strengths reflected in the different uniaxial compressive strength values (69 vs. 97 MPa) and different shear strength envelopes. In previous studies on the initiation of the 1991 rockslide this region was always considered as homogeneous (Eberhardt et al. 2004, Segalini & Giani 2004).

The investigation results also allowed for the identification of lateral release planes and the internal structure of the rock mass. The fault trace map of the study area (Figure 2-7) depicts two sets of steep faults and fracture zones that can act as lateral release planes. The fracture patterns associated with these faults and thin sections suggest that these faults are large brittle-ductile shear zones. These two sets (F2 and F3 in Figure 2-4 b) dip steeply to the north and the east and as such form a rock wedge. The internal structure of the unstable (and stable) rock mass is dominated by steep to moderately inclined faults and fracture zones dipping to the NW. The analysis of single-hole georadar reflections showed that the major fractures of this orientation have a minimum extent of up to 50 m. First integration with displacement profiles in the boreholes implied that these major fractures also accommodate the internal deformation of the rock mass.

A first conclusion to be drawn from these results is that the instability scenarios involving highly persistent pre-existing sliding surfaces are difficult to justify with the geological model. Reverting to the instability scenarios described in section 2.1.2 this applies to case the translational rockslide (a) and the bilinear-sliding surface (d). The limited presence of possible sliding surfaces suggests either a stepped or progressively developing sliding surface (cases b and c), or the formation of a rotational sliding surface by means of stress- or structurally controlled failure within the weaker gneisses. As the lithological model for the lower section of the paragneissic series is not well constrained, due to the inaccessibility of the area, the latter scenario could not be excluded at this point of the study. The last considered instability scenario of chevron toppling was contradicted by the mapped constant dip of foliation within the stable and unstable rock mass. To further improve the identification of possible instability scenarios, displacement data and verification by numerical modelling are needed (see Chapter 3 and 4).

## 2.7 Figures

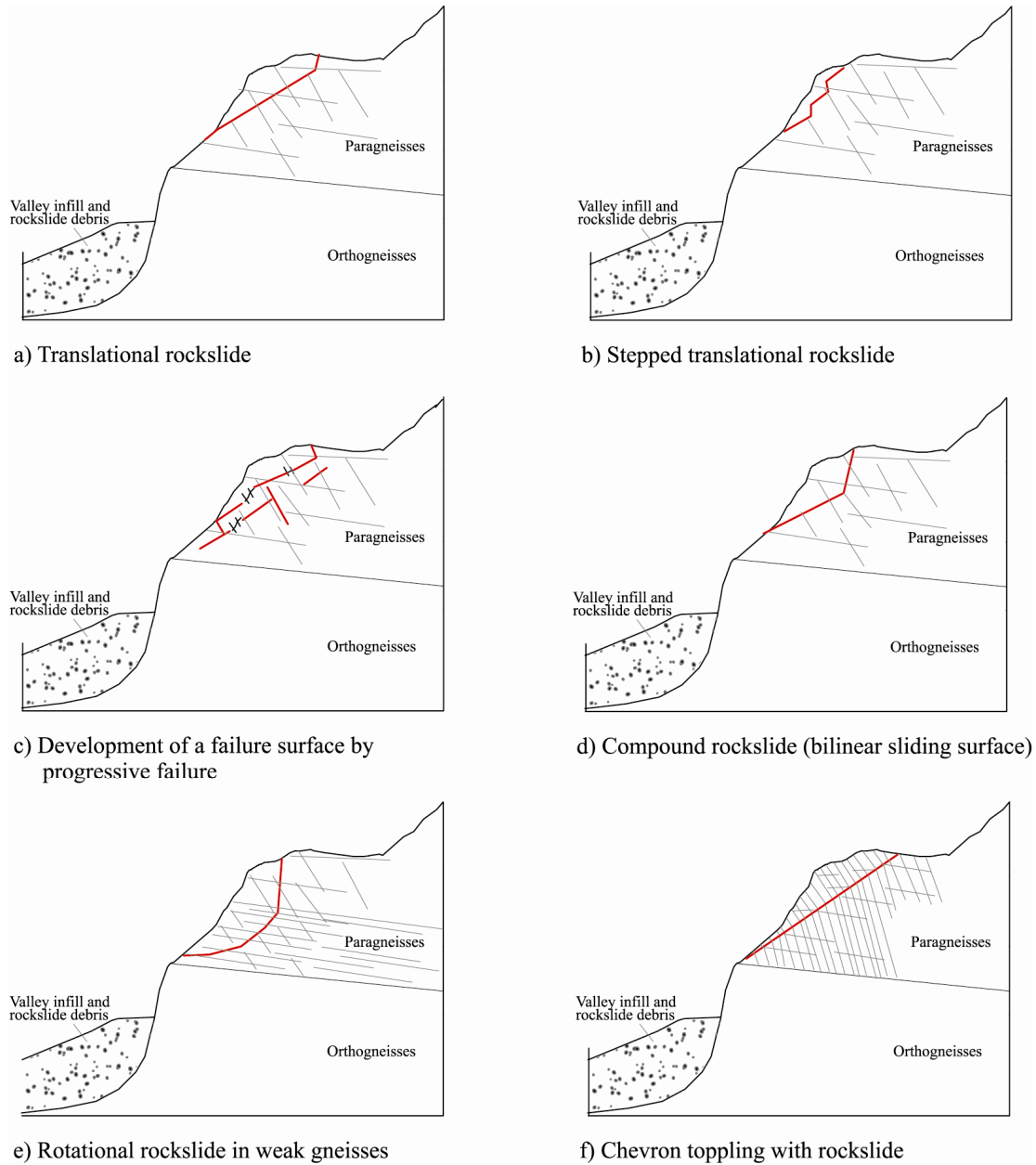


Figure 2-1: Possible instability scenarios for the investigated slope instability. The nomenclature of the rockslide types relates to Cruden & Varnes (1996) and Hungr & Evans (2004).

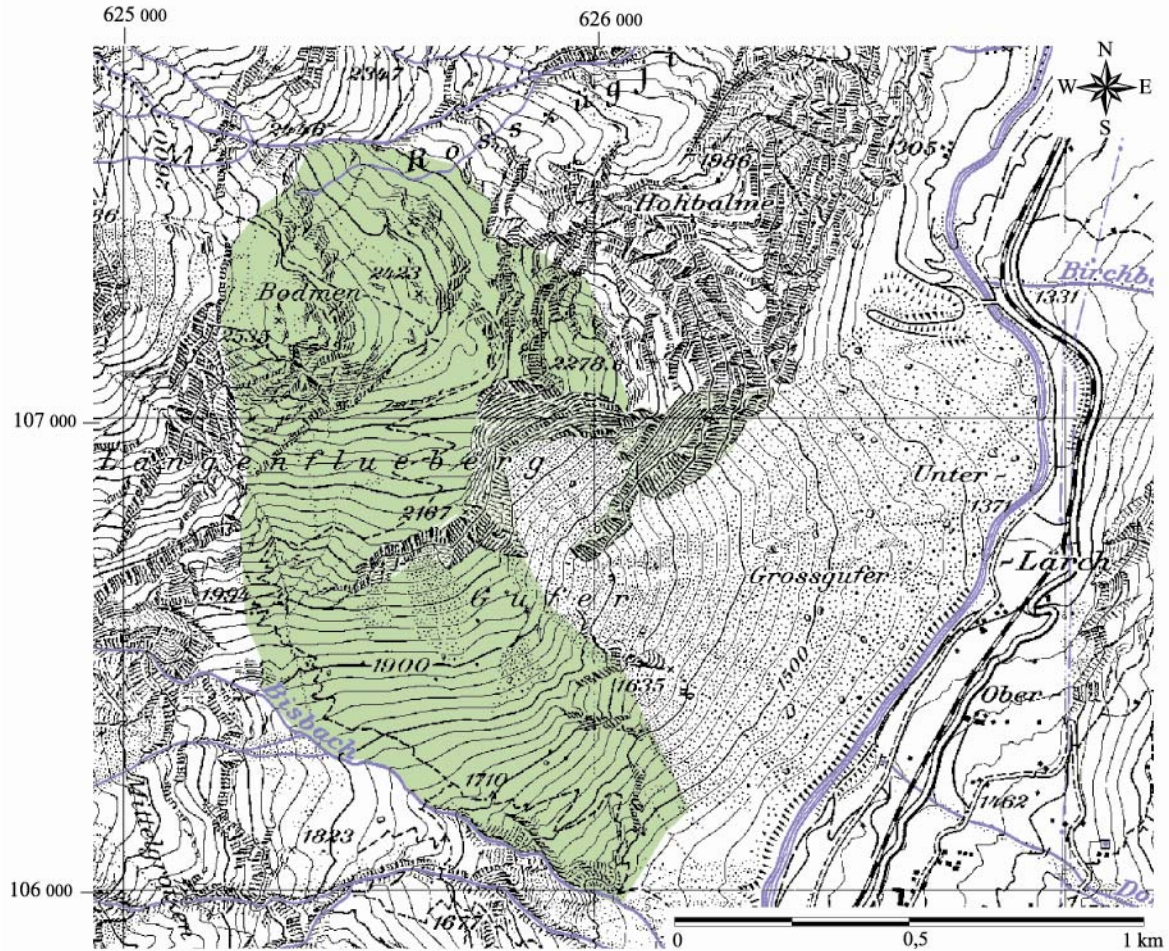


Figure 2-2: Overview of the study area around the 1991 rockslide scarp. The mapped area is highlighted in green, the scarp region of the 1991 rockslide and other steep rock faces were analysed using aerial photographs. Topography taken from Landestopographie, sheet Mischabel 1:50 000.



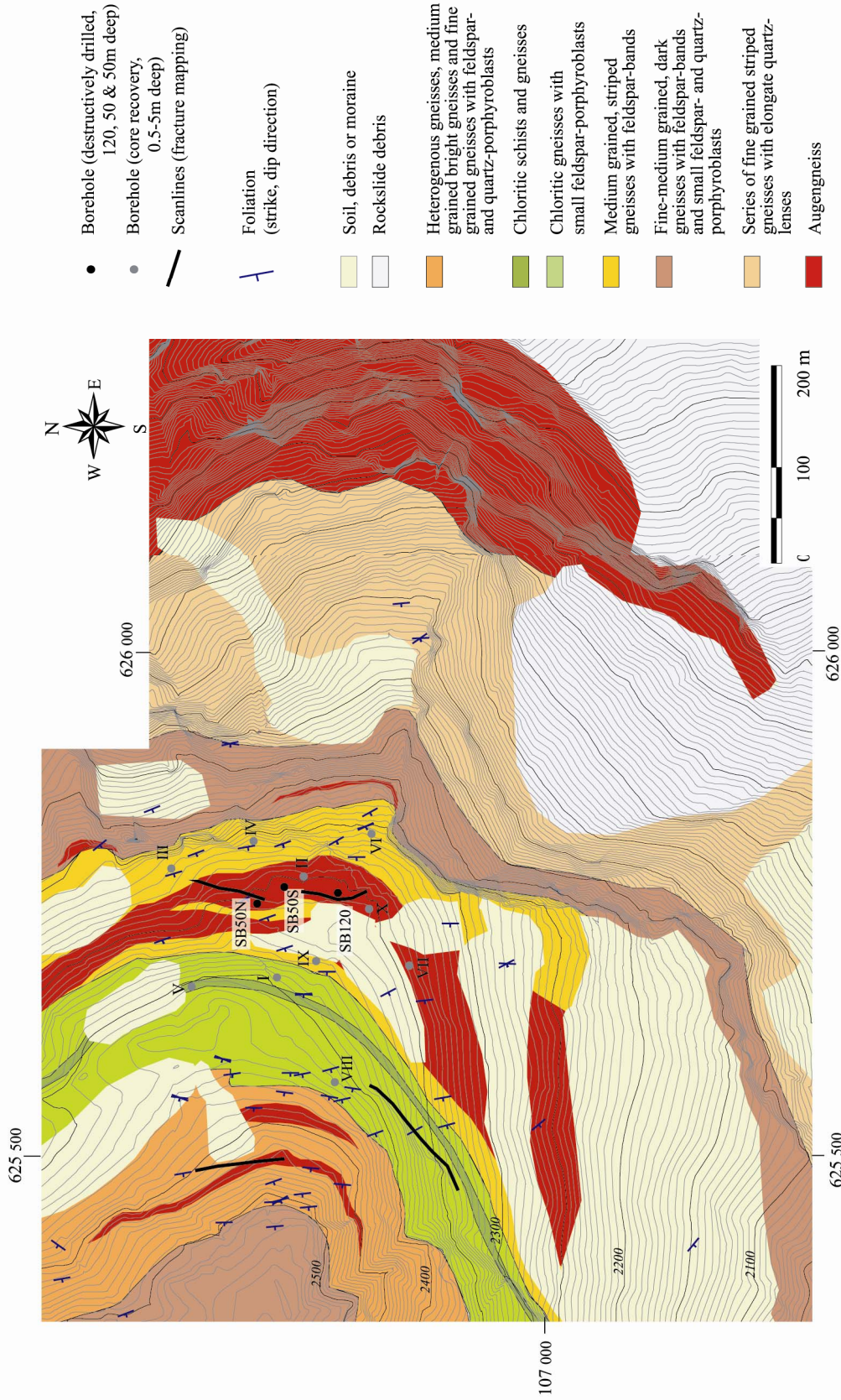


Figure 2-3: Lithological units and subunits in the study area with dip direction of the foliation fractures plotted in blue. Digital elevation model provided by CREALP.

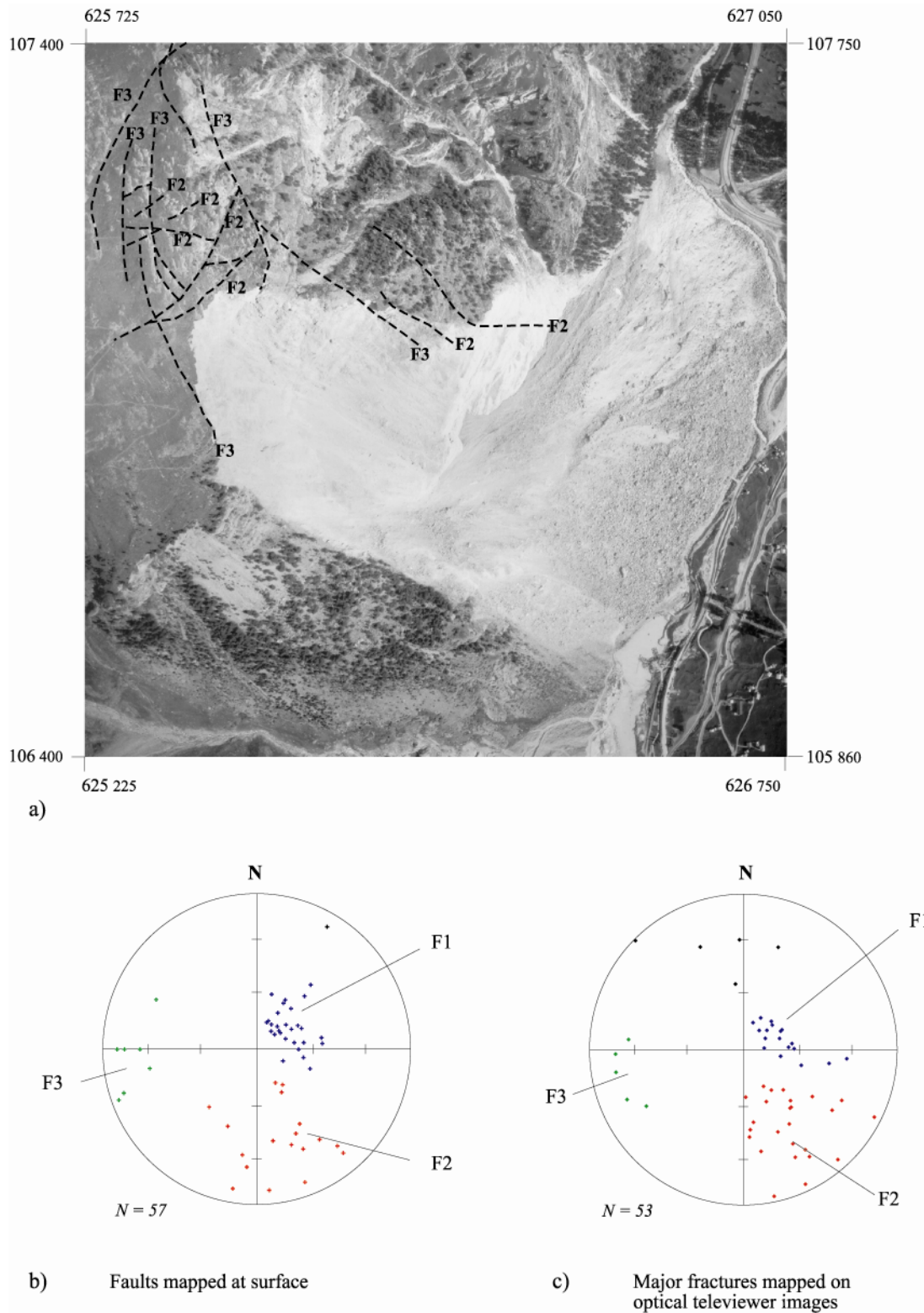


Figure 2-4: a) Aerial photograph of the study area around the scarp of the 1991 rockslides. (photo provided by Landestopographie) with the traces of faults and fracture zones. b) Stereonet of faults and fracture zones mapped at the surface. The set F1 is parallel to foliation and contains brittle-ductile shear zones. c) Stereonet of major fractures intersected by the borehole; pure phyllonites parallel to foliation (i.e. without fracture) are not plotted. The stereonet for the surface and borehole data show a good agreement of preferred fault and fracture zone orientation.



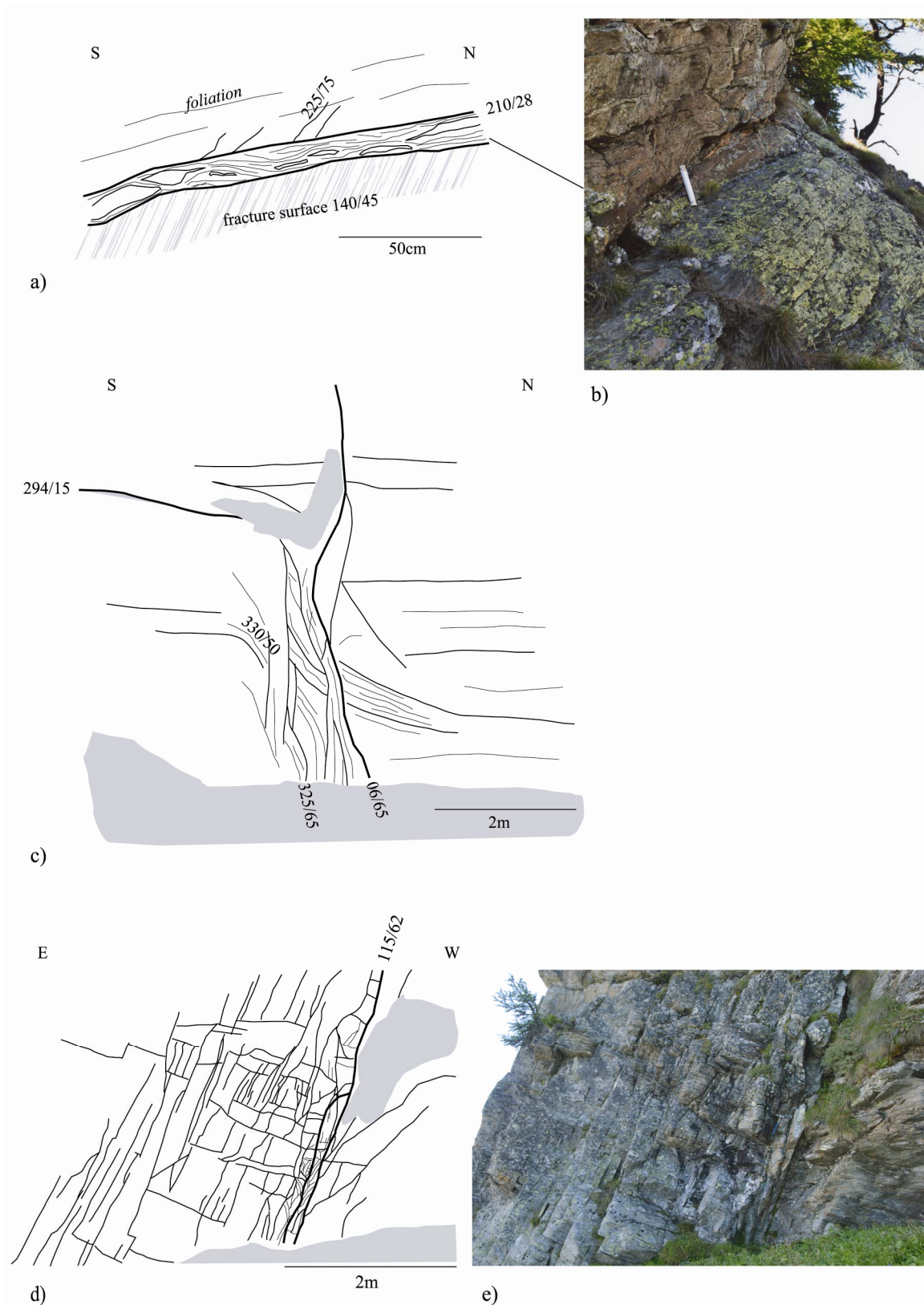


Figure 2-5: Examples of faults mapped. a-b) Outcrop photograph and expanded sketch of the fault core of a F1 fault. The lithology above and below the fault are comparable; below the fault a large fracture is exposed c) Outcrop sketch of a F2 fault. d-e) Outcrop photograph and sketch of a F3 fault.

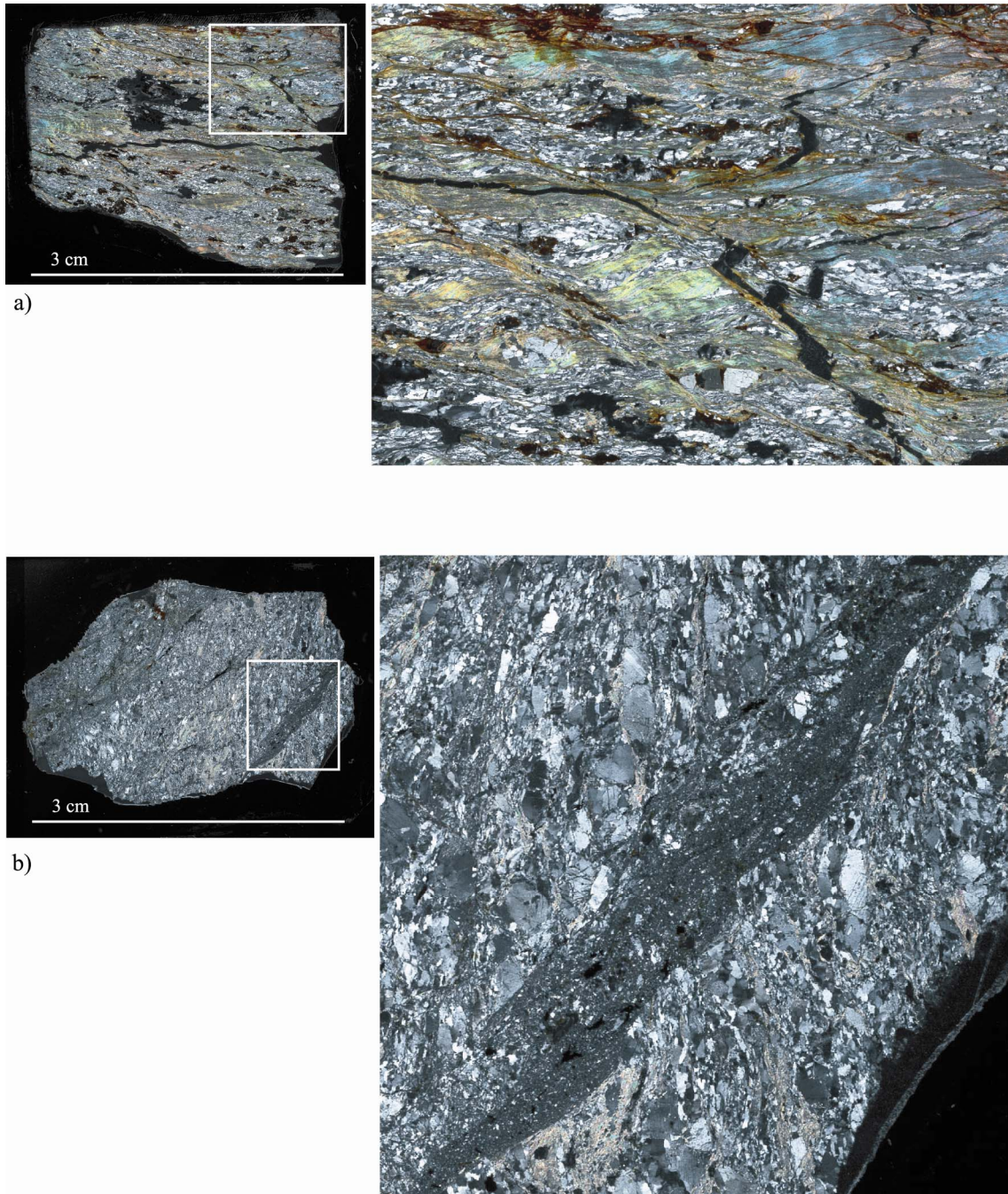


Figure 2-6: Thin sections of fault cores. a) Thin section taken from a foliation parallel fault F1. The thin section is oriented perpendicular to the foliation. In the phyllonitic fault core oxidized mylonitic bands (brown) surround rounded feldspar-rich lenses. b) Thin section taken from a steep N-S striking F3 fault (see Figure 2-5 d-e). A fine-grained fault gouge is shown in the enlarged view.



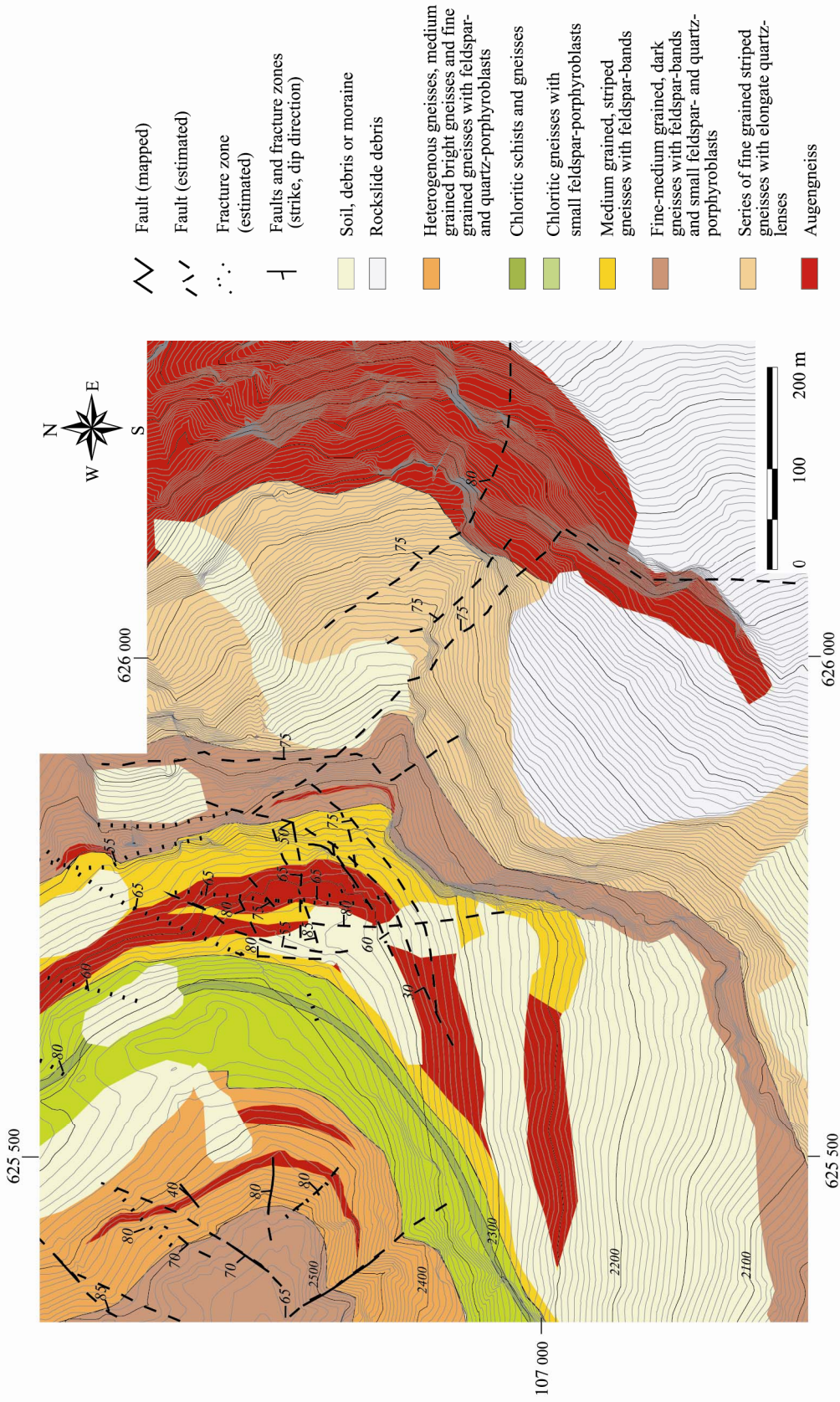


Figure 2-7: Traces, dip direction and dip of faults and fracture zones (mapped and estimated from aerial photographs). Digital elevation model provided by CREALP.



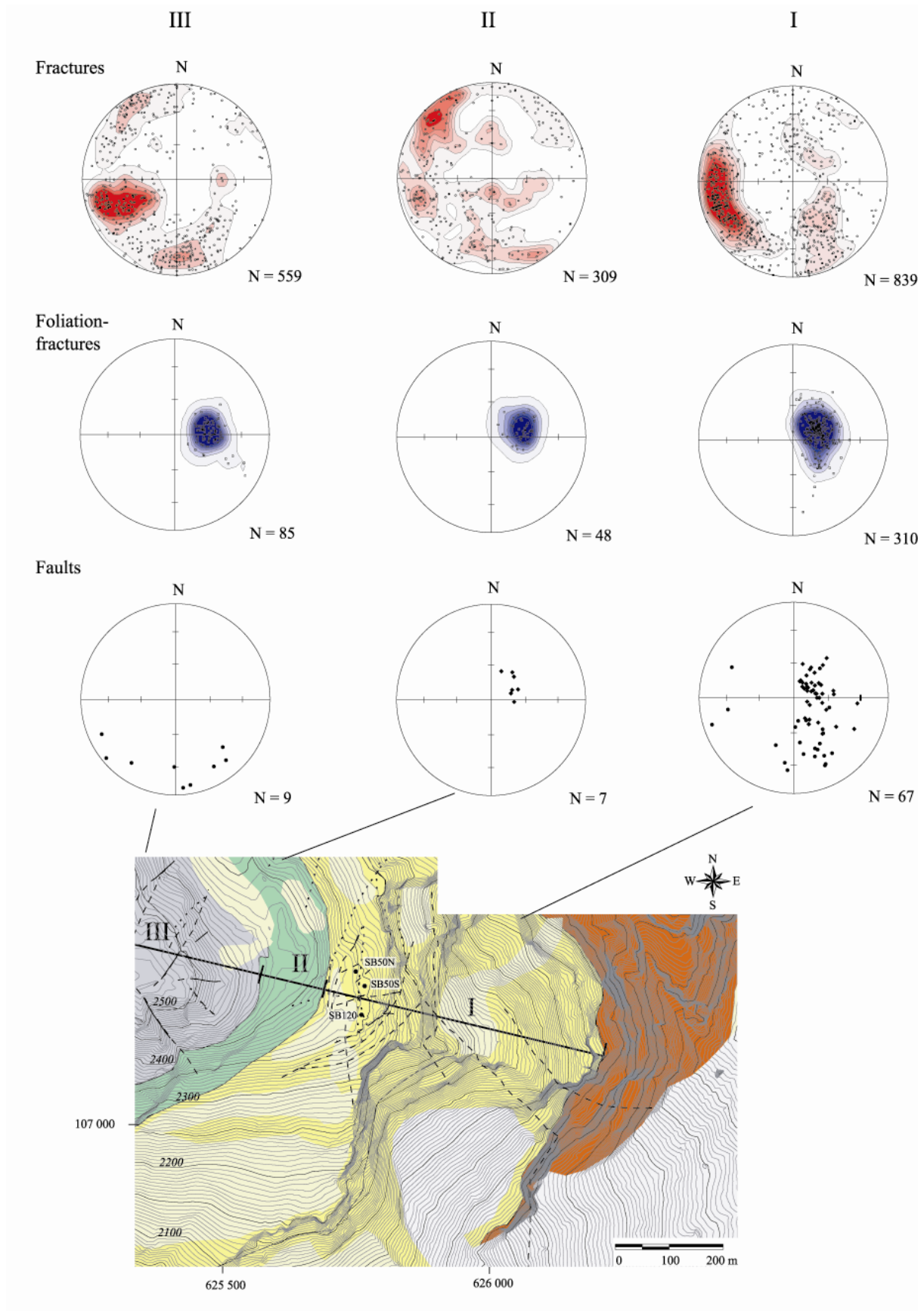


Figure 2-8: Structural compartments of the study area. For each compartment stereonet are given for the fractures, foliation fractures and faults (equal area, lower hemisphere, weighted).

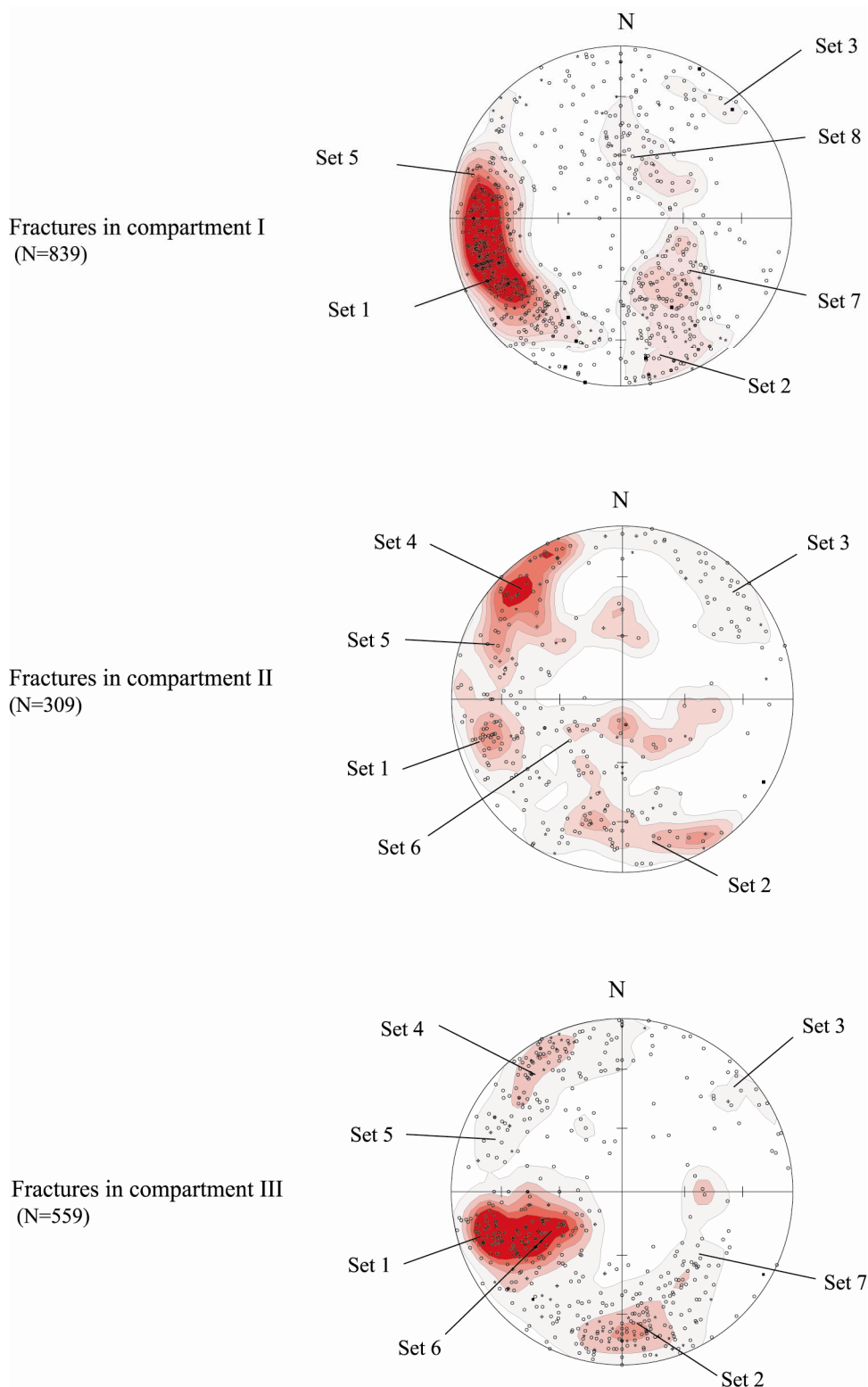


Figure 2-9: Stereonets showing fracture sets within the three structural compartments (equal area, lower hemisphere, weighted). Foliation fractures are not shown.

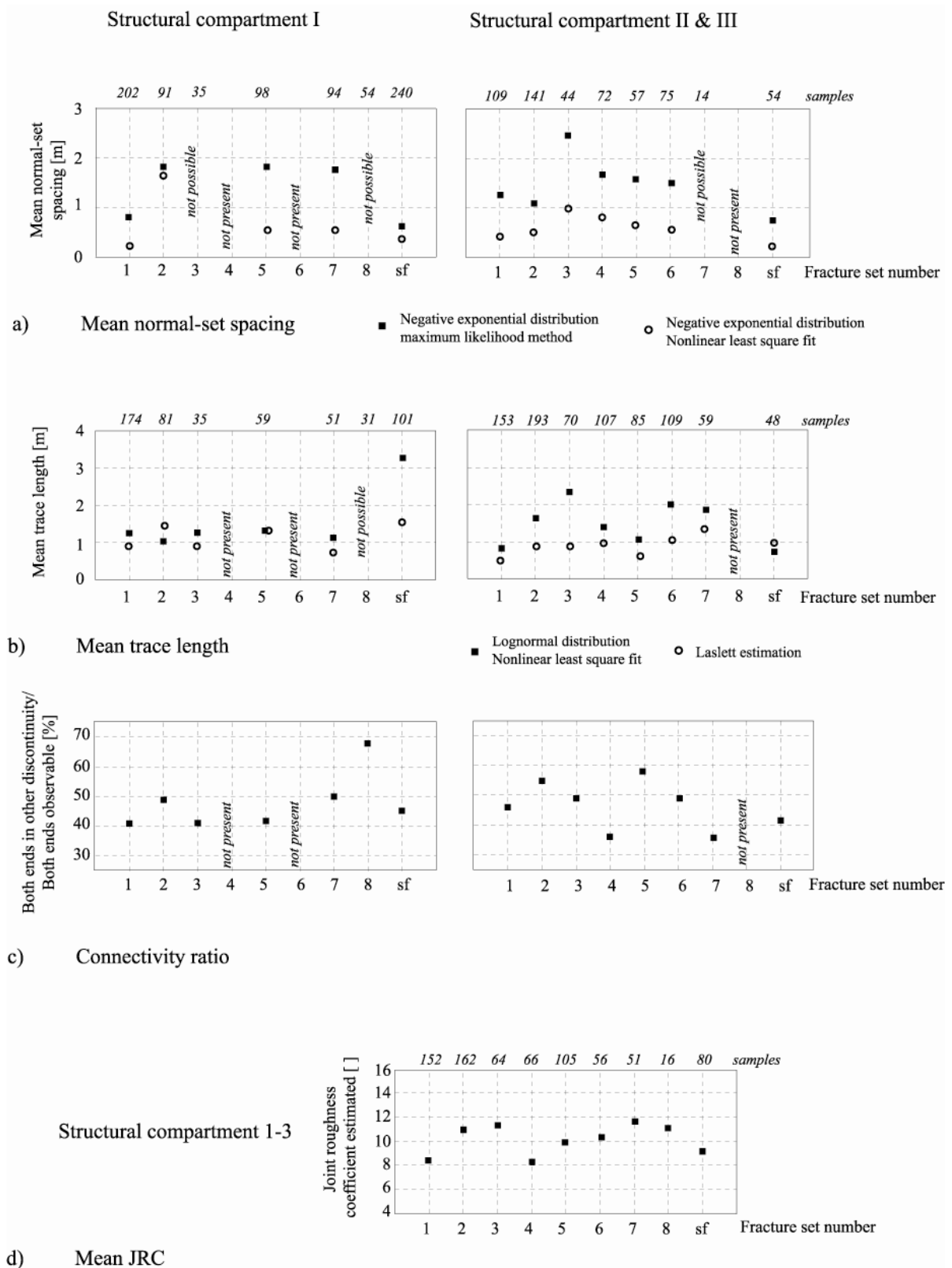


Figure 2-10: Properties of the fracture sets in structural compartment I, II & III. a) Mean normal set spacing calculated using negative exponential distribution parameters derived by maximum likelihood method and nonlinear least square fitting. For small sample numbers no reliable fit could be obtained. b) Mean trace length calculated using lognormal distribution fitted in least square sense and the Laslett estimation. c) Percentage of fractures with both ends connected to other fractures wrt number of fractures with both ends observable. d) Mean JRC values for the fracture sets in all structural compartments.

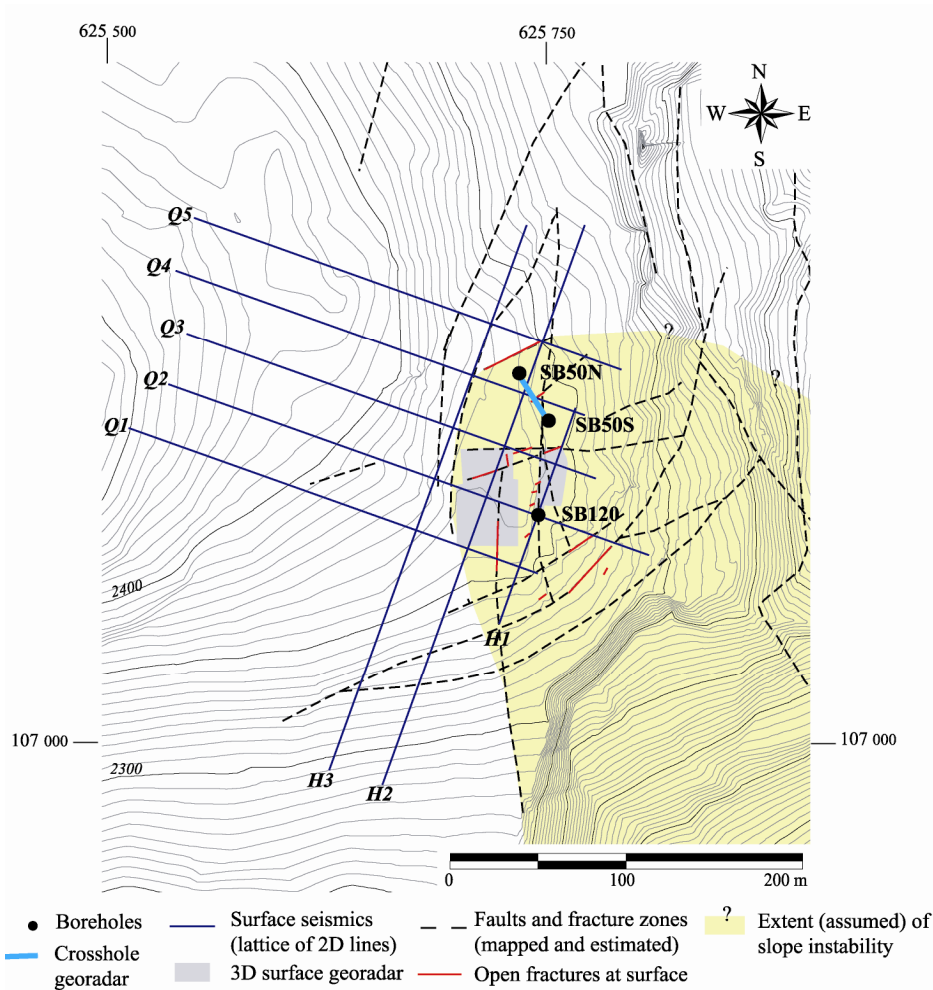


Figure 2-11: Geophysical surface and subsurface investigations. On the surface 3-D georadar (grey area) and surface seismic profiles (blue lines) were measured. In the boreholes georadar single-hole and cross-hole test (light blue line) were performed. The extent of the current instability is indicated by yellow shading; active segments that show opening are highlighted in red.

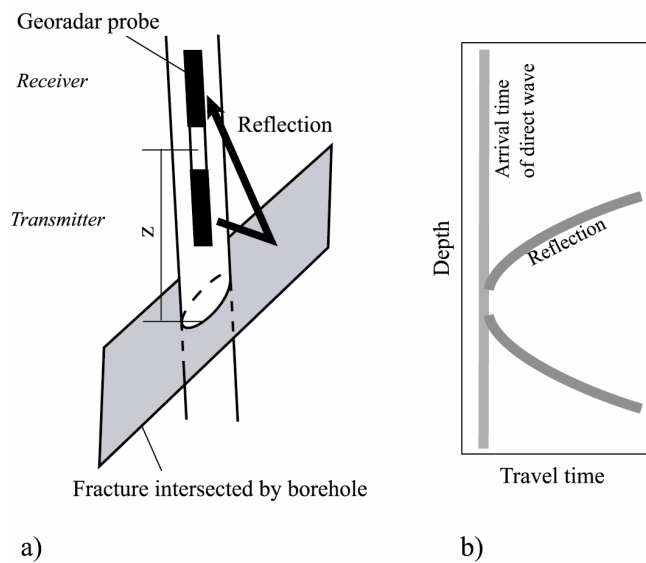


Figure 2-12: Principle of the single-hole georadar reflection method. a) Fracture plane reflecting the georadar signal. b) The characteristic reflection pattern generated by a planar reflector.



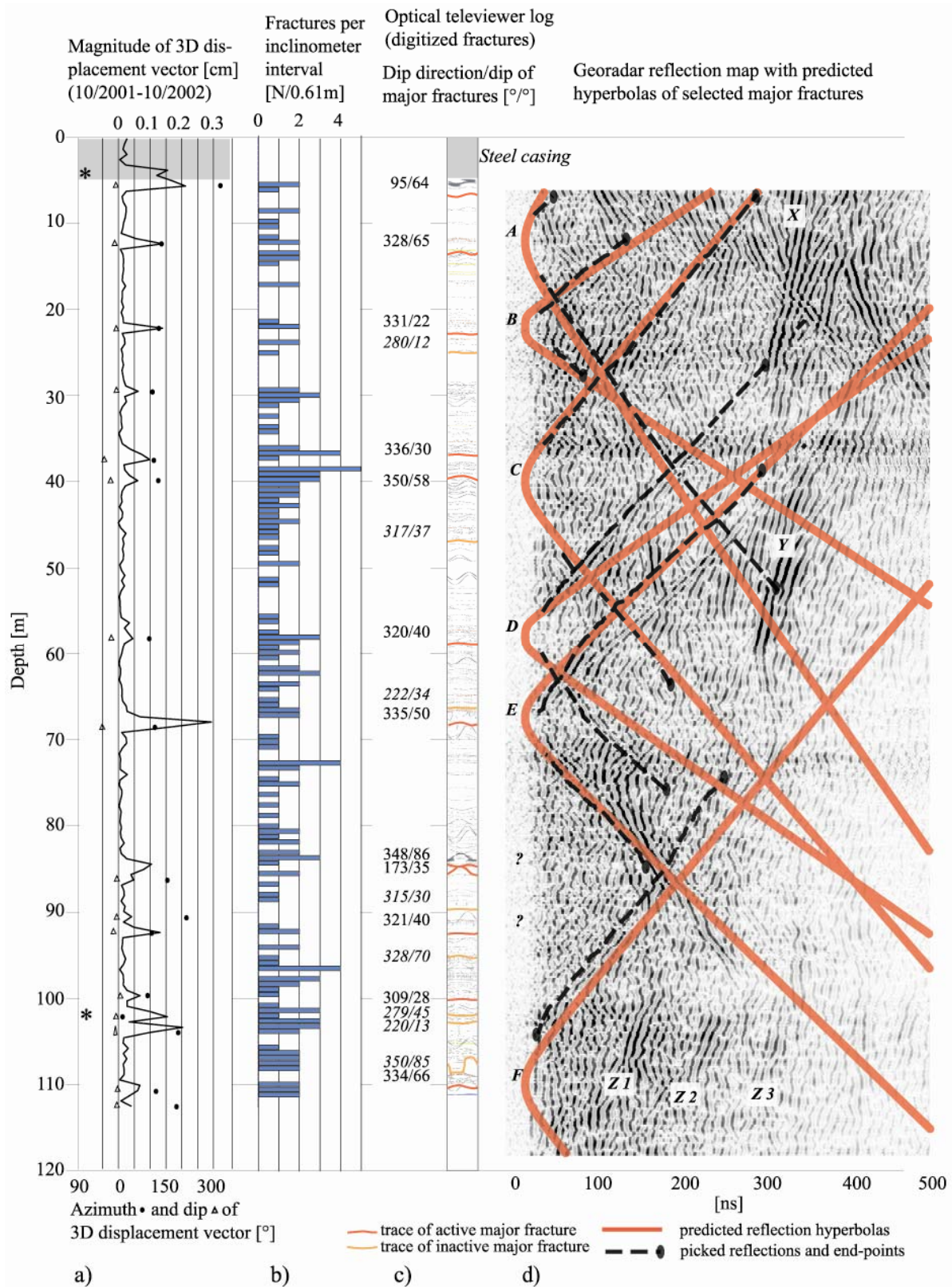


Figure 2-13: Fracture mapping in SB 120 (modified after Willenberg et al. 2004). a) Incremental displacement magnitude along the hole and azimuth,  $\theta$  and dip,  $\phi$ , of the relative displacement vectors. The stars at 5 and 103 m denote zones where casing deformation is related to ungrouted sections. b) Number of fractures per inclinometer interval (0.61m) derived from the optical televiwer image. c) Digitised fracture traces on the optical televiwer image. Major fractures are highlighted in orange and dip-direction and dip supplied. d) Georadar reflection image with predicted (solid) and picked (dashed) reflections. The six predictions shown could be associated with georadar reflections.

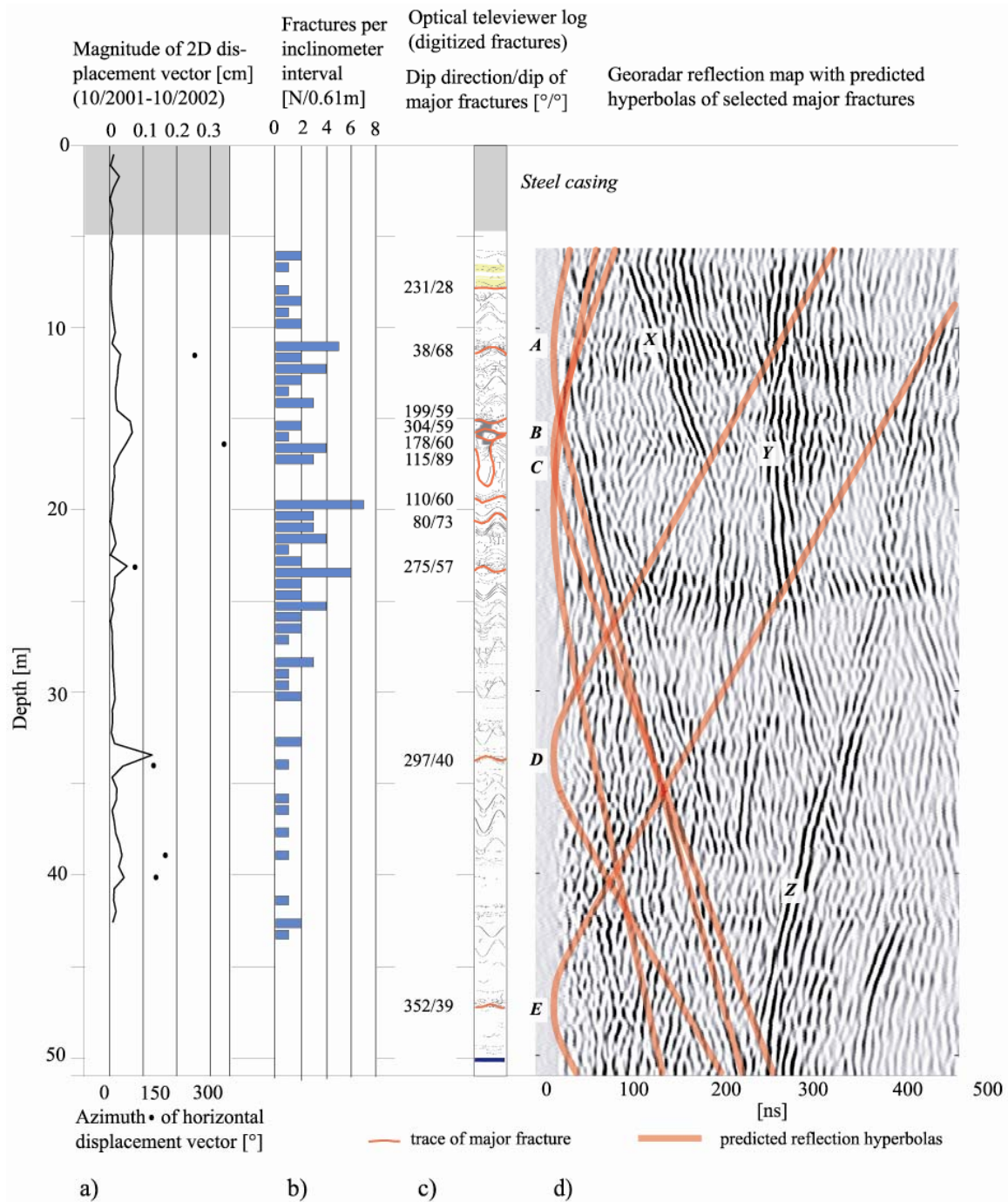


Figure 2-14: Fracture mapping in SB 50S. a) Incremental displacement magnitude along the hole and azimuth of the relative displacement vectors. b) Number of fractures per inclinometer interval (0.61m) derived from the optical televiewer image. c) Digitised fracture traces on the optical televiewer image. Major fractures are highlighted and dip-direction and dip supplied. d) Georadar reflection image with predicted (solid) reflections.

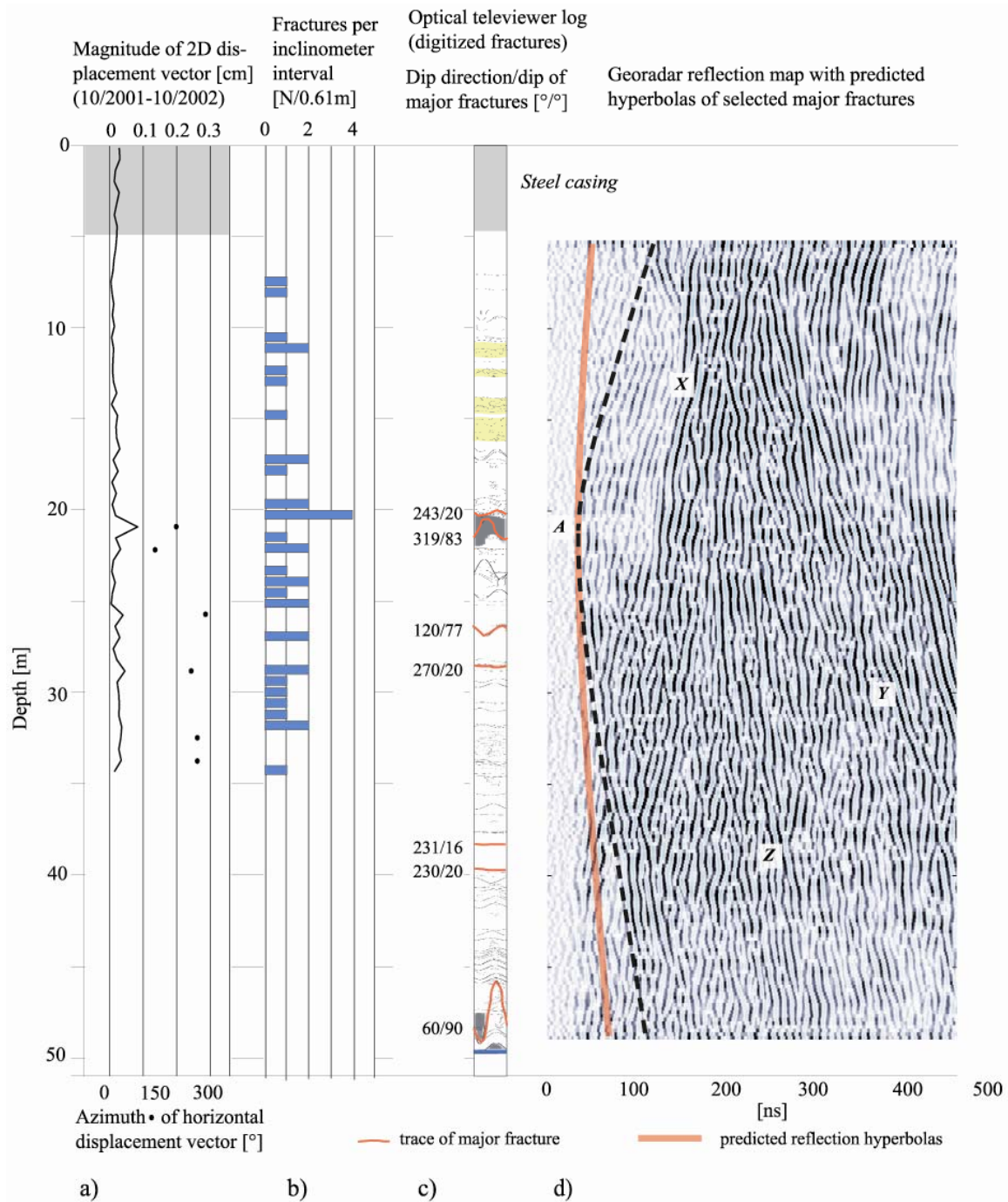


Figure 2-15: Fracture mapping in SB 50N. a) Incremental displacement magnitude along the hole and azimuth of the relative displacement vectors. b) Number of fractures per inclinometer interval (0.61m) derived from the optical televiewer image. c) Digitised fracture traces on the optical televiewer image. Major fractures are highlighted and dip-direction and dip supplied. d) Georadar reflection image with predicted (solid) reflection and reflection with corrected (dashed) dip.



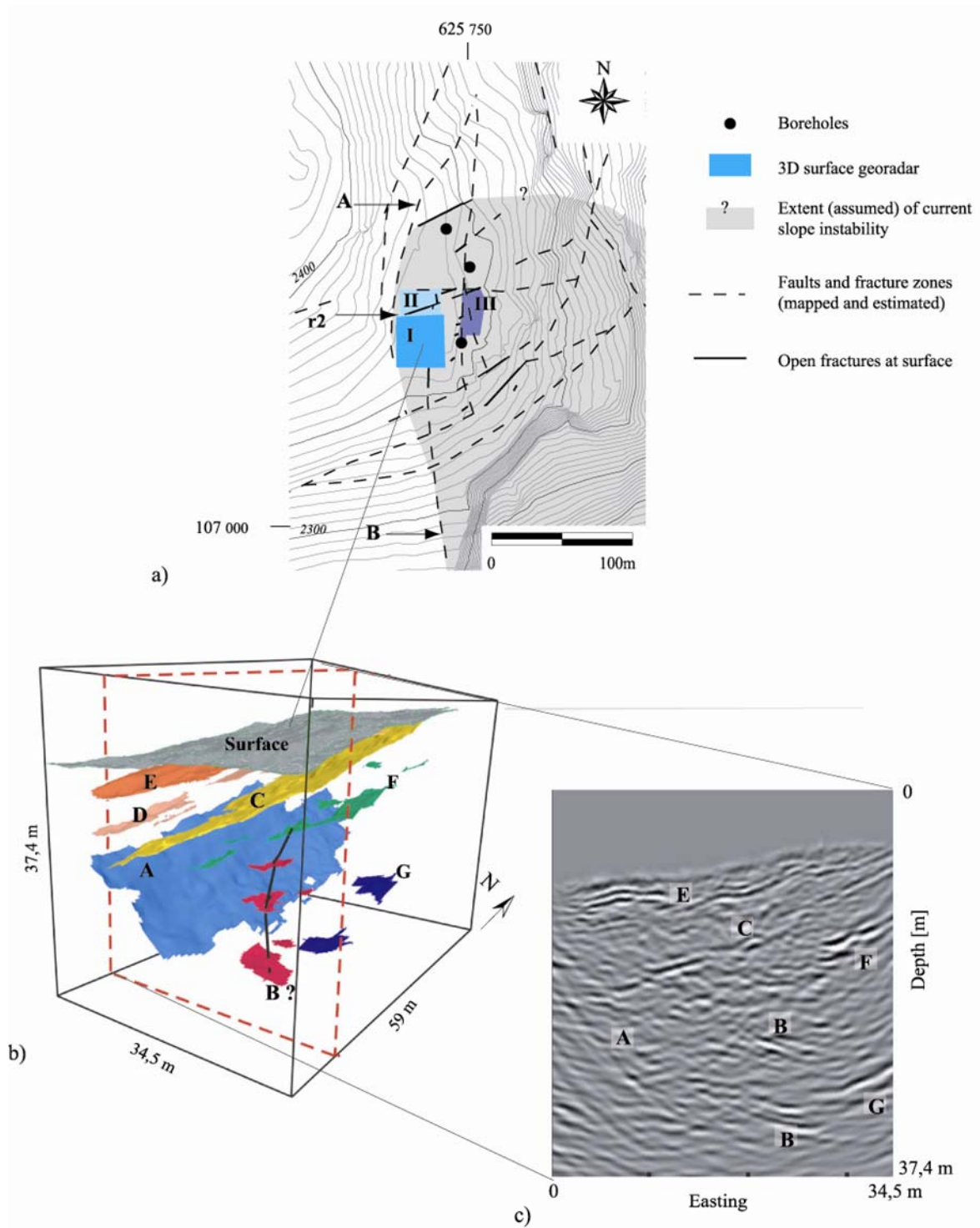


Figure 2-16: Comparison of 3-D surface georadar and mapped faults and fracture zones. a) Map of the investigation area showing the three georadar fields, the plotted two upper fields are highlighted. b) Picked reflectors and diffractors in the investigation volume for the fields I and II c) Vertical cross-section through the georadar volume; the picked reflections and diffractors are denoted A-G. b) and c) were modified after Heincke et al. (2004).



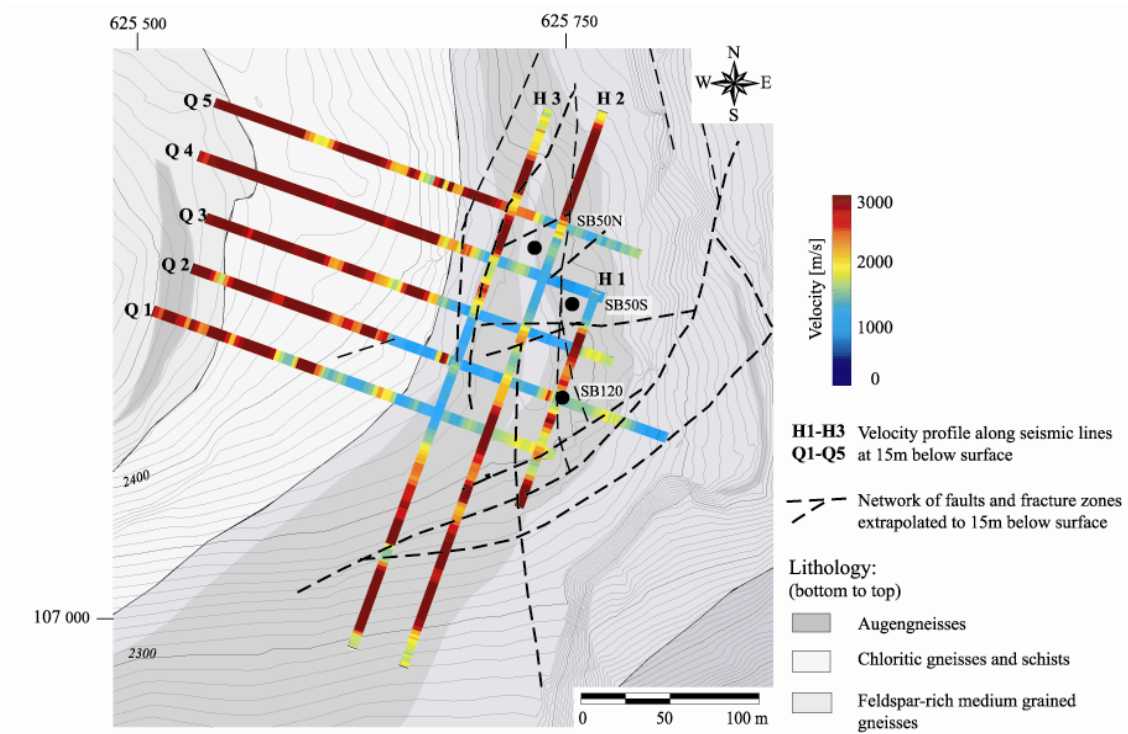


Figure 2-17: Grid of surface seismic line. Plotted are P-wave velocities derived by refraction tomography at 15m below surface together with the faults and fracture zones extrapolated to 15 m depth.

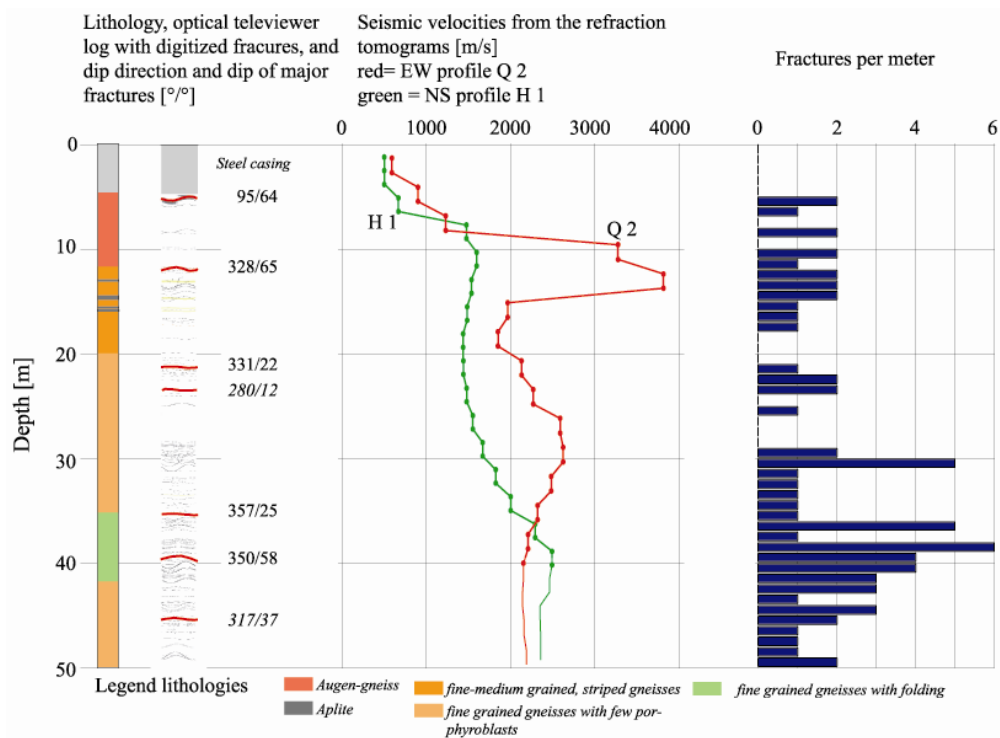


Figure 2-18: Profile of calculated p-wave velocities in SB 120 for the seismic lines H1 (north-south direction, green) and Q2 (east-west profile, red) in comparison to the lithological and fracture records derived from optical televiewer images. For each cell (2.6 m) two velocity values are plotted with red and green dots. Major fractures are indicated in red on the digitised fracture intersections at the borehole wall. The histogram to the right shows the number of fractures per meter.

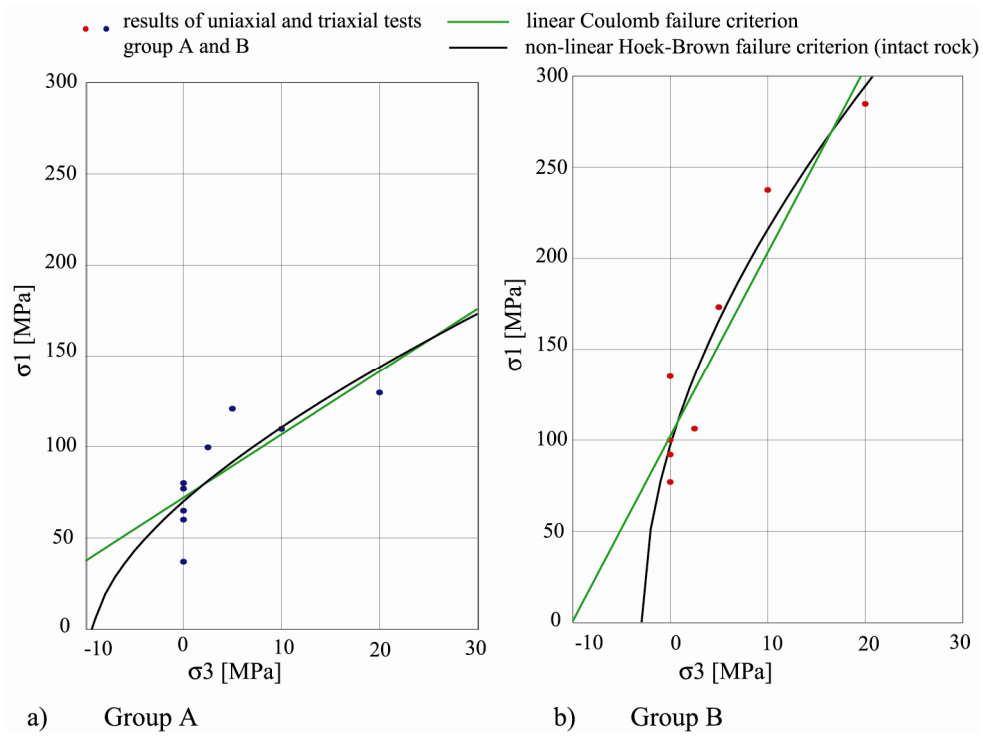


Figure 2-19: Analysis of uniaxial and triaxial laboratory testing applying Coulomb and Hoek-Brown failure criteria.

### **3 Establishing a block kinematic model for the study site using a multi-component geotechnical monitoring system**

### 3.1 Introduction

This chapter describes the results obtained from the geotechnical monitoring system set up at the study site. The geotechnical monitoring system comprises components measuring the displacement fields at the surface and at depth periodically and continuously. As demonstrated in the previous chapter, the rock mass under study is dissected into multiple blocks by foliation-fractures, joints, fracture zones and faults, resulting in a complex block assemblage. As the foliation at the study site dips away from the valley, which is generally favourable for slope stability, the slope instability has to be related to the fracture and fault system. An important issue that arose from geological mapping is the estimation of the depth of the instability. This may be complicated since the basal boundary (i.e. sliding surface) might step through several fracture sets and involve fracturing of intact rock bridges (Einstein 1993). By integrating geotechnical and geological data a detailed 3-D-model of the structure of the unstable rock mass and the distribution of movements within it could be developed. The temporal changes in displacement and its relation to climatic factors provided insights into the processes controlling the deformation.

The approach of assessing rockslide mechanisms by monitoring the displacement fields and microseismicity of a slowly moving rockslide in fractured crystalline rock is rather novel. Comparable studies are largely concerned with landslides in soil, strongly weathered rock or sliding along highly persistent bedding or fault planes in rock. Case studies of rockslides that involve geotechnical monitoring systems at depth are often related to open pit mining (Ding et al. 2000), monitoring of slopes at artificial reservoirs (Imrie & Moore 1993, Watson et al. 2004) or to early warning systems at potentially hazardous, rock slopes with accelerated displacements (Kennedy & Niermeyer 1970, Eyer et al. 1998). However rockslide studies where the monitoring system is restricted to surface measurements are much more common (Sandersen et al. 1996, Canuti et al. 2002).

The first part of the chapter focuses on the design and installation of the monitoring system and its integration into an existing early warning system. The following sections describe the measurements at the surface and those at depth performed to assess the displacement fields at the study site. As the displacements at the study site are distributed over the rock mass and hence small, a special issue was the required accuracy of the displacement measurements. A block kinematic model for the unstable rock mass was constructed to attempt to discriminate between different types of rock mass behaviour. For example whether displacement is localised and accommodated on a few, extensive through-going planar features or whether it is distributed throughout the rock mass, perhaps stepping through the various steep and inclined fracture sets of the small-scale fracture network. Reverting to the results of the continuous measurements the evolution of the recorded displacements was analysed. The combined kinematic-dynamic model is the basis for the interpretation of the rockslide kinematics and provides block geometries and displacements for numerical modelling of rockslide processes.

### 3.2 Design and implementation of the monitoring network

The monitoring network shown in Figure 3-1 and Figure 3-2 was set up in late summer 2001. The borehole array and instrumentation was designed on the basis of results from an existing early-

warning system installed after the 1991 rockslides. This early system comprises periodically-measured benchmark arrays for monitoring surface fracture opening, retro-reflectors of a large-scale geodetic network to monitor rock mass displacements and a climate station (Ornstein et al. 2001). These data (provided by Centre de Recherche sur l'Environnement ALPin (CREALP)) revealed the approximate extent of the unstable rock mass as delineated in Figure 3-1 and the orientation of the surface displacement vectors referenced to the opposite side of the valley. The latter are oriented to the SE with a dip of 15-50°, and decreased from the scarp of the 1991 rockslide back towards the NW. The fracture opening measurements for the period 1991-1999 indicated that the unstable rock mass was dissected into large blocks which acted as rigid bodies.

The three boreholes, denoted SB 120, SB 50S and SB 50N, were drilled to depths of 120, 50 and 50 m respectively and were located so as to lie between active surface fractures. Hence each borehole was situated on a separate block of the unstable rock mass. Further considerations for positioning the boreholes were drilling logistics (i.e. accessibility for the drill rig) and constraints arising from the experiment program (e.g. geophysical cross-hole experiments). The boreholes were drilled destructively with a down hole hammer and air lift of the cuttings. The drilling progress was monitored as were the cuttings and dust. For safety reasons, the existing benchmark arrays across surface fracture were measured daily during the drilling. All boreholes were found to be dry, except for the lowermost 10 meters of SB 120. As the borehole walls were stable, optical televiewer, borehole geometry and spectral gamma logs were run, and cross-hole, single-hole and borehole-to-surface experiments conducted. The borehole geometry logs indicated that all boreholes deviated significantly from vertical reaching 14° at the bottom of SB 120 and 4-6° in SB 50N and SB 50S. The deviation was consistently towards the E-SE, which is approximately perpendicular to the foliation. Thus, the trajectories were drawn towards the normal to the foliation plane.

### 3.2.1 Geological model of the study site

Based on surface mapping, two scales of discontinuity networks were recognised: a small-scale network consisting of fractures with lengths of up to 5 m, and a large-scale network of faults and fracture zones. The small-scale network consists of four steep and two inclined fractures sets (Figure 3-3a). Trace lengths were found to follow lognormal distributions with mean trace lengths between 1.0 and 1.3 m for the steep fracture sets and 3.3 m for the foliation fractures (see Chapter 2). The surface mapping was extended into 3-D using the oriented optical televiewer images from the three boreholes. The images allowed the dip, dip-direction and rank to be determined. The rank refers to whether the fractures were considered to be major or minor, and was determined from the thickness of the fracture trace on the image. Fractures with traces below 2 mm thickness were categorised as minor fractures. The orientation characteristics of the borehole fracture sets shown in Figure 3-3b were in accord with surface observations. The faults and fracture zones mapped at the surface have trace lengths longer than 10 m. The faults are drawn on the map in Figure 3-1, and their poles plotted on the stereonet in Figure 3-3c. Two dominant populations of moderately inclined and steep faults that strike N-S, ENE-WSW and NE-SW are evident. The traces of major fractures in the borehole logs (i.e. those with widths greater than 2 mm) tend to contain intensely foliated material. The poles to these fractures are plotted in Figure 3-3d. Their distribution coincides well with the orientations of faults and fracture

zones mapped at surface (Figure 3-3c). It is noteworthy that few fractures and faults dip in the same direction as the measured surface displacement vector (120-160°/15-50°).

### 3.2.2 Installation of the monitoring network components

After completion of the borehole geophysics measurements, the boreholes were completed with the geotechnical and microseismic monitoring systems listed in Table 3-1. PVC inclinometer casing was installed in all three boreholes (Figure 3-4), and the SB 120 casing was also fitted with external steel rings each meter for surveying with an induction coil transducer extensometer system (Interfels 'Increx' system). The casings were surveyed every spring and autumn. By taking differences in measurements between surveys, profiles of oriented-inclination and axial strain (SB 120 only) that have accrued along the casings in the inter-survey period were obtained. Coaxial cables for time domain reflectometry (TDR) measurements (Dowding & O'Connor 2000) were also cemented in place on the outside of the 50 m casings to compare against the inclinometer measurements.

To determine the detailed time-history of the displacements on active fractures during the inter-survey period, two in-place biaxial inclinometers were installed across prominent fractures in the 120m borehole and were sampled every 6 minutes. The inclinometers were Geokon vibrating-wire instruments and had a 2m baselength. Pressure sensors (Geokon vibrating wire piezometer) were installed at the bottoms of the holes and also sampled every 6 minutes. An additional possibility of measuring fluid pressures around a fracture zone near 100 m depth in SB 120 as shown in Figure 3-4 was realised by using a slotted section of casing which had been packed off. This permitted water to flow into the casing such that the water level could then be measured manually in the borehole with an electrical water level probe. The borehole instrumentation was completed by 3-component geophones installed at the borehole bottoms for monitoring microseismicity associated with the rock mass movements. These three sensors in the 'deep' boreholes were augmented by 9 additional sensors in shallow boreholes of depths 0.5-5 m. The plan of this 12-station microseismic array is described in Willenberg et al. 2002.

The installation of the casing was accomplished by integrating the different instrumentation modules containing the piezometers and geophones into the 3 m sections of inclinometer casing. The location of the piezometer modules was chosen on the basis of borehole televiewer images. The 3-component geophones were oriented with respect to the casing grooves so their geographic orientation could be determined after installation. The entire assembly consisting of the inclinometer casing, the protection tubes for the external wires, the TDR cable and the grout injection tubes was surrounded with geotextile stocking. The purpose of the stocking was to limit grout loss into large open fractures during cementation. Such fractures were known to be present from observations on the loss of cuttings during drilling, breakout zones in the borehole caliper log and the optical televiewer images. After building the assemblies into the three deep boreholes, the annulus was filled with grout.

In 2002, two automatically-recording surface crackmeters (Geokon vibrating wire crackmeter) were installed to supplement the manually-surveyed, surface benchmark array (Figure 3-2). So called 'benchmark quadrilaterals' were installed across the same fractures in order to compare the automatic readings against periodic manual measurements and to determine the vector of surface fracture opening.

Table 3-1: Specifications of monitoring network components at surface and at depth.

<i>Instrument</i>	<i>Type</i>	<i>Sampling period</i>	<i>Purpose</i>	<i>Reference</i>
<b>Surface</b>				
<i>Crackmeter</i>	<i>Vibrating-wire</i>	<i>Every 6 minutes</i>	<i>Dynamics of surface fracture opening</i>	
<i>Benchmark quadrilaterals</i>	<i>Beam-compass</i>	<i>Periodic (2-3 times/year)</i>	<i>Vector of surface fracture opening</i>	
<i>Benchmarks</i>	<i>Tape-measure</i>	<i>Periodic (2-4 times/year)</i>	<i>EWS, identification of active fractures</i>	<i>Ornstein et al. 2001</i>
<i>Geodetic survey</i>	<i>Retro-reflectors</i>	<i>Periodic (1 time/year)</i>	<i>EWS, vector of surface displacement</i>	<i>Ornstein et al. 2001</i>
<b>Boreholes</b>				
<i>Inclinometer</i>	<i>Servo-accelerometers</i>	<i>Periodic (1-2 times/year)</i>	<i>Horizontal displacements along borehole axis</i>	
<i>Extensometer</i>	<i>Induction-coil transducer</i>	<i>Periodic (1-2 times/year)</i>	<i>Vertical displacements along borehole axis</i>	
<i>In-place-inclinometer</i>	<i>Vibrating-wire</i>	<i>Every 6 minutes</i>	<i>Dynamics of horizontal displacements across fractures</i>	
<i>Piezometer</i>	<i>Vibrating-wire</i>	<i>Every 6 minutes</i>	<i>Water pressure conditions</i>	
<i>Geophones in deep boreholes</i>	<i>3-component (<math>f_n = 28</math> Hz)</i>	<i>Event-triggered</i>	<i>Microseismic monitoring</i>	<i>Eberhardt et al. 2004</i>
<i>Geophones in shallow boreholes</i>	<i>3-component (<math>f_n = 8</math> Hz)</i>	<i>Event-triggered</i>	<i>Microseismic monitoring</i>	<i>Eberhardt et al. 2004</i>
<i>TDR</i>	<i>Coaxial cable</i>	<i>Periodic *</i>	<i>Identification of active shearing along borehole</i>	

*EWS= early warning system of the cantonal authorities;  $f_n$  = resonance frequency*

*\* measurements stopped after the second repeat survey*

### 3.2.3 Data acquisition system

The surface crackmeters, borehole piezometers and in-place inclinometers were sampled every six minutes by a data acquisition system illustrated in Figure 3-5. The purpose of the high sample rate was to determine whether displacements occur in sudden events or are entirely gradual. The measurements are sampled by a Campbell Scientific CR-10X data logger that is connected to a PC at the on-site recording station. A wireless link connects the PC to a central facility in the Matter Valley, and allows the direct access to the measured values and to download them from the data logger using a dial-up local network connection. Seismic activity recorded by the twelve 3-component geophones is monitored using two 24-channel seismographs. These are also connected to the on-site PC which examines the seismic records and saves the waveforms to disk if the triggering criterion is satisfied. All seismic data stored on-site are regularly transmitted to the central recording facility in the Matter valley by the wireless connection. This concept allows off-site storage and easy accessibility to the seismic data files. Furthermore, recording parameters can be adjusted remotely. Power is supplied on-site by batteries charged by solar panels combined with a wind generator.

### 3.3 Methodology and results of surface displacement measurements

The displacement vectors of several retro-reflector locations expressed with respect to stationary base stations located in the valley and on the opposite slopes were provided by a geodetic survey commissioned by the CREALP-Centre (Ornstein et al. 2001). As described in section 3.2.1, the rock mass at the study site is dissected into various size blocks, separated by faults and fracture zones

(Figure 3-1). Several segments of this fault network are associated with deep open fractures at the surface. Records of surface fracture opening up to the year 2000 indicated that these open fractures accommodate the ongoing displacements. To quantify the relatively small ongoing displacements at the block boundaries, three types of surface fracture opening measurements were performed: The first method used a simple tape measure to periodically monitor the distance between a pair of benchmarks (rock bolts) placed approximately perpendicular to the opening fractures. The second method was a refinement of the first and used so called quadrilateral arrays of benchmarks measured with a purpose-built caliper gauge which had a measurement repeatability of 0.1mm. The use of four benchmarks in a square array allowed the direction of fracture opening to be determined. Quadrilateral arrays were installed on four fractures (q2, x2, l and r shown in Figure 3-2). The third approach was to install continuously recording crackmeters across two active fractures (q2 and x2) so as to determine the temporal characteristics of fracture opening.

The following sections discuss the results of the three approaches separately before comparing them against each other to assess their relative merits. After these more methodological considerations the results are integrated to obtain a description of the surface displacement fields at the study site.

### 3.3.1 Geodetic survey

The results of the valley-scale geodetic network are important because they allow the displacements measured within the on-site surface network to be referenced to an external coordinate frame thereby yielding absolute displacements. The valley-scale geodetic network was commissioned by CREALP and initially consisted of 18 1-D retro-reflectors installed in the period 1991-95 which were surveyed from two base-stations. This network was extended in 1996 with the addition of six 3-D retro-reflectors that are surveyed from four remote base-stations, two on the opposite side of the valley and one on each of two ridges to the north and south of the study area. The baseline length of these surveys varies from 1 to 2.5 km. Line-length measurements and angle changes between the 3-D retro-reflectors were performed bi-annually between 1996-1999 and annually since then by the surveying company Klaus Aufdenblatten of Zermatt who also analysed the data. The six 3-D retro-reflectors are located in two clusters: one at elevations of 1950-2100m and the other at 2300-2400m (Figure 3-1). Spatial coverage is therefore limited, with only one 3-D reflector situated within the stable part of the rock mass at 2500 m altitude. The results of the surveys between 1996 and 2003 are shown in Figure 3-6. The magnitudes of the displacement rate vectors vary from 4-14 mm/year and are in most cases constant (Figure 3-6a). Smaller rates are found in the lower part of the unstable rock mass, the higher values in the upper area where the deep boreholes are located (Figure 3-7). The best estimate of the direction of surface displacement is oriented to the SE for all stations, although the dip varies from 20-50° (Figure 3-6b/c). The formal errors per survey are relatively large due to the length of the baselines. Nevertheless, the magnitude, azimuth and dip of the displacement-rate vector at each station has remained essentially constant for the seven year time span of monitoring of the 3-D network, implying the pattern of deformation of the rock mass has been constant. A spatial variation which largely concerns the magnitudes can be observed, whereas the direction of displacement is more or less the same for all reflectors. Therefore, the spatial variation of the displacement rate vectors implies that most reflectors are located on separate blocks which are bounded by active faults and fracture zones.



Since 2002, the tops of the boreholes have been included into the geodetic survey. As these are not visible from the base-stations, an on-site network was established so that the relative displacements of the hole tops can be referenced to the retro-reflector at point 006 (Figure 3-7). The first annual repeat survey took place in autumn 2003. The absolute displacement vectors of the tops of boreholes SB 120 and SB 50S were directed to the ESE and SE respectively and thus are more or less congruent to the displacement directions observed at the retro-reflectors (Figure 3-7). In contrast, the displacement vector for SB 50N is directed to the west. However, its magnitude is small and hence the uncertainty in direction is large. Further repeat surveys are needed to establish the reliability of these results.

### 3.3.2 Simple benchmark line surveys

The initial, simple benchmark lines established across prominent surface fractures after the 1991 rockslides were measured periodically between summer 2001 and autumn 2003. In most cases the measurements were taken with a standard tape measure extended between the two rock bolts that served as benchmarks. However, the fractures q2, o and x were initially equipped with spring-tensioned wire-line extensometers between the rock bolts. For these, the measurements were made between the end-points of the spring using the same tape measure. The repeatability of the tape measurements in general is estimated as 0.5 mm. The extensions measured between the benchmark pairs during the three year survey period are shown in Figure 3-8. Annual opening rates range mainly between 1 and 3 mm/a and hence can be considered as resolved. Exceptional opening rates were measured at the wire spring across fracture q2 which indicates an accelerated opening in 2003 of more than 7 mm. This is almost certainly fictitious, and is most probably due to the tensioned wire touching against vegetation. Hereafter this array will be discounted from the analysis

The fractures were divided into 3 classes of activity based on their opening rates: i) high opening rate  $> 1.5$  mm/a; ii) moderate opening rate  $\leq 1.5$  mm/a and iii) not resolved opening (i.e. opening  $< 0.5$  mm/a). Opening rates  $> 1.5$  mm/a were measured at the fractures q2, l2', o, r, l, w, x2 and I, moderate opening rates at the fractures x, p, q and l2, and not resolved opening at the fractures s, u, s'' and t. An important finding is that active fractures (i.e. opening rates  $> 1$  mm/a; marked in red in Figure 3-2) seem to be segments of the large-scale fault and fracture zone network. Several fractures showed significant variation in the opening rates during the summer and autumn when measurements were frequent. However, the magnitude of the oscillation is in most cases similar to the precision of the measurement and hence it is uncertain whether it reflects a real signal.

### 3.3.3 Crackmeters

Two crackmeters consisting of Geokon vibrating-wire strain gages with thermistors were installed across two prominent fractures q2 and x2 (Figure 3-2). The specifications of the instruments are given in Table 3-2.

Table 3-2: Specifications for the crackmeters.

	<i>Range</i>	<i>Accuracy</i>	<i>Resolution</i>	<i>Precision</i>
<i>Geokon vibrating wire crackmeter</i>	<i>150 mm</i>	<i>0,15 mm</i>	<i>0,03 mm</i>	<i>not specified</i>

The vibrating wire frequency signal and temperature readings were logged every 6 minutes and the frequency signal converted into a length change using a linear scaling factor provided by the manufacturer. No temperature correction was applied as recommended. The anchors of the instrument are bolted into the rock mass and the sensor protected from direct sunlight and contact damage by a box-shaped casing. The instruments were installed in autumn 2002: hence 14 months of data are currently available (Figure 3-9). Both crackmeters show a large annual signal superimposed on a linear trend. For half of the year from October until March the site and crackmeters were covered in snow which acts as a temperature-stabilizing blanket (Figure 3-9). During this period the strains tend to show a linear increase. However, during the summer months when the ground temperature slowly heats then cools, a sympathetic variation in fracture strain is seen with the sense of strain reversing twice (Figure 3-9). This gives rise to the apparent annual fluctuation. Likewise the measured data show diurnal temperature fluctuations in the summer months (Figure 3-10). These topics will be further discussed in section 3.3.4.2.

The fracture opening accrued over a one year period is considered to reflect the large-scale rock-mass deformation, and is 2.5 mm for fracture q2 and 1.5 mm for x2. Later these values are compared against estimates from co-located simple and quadrilateral benchmark arrays. The implications of the evolution of fracture opening for the dynamics of the slope deformation will be discussed in section 3.3.5.

### **3.3.4 Benchmark quadrilaterals**

#### **3.3.4.1 *Method and results***

The benchmark quadrilaterals were installed to determine the direction as well as the magnitude of surface fracture opening. The term 'benchmark quadrilateral' denotes an approximately square array of benchmarks that lie in a plane (Baum et al. 1988). When used for monitoring fracture opening, pairs of benchmarks are located at either side of an opening fracture. An example is shown in Figure 3-11a. The initial quadrilateral, ABCD, shown horizontal, is cut by a fracture that crosses lines AC, AD, BC, BD. Relative displacement and/or rotation of one side of the fracture with respect to the other will affect the lengths of these lines, but not the lines AB and CD. Hereafter the line AB will be taken as the reference baseline. The new figure of the quadrilateral after deformation is ABC'D'. The line lengths AC, AD, BC and BD were measured in the initial and repeat surveys, the lines AB and CD only in the initial survey. Some assumptions about the geometrical nature of the displacement vector and rotation occurring between the fracture walls were necessary in order to interpret the measured line length changes. Dip-slip relative displacement and relative tilting of the two blocks can also generate line length changes on horizontal quadrilaterals but these are assumed to be negligible. The data constrain only the horizontal component of the relative displacement vector and its gradient along the fracture, the latter reflecting horizontal rotation of one block with respect to the other. More complete information about the 3-D relative movements requires several co-located quadrilaterals in different planes. At the study site, most of the arrays deployed were horizontal quadrilaterals although additional 2 or 4 benchmarks (at fractures x2 and 1 or fracture r respectively) were used at several locations where this was possible. Examples of benchmark quadrilaterals are shown in Figure 3-11b.

In most reported applications of the quadrilateral method to landslide studies, the relative displacements accrued between surveys were in the cm to dm range (Baum et al. 1988, Bogaard et al. 2000). For such large displacements, simple equipment such as stakes and tape measures can be used. However, at the study site, the annual displacements across fractures are only 1-3 mm. Thus, stable benchmarks and a high precision length measurement were required. In addition, exposures of stable rock suitable for benchmark locations were usually restricted to less than 0.5 m on either side of the open fractures, and these were often found at the bottom of gullies or excavated trenches giving very restricted room for accommodating the measurement device. The measurement system designed to meet these requirements is shown in Figure 3-12. The measurement tool operates according to the principle of a beam compass and consists of three blocks, A, B and C, affixed to rails. Two blocks, A and B are rigidly fixed, whereas block C is free to slide on the rails. Thus the distance between blocks C and B can be adjusted so that the locating pins affixed below blocks A and C fit snugly into conical recesses milled into the top of the benchmarks which are fixed like rock bolts. Different operating length ranges can be obtained by using different lengths of the rails between A and B. A calibration jig is used to maintain high repeatability in the measurements after tool re-assembly. Specifically, blocks B and C are moved together and clamped in position on their rails. Block A is then adjusted until the locating pins on blocks A and C are seated in holes drilled in the jig whose precise separation is known. Block A is then clamped, and the distance between the outer edges of the blocks B and C measured with a caliper. This becomes the reference for subsequent measurements. In this way, the distance between a pair of benchmarks is referenced to the distance between the holes of the calibration jig.

Two methods were applied to derive displacement vectors from the strain measurements of the repeat surveys. The first one, after Baum et al. (1988), calculates the angles in the triangles ABC, ABC' and ABD, ABD' using the law of cosines. These can be used to estimate the horizontal displacement vectors,  $u_c$  and  $u_d$  of points C and D with respect to the stable baseline AB (Figure 3-11a). If there is no horizontal rotation of one side of the fracture with respect to the other, and other assumptions are satisfied (e.g. that all benchmarks lie in one plane and suffer no vertical relative displacements), these should be equal to within measurement error. The repeatability of each length measurement is estimated to be 0.1 mm and this translates to an error in the displacement vector magnitude of typically 0.3-0.5 mm. The second method used a grid search approach to find the single horizontal displacement vector which best reproduces the linear strains AC'-AC, BC'-BC, BD'-BD and AD'-AD (Figure 3-11a). This approach thus assumes that horizontal rotation was negligible.

The results obtained from the two methods for the fractures r, q2 and x2 are shown in Figure 3-13 and are generally in accord. The magnitudes of the vectors  $u_c$  and  $u_d$  differ by 1 mm for the first six month period, but are the same for the second. A longer measurement period is required to determine whether this reflects horizontal rotation or error. One source of systematic error not accounted for in the analysis is linked to the degree to which planarity of the quadrilateral could be achieved. At the fractures q2 and x2 at least one of the benchmarks lies significantly out of plane, and at least one fracture or foliation fracture intersects the quadrilateral. The latter can produce non-homogeneous strains through different thermo-elastic strains in the blocks which can reach magnitudes of tenths of millimetres and thus influence the analysis significantly. The direction of fracture opening was found to be not always perpendicular to the strike of the fracture; however, the deviation is less than 30°.

The magnitude and direction of fracture opening derived from the horizontal quadrilateral across fracture r were rather constant over the one year survey period; the displacement was approximately 2 mm and directed 120° counter clockwise from the baseline AB (Figure 3-13). The vector from the vertical quadrilateral (location shown in Figure 3-11b) for the first repeat survey in June 2003 reveals that the displacement vector across the fracture r dips 3-37° NE with a magnitude of 1-2 mm. For the third repeat survey the measurements indicate dips of 37-52°; however the increased differences in magnitude from the two single triangles and the fit of all length changes suggest that the measurements might be affected by a measurement error.

The magnitudes of the displacement vectors at q2 and x2 show evidence of the annual fluctuation seen on the crackmeter records from these locations. This will be discussed in the next section. The displacement rate at fracture q2 was approximately 3 mm/a to the SE (the mean displacement direction is 60° from the strike of the baseline). The displacement rate across fracture x2 was only 0.5 mm/a, and the direction was poorly constrained due to the small displacements. A longer record is needed to resolve direction. Further quadrilateral results can be expected for fracture l between borehole SB 120 and SB 50S which was installed in summer 2003.

### 3.3.4.2 *Comparison with simple benchmark arrays and crackmeter monitoring*

In November 2003, co-located benchmark quadrilaterals and crackmeters were installed across two open fractures that had been monitored with simple benchmarks (bolts or springs) since 1991. This offered the opportunity to compare the different methods. Figure 3-14 shows a comparison of cumulative displacement magnitudes at all sites where multiple systems were installed (i.e. fractures r, q2 and x2). Whilst there is general agreement in the form of the curves for each location, discrepancies in magnitude are evident that are larger than the estimated errors for the various methods ( $\pm 0.5$  mm for the simple benchmarks,  $\pm 0.3-0.5$  mm for the benchmark quadrilaterals and  $\pm 0.15$  mm for the crackmeters). Thus, the discrepancies are likely to reflect real differences in the displacement magnitudes measured. Given that the displacement vector across the fractures deviates by up to 30° from the fracture normal, the magnitudes measured by the simple benchmark pairs and crackmeters which are normal to the fractures should be smaller than from the benchmark quadrilaterals. However, this is the case only at fracture q2 (Figure 3-14b). At fractures r and x2, the opposite is true. A reasonable explanation is that the discrepancy reflects the separation of the points at which the measurements are made since proximate measurements generally agree. At q2, where there was agreement, the benchmark quadrilateral was installed immediately next to the crackmeter in a deep gully. Similarly, at x2, the crackmeter and simple benchmark pair are installed next to each other in an exposed, vertical rock face and give similar results, whereas the quadrilateral array is located in the horizontal plane at the top of the fracture some five meters to the west with several fractures in between. For the fracture r, the simple benchmark pair and quadrilateral array are approximately 1 m apart.

The comparison of the crackmeter strains with those inferred from co-located benchmark arrays (Figure 3-14) indicated that the annual fracture-strain signal is real rather than an artefact of any temperature sensitivity of the sensor, and is probably of thermo-elastic origin. This is supported by the relatively small diurnal strain response of both instruments to rather large diurnal temperature fluctuations in the summer months (Figure 3-10). The strain response to diurnal air temperature fluctuations is 0.013 mm/°C at fracture q2 and 0.02 mm/°C at fracture x2. These values are smaller than the response to annual fluctuations which are approximately 0.025 mm/°C for fracture q2 and 0.125

mm/°C for fracture x2. It is noteworthy that most of the data show evidence of the annual fluctuation seen most clearly with the crackmeters, with the greatest opening rates occurring during the winter/spring seasons and smaller or even negative rates during the summer. The largest signal is seen on the crackmeter at fracture x2, and this is tracked well by the simple benchmark survey, demonstrating it is a real signal. The quadrilateral array across x2 also shows the fluctuation, but the amplitude is smaller by a factor of more than 2. Similar, annual fluctuations are seen on both the quadrilateral and simple benchmark data across fracture q2, and in the simple benchmark survey across fracture r but not by the quadrilateral data for fracture r, perhaps because sampling is too sparse. As noted earlier, the correlation of the form of the annual signal with the temperature cycle, and the stronger response to temperature fluctuations at annual rather than diurnal periods suggests the strains are thermo-elastic in origin. A simple scoping calculation can be performed to check whether thermo-elastic strains could account for fracture opening fluctuations of 1-2 mm. Assuming a linear thermal expansion factor  $\alpha=10^{-5}$  /°C and annual temperature variations in the rock  $\Delta T=5^\circ\text{C}$ , a uniformly heated, unconstrained block of 10 m side length (e.g. a block separated by open fractures and decoupled from the underlying medium by say a through-going foliation fracture) would expand by 0.5 mm. A fracture between two such blocks thus would show thermo-elastic fluctuations in aperture of 0.5 mm. Thus, thermo-elastic strains are a reasonable explanation for the fluctuations in fracture aperture at diurnal and annual periods seen at the study site. Thermo-elastic strains depend not only on elastic heterogeneity and depth of thermal wave penetration, but also upon topography (Harrison & Herbst 1977). Thus, large variability in the amplitude of the induced opening fluctuation can be expected, even along the same fracture. Large fluctuations might be expected on benchmark arrays installed on vertical rock faces with long exposure to the sun, such as the crackmeter and benchmark at fracture x2, or at the corner of a rock block with a vertical and horizontal free rock face, such as the simple benchmark pair at fracture r. These positions favour greater penetration of temperature variations into the rock mass.

Considering these fluctuations and the effect the position of the measurement line has on their magnitude, the three methods to monitor surface fracture opening show reasonable agreement. We conclude that the annual fluctuation is cyclical and of primarily thermo-elastic origin, and that the long-term trend of fracture opening reflects deeper processes related to rock mass instability.

### 3.3.5 Displacement fields at the surface

The geodetic survey and fracture opening measurements provided a valuable description of the pattern of deformation at the surface. The results are summarised in Figure 3-7 where the absolute horizontal displacement rate vectors for the retro-reflectors of the large-scale geodetic network (black-arrows) and the wellhead reflectors of the site geodetic network (green arrows) are plotted with the relative opening displacement rate vectors across the fractures (red arrows: see figure caption for convention). The surface displacement field is clearly heterogeneous with several surface fractures that follow the fault and fracture zone network accommodating most of the rockslide-related displacements. Displacement rates generally decrease from the scarp edge towards the north and fall to zero at or close to the fracture x2. There is no main back scarp where the displacement gradient is concentrated; rather, the displacement rate discontinuities are distributed over the assembly of blocks and boundaries within the active zone (shown shaded in Figure 3-7) and thus are relatively small.

Generally, the fracture opening was found to be approximately normal to the strike of the fracture, at least wherever it was measured.

It has to be considered that the instrumented area represents only the uppermost part of the unstable rock mass whose estimated extent is shown by the shaded area in Figure 3-7. The steep, unstable nature of the southern end of the active area renders access difficult and prohibits the use of instrumentation to identify any key features that may accommodate large displacements and serve as a local basal sliding surface. Alternative techniques for determining the surface displacement field in this area could be satellite or ground based synthetic aperture radar or GPS stations (Fruneau et al. 1996, Gili et al. 2000, Canuti et al. 2002).

### 3.4 Methodology and results of displacement measurements at depth

Knowledge of the displacement field at depth is crucial for assessing the processes leading to the instability of the rock mass. This is especially true in the geological situation under consideration where few if any highly persistent sliding planes are expected. In order to identify the type of structures which accommodate rock mass deformation at depth, the three deep (i.e. 120, 50 and 50m) boreholes were equipped with inclinometer casing which had extensometer rings mounted outside in the case of the 120 m borehole. These could be surveyed to provide profiles of inclination and axial strain measured over baselengths of 61 cm and 1 m respectively. Unfortunately, the data obtained from the TDR coaxial cable measurements was not considered interpretable. This is probably due to the small displacements which the TDR technique is not able to detect (O'Connor & Dowding 1999), and the location of the cable in the grouted annulus around an inclinometer casing appears to be unfavourable for obtaining good reflection data. Thus, the following sections focus on the analysis of the inclinometer and extensometer data and the correlation of the measured displacements with the fractures mapped in the boreholes. These results form the basis for the construction of the block kinematic model proposed in section 3.5.

#### 3.4.1 Methodology of inclinometer/extensometer surveys

The use of inclinometer/extensometer surveys in boreholes is common in geotechnical engineering since the combination of the measured inclination changes and axial strains along the borehole allows the profile of 3-D displacement vectors to be derived, subject to the assumptions discussed later. The survey of the grouted PVC casing was performed with two separate probes for inclination and extension (for specification of the probes deployed at the study site see Table 3-3). However, probes exist which combine both sensors (Amstad et al. 1988, Lavisolo et al. 2003).

The biaxial inclinometer probe is shown in Figure 3-15a. It is 61 cm long with two pairs of wheels at either end which run in grooves cut diametrically-opposite each other into the casing (Figure 3-16a). The inclination of the probe axis from the gravity vector is measured with two orthogonal, force-balanced accelerometers with a precision of approximately  $0.0002^\circ$ . Thus, the output of the instrument at a measurement location is proportional to the inclination of the tool axis in each of the two orthogonal planes defined by the local orientation of the two orthogonal groove pairs in the casing. These planes are denoted in Figure 3-16 by  $X^+/X^-$  and  $Y^+/Y^-$  with the former being the groove pair used to guide the wheels of the probe (the other pair is not used).

Table 3-3: Specifications for the inclinometer/extensometer and spiral probes.

	<i>System</i>	<i>Interval</i>	<i>Operating range</i>	<i>Accuracy</i>	<i>Precision</i>
<i>Inclinometer (Slope Indicator)</i>	<i>Force balanced accelerometers</i>	<i>0.61 m</i>	<i><math>\pm 30^\circ</math> from vertical</i>	<i>vertical: 0.21mm <math>\pm 15^\circ</math>: 0.75mm</i>	<i>vertical: 0.092mm <math>\pm 15^\circ</math>: 0.2 mm</i>
<i>Spiral probe (Slope Indicator)</i>	<i>Rotary potentiometer</i>	<i>1.5 m</i>	<i><math>\pm 4^\circ/1.5m</math></i>	<i><math>\pm 0.17^\circ/1.5m</math></i>	<i>no information provided</i>
<i>Extensometer INCREX (Slope Indicator)</i>	<i>Induction-coil transducer</i>	<i>1 m</i>	<i><math>\pm 20mm/m</math></i>	<i><math>\pm 0.01mm/m</math></i>	<i>no information provided</i>

The surveys are conducted following standard procedures (Mikkelsen & Wilson 1983, Dunningcliff 1988). The procedure used in the present measurements consisted of first lowering the probe to the bottom of the casing and waiting 0.5 hrs for it to thermally equilibrate. The probe was then raised up the casing stopping every 61 cm to measure inclination. The same groove pair and measurement locations were used in all surveys. Depth was controlled by tape markers affixed to the cable. The probe was then rotated through  $180^\circ$  and the procedure repeated, the so-called reverse run, to eliminate the bias shift (i.e. the zero-offset error) of the sensors (Mikkelsen 2003).

The objective of the inclinometer surveys is to identify the location of the active fractures within the rock volume penetrated by the borehole, and to estimate the magnitude and direction of the displacements occurring on them. These must be expressed in geographic coordinates for correlation with other data. Since the inclinometers measure the angle between vertical and the two locally-defined orthogonal planes  $X^+/X^-$  and  $Y^+/Y^-$  defined by the grooves, it is necessary to determine the local geographic orientation of the grooves along the casing so that the measured inclinations can be expressed in geographic coordinates. The orientation of the grooves and the planes they define can be readily determined at the surface to within  $\pm 5^\circ$  using a compass. The planes of the groove pairs at the surface are denoted as  $A^+/A^-$  and  $B^+/B^-$ . For a vertical, free-hanging casing it is expected that  $X^+/X^-$  and  $Y^+/Y^-$  correspond to  $A^+/A^-$  and  $B^+/B^-$  at all depths. However, inclinometer casings in inclined or deep boreholes (i.e.  $>60$  m) are prone to contortion and spiralling of the grooves around the casing axis (Dunningcliff 1988). Thus, a torsion survey is run to measure the degree of spiralling of the grooves. The interpretation of the torsion survey in vertical holes is straightforward: the integral of the torsion profile gives the orientation of the grooves at depth with respect to their orientation of the surface. Thus, given the measured orientation of the groove planes at the surface (i.e.  $A^+/A^-$  and  $B^+/B^-$ ), the local orientation of the planes at depth (i.e.  $X^+/X^-$  and  $Y^+/Y^-$ ) can be determined (Figure 3-16a). Unfortunately, in situations where the hole is not vertical, the interpretation of torsion measurements becomes more complicated and the orientation of the grooves is no longer uniquely related to torsion, as will be discussed later.

The casing in SB 120 was also equipped with metal INCREX-extensometer rings mounted every meter on the outside of the casing. The measurement probe is 2m long and is used without guiding wheels (Figure 3-15b). The probe is equipped with two induction coils separated by 1m. The distance between neighbouring pairs of rings is estimated from the current induced in the two coils in the probe which is proportional to the distances to the metal rings (Dunningcliff 1988). The measurements are conducted by raising the probe from the bottom of the borehole to the top after an equilibration time of 30 minutes, stopping each metre to perform the measurement. Two runs are performed for each survey, both from the bottom to the top. For the analysis, the mean of two readings is calculated

and corrected for the offset determined from the difference between control measurements performed before and after the survey with the probe inserted into a control tube under laboratory conditions at constant ambient temperature.

The initial surveys for the inclinometer/extensometer measurements were performed after cementing of the PVC casings in autumn 2001. A survey of casing torsion was also conducted with a spiral probe. The repeat surveys that followed were performed twice a year in spring and autumn. The differences in inclination and inter-ring distance between a repeat survey and the initial survey reflect accrued horizontal and vertical displacements plus errors.

### 3.4.2 Inclinometer raw data

The inclination profile along the X and Y axes of the inclinometer casing in SB 120 as obtained from the initial inclinometer survey is shown in Figure 3-17a. The inclination measurements in this borehole can be performed to a depth of 112 which is the top of the geophone and piezometer modules. It should be noted that in this study the inclination is given for the inclination of the bottom of the inclinometer probe with respect to (wrt) the top (Figure 3-16b/c). This convention is opposite to the convention commonly used in the industry and was chosen to better integrate surface displacement vectors and displacements along the borehole and in order to be independent on whether the borehole bottom is situated in non-moving rock or not. From Figure 3-17a it is clear that the borehole trajectory of SB 120 deviates significantly from vertical in the direction of the Y-axis which is orientated ENE ( $70^\circ$ ) at the surface. The deviation begins at 10 m and increases steadily to  $12^\circ$  at 60 m depth and then more slowly to stabilise at  $16^\circ$  in the lowermost 30 m. In contrast, the x-axis inclination remains smaller than  $4^\circ$  at all depths. Both inclination profiles show a prominent fluctuation with 7m wavelength which is ascribed to buckling of the 70 mm OD casing bundle in the approx 150 mm diameter borehole under self-weight. The results of the torsion survey are shown in Figure 3-17b expressed as the angle between the orientation of the casing grooves at the surface and at depth. Positive torsion angles reflect an anti-clockwise cumulative rotation of the grooves at depth looking down. Torsion increases rapidly from the surface to reach  $4^\circ$  at 15 m, remains stable to 50 m, and then increases steadily to  $9^\circ$  at 90 m before falling back slightly to the survey bottom. In the simple case of a vertical borehole, the torsion data allow the geographic orientation of the grooves at depth to be determined by simple rotation of the surface orientation through the local cumulative spiral angle. This standard method was first used to derive the trajectories of the inclinometer casing from the initial survey data. The results are shown by the green dotted curves in Figure 3-17c together with trajectory profiles derived from the borehole geometry (black solid curve) and optical televiewer (red solid curve) sondes during open-hole logging prior to casing. The inclination profiles agree well, with the exception of the 7 m wavelength fluctuation which reflects a buckling of the casing and is thus absent from the log-derived profiles. However, a serious discrepancy between the orientation profiles from the inclinometer and the logging sondes is evident. The latter suggest that the borehole inclination is drawn steadily towards the east, whereas the inclinometer profile suggests the inclination initially tends to the east but then tends to spiral anti-clockwise looking down. This discrepancy has a significant impact on the analysis and thus will be discussed in detail in section 3.4.4.

The groove inclination and torsion profiles derived from the initial surveys of the two 50 m deep boreholes, SB 50S and SB 50N, are shown in Figure 3-18a-d. The orientation of the grooves at the



surface was chosen to be similar to those for SB 120. Borehole SB 50S could be surveyed to 42.5 m depth. The inclination profiles are similar to SB 120, inasmuch as the y-axis inclination deviates increasingly from vertical but the x-axis is almost vertical. A weak fluctuation in inclination with a wavelength of 12 m is evident, which is longer than the wavelength of the buckling-related fluctuation observed in SB 120. This is probably a consequence of the larger diameter (84 mm OD) of the casing that was installed in the 50 m deep boreholes and the smaller weight. The torsion survey revealed a constant increase of the torsion angle with depth, reaching  $-8^\circ$  at the end of the survey bottom. In SB 50N only the upper 35 m of inclinometer casing is open. The inclination profiles of both groove pairs deviate increasingly from vertical, although the superposed fluctuations are more irregular and stronger than in SB 50S. The torsion survey indicated a constantly increasing torsion angle between 10 and 35 m depth.

### 3.4.3 Standard reduction of inclinometer data from a repeat survey

Results of inclination surveys are normally expressed in terms of implied horizontal displacement rather than angles. This is illustrated for one interval in Figure 3-16c where an inclination from vertical measured by the x-sensor for the first repeat survey of  $\beta$  corresponds to a horizontal 'displacement' along the local x-axis given by,

$$\Delta x_0 = (61\text{cm}) \cdot \sin \beta \quad (\text{equ. 3.1}),$$

where 61 cm is the distance between the wheels of the probe. For a single survey this 'displacement' is just a measure of deviation from vertical and is not a displacement in the conventional sense. If the corresponding 'displacement' measured during the initial survey was  $dx_0$ , then the implied x-component of horizontal displacement that occurred between the initial and first repeat survey is given by,

$$\Delta x = dx_1 - dx_0 \quad (\text{equ. 3.2}), \text{ and}$$

$$\Delta y = dy_1 - dy_0 \quad (\text{equ. 3.3}).$$

These are referred to as the incremental displacements and represent the movement of the bottom of the probe with respect to the top. Note that the difference calculations assume that the inclinometer probe was located across precisely the same section of the inclinometer casing for the initial and repeat surveys. In practice, the horizontal displacements are computed directly from the sensor outputs. Details will not be given here save to note that the forward and reverse runs of a survey are combined to eliminate bias-shift resulting from calibration error, as discussed later.

The profiles of incremental displacements,  $\Delta x$  and  $\Delta y$  measured for the first repeat survey in SB 120 are shown in Figure 3-19b. These displacements are referenced to the local borehole coordinates, x,y which lie in the plane perpendicular to the borehole axis and which generally rotate with depth. In order to reference the incremental displacements to the consistent orientation defined by the axes A and B, which are the orientations of the X, and Y axes at the surface (Figure 3-16a), a simple 2-D rotation through an angle  $\alpha$  (Figure 3-16c) is used.

$$\Delta_A = \Delta_x \cdot \cos \alpha - \Delta_y \cdot \sin \alpha \quad (\text{equ. 3.4a}),$$

$$\Delta_B = \Delta_x \cdot \sin \alpha + \Delta_y \cdot \cos \alpha \quad (\text{equ. 3.4b}).$$

In the standard analysis,  $\alpha$  is given by the torsion survey profile (Figure 3-17b). The use of a simple 2-D rotation is strictly valid only for vertical boreholes. For boreholes with inclined and contorted casings such as in the present study, it represents an approximation that will introduce a systematic error into the estimates of the incremental displacements,  $\Delta_A$  and  $\Delta_B$  in the directions A and B respectively (Figure 3-19c). Since the incremental displacements are now expressed in terms of the same coordinate system, the components may be individually summed along the borehole to derive the cumulative horizontal displacement,  $V_A$  and  $V_B$  in the A and B directions respectively (Figure 3-19c). The magnitude and orientation of the incremental displacements can be derived using basic vector representations. The orientation may be readily expressed with respect to geographic coordinates since the orientation of the A-axis is known.

The cumulative horizontal displacement profile is the primary information used in identifying and quantifying rock mass displacements (Figure 3-20). Positive steps over one measurement interval indicate localised relative displacement in the horizontal plane. Distributed displacements such as rigid block rotations reveal themselves as sections of profile with constant inclination changes. Positive incremental displacement values indicate that the bottom of the probe has been displaced in direction of the positive X+/Y+ or A+/B+ axes between the surveys (the opposite to the convention normally used in geotechnical engineering). Similarly, for a cumulative displacement profile in crystalline rock, positive steps indicate that the bottom block has been displaced in direction of the A+ or B+ axis, and positive slopes between the steps suggest a block rotation where the bottom of the block rotates in A+ or B+ direction wrt the top.

Examination of the profile of cumulative displacement for SB 120 for the first repeat survey in Figure 3-19c suggests slope changes at 35 m and 70 m which might delineate large blocks which rotate individually. At smaller-scales, steps and slope changes are evident in the uppermost 35 m. However, below that depth, the profiles become noisy, the primary signal being seemingly coherent with the 7 m wavelength fluctuations in casing inclination (Figure 3-19a). It seems unlikely that the displacements should be dependent upon casing inclination and thus may reflect a systematic error. In general, the noise level below 35 m is so large as to obscure steps and slope-changes reflecting slip on fractures and block rotations. Thus, it is essential to reduce the noise to resolve the signals of interest. This will be discussed in the following section.

#### 3.4.4 Error sources and correction schemes for inclinometer survey data

Inclinometer surveys are subjected to numerous sources of error that can influence the results significantly. The total error of such surveys can be broken down into a random and systematic error. The random error includes sensor noise (i.e. the precision of the probe) and the influence of environmental factors (Dunncliff 1988). Moormann (2003) estimated the random error in vertical boreholes under field conditions by conducting a series of repeated measurements under stable conditions and found a standard deviation of 0.1-0.16 mm/measurement interval. This corresponds to Mikkelsen's (2003) empirically determined estimate of 0.16 mm/interval. The random error  $e_r$  of cumulative displacement measurement with such a standard deviation grows as:

$$e_r = 0.16mm\sqrt{n} \quad (\text{equ. 3.5}).$$

where  $n$  is the number of times the error is repeated. For SB 120 which has 185 measurement intervals, the cumulative random error at the bottom of the profile is 2.18 mm. Systematic errors are usually greater than the random errors because they add directly rather than as the square root of the number of times the error can be repeated. The sources of these systematic errors mostly relate to the inclination and curvature of the inclinometer casing. Mikkelsen (2003) suggested four main sources of systematic errors of which two depend strongly on the inclination of the inclinometer casing. These are i) the depth-positioning error due to settlements of the casing or changes of the depth markers on the measurement cable and ii) a 'rotation error' due to a change in the alignment of the sensor and the survey axis defined by the wheels on the probe slides along the grooves. The other two errors include the so called bias-shift, which is a calibration error that is eliminated by the reverse run, and the sensitivity-shift, which is a shift in the gain of the amplifier of the probe that, according to Mikkelsen (2003), is rarely significant. The size of the systematic errors is thus highly variable. Mikkelsen (2003) suggests systematic errors may be as large as 0.11 mm per measurement interval. If this value were to apply to SB 120, the estimated systematic error at the bottom of the profile would be 20.4 mm, which would exceed the annual surface displacement rates. Fortunately, the systematic error can be significantly reduced by careful data analysis. Hence considerable attention was given to the analysis of inclinometer data in inclined boreholes with buckling casings. The following sections describe the correction schemes developed on basis of the inclinometer data from SB 120.

#### *Torsion correction*

As shown in Figure 3-17c the borehole trajectory derived from the torsion-corrected inclinometer survey differs from the trajectories measured by the borehole geometry and optical televiewer sondes during open-hole logging prior to casing. Whilst the inclinations derived from all three measurements are consistent, the azimuth inferred from the inclinometer survey deviates significantly from the two log-derived estimates, both of which agree. The discrepancy develops at 40m where the borehole deviation from vertical reaches  $10^\circ$ , and grows consistently to attain  $15^\circ$  at borehole bottom. Thus, when viewed in plan, the trajectory from the inclination survey initially deviates from vertical towards  $N100^\circ E$  at about 40 m and then begins to curve continually in an anti-clockwise sense. In contrast, the logs indicate that the trajectory consistently deviates towards  $N100^\circ E$ , which is approximately normal to the foliation strike. Given that the deviation of the holes from vertical probably reflect preferential drill bit movements that tend to draw hole advancement towards the normal to the foliation plane, and that the sonde azimuths are directly referenced to magnetic north, the azimuth of the torsion-corrected inclinometer profile is considered to be in error. The source of the error is uncertain, but it would seem to be systematic in nature and affect primarily the azimuth of the incremental borehole inclination estimates. Thus, the problem would seem to lie with the torsion correction. The error is too large to attribute to the limited accuracy of the torsion probe which is  $0.1^\circ/m$ . Rather, the evidence suggests it reflects fundamental inadequacies in the standard torsion-correction in situations where the casing is contorted and inclined.

The error in trajectory leads to incorrect locations for the boreholes at depth (the bottom of SB 120 estimated from the inclinometer survey is 6 m away from the location obtained from the logging sonde data). Such an error would be unacceptable for the borehole geophysics experiments. However, the error will also affect the estimated azimuth of the change in inclination derived from differencing two surveys and thus must be corrected. Since the source of the error is believed to be the torsion

correction, an alternative method was used to correct the measured inclination data for changes in groove orientation (due to both spiralling and axial contortions). Specifically, in rotating the measured inclinations from local, casing coordinates (i.e. X-Y) to consistent, geographic-referenced coordinates (i.e. A-B), an empirically-determined rotation was applied. The rotation was computed at each depth as the value needed to bring the trajectory at that depth into accord with the trajectories from the two logging sondes (Figure 3-17c). Prior to computing the rotation, the data were smoothed with a low-pass filter with a cut-off at wavelength of 3.5 m to preserve the regular 7 m wavelength undulations in the azimuth and inclination of the casing which are considered to be real. The trajectory derived from this method is shown by the black dashed line in Figure 3-17c, and is the same as the trajectory derived from the logging sondes at wavelengths longer than 7 m.

### *Depth matching*

The profile of cumulative horizontal displacement derived from the first repeat survey shown in Figure 3-19d shows a significant correlation with the 7 m wavelength undulations associated with the buckling of the casing. This does not reflect a true dependence of inclination change on casing attitude, but rather is an artefact of the presence of small yet significant offsets in the depth scale of the two surveys. Small offsets have a disproportionately large effect because the initial and repeat profiles, whose difference defines the inclination change, both contain the same large signals due to borehole deviation from vertical and casing buckling. These signals cancel in the difference only if the profiles are precisely aligned. Thus all surveys were depth-matched prior to differencing using cross-correlation. Better depth-matches were usually obtained by stretching one profile with respect to the other so that the offset increased linearly from 0 cm at the borehole top to about 2 cm at the bottom, rather than constant offset. A linearly-increasing offset (i.e. uniform stretch) is consistent with the depth error expected from the variable stretch characteristics of the measurement cable used to lower and raise the probe which tends to develop kinks and twists when coiled for storage and transportation.

The effect of correcting for this depth offset is illustrated in Figure 3-21 b/c. The profile of cumulative inclination changes along SB 120 between the initial and first repeat surveys obtained using the standard torsion correction is shown in black. The grey lines denote the profiles after applying a uniform stretch to the depth scale of the first repeat profile ranging to  $\pm 5$  cm in steps of 1 cm. The figure shows that the strength of the fluctuation signal due to the casing buckling (Figure 3-21a) changes with the applied stretch. The stretch which produces the best match between initial and repeat profiles obtained from cross-correlation was -2 cm (red curves in Figure 3-21 b/c).

### *Sensor rotation*

Another source of systematic error arises from small changes in the alignment of the sensor and the wheel assembly of the inclinometer probe. The changes are small and are within the tolerance of sensor alignment in the probe which is  $0.5^\circ$  (Mikkelsen 2003). In inclined boreholes, a change in sensor orientation between surveys leads to a change in the distribution of the absolute casing inclination on the two groove axes, and this in turn will show as an apparent change in inclination of the two axes between the surveys. For a shift in sensor orientation within the housing of  $\gamma$ , the initial casing inclination profiles,  $x_0$  and  $y_0$ , will be now measured as apparent inclinations,  $x_a$  and  $y_a$ , given by,

$$x_a = x_0 \cdot \cos \gamma - y_0 \cdot \sin \gamma \quad (\text{equ. 3.6a}),$$

$$y_a = x_0 \cdot \sin \gamma + y_0 \cdot \cos \gamma \quad (\text{equ. 3.6b}).$$

For small  $\gamma$ , the term  $\cos \gamma$  approaches 1 and  $\sin \gamma$  approaches  $\gamma$ . The error introduced by the sensor rotation is given by:

$$e_x = x_0 - x_a \quad (\text{equ. 3.7a}),$$

$$e_x = x_0 - (x_0 - \gamma y_0) = \gamma y_0 \quad (\text{equ. 3.7b}).$$

Similarly

$$e_y = y_0 - y_a \quad (\text{equ. 3.8a}),$$

$$e_y = y_0 - (y_0 + \gamma x_0) = -\gamma x_0 \quad (\text{equ. 3.8b}),$$

This error considers only the effects of sensor orientation change on borehole inclination. The change also affects any horizontal displacement that accrues between surveys, but this is second order since inclination changes are usually much smaller than absolute inclinations. As is evident from the above analysis, the error primarily affects the axis orthogonal to the inclined axis. In principle, this offers the possibility of distinguishing the sensor rotation and the depth offset errors since the latter produce apparent inclination changes in the same direction as the borehole inclination. However, this can only be realised in practice if an inclined section of borehole lies in what is known to be stable ground where the displacements should be zero. The cumulative displacement profiles after the depth-offset correction (Figure 3-21 and Figure 3-20) indicate that this not the case for the boreholes in question. For the case of SB 120 which is inclined primarily in the Y-axis direction, the error due to sensor rotation would affect the X-components of displacement and hence the A-component of cumulative horizontal displacement. This is approximately the direction of rock mass displacement signal anticipated from the geodetically-determined surface displacement vectors.

The sensor-rotation error is of considerable importance to the present study since anomalous results were obtained for the third repeat survey of SB 120 which might be explained by it. The profiles of cumulative horizontal displacement derived from the three repeat surveys conducted are shown in Figure 3-22a. All aforementioned corrections have been applied to these data. The steps associated with slip on discrete fractures correspond in location and direction of the inclination change on all three profiles. However, the slopes of the profile sections between the steps change drastically from the second to the third repeat survey resulting in a major change in the inferred azimuth of the horizontal displacements. For the first two repeat surveys, the azimuth of the horizontal displacement vector of the bottom of the hole is primarily in the A+ direction, which is in agreement with the geodetically-determined displacement vector of the surface. However, the azimuth implied by the third survey (referenced to the initial survey) is in the B+ direction and thus is orthogonal to the geodetic vector. It seems improbable that such a change in the pattern of displacements at depth would occur without a corresponding disturbance of the absolute motion of the surface. The seemingly anomalous results of the third survey can largely be explained by a small change in the orientation of the sensor in the housing that occurred between the second and third repeat surveys. The impact of small sensor rotations on the profiles of cumulative horizontal displacement in the A and B-axis directions for the third repeat survey are shown in Figure 3-22b/c. The profiles have been derived assuming sensor rotation angles ranging from -0.1 to 0.02 degree in steps of 0.02 degree. Evidently the profiles are extremely sensitive to small changes in sensor orientation in the housing. A

rotation of only -0.08 degree is needed to restore the displacement profiles to consistency with the pattern defined by the first two repeat surveys (recall that the tolerance in orientation of the sensor within the housing is 0.5 degree). Investigation of the history of the probe used in the measurements during the period between the second and third surveys failed to identify any obvious reason why the sensor orientation might be disturbed, such as probe rebuild or recalibration. Nevertheless, sensor rotation is the best explanation of the radical change in the third repeat profile. The sensitivity of the profiles to small changes in sensor orientation is so large that shocks during transit or temperature changes might conceivably cause troublesome shifts. This emphasises that the technology must be worked at its limits in order to resolve the displacements of interest.

In summary, the analysis and correction of systematic errors in the inclinometer and torsion surveys led to a vital improvement in the definition of the displacement profiles along the boreholes. The corrections applied to each of the four repeat surveys are listed in Table 3-4. The depth offsets correction was facilitated by cross-correlation of the two profiles, and the empirical torsion correction was facilitated by the availability of borehole geometry logs which provided a 'ground-truth' from which an empirical correction could be defined. By applying these corrections, the peaks in the incremental inclination change profile become clearer and more localised, and the calculated horizontal displacements could be referred to geographic coordinates. However, the balance of evidence suggests that the third repeat survey is contaminated by a systematic error arising from a small disturbance of the orientation of the accelerometer module within the housing. Unfortunately, the conditions required for deriving a quantitative correction for this error were not met (i.e. the bottom of the boreholes lay in unstable ground). Thus, for the analysis it was assumed that the rotation of -0.08 degrees which produced the best agreement with the earlier repeat surveys and the geodetically-determined displacement vector of the surface was used.

Table 3-4: Corrections and resulting displacements of the borehole bottom wrt top for the repeat surveys in SB 120.

<i>Repeat survey</i>	<i>Date</i>	<i>Depth stretch [cm]</i>	<i>Sensor rotation [°]</i>	<i>Azimuth, dip and magnitude of the displacement vector of the bottom of the borehole wrt the top [° / °, cm]</i>
1	06/2002	-2	0	187 / -30 / 1.19
2	10/2002	-2	0	189 / -29 / 1.78
3	07/2003	0	-0.08	201 / -31 2.54
4	10/2003	0	-0.06	191 / -42 2.60

### 3.4.5 Calculation of the 3-D displacement vector along the boreholes

The profile of 3-D displacement for SB 120 was obtained by combining the corrected incremental horizontal displacement vectors of Figure 3-23a with the axial strains (i.e. vertical displacements) derived from the INCREX measurements shown in Figure 3-23b. The convention for the strains is that extension is positive. Since the baselength of the horizontal displacement estimates of 61 cm differs from the 1 m baselength of the INCREX measurements, the INCREX profiles were interpolated and re-sampled at the 61 cm-separated measurement points of the inclination surveys to facilitate combination as in Figure 3-16d. The resulting profiles of 3-D displacement magnitude for the four

repeat surveys are shown in Figure 3-23c, and the magnitude and orientation of the displacement of the bottom of SB 120 with respect to the top is listed in Table 3-4.

### 3.4.6 Results: displacement fields measured in the deep boreholes

#### *SB 120*

The profiles of displacement vector magnitude in SB 120 presented in Figure 3-23c show fifteen peaks which indicate potential dislocation zones. Most peaks are contained within one measurement interval, indicating that the deformation is highly localised. However, several extend over more than one interval, reflecting movement across a broad zone defined by the intersection of steep fractures, or wide fracture zones. The magnitude, azimuth and dip of the dislocation vectors across each of the fifteen zones developed over 2 years (i.e. up to the fourth repeat survey) are shown in Figure 3-23d/e/f respectively. The values are listed in Table 3-5. The vector orientation denotes the displacement of the footwall with respect to the hanging wall and dips are positive downwards. In cases where the displacement is distributed across several adjacent points, the dislocation vector is summed across all points where the displacement magnitude exceeds a threshold of 0.04 cm. Dislocation magnitudes for the 2 year period are typically several millimetres with a maximum of 10 mm. Displacement azimuths to the SE (i.e. 110-160°) dominate. The dislocation vectors are mostly horizontal with the exception of two major dislocation zones at 38 and 68 m depth where it is inclined 36 and 50° upwards. This is evident from the axial displacement profiles which are flat except for two compressive steps concentrated at these two depths (Figure 3-23b). The blocks between active fractures in the lower section of the borehole are not only displaced towards the SE due to dislocation at the fractures, but also undergo rotation such that their lower part is displaced more to the SE than the upper part. These rotations add significantly to the cumulative displacements and become stronger with depth.

Three sections of different displacement behaviour can be recognised on the basis of the slope of the cumulative horizontal displacement profiles. The boundaries of the three zones lie at 37 m and 68 m, and coincide with the two fractures which the INCREX measurement indicate are undergoing vertical shortening (Figure 3-24g). These sections are interpreted as intact blocks undergoing different types of displacements according to the criteria described in section 3.4.3 and Figure 3-20: The upper zone extending to 37.3 m is characterised by negative slopes of the cumulative horizontal displacement profile in the A direction (Figure 3-24f), whereas the slope of the cumulative horizontal displacement profile is positive. This indicates that every interval has been subjected to inclination changes in direction -A/+B which indicates a toppling movement with the top of the block being displaced to the ESE. The middle zone, extending from 37.3 to 68.5 m is characterised by cumulative horizontal displacement profiles without incremental changes in both A and B directions which indicates translational sliding (e.g. in Figure 3-20). The lower zone extending from 68.5 to the casing bottom at 113 m has positive slopes of the cumulative horizontal displacement profiles in both A and B directions, which indicates block rotation with the lower part being displaced towards the SE.

The cumulative displacement vector of the bottom of the borehole with respect to the top is inclined upwards at a dip of -30 to -40° and is directed to the S (Table 3-4). The azimuth agrees with that of the geodetically-determined absolute displacement direction of the surface near SB 120, but the latter dips downwards at 46°. Thus the cumulative horizontal displacement profiles indicate that the bottom of the borehole did not reach stable ground, and that further detachment surface lie below.



Figure 3-24 compares the 3-D displacement and dislocation data from the fourth repeat survey against the geological data from the optical televiewer images of: (c) fracture trace geometry, (d) lithology, and (e) fracture intensity given by the number of fractures per inclinometer interval. In most cases, the dislocations correlate with distinct major fractures identified on the optical televiewer images and shown highlighted in Figure 3-24c. Moreover, most major fractures are active. Out of 20 major fractures, only 8 are inactive, the majority of these lying in the foliation plane. In contrast, zones of high fracture density (i.e. more than 3 fractures per 0.61 m) generally do not show distributed displacement. Thus, dislocations are very localised, and the blocks they bound do not suffer internal deformation. The only possible correlation of dislocation with the lithology is at 38 m depth where a 2 m wide zone of increasing axial strain coincides with an intercalation of fine grained, folded gneisses within the series of unfolded gneisses. Thus, the displacement profiles suggest that displacement patterns are governed by differential movements at the boundaries of blocks defined by major fractures (Table 3-5).

Table 3-5: Correlation of dislocation zones, 3-D displacement vectors and fracture data for SB 120. The rake angle is the direction of slip in the plane of the fracture measured anticlockwise from the dip direction looking down. Most dislocations above 100 m imply predominantly shear movement with the footwall moving up-dip with respect to the hanging wall.

<i>Depth of dislocation zone</i>	<i>Orientation of active fracture</i>	<i>Azimuth, dip and magnitude of 3-D dislocation vector (bottom block wrt to upper, 2 year period)</i>	<i>Dislocation component in plane of the fracture</i>	<i>Dislocation component normal to the fracture</i>	<i>Rake angle</i>	<i>Characteristics on televiewer image</i>
[m]	[° / °]	[° / °] [cm]	[cm]	[cm]	[°]	
5.62*	95 / 64					
12.3	328 / 65	141/-12	0.39	0.24	191	open fracture with fine infilling
22.1	331 / 22	143 / -01	0.30	0.28	189	schistous, rotated blasts
29.4	265 / 15	115/-04	0.14	0.14	150	dark (mica rich) section
37.3	336 / 30	118/-37	0.46	0.45	210	phylionite
39.8	350 / 58	127/-27	0.19	0.18	220	fracture with fine infilling
68.5	335 / 50	141/-51	0.97	0.97	189	densely foliated and fractured zone, fine infilling
84.9	348 / 86	158/-01	0.35	0.07	244	densely foliated and fractured zone
92.2	321 / 40	102/-07	0.27	0.25	223	densely foliated and fractured zone
95.9	328 / 70	245 / 02	0.18	0.18	94	partly open fracture, with fractured zone
99.6	309 / 28	110 / 06	0.11	0.09	203	phylionite
103.8*						
108.7	350 / 85	179 / -06	0.17	0.04	141	fracture
110.5	334 / 66	166 / -03	0.16	0.08	155	densely foliated and fractured zone

\* related to ungrouted casing sections

Since the dislocations can be correlated to distinct fractures, the dislocation vectors can be resolved onto the fracture plane to determine the shear and normal components, and the direction of in-plane shear with respect to fracture dip (i.e. rake angle). This was done for all fractures which show dislocation magnitudes >0.05 cm/a. The results are listed in Table 3-5 and indicate that above 100 m the

dislocations largely involve shear movement in a normal faulting sense (i.e. footwall moves up-dip with respect to hanging wall). In all cases, in-plane slip directions are within 30° of alignment with the fracture dip directions. However, several fractures also show a significant component of opening.

#### SB 50S

The inclinometer data from SB 50S required the correction for torsion only (Table 3-6). No depth mismatch was found, and the effects of sensor rotation were negligible because the borehole inclination is much less than SB 120. The corrected cumulative horizontal displacement profiles in the A- and B-directions for the four repeat surveys are shown in Figure 3-25a-d together with the corresponding azimuth and magnitude of the horizontal component of the dislocation vector. As no axial strain measurements were performed in the 50 m deep boreholes, the vertical component of the displacement vector is unknown.

In SB 50S the displacements were found to be only partially localised; between 10 and 20 m depth the displacements are distributed over several inclinometer intervals. In this borehole section, a characteristic zigzag-pattern in the cumulative horizontal displacement profile is seen that possibly reflects the incomplete cementation of the casing along sections with steep open fractures. Aside from these irregularities, the slope changes along the profile indicate that the borehole penetrates four blocks bounded by active fractures. The cumulative horizontal displacement profile exhibits a negative slope along the complete borehole which is consistent with toppling motions of the blocks between active fractures. The azimuth of the derived horizontal displacement of the borehole bottom with respect to the top is directed to WNW (Table 3-6), which is opposite to the geodetically-determined absolute displacement vector of the wellhead (Figure 3-7). This indicates that absolute displacements decrease with depth.

Table 3-6: Corrections and resulting displacements of the borehole bottom wrt top for the repeat surveys in SB 50S.

<i>Repeat survey</i>	<i>Date</i>	<i>Depth stretch [cm]</i>	<i>Azimuth and magnitude of the displacement vector of the bottom of the borehole wrt the top [°, cm]</i>
1	06/2002	0	341 0.35
2	10/2002	0	193 0.23
3	07/2003	0	304 0.26
4	10/2003	0	316 0.50

In Figure 3-26, the measured displacements are plotted against the fracture and lithology data derived from the optical televiewer images. Evidently, the zone of distributed deformation between 10 and 20 m depth corresponds to the intersection of several major fractures and fracture zones which is the expression of a major E-W trending fault mapped on the surface. The zone is too complex to associate dislocations to specific fractures, and the broad extent of the displacements may largely be due to the fact that a sub-vertical fracture extends over 5 m in the borehole. The televiewer derived orientation of these fractures is provided in Table 3-7. Again the azimuth of the dislocation vector does not align with the dip direction of the active fractures.

Table 3-7: Correlation of dislocation zones, 3-D displacement vectors and fracture data for SB 50S.

Depth of dislocation zone	Dip direction and dip of active fracture [°/°]	Azimuth and magnitude of the horizontal dislocation vector (bottom block wrt to upper, 2 year period)		Characteristics on televiewer image
		[°]	[cm]	
13.9	38/68	110	0.19	at 11.5 m: open, silt coated fracture
18.1	115/89	163	0.15	open fracture
34.0	297/40	323	0.28	densely fractured zone

### SB 50N

The 2-D cumulative horizontal displacement profiles for the four repeat surveys derived using the corrections listed in Table 3-8 are shown in Figure 3-25e-h. Only one major active fracture is present at 21 m depth. The cumulative horizontal displacement profiles indicate rotational displacement patterns of the blocks consistent with toppling below and above this zone, as was the case at SB 50S. The displacement directions of the bottom of the borehole with respect to the top for the four repeat surveys are listed Table 3-8, and vary between W, NW and NE. The profiles of cumulative horizontal displacement and dislocation vectors in SB 50N are shown in Figure 3-27 together with the geological data from the optical televiewer images. The single major dislocation zone in the borehole at 21 m correlates with the location of a steep, open, major fracture (Figure 3-27 and Table 3-9). The curvature of the cumulative displacement profiles below 25 m in principle suggests distributed deformation, although this is not consistent with the fracture distribution seen on the optical televiewer log.

Table 3-8: Corrections and resulting displacements of the borehole bottom with respect to (wrt) top for the repeat surveys in SB 50N.

Repeat survey	Date	Depth stretch [cm]	Azimuth and magnitude of the dislocation vector of the bottom of the borehole wrt the top [°, cm]
1	06/2002	-1	341 0.43
2	10/2002	-2	268 0.34
3	07/2003	-2	28 0.56
4	10/2003	0	285 0.80

Table 3-9: Correlation of dislocation zones, 3-D displacement vectors and fracture data for SB 50N.

Depth of dislocation zone	Dip-direction and dip of active fracture [°/°]	Azimuth and magnitude of horizontal dislocation vector across displacement zones (bottom block wrt to upper, 2 year period)		Characteristics on televiewer image
		[°]	[cm]	
20.9	319/83	41	0.25	open fracture

## 3.5 Integration of monitoring results to a block kinematic model

As shown in the previous sections, the displacements at the surface and at depth are localised across active discontinuities within the rock mass. Thus the kinematic behaviour of the unstable rock mass is dominated by complex internal block movements rather than being a coherently-sliding mass.

The displacements occur on the network of faults, fracture zones and major fractures that define the block boundaries. The vast majority of active fractures at the surface and also in the boreholes dip to the NNW at angles between  $30^\circ$  and  $90^\circ$  (Figure 3-28). A similar distribution is found for all faults and fracture zones mapped at the surface (Figure 3-3).

The blocks defined by the active discontinuities have sizes ranging between 7 and 15 m according to the spacing seen along the borehole. At the surface, the inferred block sizes are larger, ranging from 15 to 30m. This apparently larger size may be an artefact of some active fractures being hidden under vegetation and debris. Smaller block sizes are more in accord with observations made during the 1991 rockslide. The prolonged nature of the second slide event was attributed to the well developed segmentation of the rock mass (Schindler et al. 1993, Sartori et al. 2003).

The construction of a block kinematic model for the investigated rock mass was based primarily on the geometry of the fault and fracture zone network as inferred from the surface and borehole mapping. This was complemented by the results of single-hole georadar reflection measurements which allowed bounds to be placed on the minimum extent of several active major fractures intersecting the boreholes (see Chapter 2). Figure 3-29a shows an approximate SE-NW profile across the study area which becomes more N-S between SB 120 and SB 50S. Active fractures identified by the borehole and surface displacement surveys are shown extrapolated with the dips seen in their exposure. Also plotted are the relative displacement vectors across dislocation zones. Most dislocations involve predominantly shear movement which is oriented within  $30^\circ$  of the fracture dip directions. Thus the vectors can be sensibly represented on the 2-D projection. In SB 120 the lower blocks are displaced towards the valley with respect to the upper by slip on the fractures in a normal-fault sense. The rotation of the blocks inferred from the slope of the cumulative horizontal displacement profiles (e.g. Figure 3-23a) further increases the displacement of the lower blocks to the SE. Further to the northwest in the vicinity of the 50 m boreholes where the geodetically-determined displacements suggest the rock mass is more stable, the opposite depth-trend is seen with upper blocks exhibiting larger displacements towards the valley (i.e. towards SE).

An alternative view of rock mass displacements can be obtained by determining the absolute displacement vectors developed along the borehole in the two years up to the fourth repeat survey. This was done by calculating the 3-D displacement vector with respect to the wellhead at selected points along the borehole from the cumulative horizontal displacement and vertical strain profiles in Figure 3-24f/g respectively. These were transformed to absolute displacement vectors by adding an estimate of the absolute displacement vector of the wellhead. To this end, the surface displacement vector at retro-reflector 153 which lies 25 m to the southeast of SB 120 was derived for the period between the initial survey and the fourth repeat survey. This was found to be 3.03 cm towards azimuth  $143^\circ$  with a dip of  $46^\circ$ . The resulting profile of absolute displacement vectors are plotted in Figure 3-29b, which clearly shows that the bottom of the hole did not reach stable ground, and that further sliding surface lie below. Thus, the lower limit of displacement could not be determined.

### 3.6 Analysis of the continuous measurements

The automatically-recording crackmeters, in-place inclinometers and piezometers were sampled at the high rate of 6 minutes to determine whether displacements associated with sliding are

always gradual or occasionally episodic. The high sampling rate also allowed the effects of meteorological parameters to be evaluated. In the following we examine the data for episodic deformation events and consider the impact of atmospheric pressure, precipitation and snow melt on the data. The data are shown in Figure 3-30. All climate data provided by Meteoschweiz are from a meteorological station in nearby Zermatt which is approximately 10 km south of Randa at an altitude of 1638m. Barometric pressure and temperature from the station were extrapolated to the altitude of the study site using the gradients 11.3 mbar/100m and 0.51°C/100m (Figure 3-30d).

### *Crackmeters*

The continuously recording crackmeters serve to determine whether surface fractures open at constant rates or whether fracture opening occurs in specific events. The crackmeters deployed for monitoring the fracture opening at the study site have been described in section 3.3.3 and their results validated by comparing them with the results of benchmark measurements. The time series of crack opening and temperature at two fractures extends over 1.5 years and is shown in Figure 3-9. As already discussed, the strain measurements exhibit diurnal and annual cycles which correlate with temperature cycles and are probably of thermo-elastic origin. Correlation of fracture opening, temperature and piezometric data as described could not be observed as was the case in Watson et al. (2004). In the latter case, thermal contraction within the rock mass is assumed to have led to slip on discontinuities and to change the drainage system in the slope likewise.

At the study site, the fracture opening measurements also show long-term trends which most likely reflect fracture opening due to rock mass sliding. Examination of the records showed only one short-term strain signal that did not correlate with a temperature fluctuation. This occurred in March 2003 (see arrow on Figure 3-9 and Figure 3-30a) and coincides with the onset of snow-melt. A sudden offset in the opening at crackmeter q2 occurs and is followed 5 days later by an opening at x2. Following these events, the opening curve becomes flat as the rate drops to zero. However, the signal at x2 coincides with a temperature change and thus could be of thermo-elastic origin, and the flattening is part of the annual cycle (again believed to be thermo-elastic in origin). Thus there is doubt that these signals represent an episode of rock-mass sliding. The results rather point to sliding as being a rather continuous, creep like process.

### *In-place-inclinometers*

Two vibrating-wire, in-place inclinometers with 2 m baseline length were deployed to continuously monitor inclination changes across prominent fractures in borehole SB 120. The instruments must be removed to conduct repeat surveys of the inclinometer casing, and sometimes they were replaced in different positions. For the period between the initial inclinometer survey and the second repeat survey the in-place inclinometer midpoints were located at 110 and 68 m depth, which coincide with the location of major fractures seen on the optical televiewer images. After the second repeat survey, the in-place inclinometers were positioned at 84.5 and 68 m depth, so as to straddle major fractures known to be active. Unfortunately, several features of the data sets suggested that the measurements were in error. Thus, the instruments were removed after the third repeat survey and returned to the manufacturer who confirmed they were defective. These instruments are prone to drift and suffer offsets. Such deficiencies in vibrating-wire in-place inclinometers have already been recognised in laboratory test conducted by independent laboratories (LaFonta & Beth 2001) and in field

studies (Simeoni & Mongiovi 2003). The defective instruments were replaced with devices of a new design that attempt to correct the deficiency. These instruments were installed at the same depths they were removed from in December 2003 and have since been operational. The data series will be evaluated after the next repeat survey of the inclinometer casings.

#### *Piezometric monitoring and climate data*

The continuous records from the crackmeters and the piezometers at the bottom of the three deep boreholes were compared against the hourly-sampled climate data. The vibrating wire piezometers are equipped with a thermistor (for specifications see Table 3-10) and are positioned in filter gravel within the lowermost, slotted inclinometer casing section in SB 120, SB 50S and SB 50N. The annulus between the casing and the rock was left open. This was accomplished by using cemented packers to isolate the slotted section from the grouted annulus. Information on the fractures intersected by the borehole at the piezometer intervals is only available for SB 50N: here two large open fractures could be identified on the optical televiewer images. In SB120 and SB 50S muddy water at the lowermost borehole meters prohibited the identification of the fractures in the piezometer intervals.

The frequency output of the vibrating wire sensor is proportional to the absolute pressures (i.e. water and atmospheric pressure) at the piezometer. The pressure values are corrected for temperature effects by applying a linear thermal correction factor that depends on the temperature difference between the initial and the current reading. The raw data includes numerous single-value outliers, defined as values where the difference between the actual and a running-mean of the series taken over the previous 1 hour of data exceeded two standard deviations of the 1 hour window. The outliers were replaced by the running-mean values. The pressure time series for SB 120 and SB 50S after outlier removal are shown in Figure 3-30b and in Figure 3-31 with two expanded views. No data were obtained in SB 50N for unknown reasons.

Table 3-10: Specifications for the piezometers.

	<i>Borehole</i>	<i>Range</i>	<i>Resolution</i>	<i>Accuracy</i>	<i>Thermal zero drift</i>	<i>Output</i>
<i>Geokon vibrating</i>	<i>SB 50N+S</i>	<i>3.5 bar</i>	<i>0.875 mbar</i>	<i>±17.5 mbar</i>	<i>1.75 mbar/°C</i>	<i>frequency, temperature</i>
<i>wire piezometer</i>	<i>SB 120</i>	<i>7 bar</i>	<i>1.75 mbar</i>	<i>±35 mbar</i>	<i>3.5 mbar/°C</i>	<i>frequency, temperature</i>

The water level in the boreholes corresponds to the measured absolute pressure minus the atmospheric pressure. The difference between the two at the start of the record suggests the piezometers at the bottom of SB 120 and SB 50S were installed under 1 and 2 m of water respectively (Figure 3-31a). Thereafter, the evolution of the water levels in the two holes is quite different and not well understood. The record from SB 50S is very stable for the first 6 months and then suddenly undergoes a fast increase of 2 m during snow melt. Thereafter the water level fluctuates just below this level with major responses of 1 m to snow melt and minor responses of decimetres to major precipitation events which occurred mostly in the summer and autumn of 2002. In contrast, the SB 120 piezometer shows only small water pressure changes with a dominant signal at annual periods of 0.5 m amplitude and seemingly erratic steps at short periods. The highest water levels are recorded two months after the SB 50S piezometer reacts to the snow melt. Both pressure records show small fluctuations sympathetic

with atmospheric pressure changes. In SB 50S, the amplitude of the fluctuation is almost as large as the atmospheric pressure variation (Figure 3-31b/c), indicating good hydraulic connection with the surface. However, the fluctuation in SB 120 is much smaller than the atmospheric fluctuation but not phase-shifted (Figure 3-31d). This suggests that the piezometer interval is partly separated from the atmosphere and implies the piezometer interval is confined or semi-confined at periods of at least 1 day. From summer 2002 on, the water pressure decreases in a saw-tooth pattern, with slow increases terminating in a more rapid decline over 1 day. The nature of this fluctuation is not understood as it does only partially correlate with atmospheric pressures (Figure 3-31e).

These observations suggest the presence of several small perched groundwater tables distributed within the rock mass. Observations during drilling and borehole logging showed that open fractures exist to a depth of at least 85 m below surface. Therefore large water pressures are unlikely to build up within the rock mass, especially during low-precipitation years like 2003. The different responses of the two piezometers to hydraulic disturbances (i.e precipitation, snow melt and atmospheric pressure changes) indicate that they sample different localised, perched groundwater tables which behave independently of each other. The bottom of SB 50S is located close to steep faults and fracture zones that connect the piezometer directly to infiltrating water, as shown by the full barometric signal in the pressure series. In contrast, the bottom of SB 120 is located at greater depth within the dissected rock mass and hence is more hydraulically isolated from the surface.

### **3.7 Implication for the analysis of the acting rockslide processes**

The surface and borehole displacement measurements at the study area confirmed the expectation from geological mapping that the displacement field is complex. The mapping showed that no highly persistent discontinuities dipping in the direction of the geodetically determined surface displacements exist that might facilitate simple translational sliding of the rock mass in a coherent manner. Rather, active fractures are largely high-angle and dip in the opposite direction. Displacements on these fractures largely involve shearing in a normal fault sense which accommodate complex internal displacements of blocks within the moving rock mass. These deformations were used to build a kinematic model that described the relative movements within the rock mass. In the next chapter the measured displacement patterns will be compared with modelled displacement patterns as a function of spatial variations and geometries constituting the failure mode and nature of the sliding surface(s).



### 3.8 Figures

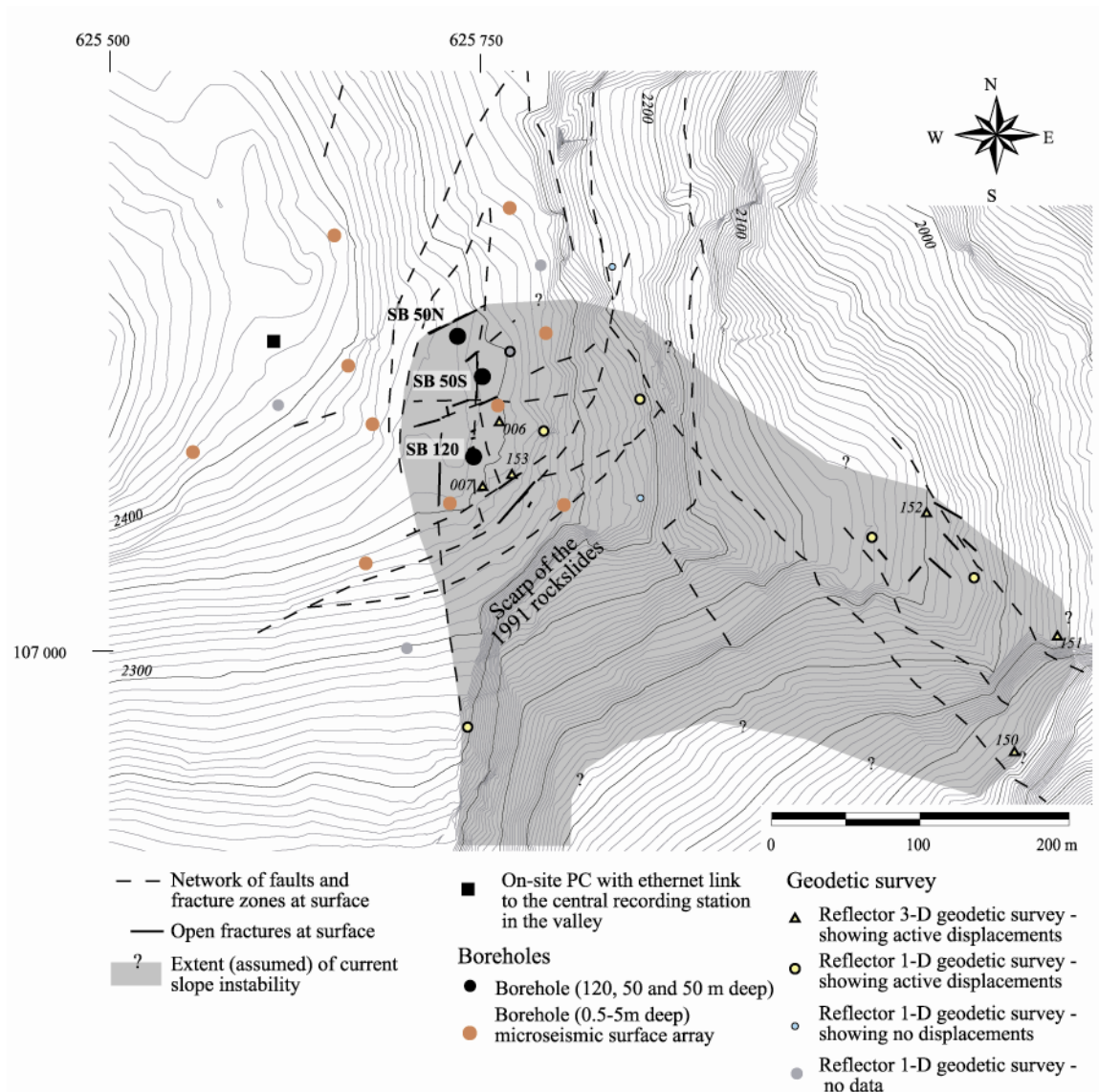


Figure 3-1: 5-m contour map of the study area showing the faults and fracture zones and instrumentation locations. The extent of the unstable rock mass is shown shaded. Active fractures and the location of monitoring devices for surface fracture opening are shown in Figure 3-2.

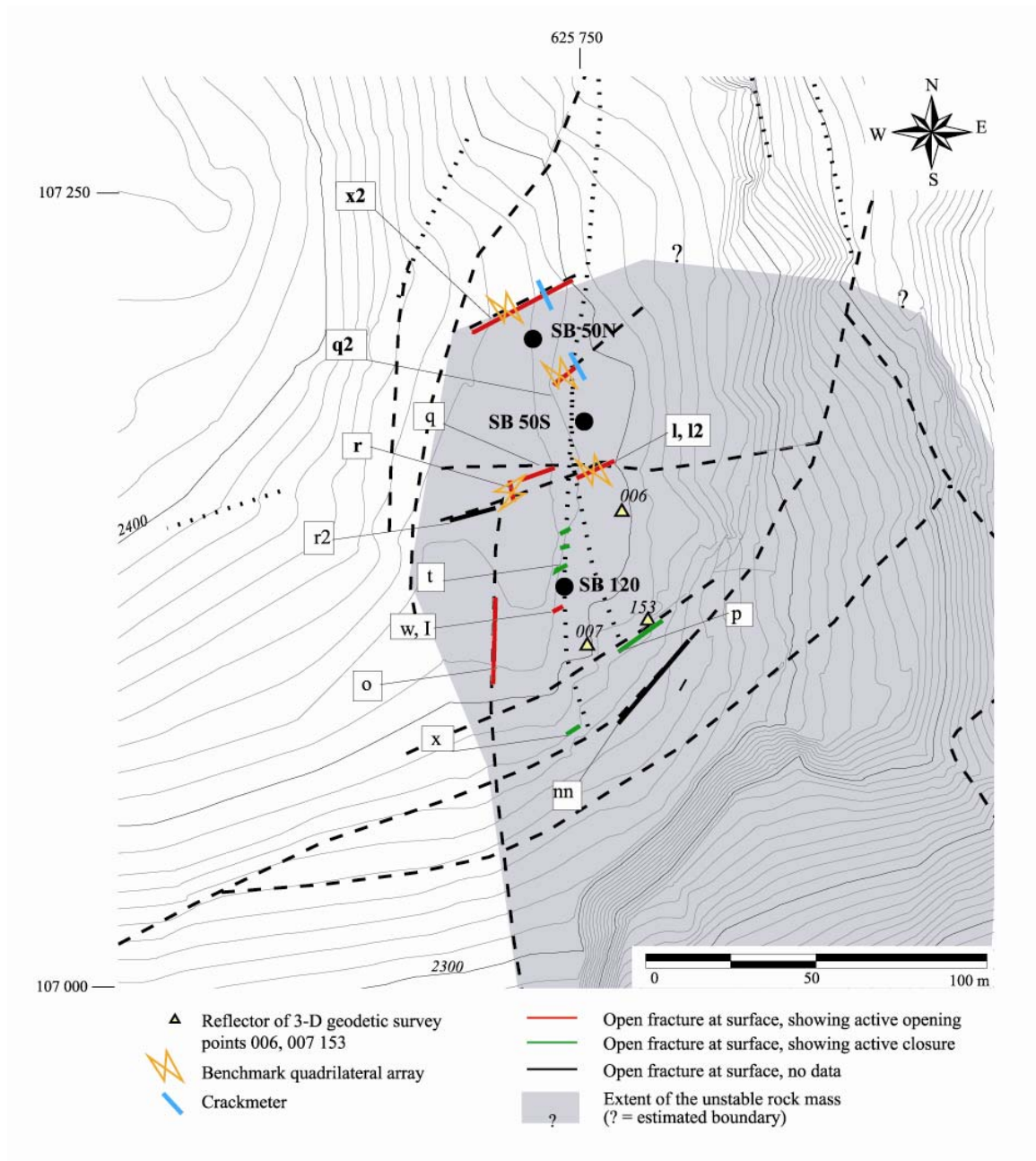


Figure 3-2: Location of retro-reflectors and benchmark arrays across fractures. Open fractures at the surface are shown as solid lines on the network of faults and fracture zones (dashed lines). Major open fractures are labelled. Fractures equipped with a benchmark quadrilateral are highlighted.

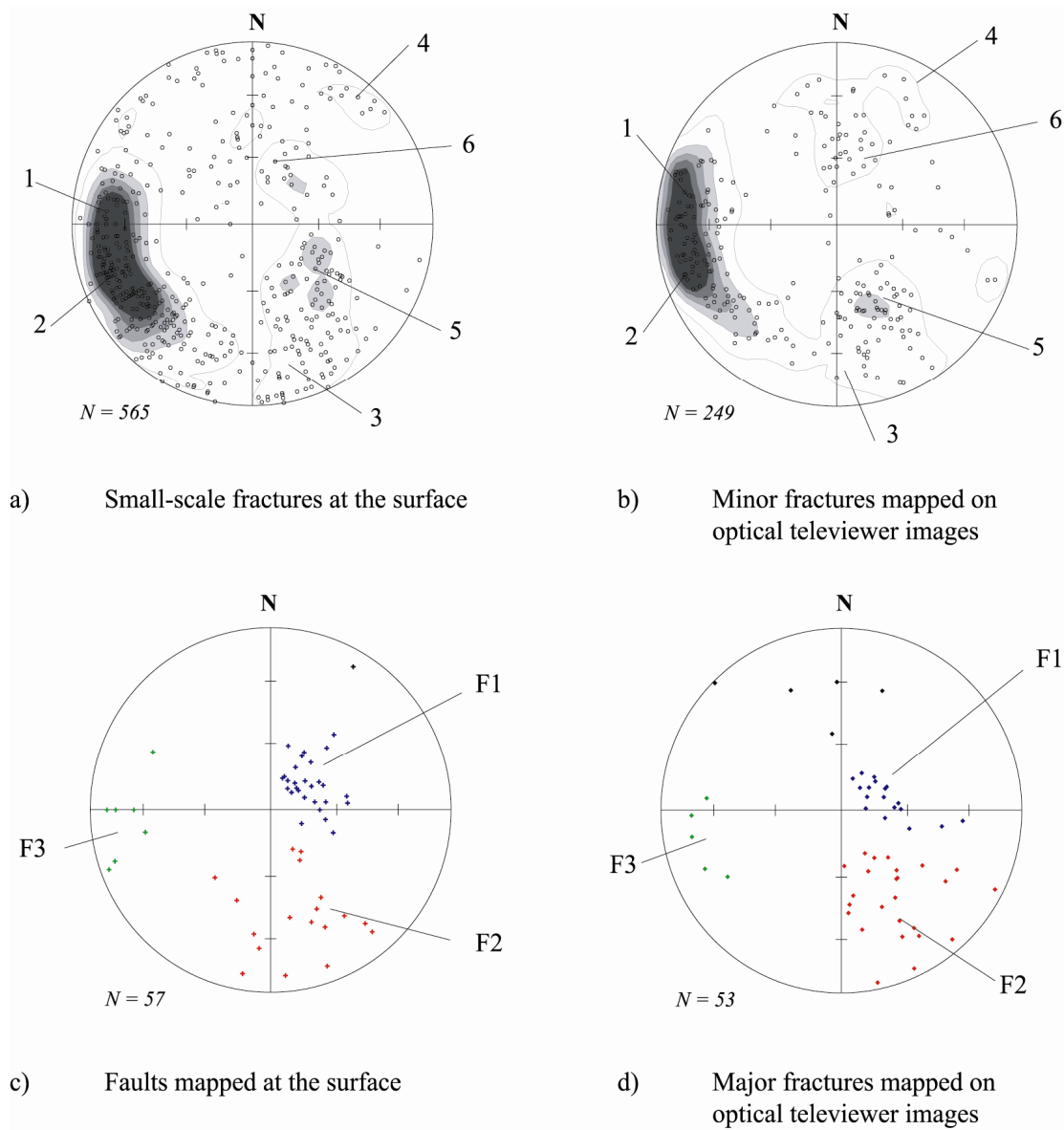


Figure 3-3: Orientation of the fractures in the study area shown in lower hemisphere, equal area stereographic projection. Isolines follow 5,10,15,20% densities. Foliation fractures are not plotted. a) Small-scale fracture network mapped at the surface. Six fracture sets were identified. b) Minor fractures mapped within the boreholes SB 120, SB 50S and SB 50N. c) Faults and fracture zones mapped at the surface. d) Major fractures mapped within the boreholes. Three dominating families of faults and fracture zones were accounted for (F1-F3).

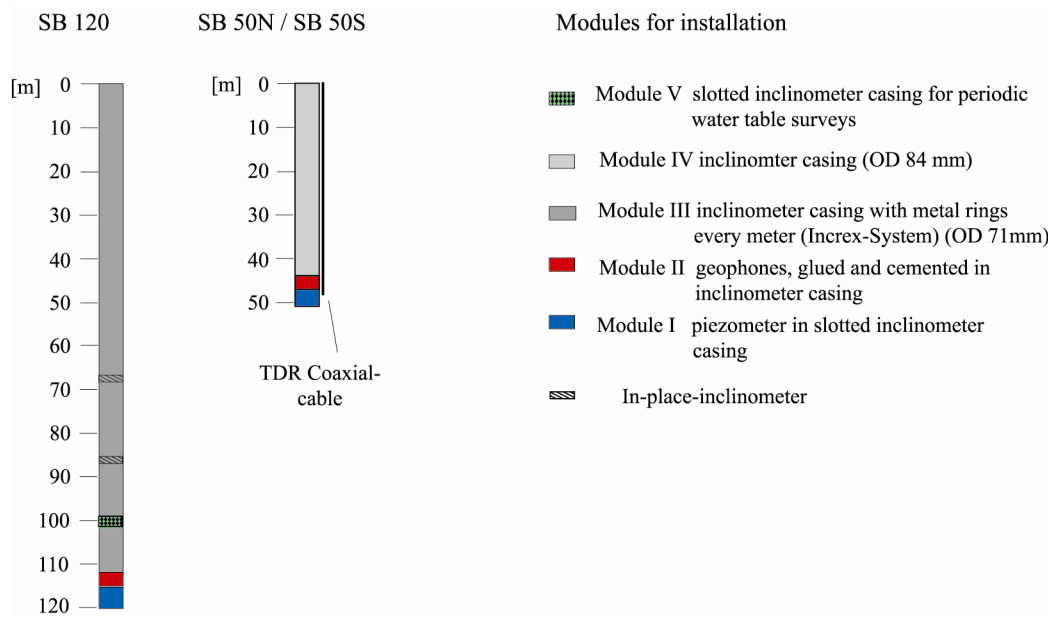


Figure 3-4: Composition of the casing installed in the boreholes showing the various integrated modules.

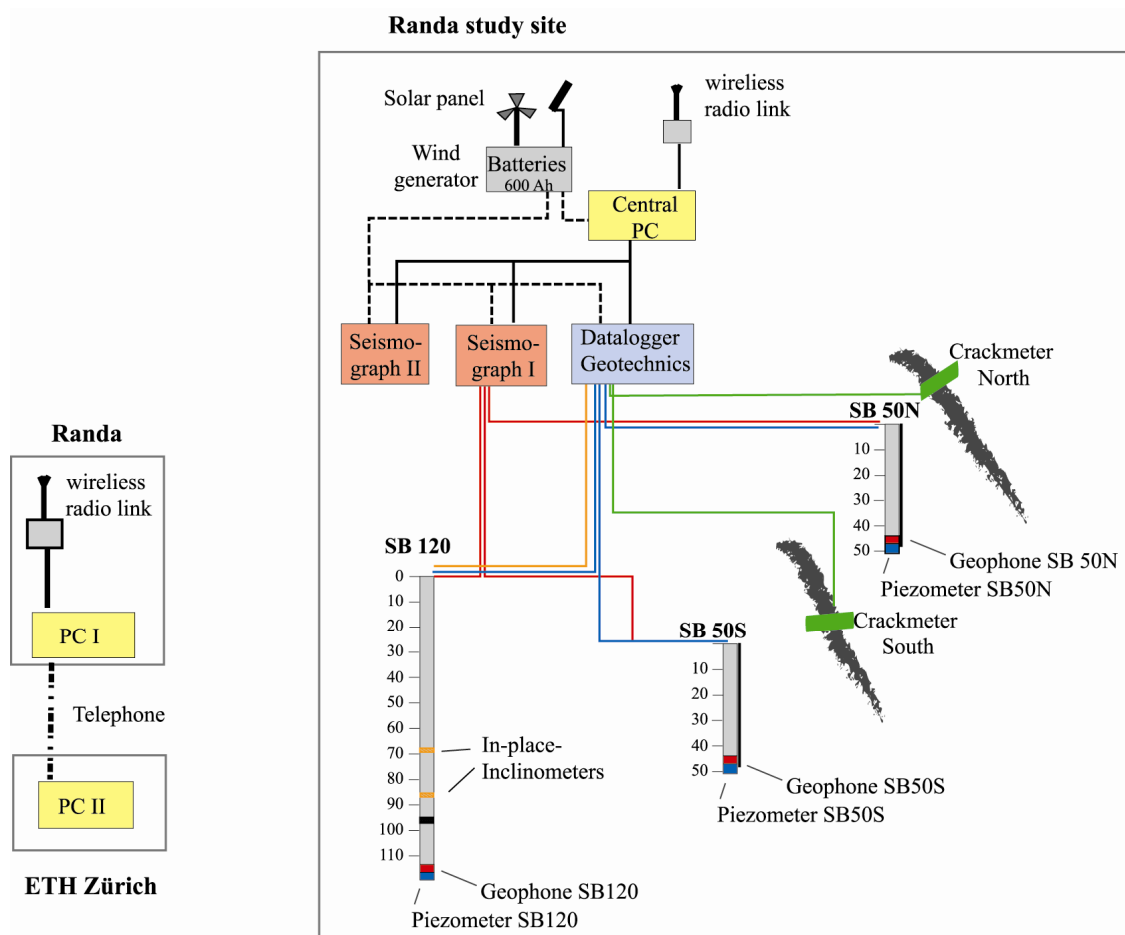
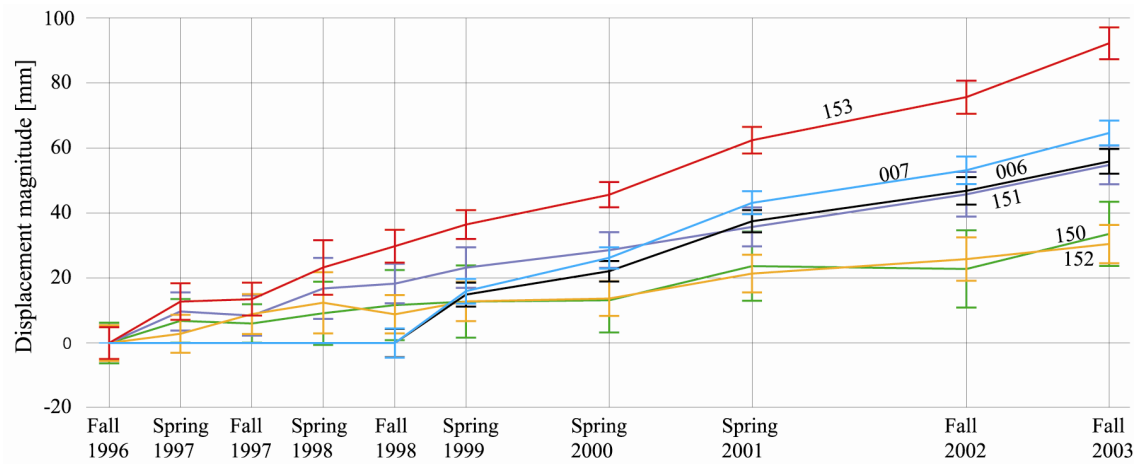
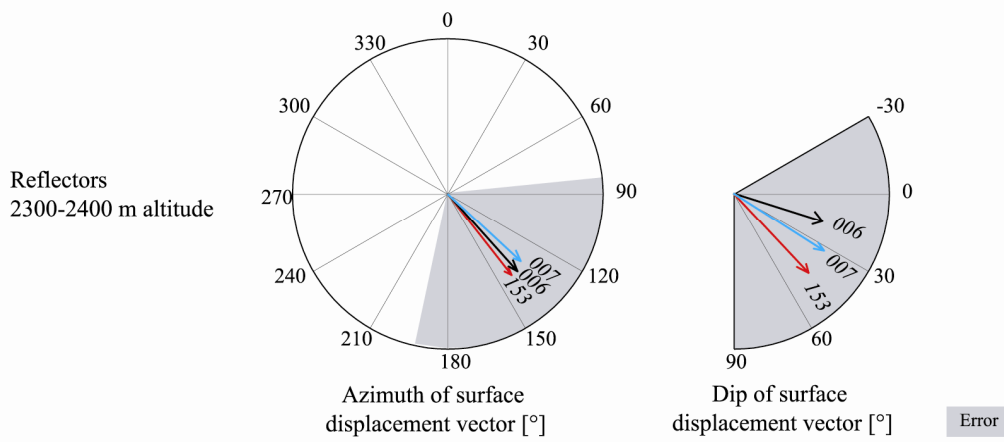


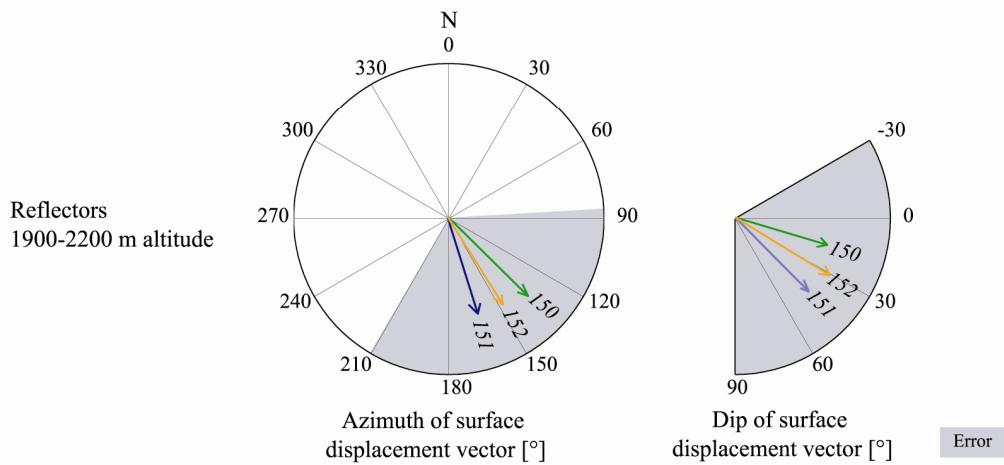
Figure 3-5: On-site data acquisition system and wireless radio link to the station in the valley. The seismometers in the shallow boreholes are not shown.



a)



b)



c)

Figure 3-6: Surface displacements 1996-2003 derived from geodetic survey (results provided by CREALP). The locations of the retro-reflectors are shown in Figure 3-1. a) Magnitude of displacement vectors with error bars. b) Mean azimuth and dip of the displacement vector for reflectors between 2300 and 2400 m altitude. The shaded area denotes the error estimate. c) Mean azimuth and dip of the displacement vector for reflectors between 1900 and 2200 m altitude.



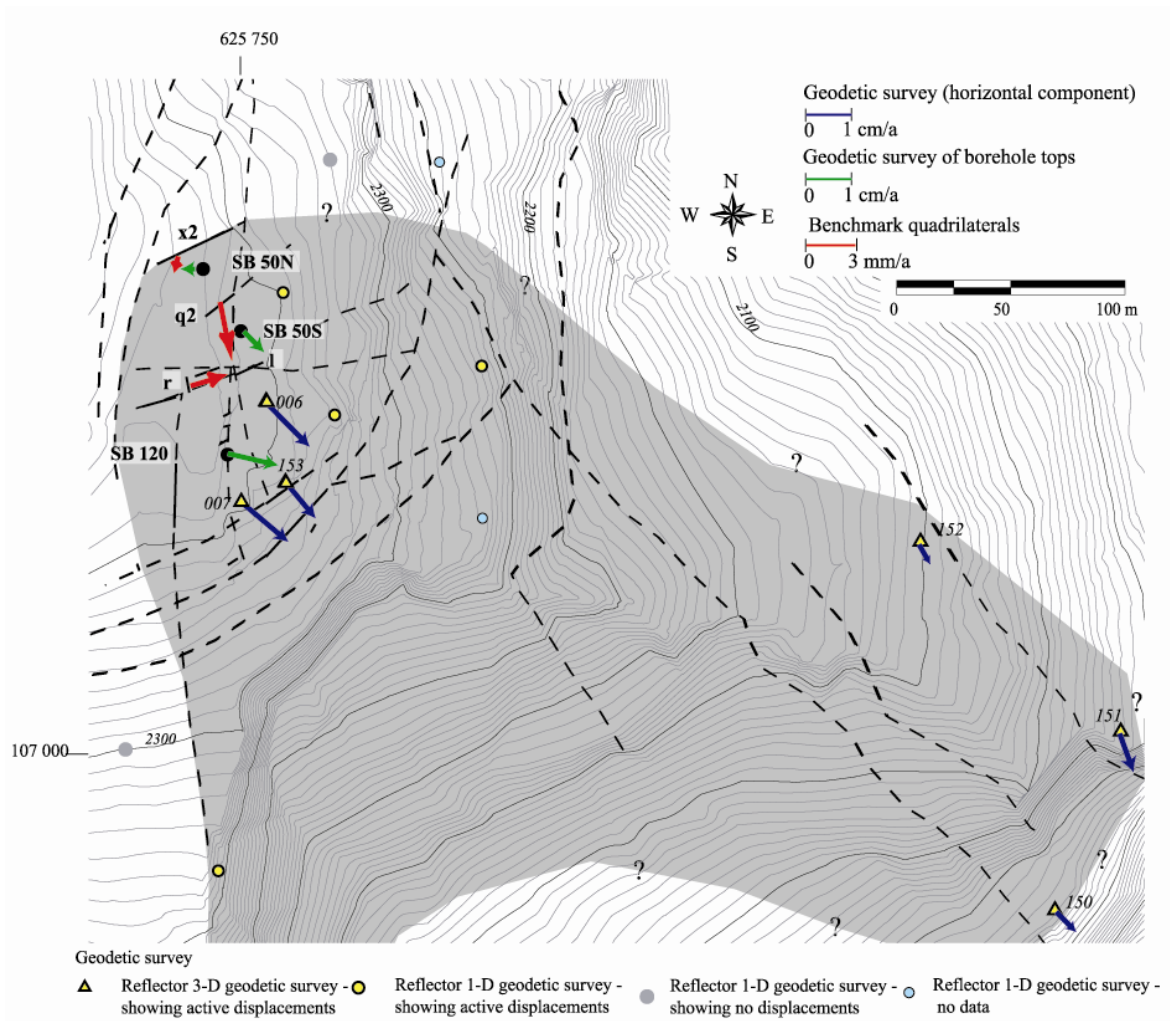


Figure 3-7: Horizontal component of the surface displacement vectors plotted on a map of the site which shows active fractures (dashed lines) and the likely extent of the unstable part of the rock mass (shaded). The displacement vectors of the retro-reflectors of the geodetic survey (blue) and the borehole tops (green) are absolute since they are referenced to an external coordinate system. The displacement vectors across active fractures (red) indicate the relative displacements of the southern or eastern side with respect to the northern or western side.

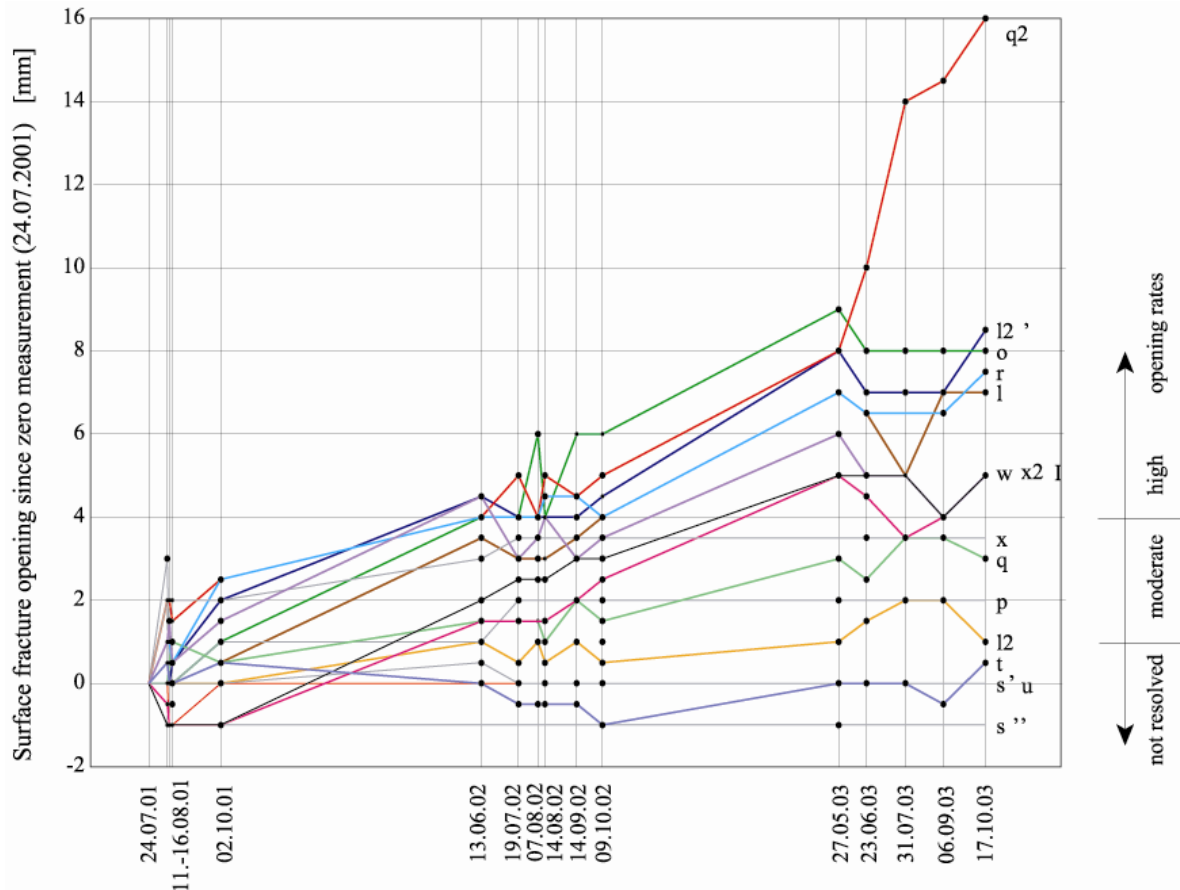


Figure 3-8: Results of all resurveys of the simple benchmark pairs during the period 2001-2003. The benchmark pairs at q2, o and x are equipped with wire-spring assemblies: the others are rock bolt pairs. Black dots denote measurements taken.

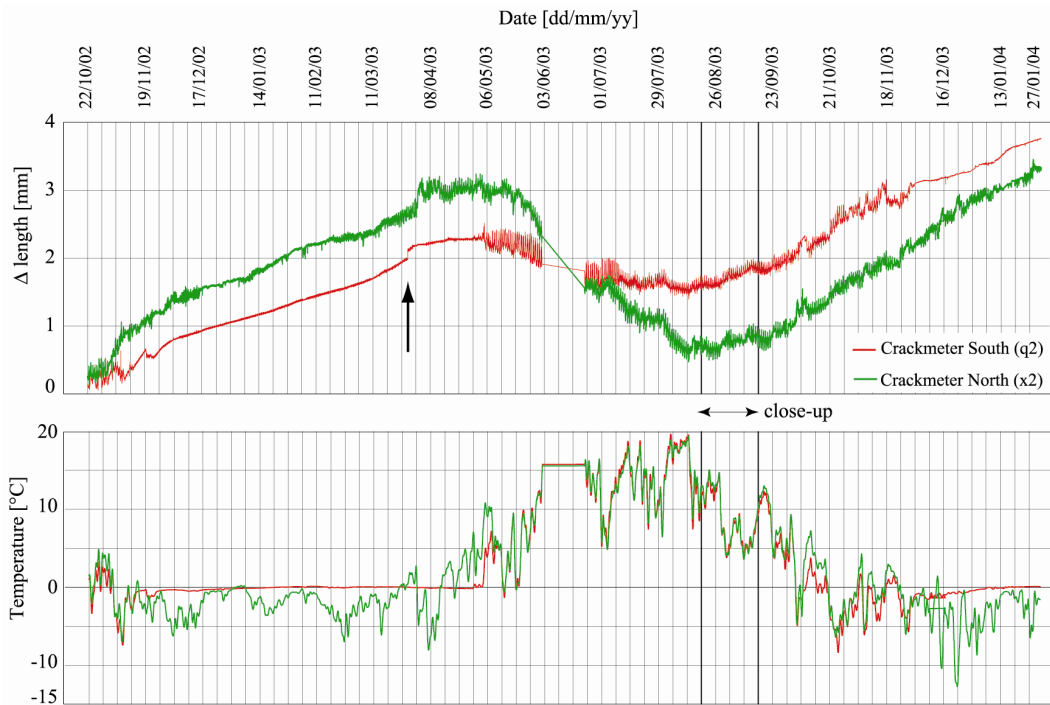


Figure 3-9: Fracture-opening and temperature recorded by the crackmeters North (x2) and South (q2). The length-change curve is shown unfiltered after outlier-removal whereas the temperature curve was filtered using a 2-days low-pass filter. An expanded view of the data between August and September 2003 is shown in the Figure 3-10. The arrow indicates a sudden offset in q2 followed 5 days later by a gradual offset in x2. The latter is possibly of thermo-elastic origin.

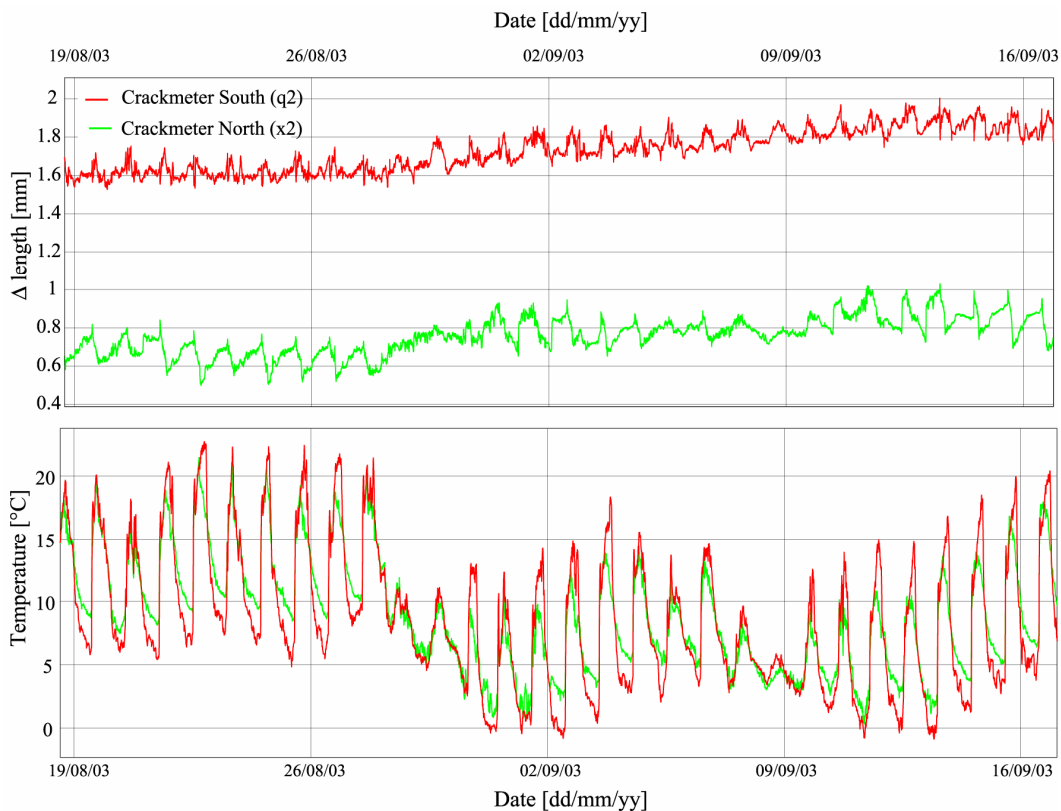


Figure 3-10: Expanded view of Figure 3-9 showing four weeks unfiltered records of crackmeter length-change (with outliers removed) and temperature. The diurnal length change fluctuations of  $\pm 0.1$ mm correlate with the daily temperature variations of  $\pm 7^\circ\text{C}$ .



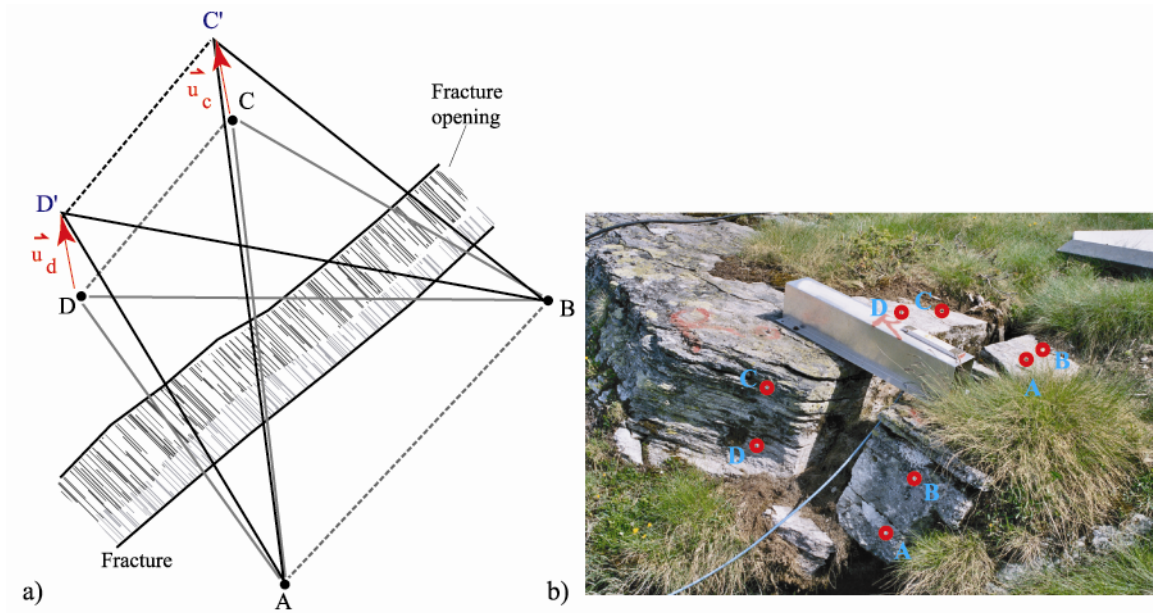


Figure 3-11: a) Illustration of the benchmark quadrilateral measurement and analysis principle. The initial quadrilateral geometry, ABCD, is delineated in grey and the deformed quadrilateral, ABC'D', in black. b) A pair of benchmark quadrilaterals in different planes across fracture 'r' (horizontal and vertical).

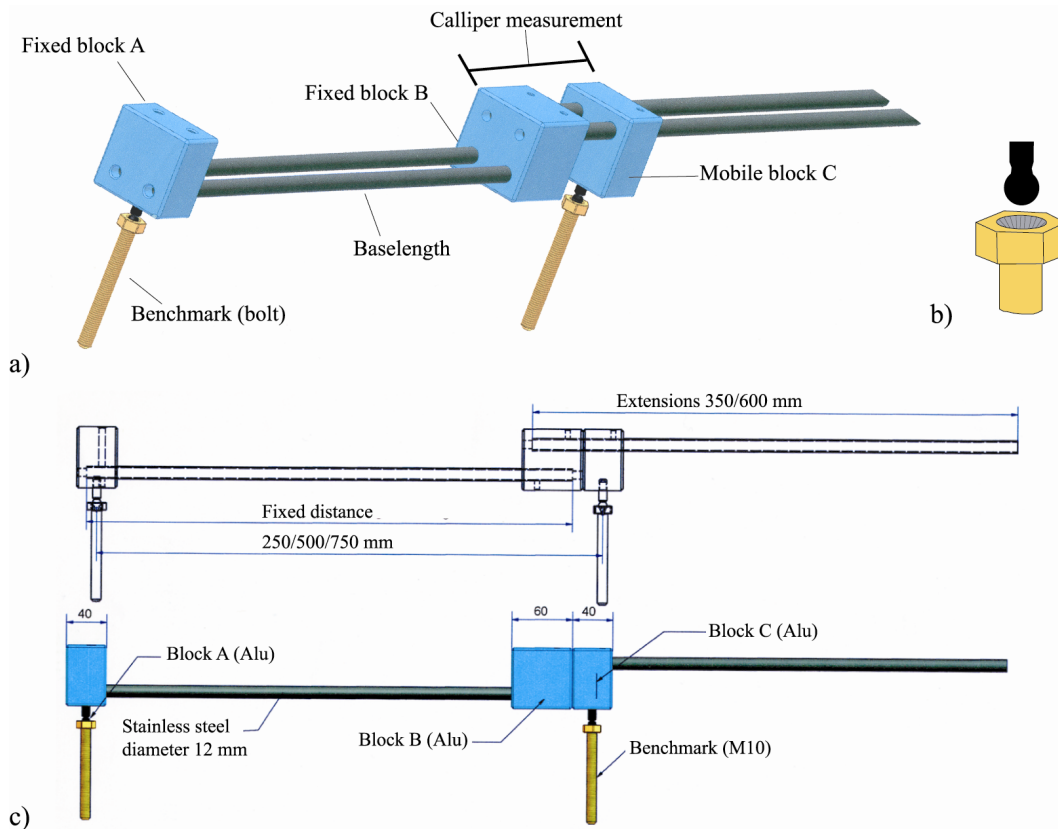


Figure 3-12: a) The benchmark quadrilateral tool and benchmarks developed for the project. In operation, blocks A and B are clamped to their rails and block C slides until the pins below blocks A and C locate in the benchmarks. Block C is then clamped and the distance between the outer edges of blocks B and C measured with a caliper. b) Illustration of benchmark and locating-pin seating. The benchmarks are rockbolts which have a hemispherical recess milled into their heads into which the ball of the locating pin seats. c) Technical details of the tool. (design Solexperts, Schwerzenbach, Switzerland; sketch modified after Peter Giger).

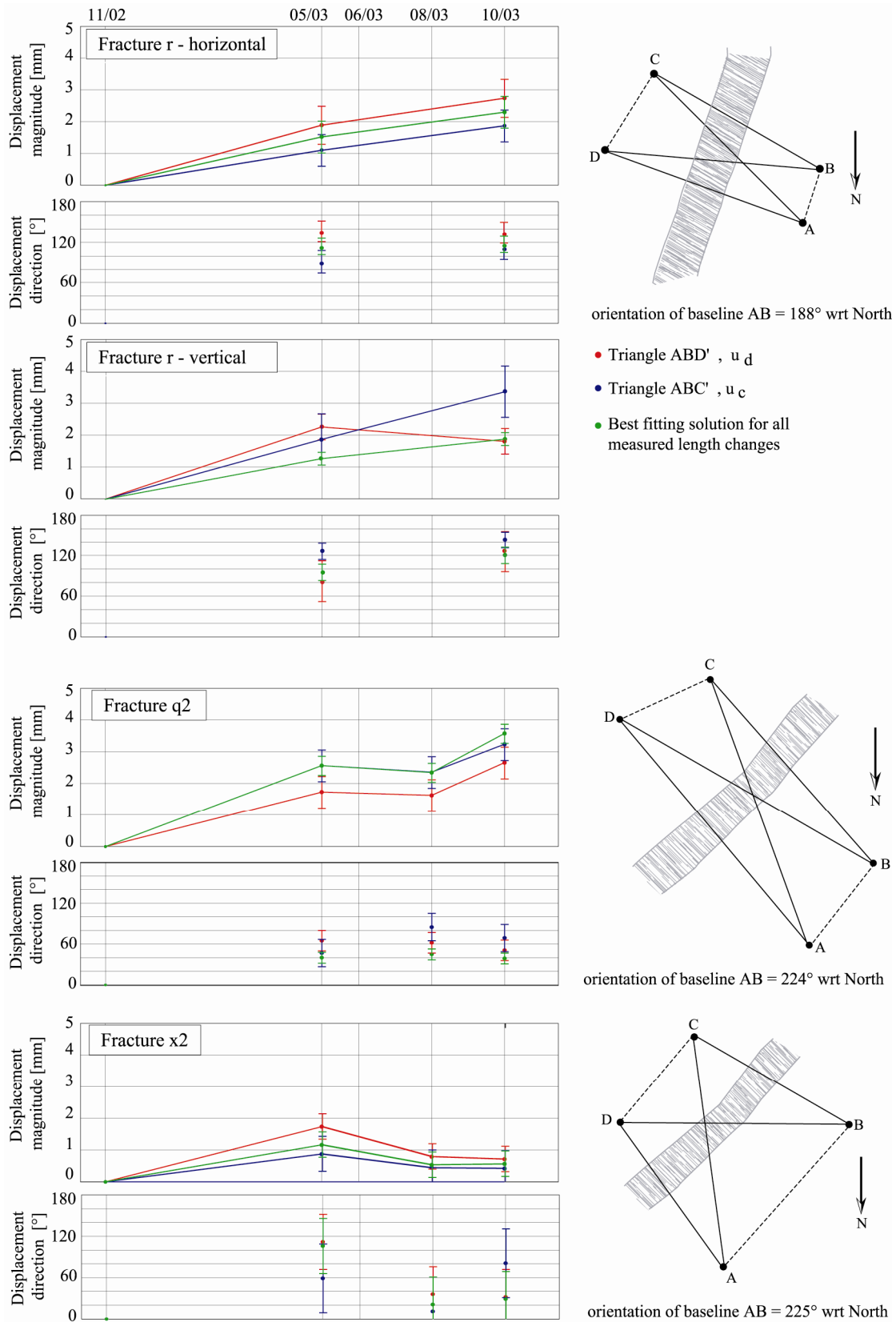


Figure 3-13: Displacement magnitude and direction estimates derived from two different analysis procedures applied to the benchmark quadrilateral measurements at the fractures r, q2 and x2. The geometry of the arrays are shown at right and are essentially horizontal, except for the quadrilateral r-vertical (see Figure 3-11b). The direction of the displacement vectors are measured anticlockwise from the baseline AB looking down. Error bars were estimated by taking an error of 0.15 mm per length measurement.

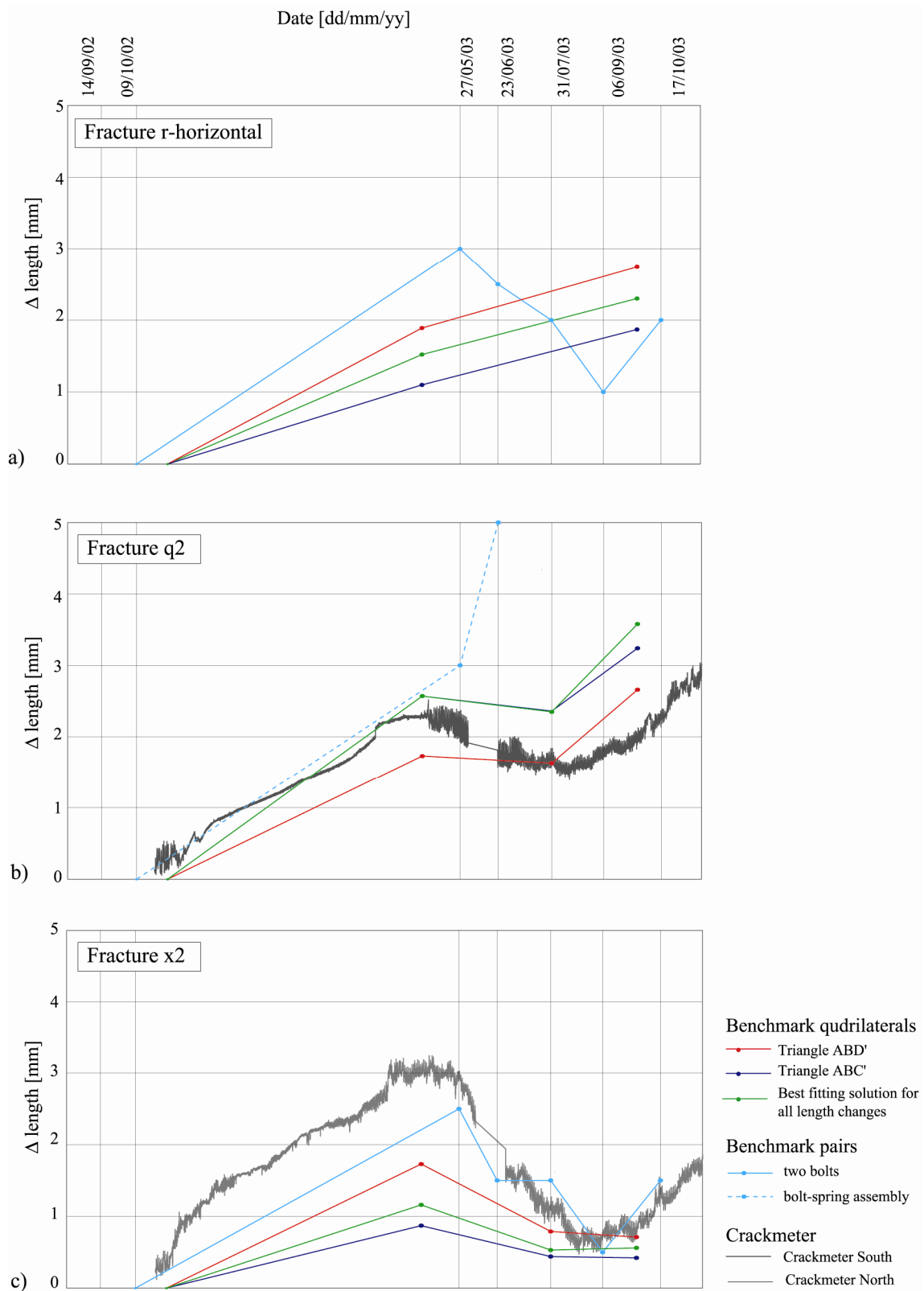


Figure 3-14: Comparison of displacement magnitude estimates from quadrilateral arrays, simple benchmark pairs and crackmeters at three active fractures where multiple measurements were made. The quadrilateral results are from Figure 3-13.: a) results for fracture r; b) results for fracture q2 and c) results for fracture x2.



Figure 3-15: a) Photograph of the inclinometer probe which is 61 cm long. b) Photograph of the 2 m long INCRES extensometer probe being lowered into a casing. (Photographs by E. Eberhardt)

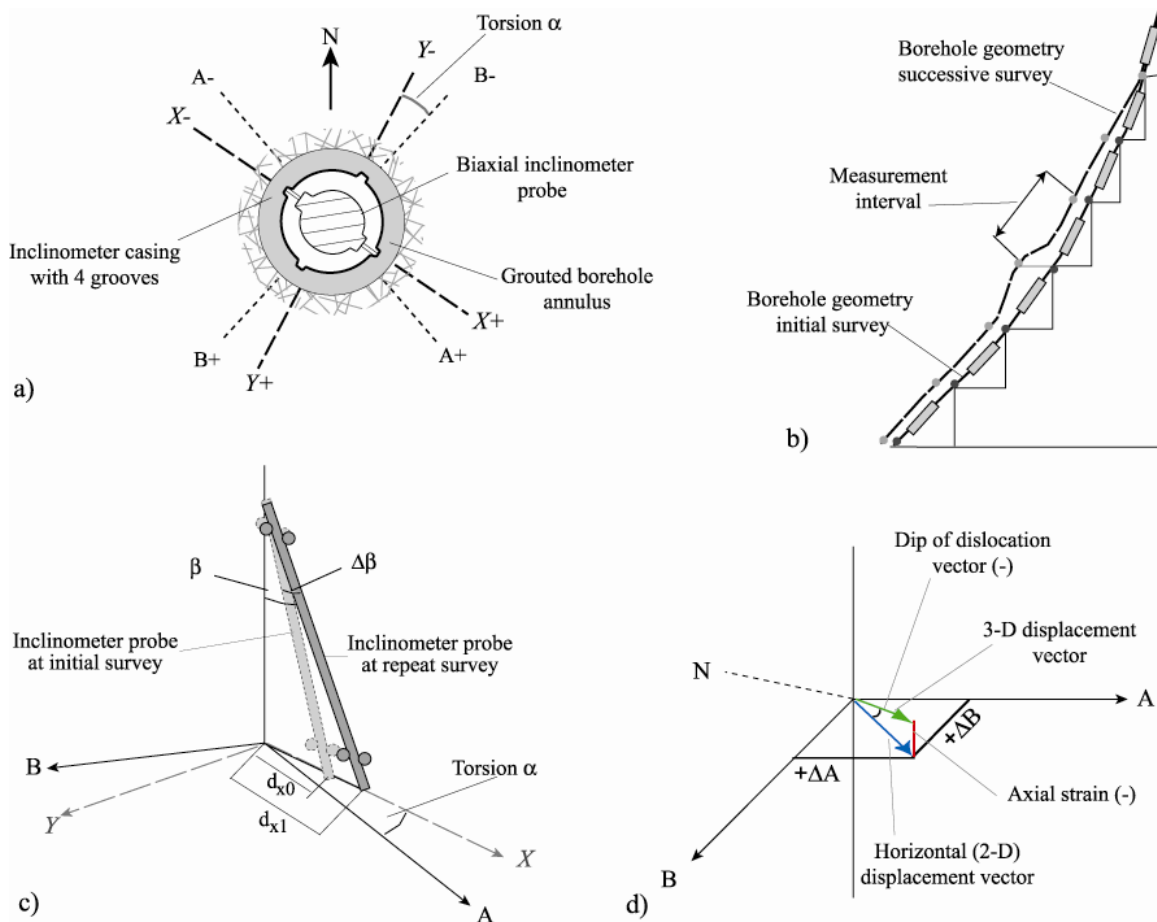


Figure 3-16: Coordinate systems used in the inclinometer/extensometer measurements. a) Top view of vertical inclinometer casing showing the groove pairs. A and B are the groove pairs at the surface and X and Y are the same groove pairs at depth. b) Series of inclinometer measurements which yield the inclination profile along the borehole. c) Illustration of the conversion of inclination change to inferred horizontal displacement vector. An angle change,  $\Delta\beta$ , in the x-direction implies a x-displacement of  $d_{x1}-d_{x0}$ . d) Conventions for deriving the 3-D displacement vector.

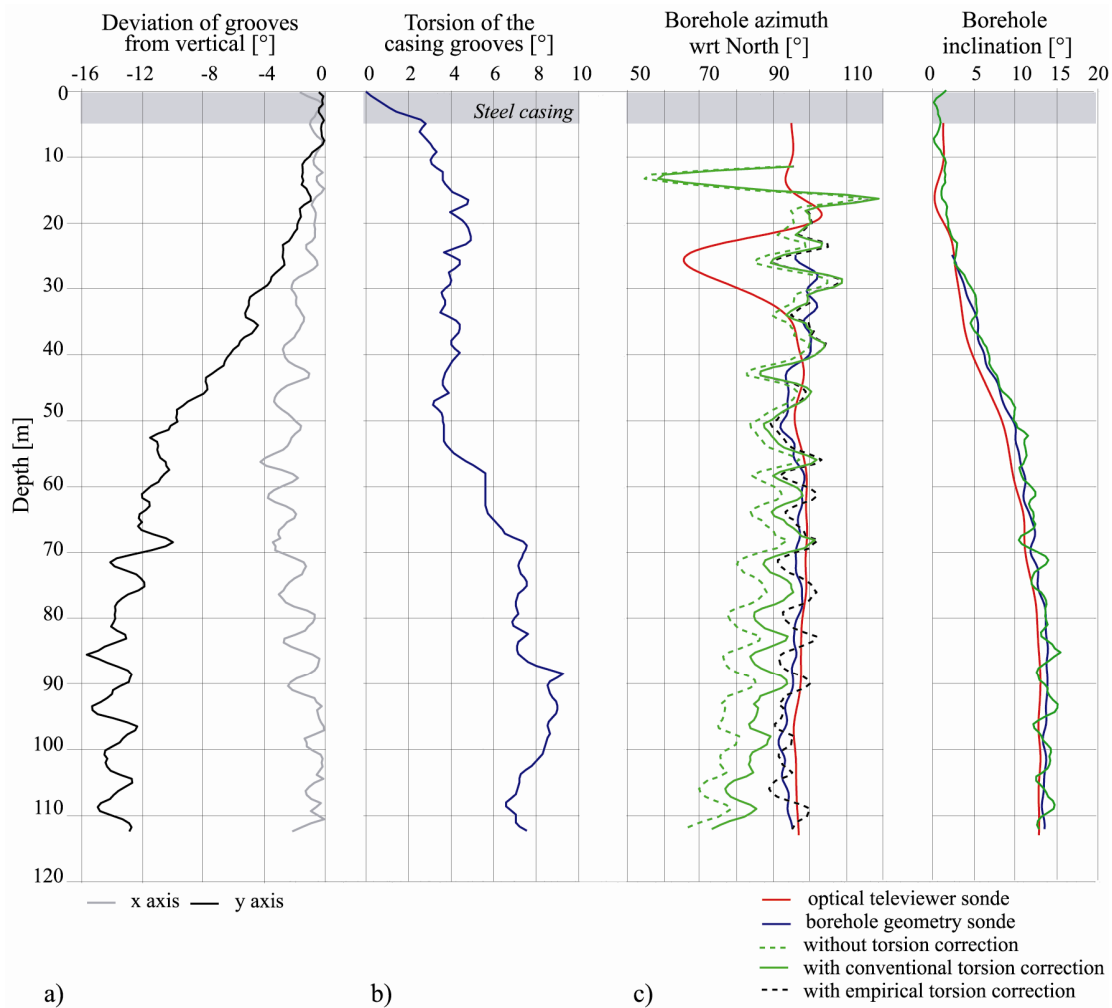


Figure 3-17: a) Raw inclination data (X and Y-axes) of the initial survey of SB 120 expressed in degrees from vertical. b) Torsion profile measured with the spiral probe. c) Borehole trajectory (azimuth and dip) derived from the borehole geometry and optical televiewer logs. The trajectories derived from the raw inclination profiles in (a) are also shown for several different torsion corrections (see legend).

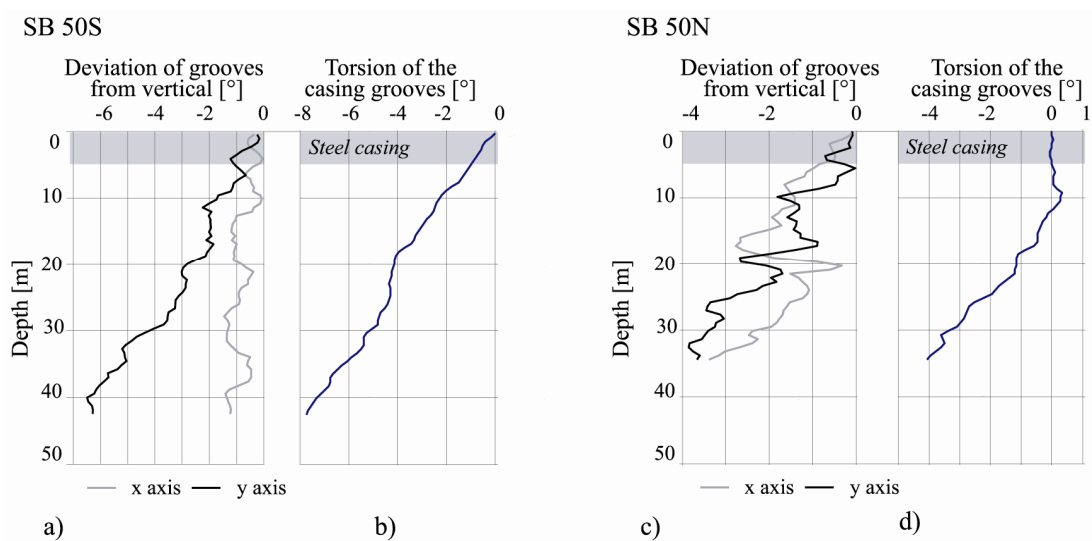


Figure 3-18.: SB 50S and SB 50N raw data. a) Inclination profile of X- and Y-axes in SB 50S. b) Torsion measured with the spiral probe in SB 50S. c) Inclination profile of X- and Y-axes in SB 50N. d) Torsion measured with the spiral probe in SB 50N.

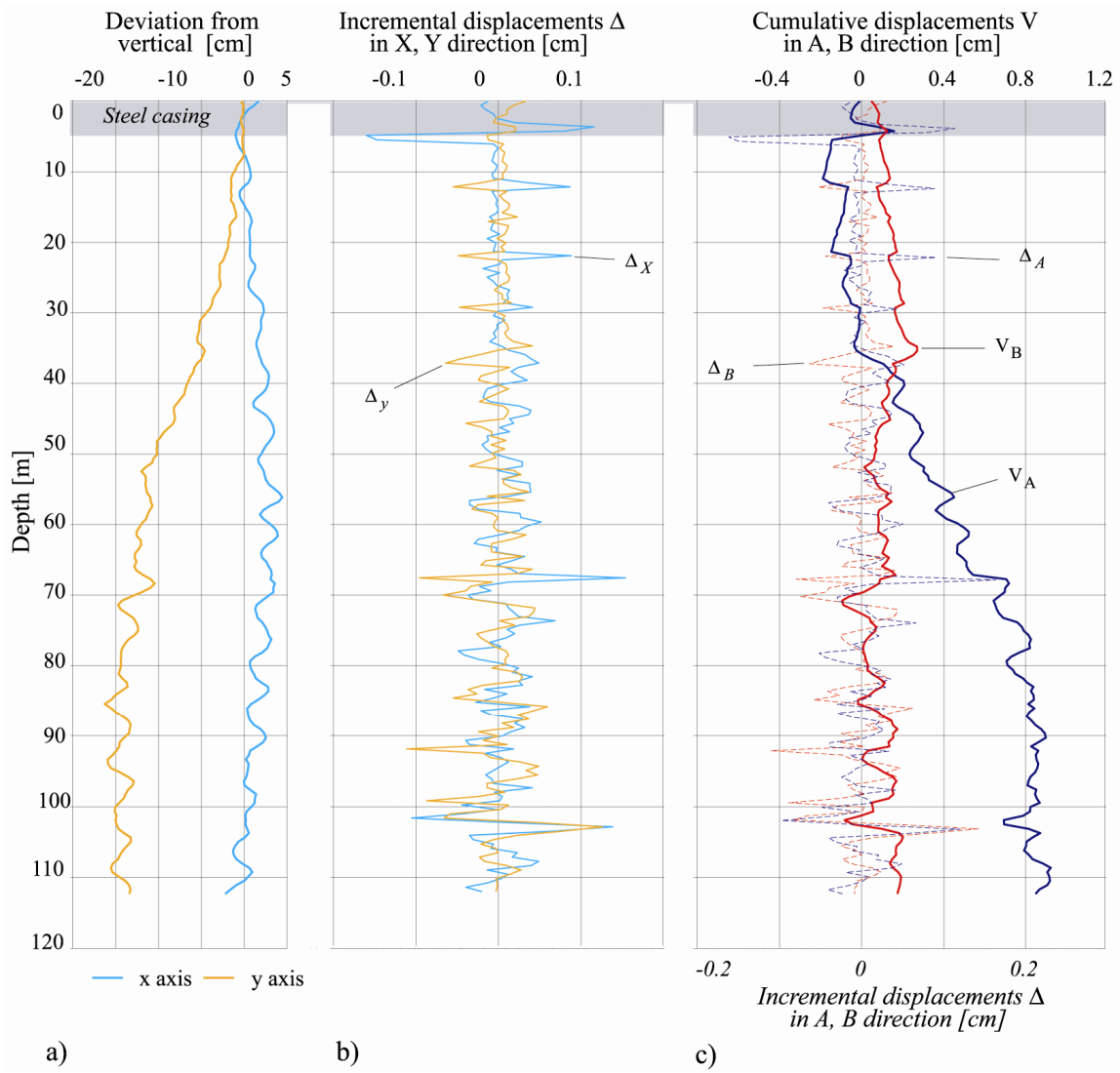


Figure 3-19: Illustration of standard method of inclinometer data reduction for S B120 using first repeat survey. a) Inclination profiles along the local X- and Y axes of the initial survey expressed in terms of deviation from vertical. b) Incremental displacements along the X- and Y-axes developed between the initial and first repeat survey. c) Incremental displacements along the A- and B-axes after rotation using the standard torsion correction (dashed lines). The corresponding cumulative horizontal displacement profiles,  $V_A$  and  $V_B$ , obtained by integration are shown in solid lines.



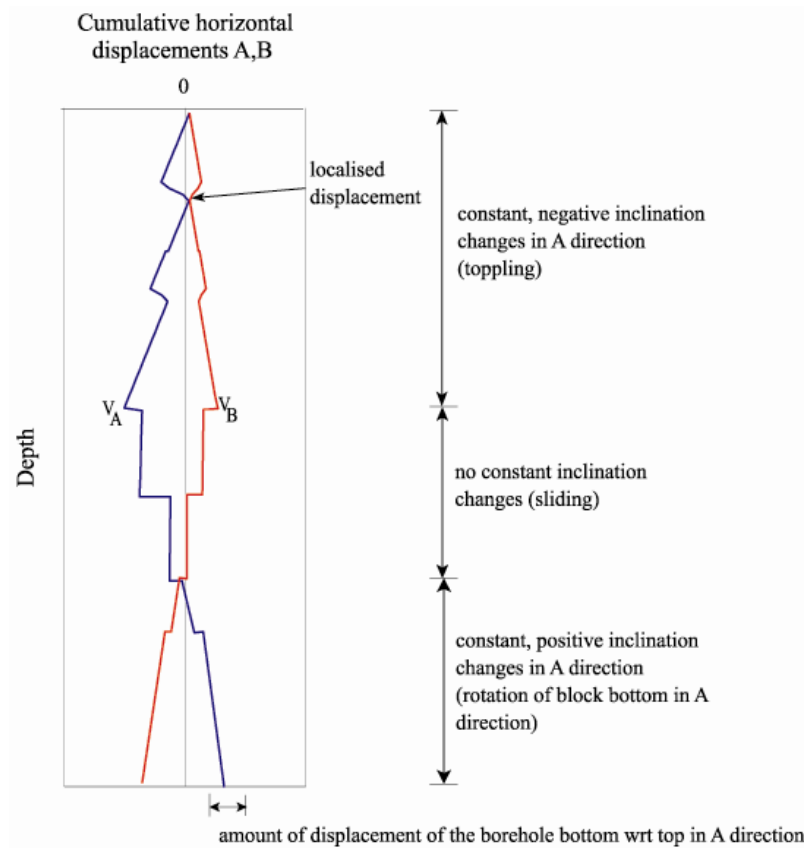


Figure 3-20: Conventions used for the analysis of cumulative horizontal displacement profiles. Steps in the cumulative inclination change curve indicate localised displacements. In crystalline rock, the slope between the steps depends on the presence of constant incremental inclination changes due to different block rotations.

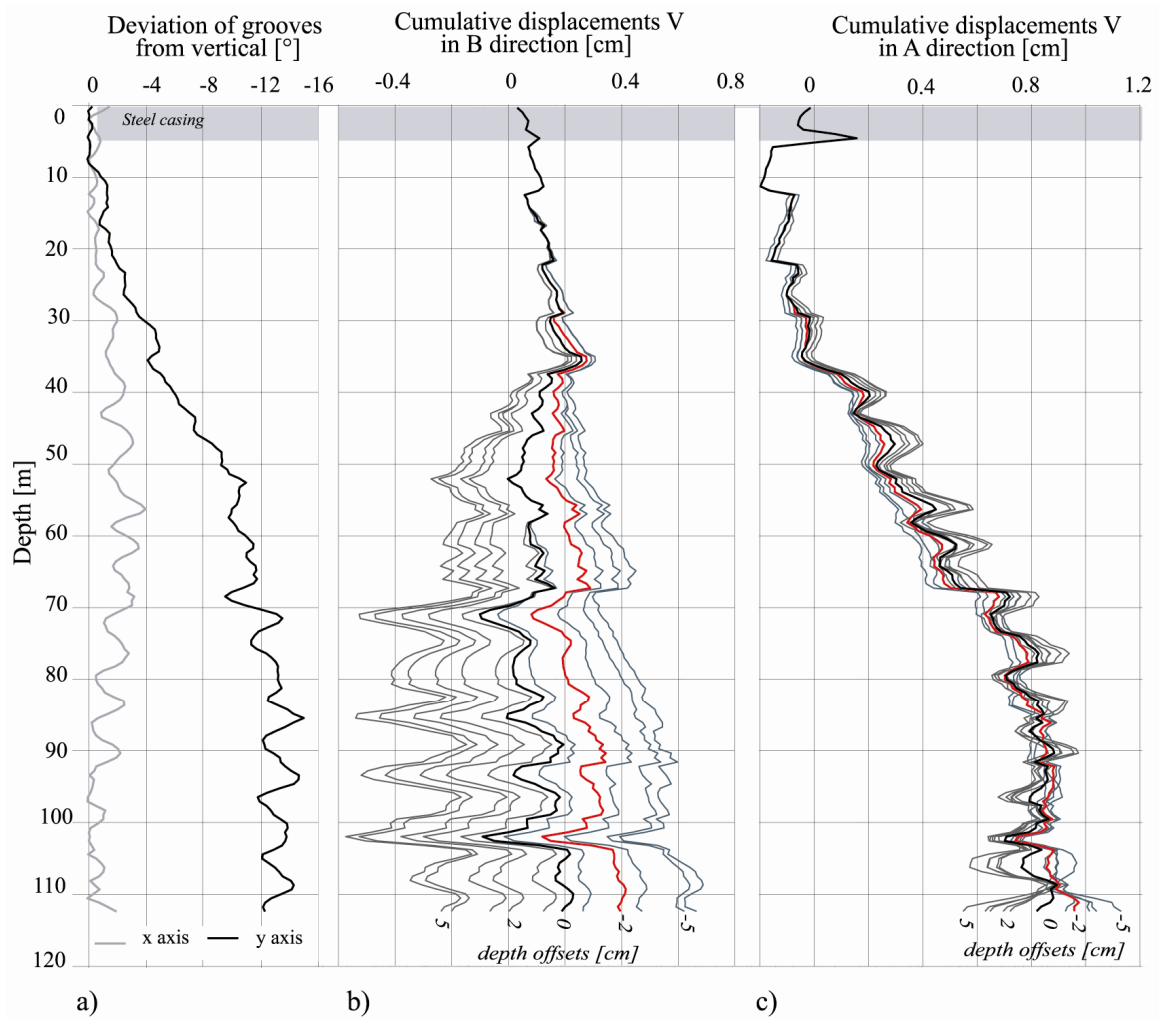


Figure 3-21: Illustration of the depth offset error and its correction for the first repeat survey in SB 120 a) Inclination profiles along the local X- and Y axes of the initial survey b-c) Effects of depth offsets on the cumulative A- and B-axis horizontal displacement change profile. The uncorrected form is shown in black. The grey lines denote the profiles after applying a uniform stretch to the depth scale of the first repeat profile with a range of extensions at the bottom to  $\pm 5$  cm in steps of 1 cm. The profile which best-matches the profile of initial survey was determined by cross-correlation and is shown in red.



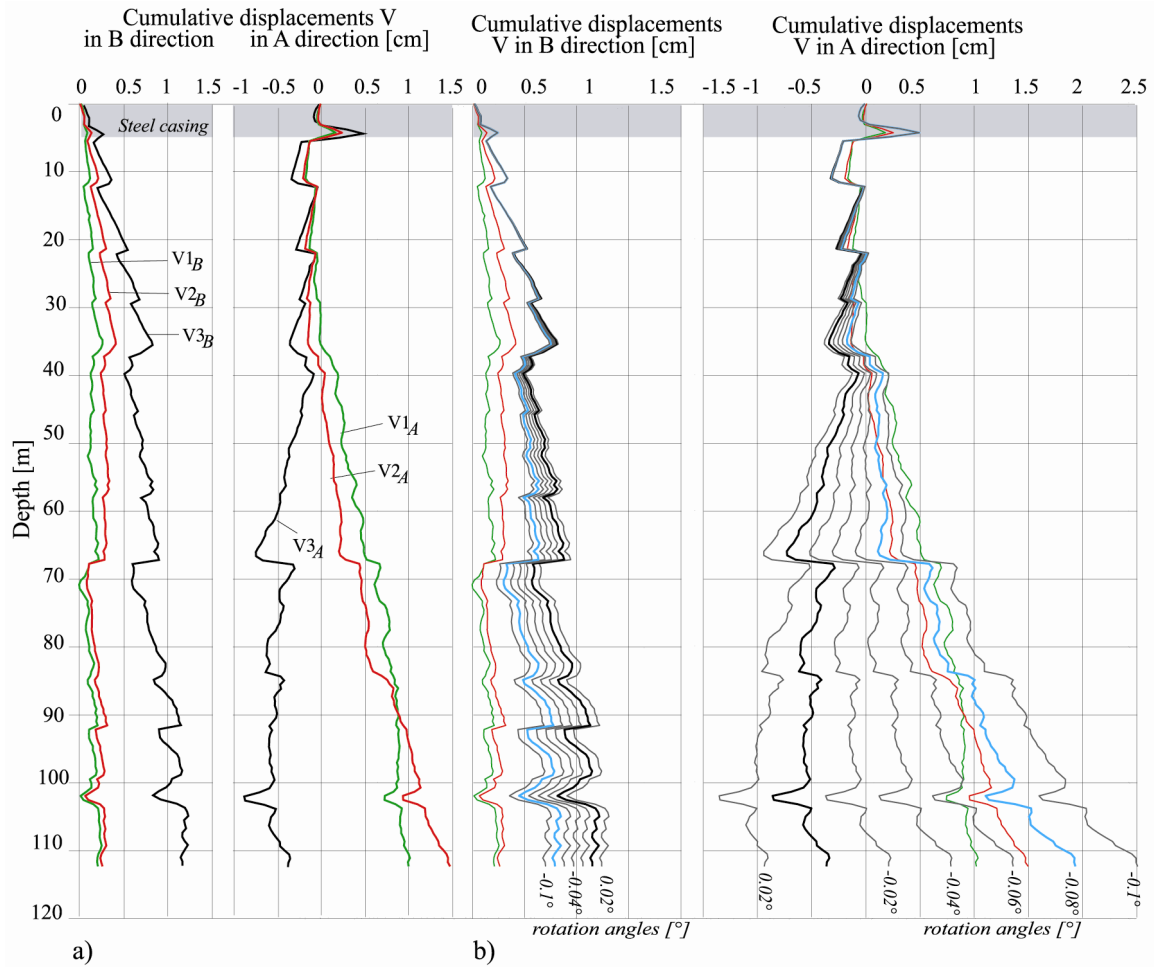


Figure 3-22: Illustration of the sensor rotation error and its correction for the third repeat survey in SB 120. a) Cumulative horizontal displacement profiles in the A- and B-directions for the first (green), second (red) and third repeat surveys after depth offset and empirical torsion correction. b) Effects of sensor rotation on the cumulative A- and B-axis cumulative displacement profiles obtained for the third repeat survey. The uncorrected profiles are shown in black whereas corrected profiles for various rotation angles are in grey. A sensor rotation of  $-0.08^\circ$  (light blue curve) gives a profile that is more in accord with the profiles of displacements obtained in the first (red) and second (green) repeat surveys.

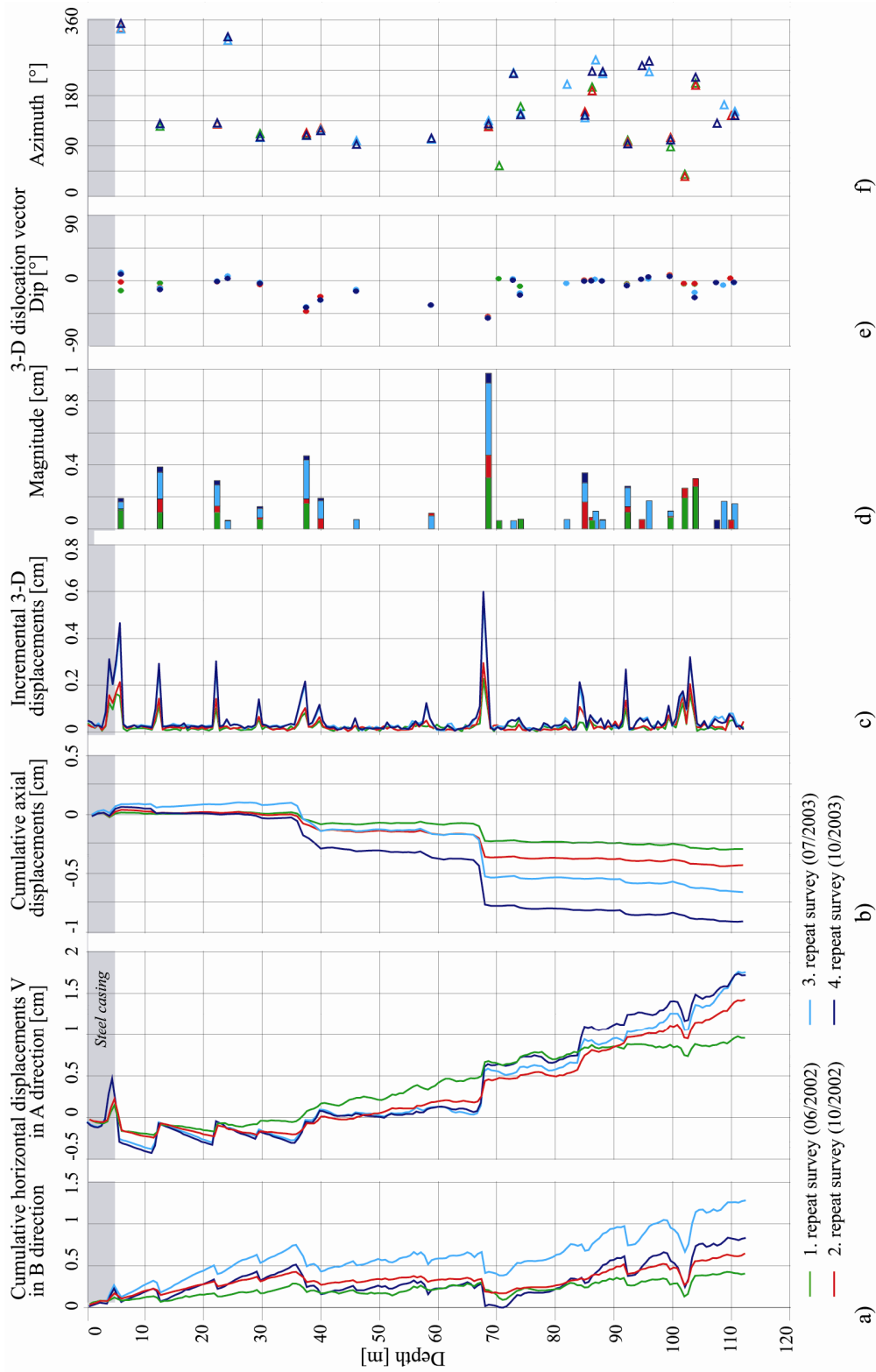


Figure 3-23: Derivation of 3-D displacement vector profiles from the combination of inclinometer and extensometer profiles for SB 120 a) Cumulative horizontal displacement profiles for the three repeat surveys after applying depth offset, sensor rotation and empirical torsion corrections (see Table 1-4). b) Cumulative axial displacement obtained by the INCRES surveys. c) Incremental displacement magnitude. d-f) magnitude, dip and azimuth of the 3-D displacement vector.

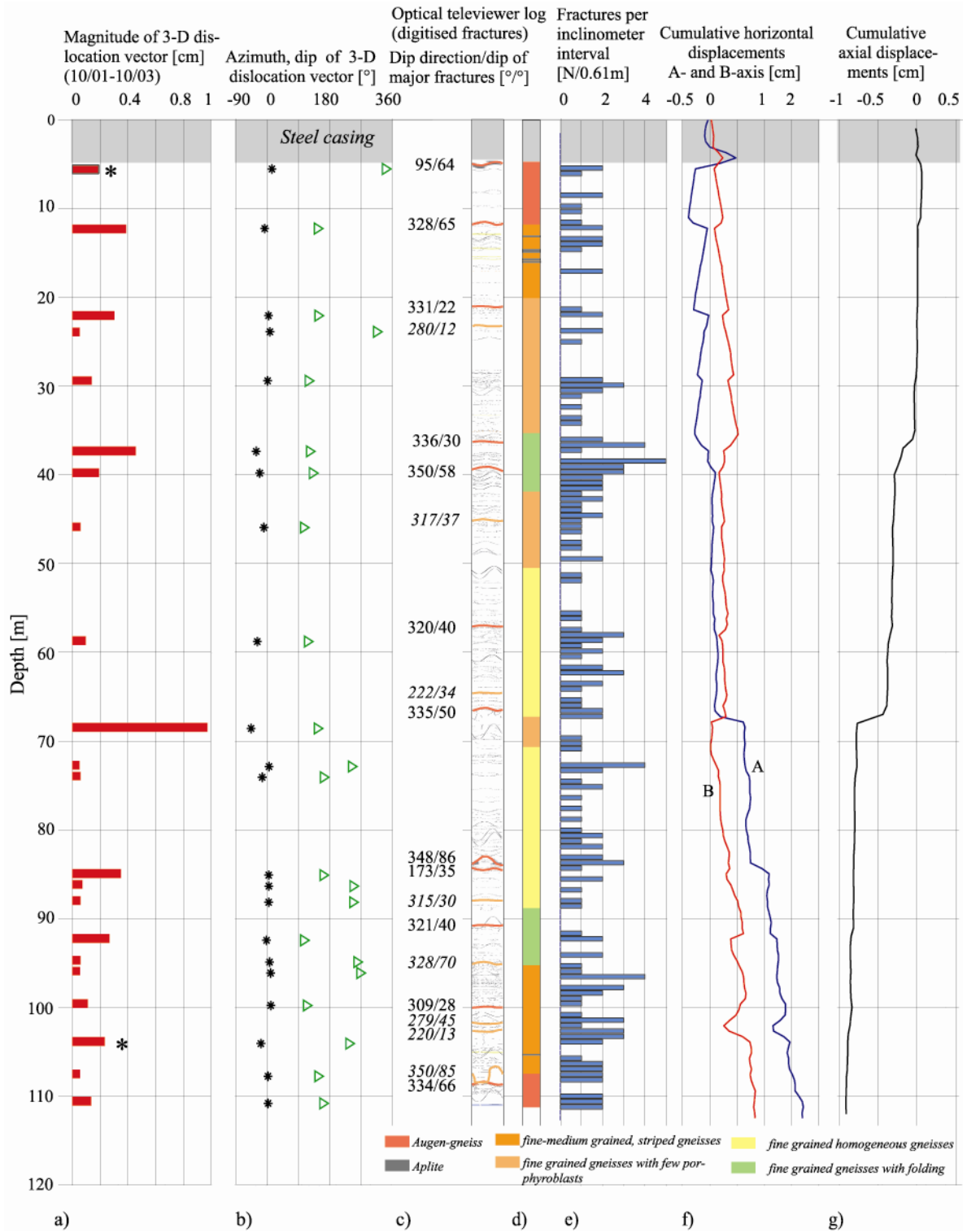


Figure 3-24: Comparison of the 3-D displacement data from the fourth repeat survey of SB 120 with geological data from the optical televiwer images a) Magnitude of the 3-D dislocation vectors across localised displacement zones. b) Orientation of the 3-D dislocation vectors. c) Fracture traces from the optical televiwer images. Major fractures are highlighted and the dip vector given. d) Lithology (see legend for colour key). e) Fracture intensity f) Cumulative horizontal displacement. g) Cumulative axial displacement.

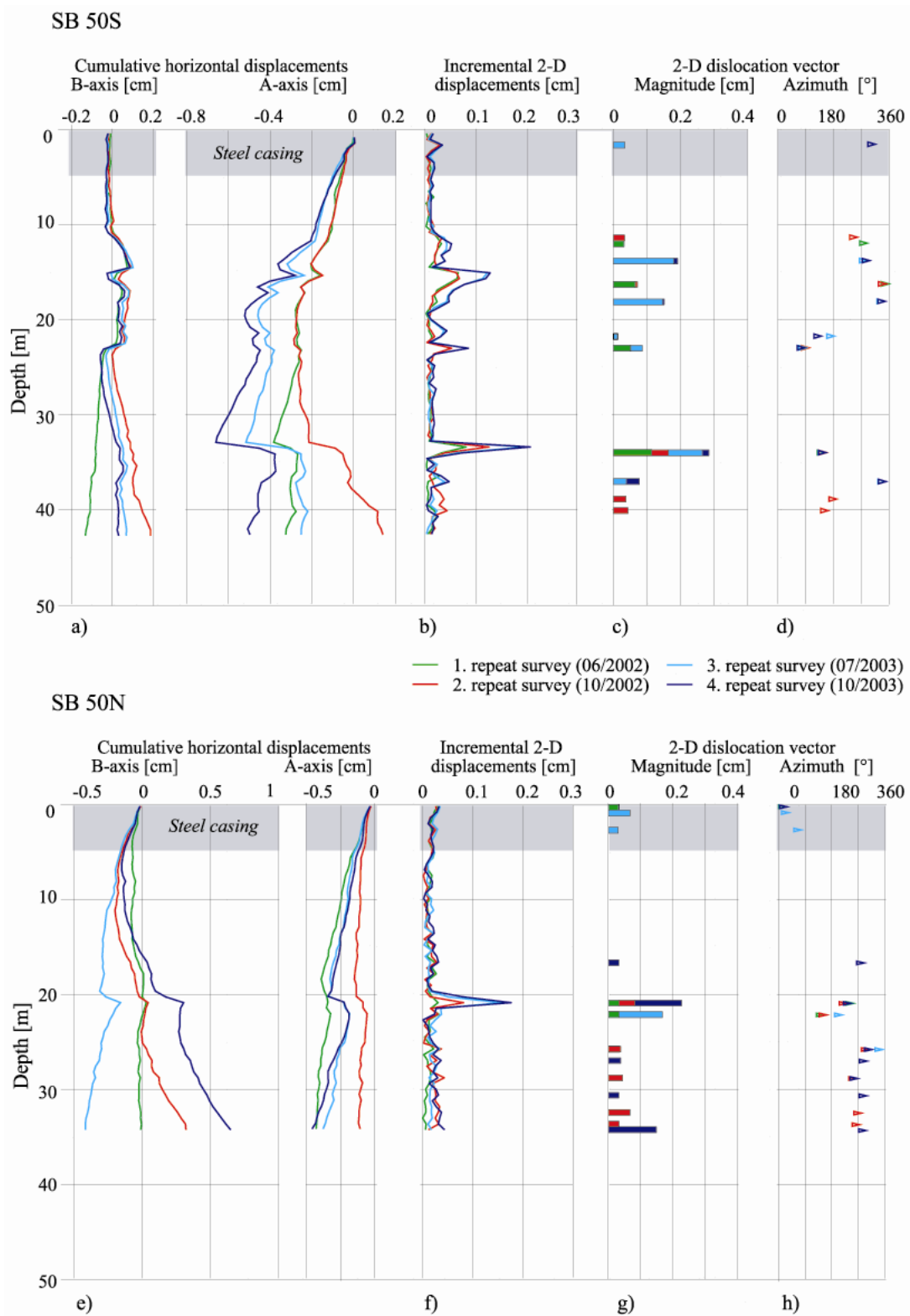


Figure 3-25: Displacement data for SB 50S (top row). a) Cumulative horizontal displacements for the repeat surveys, with empirical torsion correction and application of depth offset. b) Incremental 2-D displacement vector. c) Magnitude of 2-D dislocation vector. d) Azimuth of 2-D dislocation vector. Displacement data for SB 50N (bottom row). e) Cumulative horizontal displacements for the repeat surveys, with empirical torsion correction and depth matching. f) Incremental 2-D displacement vector. g) Magnitude of 2-D dislocation vector. h) Azimuth of 2-D dislocation vector.

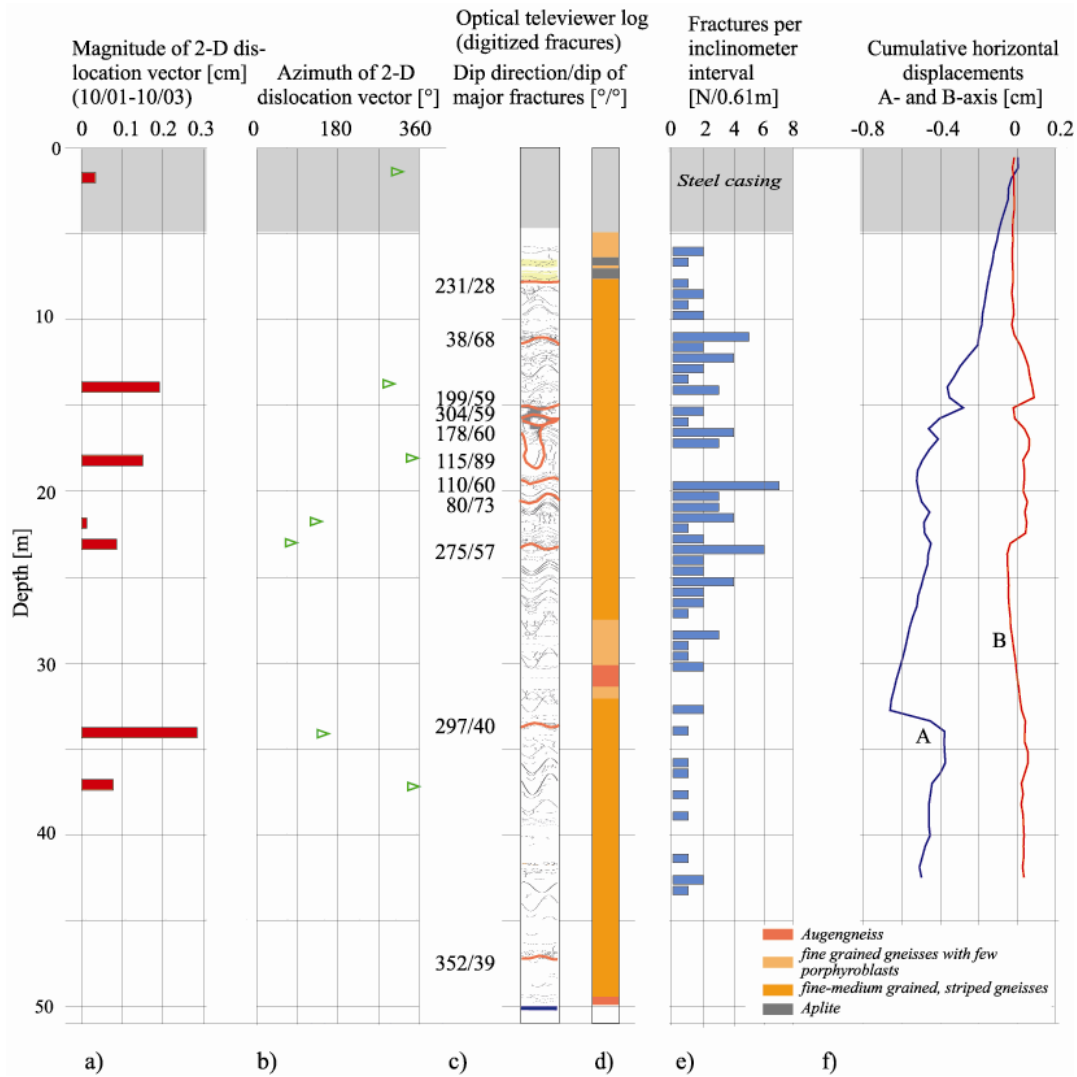


Figure 3-26: Comparison of the 2-D displacement data from the fourth repeat survey of SB 50S with geological data from the optical televiewer images. a) Magnitude of the 2-D dislocation vectors across localised displacement zones. b) Orientation of the 2-D dislocation vectors. c) Fracture traces from the optical televiewer images. Major fractures are highlighted. d) Lithology (see legend for colour key). e) Fracture intensity. f) Cumulative horizontal displacement with empirical torsion correction and depth matching.

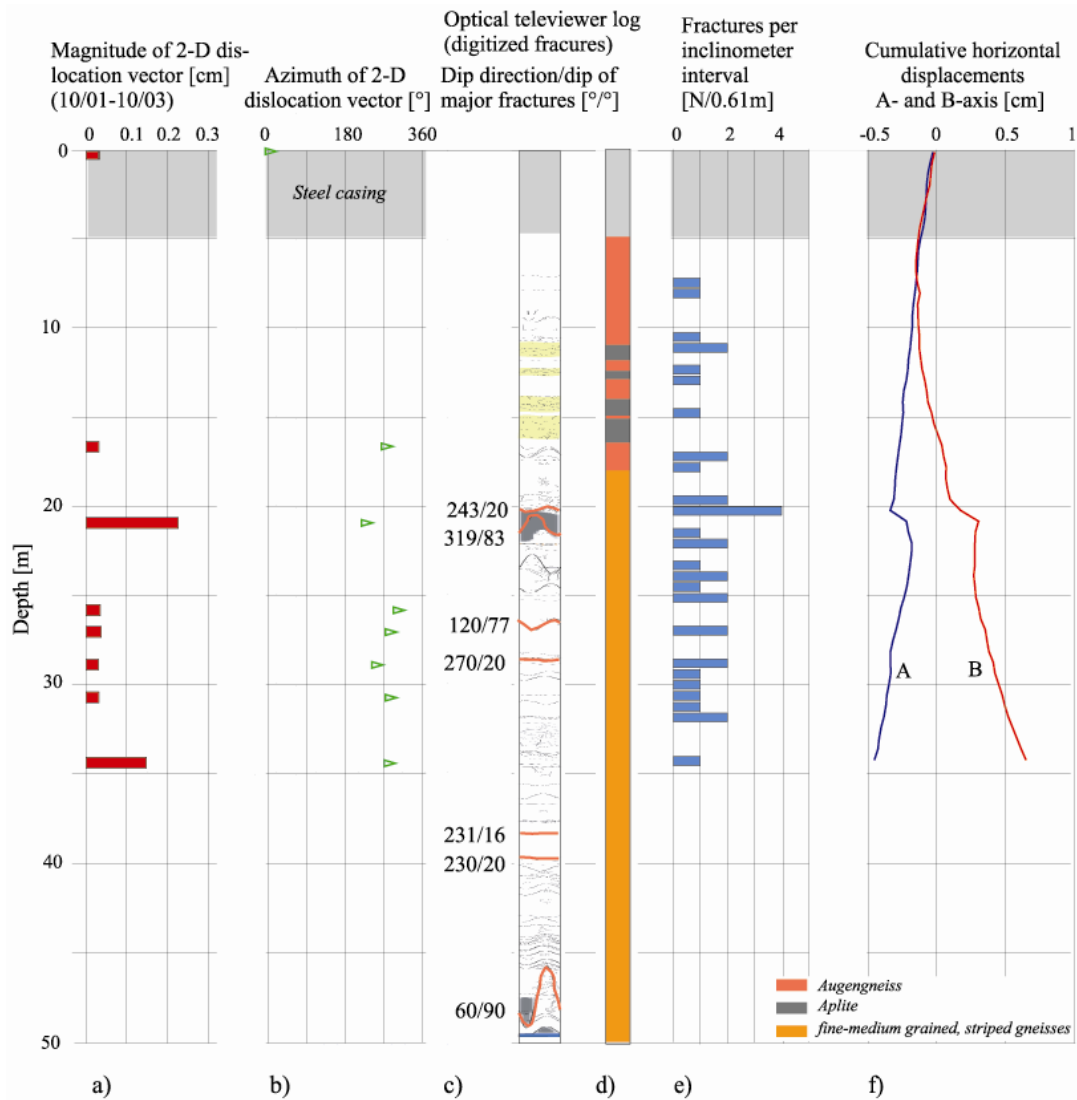


Figure 3-27: Comparison of the 2-D displacement data from the fourth repeat survey of SB 50N with geological data from the optical televiewer images a) Magnitude of the 2-D dislocation vectors across localised displacement zones. b) Orientation of the 2-D dislocation vectors. c) Fracture traces from the optical televiewer images. Major fractures are highlighted. Shaded zones are open fractures. d) Lithology (see legend for colour key). e) Fracture intensity. f) Cumulative horizontal displacement with empirical torsion correction and depth matching.

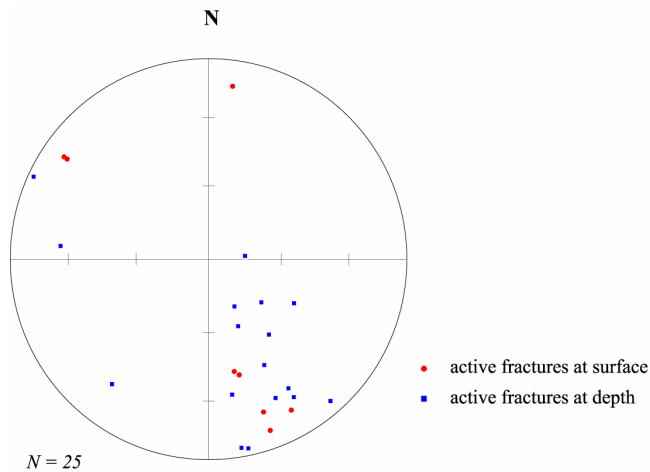


Figure 3-28: Orientation of active fractures mapped on the surface and at depth in the three deep boreholes. Lower-hemisphere, equal-area projection.

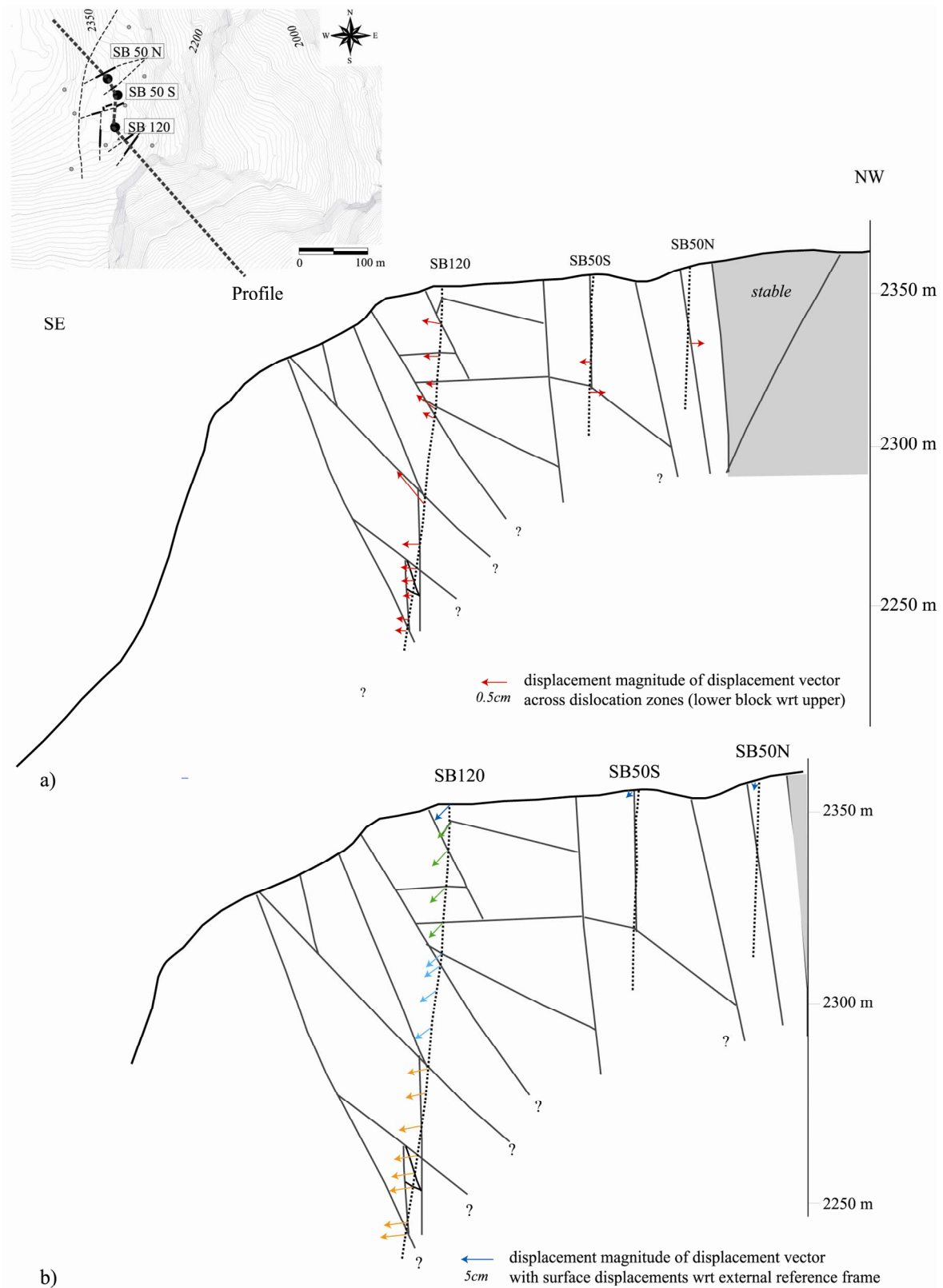


Figure 3-29: 2-D block kinematic model of the investigated rock mass along the profile shown in the inset. a) Relative displacement vectors across dislocation zones, denoting the movement of the lower block wrt the upper. b) Absolute displacement vectors (i.e. expressed with respect to an external reference frame) for points along SB 120 Blue arrows denote surface displacement vectors, green arrows denote toppling of the blocks, light blue arrows translational sliding and brown arrows rotation as determined from the cumulative horizontal displacement profiles. For the two 50 m boreholes neither the surface displacement vector nor the inclination of the borehole displacement vectors are known.

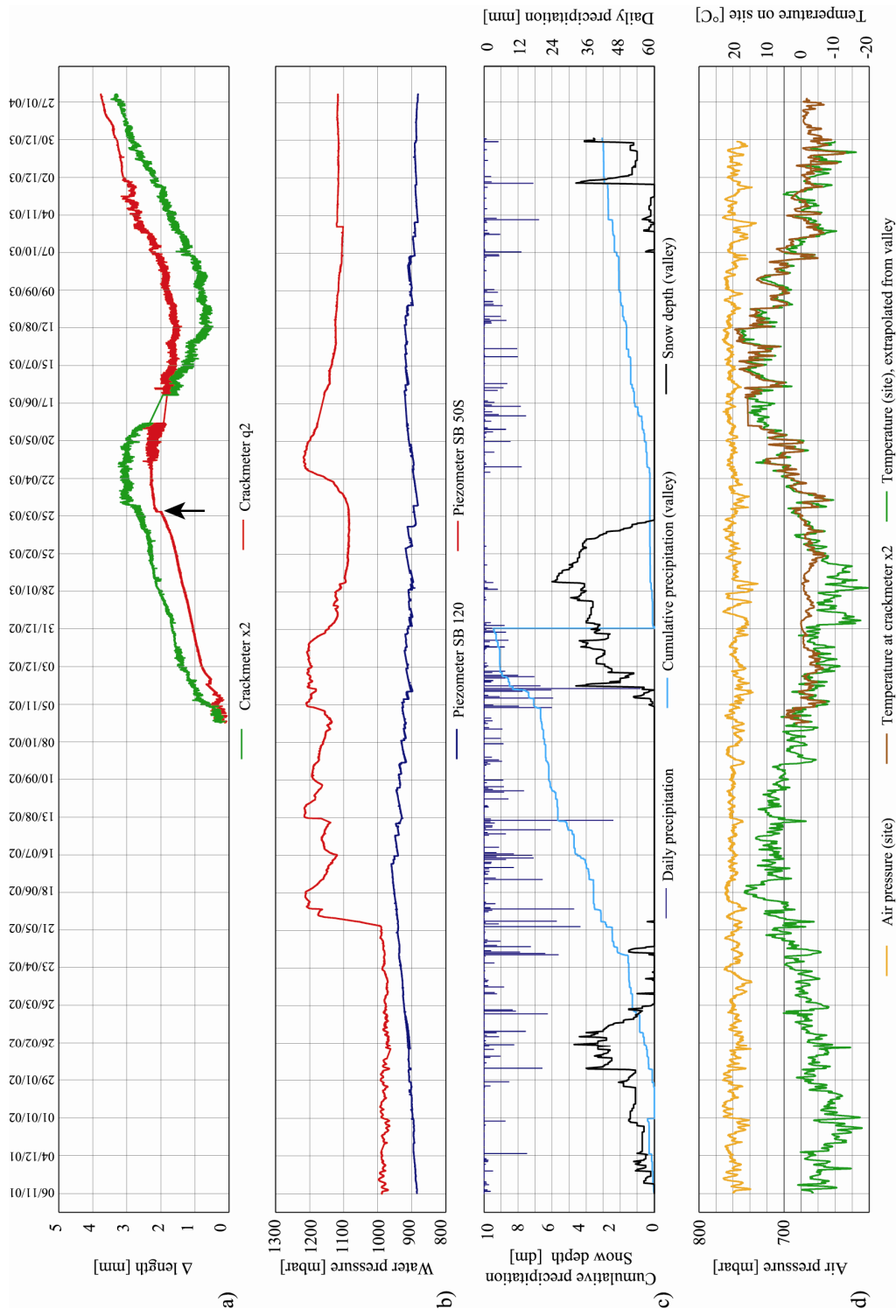


Figure 3-30: Continuous monitoring time series. a) Crackmeter record of surface fracture opening at fractures q2 and x2. b) Water pressure in SB 120 and SB 50S. c) Meteorological data provided by METEOSCHWEIZ: Precipitation (daily and cumulative annual) and snow height measured at Zermatt (station elevation 1638 m), both filtered with a 2-day lowpass filter. d) Temperature at the study site calculated from meteorological data from the valley using a linear temperature lapse of 0.51°C/100m and temperature record of the crackmeter x2. Atmospheric pressure extrapolated to the study site using a pressure lapse of 11.3 mbar/100m.



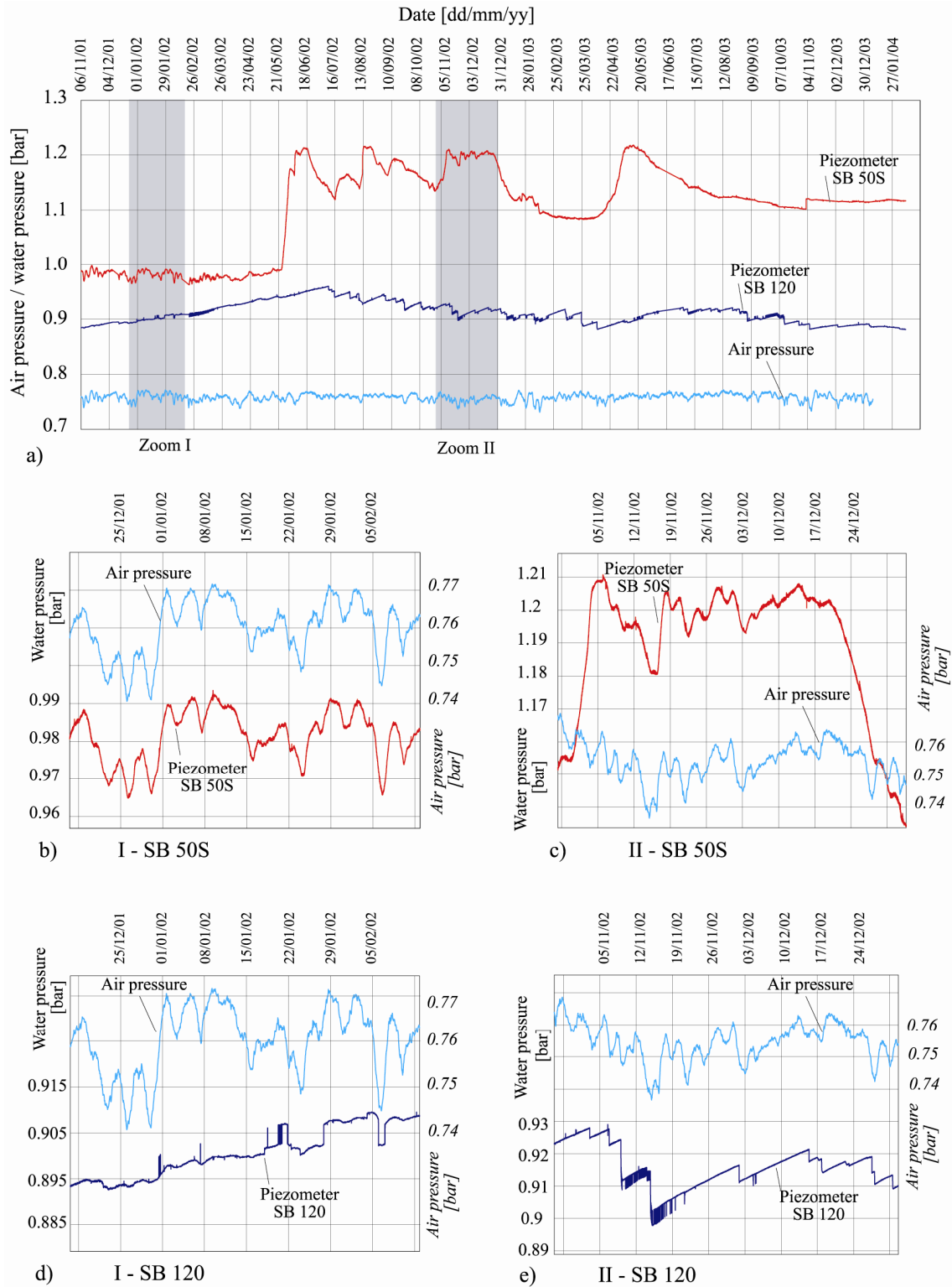


Figure 3-31: a) Piezometer pressure measurements in SB 120 (blue) and SB 50S (red) with atmospheric pressure measured in the valley (data provided by METEOSCHWEIZ) and extrapolated to the study site. b) Expanded view I for SB 50S. c) Expanded view II for SB 50S. d) Expanded view I for SB 120. e) Expanded view II for SB 120. b-e show water pressures (not corrected for atmospheric pressure) from the left (red and blue) and atmospheric pressures from the right (light blue).



#### **4 Modelling the internal kinematics and deformation of a complex rockslide based on field data constraints obtained at the study site**

## 4.1 Introduction

Field reconnaissance, geological and geophysical investigation, and geotechnical monitoring, when combined, helped to provide significant insights into the internal structure and the displacement patterns developing within the unstable crystalline rock mass; nevertheless the location and geometry of the sliding surface remained unconstrained. This chapter focuses on the investigation and evaluation of different slide-surface scenarios for the investigated slope using numerical modelling techniques. The geometry and location of the basal shear surface that separates the unstable from the stable rock mass, and the role of pre-existing fractures in its development is crucial to the discussion of progressive failure processes. As such, the issue of identifying the acting instability mechanisms can only be addressed if the known geological structures and the measured displacement fields can be used to deduce/constrain the location and geometry of the sliding surface(s).

In the described modelling study the question of how characteristic deformation patterns relate to different basal sliding surface geometries is addressed by modelling different instability scenarios for the investigated slope and comparing the obtained displacement patterns with field measurements. This inverse approach is based on results from previous monitoring surveys which suggest that by combining geotechnical monitoring at the surface and depth, characteristic displacement patterns for different block displacement types can be captured (Kovari 1990). As such the chosen approach differs significantly from the classical inverse back-analysis approaches that are used to derive rock mass or shear failure properties where known geometries of the failure planes and displacements are typically used (e.g. Sonmez et al. 1998).

The issue of calculating displacements in a fractured crystalline rock slope limits the choice of applicable rock mass modelling methods. The demands on the modelling technique to be applied include the representation of a highly fractured rock mass and the calculation of displacement patterns induced by movements along discrete fracture planes. Generally, for slope stability analyses involving jointed rock masses, either kinematic analyses, limit equilibrium or numerical methods are used. Limit equilibrium methods only consider the balancing of acting and resisting forces and/or moments, and thus are not able to model the internal deformation of a slope or displacements along a failure plane. As such, these methods are generally restricted to the analysis of simple translational or rotational slides. Similar limitations apply to kinematic analyses that involve stereographic projections (e.g. Norrish & Wyllie 1996, Yoon et al. 2002) or key block theory (e.g. Goodman & Shi 1985, Mauldon & Goodman 1990). Numerical methods are commonly used for modelling rock slope instabilities and the resulting displacements. These methods include finite element modelling, discrete element modelling, hybrid modelling and particle flow codes (Jing 2003). Various case studies on rock slope instabilities have been performed using discontinuum methods like the distinct element method or discontinuous deformation analysis (Coggan & Pine 1996, Hencher et al. 1996, MacLaughlin et al. 2001, Bhasin & Kaynia 2004) and provide valuable information on rock mass deformation depending on the modelled fracture network and sliding surface geometries. These previous studies confirm that discontinuum codes are appropriate tools for the modelling of rock slope displacements, leading to their adoption for this study.

The numerical modelling for the study site was completed using the two-dimensional distinct (i.e. explicit discrete) element code UDEC (ITASCA 2000). For the model generation, detailed informa-

tion regarding the lithologies, the fracture network and the identified displacement-accommodating structures were utilised. The implementation of active fractures at the surface and at depth, in combination with strain recording elements, allowed direct comparisons to be made between the modelled and measured displacement fields.

The first part of this chapter summarises the results of the geological mapping and the geotechnical monitoring results that are relevant for establishing the required model input and rock slope constraints. As the modelled rock mass is located adjacent to the scarp of the 1991 Randa rockslides, the results of previous kinematic and numerical modelling studies focussing on these earlier rockslides (Sartori et al. 2003, Eberhardt et al. 2004, Segalini & Giani 2004) are described. Of particular interest is the question whether model geometries and/or representations of rock mass strength degradation used in these studies are applicable to the modelling of the current slope instability. The following part of the chapter then focuses on a parametric study in which the geometry of a basal sliding surface is varied and the resulting displacement patterns within the rock mass and along simulated boreholes are analysed. By comparing these against measured displacement data, the number of possible instability scenarios for the investigated slope is constrained and reduced.

## 4.2 Site description

As demonstrated through the geological map (Figure 4-1) the unstable rock mass is situated in a sequence of gneissic and partly schistose rocks that are dissected by faults and fracture zones. The map shows seven lithologies distinguished by their mineralogical composition, the dominating grain size, the presence of quartz-feldspar porphyroblasts and the petrographic heterogeneity of the gneisses and schists. For simplicity reasons, these seven lithologies were separated into two groups: Group A includes mostly fine grained chloritic gneisses that are relatively more ductile and often deformed by small-scale folding. Group B comprises feldspar-rich, homogeneous or porphyritic gneisses and the quartz-rich dark gneisses which represent massive, brittle rocks. Rock mechanics testing of samples from both groups revealed different strength properties for the two gneissic rock mass types (see section 2.5).

The fracture network (Figure 4-1b) was found to be dominated by various steep fracture- and fault sets. The foliation, foliation fractures and phyllonitic faults parallel to foliation are dipping favourably away from the valley. Possible sliding planes, dipping to the SE and hence into the valley were found to be scarce.

Displacement measurements at the surface revealed that the displacements are localised on faults and fracture zones. The displacement fields at the surface are plotted in Figure 4-2, combining relative displacement vectors across opening fractures and absolute, geodetically determined surface displacement vectors. The figure depicts that displacement directions to the SE dominate. The dips of the geodetically determined surface displacement vectors vary from 20 to 50°. At the wellhead of SB 50N, where only small displacements were measured, the dip increases to 80° and is oriented to the west. The extension of knowledge of the displacement fields into depth was possible by means of the boreholes. Figure 4-3 shows the results of the inclinometer-/extensometer surveys in SB 120. The graphs to the left show the cumulative horizontal displacement curves which reveal the dislocation zones as steps. The slope of the cumulative inclination change curve could be used to infer rotational

block movements (see section 3.4.6); thus these curves suggested that the upper 37 m are subjected to toppling, the blocks in the middle (i.e. between 37 and 68 m depth) are apparently subjected to translational sliding, whereas those in the lowermost section are rotating with their lower parts being displaced towards the valley. The bars for the magnitude of the 3-D dislocation vector, derived by combining horizontal and vertical displacements, coincide with the location of major fractures in the borehole (Figure 4-3). Analysis of optical televiewer images of the traces of active fractures and geophysical borehole experiments indicated that they represented key faults and fractures zones. The dips of the 3-D dislocation vectors across the active fractures, which denote the dislocation of the lower block with respect to the upper, vary between  $6^\circ$  and  $-51^\circ$  where negative values indicate that the block in the footwall has been displaced upwards with respect to the block in the hanging wall (Figure 4-3a). Figure 4-4 shows the network of extrapolated active fractures along a NE-SW profile with a kink between SB 120 and SB 50S. Most active fractures dip to the NW and strike normal to the profile. In the upper 85 m of SB 120 active fractures were found to accommodate shear movements whose direction in the plane of the fracture lies within  $30^\circ$  of the back-projection of the dip vector of the fracture (i.e. normal fault movement). Below 85 m depth, several fractures exhibit a larger dislocation component normal to the fracture. Also plotted in Figure 4-4 are the absolute displacement vectors along the borehole, derived by adding the cumulative 3-D displacement vectors to the geodetically determined displacement vector of the wellhead. Generally, the dip of the displacement vectors decreases with depth such that at the borehole bottom the blocks are subjected to near-horizontal dislocations.

Based on the aforementioned observations and measurements, the geological structure of the slope and the displacement patterns relating to its instability are well constrained between 2200 and 2400 m elevation. Below 2200 m, information is limited with respect to on-going displacements, their directions and the geological structures accommodating them. This is unfortunate since this depth interval is likely to host the basal sliding plane(s), knowledge of which is important to understand the underlying processes driving the current instability. Thus, the location and the geometry of the basal sliding plane must be constrained by other means. By using numerical modelling, key input for addressing this issue can be gained by searching for the basal sliding surface geometry that best reproduces the measured displacements under the given geological constraints.

### 4.3 Previous modelling studies of the 1991 Randa rockslide events

The results of previous studies based on the 1991 rockslide events were analysed to extract any important information that could be used to provide insights into the kinematics of the current instability or the range of possible geometric configurations of the sliding surface(s) controlling it. Previous studies of the 1991 rockslides include descriptive documentations of the events (Ischi et al. 1991, Schindler & Eisenlohr 1992, Schindler et al. 1993), a structural analysis of the area (Wagner 1991) and a study of the weathering processes within the massive augengneiss body (Girod & Thélin 1998, Girod 1999). Three more recent studies focus on the kinematics and processes leading up to the 1991 rockslides; these three studies include a summarised interpretation of the rockslide kinematics (Sartori et al. 2003) and two numerical modelling studies investigating the failure mechanisms (Eberhardt et al. 2004, Segalini & Giani 2004). The following sections focus on these two numerical modelling studies, which both applied 2-D modelling techniques.

In the study by Segalini & Giani (2004) a key-block analysis based on Goodman & Shi (1995) was performed prior to modelling the 1991 rockslide with the 2-D discontinuum code UDEC. Their models examined the failure dependency on the ground water table within the slope. The 2-D section along a NW-SE profile (marked in Figure 4-5) is shown in Figure 4-6b. The model includes persistent fractures dipping moderately towards the valley and steep fractures that dip as well towards the valley. In contrast, Schindler et al. (1993) identified the NE-SW striking fractures as being active before the rockslide based on displacement monitoring data before the second major rockslide event (Ischi et al. 1991). These NE-SW striking fractures however dip away from the valley and should be included in the 2-D models, especially as they are less oblique to the chosen modelling sections. Furthermore simplifying the triggering mechanism to one solely controlled by increasing water pressures is questionable, as the analysis of the meteorological data prior to the 1991 rockslide events revealed no unusually large precipitation or snow melt events (Eberhardt et al. 2001). Given these drawbacks the study of Segalini & Giani (2004) did not offer any notable input constraints that could be used for the modelling of the present-day instability.

In the studies presented by Eberhardt et al. (2004), 2-D finite-element, distinct-element and hybrid finite-/discrete-element codes were used to model progressive failure in crystalline rock slopes using the Randa rockslides as a working example. The focus of this modelling study was directed towards the conceptualisation of progressive rock strength degradation and worked mostly with simplified assumptions of the rock mass properties. For these modelling studies a WNW-ESE striking section was chosen comparably to the profile of Segalini & Giani (2004). For the discontinuum modelling in UDEC, Eberhardt et al (2004) chose a fracture geometry with one persistent fracture set dipping with  $50^\circ$  towards the valley and a sub-vertical set (Figure 4-6a), which is comparable to the profile used in the study of Segalini & Giani (2004). The failure was modelled by decreasing joint cohesion. In contrast, both the finite- and the hybrid finite-/discrete-element modelling approaches used in the study were applied to a homogeneous rock mass without including lithological variations or fractures. The finite-element models by Eberhardt et al. (2004) were run to investigate the influence of deglaciation on stress changes and damage processes in the slope resulting from over-steepening. On the basis of the obtained deformation distributions in the slope Eberhardt et al. (2004) suggested that the instability promoting fractures might have developed due to stress changes within the slope after deglaciation. The hybrid models focussed on modelling the progressive development of the slide surfaces of the 1991 rockslides. By varying the fracture constitutive models (i.e. combined Mohr-Coulomb/Rankine crack or Rankine rotating tensile crack) the generation of sub-vertical tension fracture, or  $40\text{-}50^\circ$  inclined tensile, stress-relief fractures dipping towards the valley was modelled respectively. On the basis of these results Eberhardt et al. (2004) concluded that pre-existing, persistent fractures dipping towards the valley were not necessary for the development of the failure. This conclusion, together with the field mapping results, justify including non-persistent sliding surface geometries in the modelling study of the current instability. However, the transfer of other attributes of Eberhardt et al.'s (2004) model geometries for the 1991 event to the analysis of the present-day instability is limited by their simplifications in representing the rock mass. The first limitation is based on the fact that the section is oblique to the direction of movement and the active fractures of the present-day instability. It should also be noted that the topography used for the models by Eberhardt et al. (2004) does not follow the U-shape form below the valley fill sediments as described in Schindler et al. (1991). However, for the modelling of the present day instability, which is situated more than

500m above the valley floor, this should not play an important role. The second limitation is linked to the observation from field mapping that fractures parallel to the failure surface of the second 1991 rockslide occur mainly in combination with foliation-parallel faults in the more brittle gneisses, suggesting a tectonic origin rather than stress relief fractures.

To summarise, several key differences were found between the geometrical frameworks of the models of the 1991 rockslides and the geometry of the current instability as suggested by field investigation results. As a result, transferability of the previous modelling results to the study of the present-day instability was limited.

## **4.4 Modelling internal deformation of an unstable slope in dependence on the geometry of the basal sliding surface(s)**

### **4.4.1 Modelling task**

The task of the modelling study was aimed at deriving characteristic displacement patterns for the investigated slope as a function of the geometry and location of the basal sliding surface. The modelling procedure began with the development of a block kinematic model established on the basis of mapping, geophysical investigations and displacement surveys in the boreholes. As such, it was determined that the modelled block structure in combination with varying sliding surface scenarios must account for both translational and rotational block movements in order to match the displacement fields measured by the inclinometer/extensometer system. On the basis of this model setup, the fit of the modelled displacement patterns with the measured ones could be compared. However, the models were not intended to exactly match of the measured displacement magnitudes and rates. The criteria for the quality of the fit between the modelled and measured displacement fields are the following:

- generally the surface displacement vectors dip 20-50° from horizontal; only those close to the back scarp dip at 80°;
- along the 120m deep borehole, the top part is affected by toppling, the middle part is sliding without rotation and the bottom part is situated in a block with the lower part rotating towards the valley with respect to the top part;
- active fractures along the 120 m deep borehole accommodate shear movements; only some fractures below 85 m show a significant component of opening.

As the described modelling task is considered as a kinematic problem, a representation involving fully interconnected fractures was regarded as adequate. Another simplification involves restricting the dimensionality of the problem to 2-D, an assumption which can be justified by the approximate alignment of the dip direction of the active fractures, the displacement vectors across them and the geodetically measured surface displacement vectors. For the modelling, a 2-D section through the 120 m deep borehole was chosen with an orientation perpendicular to the active fractures, the assumed sliding plane(s) and parallel to the measured displacement vectors. Accounting for the orientation distribution of the active fractures (Figure 4-2b) and the measured displacement vectors (Figure 4-2a), a NW-SE trending section was considered suitable as depicted in Figure 4-5 and is an extension of the profile shown in Figure 4-4. The model section is shown in Figure 4-7, where the existing geo-



logical information is included in the form of the two distinguished lithological types A and B as well as the location of the active fractures. The models were calculated without ground water, even though the borehole piezometer data described in section 3.6 indicated the presence of small perched groundwater tables.

#### 4.4.2 Theoretical background

For the numerical modelling the distinct-element code UDEC (ITASCA 2000) was used. This code allows for modelling of the rock slope as a discontinuum, explicitly incorporates numerous fractures, hence it is well applicable to the modelling of large block displacements and rotations. As such, it was considered the best-suited tool for the described modelling study.

In UDEC, the modelled discontinuous medium is represented in the form of an assemblage of solid blocks that are separated by interfaces along which contact forces and displacements are calculated (Cundall & Hart 1993, Hart 1993). UDEC is therefore restricted to interconnected fracture geometries. The solid blocks themselves can be modelled as either rigid or deformable; in the case of deformable blocks, they are discretised into a triangular finite difference mesh. The block behaviour can be chosen to follow different block constitutive models, which include the linear elastic and elastoplastic Mohr-Coulomb models used in this study. The rock joints are modelled as contact points along the block interfaces. The movements of the block system result from applied loads or forces. The resulting displacements at the contacts, obtained by a Coulomb-slip joint area contact model, are used to derive the contact forces and the motions and deformations of the blocks according to a force-displacement law and Newton's second law of motion (Hart 1993). The distinct element code performs its calculations in small time steps such that the disturbances due to the applied loads and forces are calculated for each discrete element separately. As this time-stepping procedure is not based on real time but the calculation cycle itself (which is a function of the internal block displacements and degrees-of-freedom between blocks), the calculated displacement rates are not true velocities but are related to changes between time steps (i.e. they represent relative velocities between blocks).

#### 4.4.3 Modelling inclinometer/extensometer in UDEC

Inclination changes and axial strain along the borehole trajectories can be simulated in the models in order to directly compare them against the field-based in situ inclinometer-/ extensometer measurements. To this end, cable-elements are available in UDEC to model reinforcing anchors which can be adapted into strain recording anchors capable of recording horizontal and vertical displacements along a linear element with variable segment lengths. For each of these segments the displacements resulting from the block deformation is calculated. Another alternative is to record linear strains along a series of history points for which the displacements of the closest grid-points could be plotted by means of interpolation. This more traditional method however is not able to clearly distinguish block rotations and displacements across active fractures, unless the size of the mesh elements is significantly decreased. This would then lead to increased calculation times. Due to these drawbacks, the cable-elements were used to predict borehole displacement profiles.

The use of the cable-elements, however, required material inputs representing steel and grout. To compensate for this, the cross sectional area of the "steel" was set to 1 mm<sup>2</sup>, and the density of this

element to 2700 kg/m<sup>3</sup> and its Young's modulus to 10-11 GPa (representative of the gneisses). Whereas the shear stiffness of the grout was set to 1 GPa, the two remaining parameters, i.e. the shear strength of the grout and the steel tensile yield force, had to be adjusted for each model run. This adjustment was necessary to obtain strains in the cables that corresponded to the block displacements and deformations. Small variations of these two parameters were found to introduce spikes in the cable strain data that could not be explained by the movements of the blocks adjacent to the cable. These noise spikes are possibly related to the unusual cable element lengths required, ranging from 120 to 420 meters. Those spikes that could not be avoided by adjusting the cable yield force and grout shear strength, had to be accepted as "artefacts" in the corresponding model-inclinometer plots. Before the final implementation of these cable elements, comparative runs were made with and without cables to ensure that their influence was insignificant with respect to the modelled displacement patterns and magnitudes.

#### 4.4.4 Modelling methodology and considered scenarios

Based on the lithological composition and the network of active fractures shown in Figure 4-7, additional fractures and the basal sliding surface were added to the model. Displacement patterns were modelled for four general modes of rock slope failure that are distinguished by the geometry of the sliding surface: planar, circular, bilinear and step-path. These four geometries represent those most commonly used in rock slide failure classifications (Norris & Wyllie 1996), with the exception of wedge-type translational slides (the analysis of which is a 3-D problem) and toppling mechanisms. The four rock slide types considered are shown in Figure 4-8. By focussing on these four scenarios, it is hoped that numerical modelling can be used to provide significant insights into the displacement patterns associated with the sliding surface geometry. However, each of the models represents only one of numerous geometries that could be obtained by varying the location and inclination of the sliding surface(s) or by varying the number, orientation, extent, spacing and persistence of the chosen fracture sets.

The first model (*Case I - planar sliding surface*) is characterised by a single through-going fracture that represents an extension of the moderately inclined failure surface of the second 1991 rockslide event. In the second model (*Case II - circular sliding surface*) a large circular sliding surface was included in the model in order to test whether the block rotations indicated by the inclinometer survey could be reproduced in the model. The depth of the circular sliding surface was set such that all reflectors of the geodetic survey which indicate surface displacements are situated above the sliding surface. The enclosed rock mass was dissected by additional steep fractures with dip directions away from the valley. These fractures represent the set of faults and fracture zones with moderate to steep dip angles that were found to accommodate the internal deformation. In model *Case III - bilinear sliding surface*, two inclined sliding planes (with 20 and 80° dip) form an open hinge. This model was chosen as it represents a more plausible failure geometry than the circular sliding surface, since some of the surface displacement vectors recorded in the lower part of the unstable rock mass are dip at approximately 20° towards the valley. However, field investigations did not give evidence of a large sliding surface with such an orientation. As in the previous model, steep fractures were added. The fourth model (*Case IV - stepped sliding surface*) incorporates a network of three fractures sets: one dipping towards the valley, one sub-horizontal set resembling the foliation fractures and one set dipping

steeply away from the valley. All fracture sets have limited persistence. Thus, the sliding surface has to step through these various fractures. As such this fourth model is closer to the mapping results which suggest the absence of large through-going fractures or faults that dip towards the valley.

Each model was run with three different block representations: a) with linear elastic blocks; b) with linear elastic blocks dissected by an additional sub-horizontal fracture set that represents foliation fractures; and c) with elasto-plastic intact blocks obeying a Mohr-Coulomb yield criterion. In the latter case, the incorporation of elasto-plastic yielding allowed the different strength properties of the two gneiss types to be included in the model. The measured strength properties of the intact samples from both gneiss types were decreased to incorporate the strength reduction due to the presence of the small-scale fracture network within the blocks. In addition it should be noted that the representation of the foliation fractures as sub-horizontal fractures (cases b) is a simplification of what is really a 3-D situation, since the foliation dips to the W at 25° and hence perpendicular to the model section. Below the unstable section of the slope, large blocks were modelled as being elastic to make the calculation procedure more efficient. In total, twelve different model combinations were analysed based on the four failure mode geometries and the three different material representations of the intact blocks (Table 4-1).

Table 4-1: Modelled instability scenarios.

<i>Geometry of the sliding surface</i>	<i>Elastic blocks</i>	<i>Elastic blocks with foliation fractures</i>	<i>Elasto-plastic blocks</i>
<i>Planar sliding surface</i>	<i>I a</i>	<i>I b</i>	<i>I c</i>
<i>Circular sliding surface</i>	<i>II a</i>	<i>II b</i>	<i>II c</i>
<i>Bilinear sliding surface</i>	<i>III a</i>	<i>III b</i>	<i>III c</i>
<i>Stepped sliding surface</i>	<i>IV a</i>	<i>IV b</i>	<i>IV c</i>

Strain recording elements were added to each model in order to permit the direct comparison between simulated and measured inclinometer-/extensometer-based displacement patterns. Each model included four of these elements, one inclined borehole at the location of SB 120 (marked in red in Figure 4-8) and three vertical elements to simulate deep boreholes that intersect the sliding surface (marked in blue). The horizontal and vertical displacements were exported and used to simulate inclinometer/extensometer survey data as recorded in the field and with the same frame of reference (i.e. borehole bottom with respect to top). The simulation included the distribution of the displacements on two inclinometer casing groove axes, keeping in mind that, the modelled section subtends a 20° angle with the direction of the inclinometer casing grooves in SB 120 at the surface (A+ and A-) as shown in Figure 4-9. As the model is a 2-D simplification, only two azimuth directions of the displacement vector were possible.

The interpretation of the horizontal displacement profiles assumed rigid body deformations; an explanatory sketch is shown in Figure 4-9. A displacement across a fracture was indicated by a peak in the incremental horizontal displacement curve and a step in the cumulative curve. The block movements were identified as translational sliding if the slope of the cumulative displacement profile in A and B direction between dislocation zones was vertical. If the modelled inclination change curve in the A direction exhibited a positive slope, then rotation of the block bottom towards the SW with respect to its top was inferred; if the slope was negative, then toppling was indicated. The axial strain profile was combined with the incremental horizontal displacement curve to derive the magnitude and

orientation of the displacement vectors in the plane of modelling. This data representation and interpretation procedure allowed the derived plot to be directly compared against the measured displacement data in SB 120.

The modelling procedure consisted of an initial run to allow for the initialisation of the in situ stress conditions under gravitational loading. Joint shear strength properties (i.e. cohesion and friction) were set purposely high to guarantee slope stability during this initialisation run. The boundary conditions for all models were set using zero velocities normal to the side and bottom boundaries. Based on these initial conditions, the following runs allowed for destabilization of the slope by setting the joint cohesion to zero and decreasing the friction angle of the sliding surface. For the elasto-plastic models, the intact rock cohesion, tensile strength and internal friction were likewise decreased. The analysis of the resulting displacement patterns is presented for model runs with significant displacements (>1m). Given the objectives for the modelling, it was not necessary to run the models to catastrophic failure. Typically, limits of 50'000-70'000 time steps were used, with most models showing continuing displacements after the limit of 50'000 time steps was reached. As neither strain-hardening nor -softening effects were included in the models, further time-stepping would not have provided any additional meaningful data. This limits the study to the analysis of the kinematics of the rockslide, since the dynamics of the slide will depend on the aforementioned processes. This relates to observations made in many studies which suggest that the strength parameters in a sliding rock mass change with time, displacement magnitude and velocity (e.g. Eberhardt et al. 2004, Helmstetter et al. 2004).

#### 4.4.5 Model properties

##### 4.4.5.1 Rock joint properties

In the UDEC models described, the behaviour of the rock joints is controlled by the friction angle, cohesion, and the shear- and normal stiffness assigned to them. These strength parameters were neither measured during the field reconnaissance nor in the laboratory; instead estimates based on literature values (e.g. Barton 1973, Hoek & Brown 1997, Duzgun et al. 2002, Zangerl 2003) were used. As such, the joint normal and shear stiffness were set to  $1e9$  Pa/m. Tensile strength and cohesion values for all fracture sets were set to zero. Friction angle variations were used to invoke displacements in the slope, either along the sliding surface or the joints where the changes in friction angle were used in order to restrict or favour internal deformation within the sliding rock mass. Given their controlling role, the range of friction angles used in the modelling was broader than the range estimated using the mapped joint roughness coefficients (JRC) of between 8 and 12. For the sliding surfaces, friction values of 25-45° were used; for the steep fractures 30°; and for the foliation fractures 20-30° (Table 4-2). Such values are often used in modelling the slope stability in crystalline rock (e.g. MacLaughlin et al. 2001, Bhasin & Kaynia 2004, Cappa et al. 2004).

Table 4-2: Overview of joint parameters for modelling.

<i>Fracture properties</i>	<i>Fractures</i>	<i>Foliation fractures</i>	<i>Basal plane</i>	<i>Unit</i>
<i>Joint normal stiffness</i>	<i>1e9</i>	<i>1e9</i>	<i>1e9</i>	<i>Pa m<sup>-1</sup></i>
<i>Joint shear stiffness</i>	<i>1e9</i>	<i>1e9</i>	<i>1e9</i>	<i>Pa m<sup>-1</sup></i>
<i>Cohesion</i>	<i>0</i>	<i>0</i>	<i>0</i>	<i>Pa</i>
<i>Friction</i>	<i>25-35</i>	<i>15-30</i>	<i>25-42</i>	<i>°</i>

#### 4.4.5.2 Rock block properties

As previously noted, both linear elastic and elasto-plastic constitutive models for the intact rock blocks were applied in the modelling study. Bulk- and shear moduli for the blocks were derived directly from Young's modulus and Poisson ratio values measured through laboratory testing of the two gneissic rock types (Table 4-3a,b). Values for bulk modulus (10 GPa for gneiss-type A, 18 GPa for gneiss-type B), and shear modulus (7 GPa for gneiss-type A and 13 GPa for gneiss-type B) were not varied in the linear elastic model runs. Rock density was set to 2700 kg/m<sup>3</sup> for both gneiss-types, even though the values determined by laboratory test varied slightly,

For the elasto-plastic model runs the parameters bulk- and shear modulus, block cohesion, friction and tensile strength were intended to represent both the intact rock and the small-scale fractures that are not explicitly represented as discrete rock joints in the model. Therefore, these parameters had to be chosen in the sense of rock mass strength parameters. A first estimate was obtained from the application of the Geological Strength Index (GSI) rock mass classification system (Hoek & Brown 1997). With this classification system the intact rock and small-scale fracture network properties are combined to derive rock mass strength estimates. The classification results obtained by the software RocLab (ROCSCIENCE 2002) are presented in Table 4-3a/b.

Table 4-3: Measured intact rock properties and rock mass properties based on GSI.

a) for the fine grained, chloritic gneisses (group A).

Type	Property	Value	Unit
Laboratory test	Density	2700	kg m <sup>-3</sup>
	Youngs modulus E (mean)	21	GPa
	Poisson ratio	0.14	
	UCS (mean)	69	MPa
	Friction angle (intact rock)*	32	°
	Cohesion (intact rock)*	1.9	MPa
GSI scaling using RocLab	GSI index	50	
	<i>m</i> <sub>i</sub>	20	
	Tensile strength (rock mass)	-0.08	MPa
	Deformation modulus (rock mass)	8.3	GPa
	Friction angle	41	
	Cohesion	3	MPa

b) for the fine-medium grained gneisses with feldspar porphyroblasts (group B).

Type	Property	Value	Unit
Laboratory test	Density	2640	kg m <sup>-3</sup>
	Youngs modulus E (mean)	32	GPa
	Poisson ratio	0.21	
	UCS (mean)	97	MPa
	Friction angle (intact rock)	55	°
	Cohesion (intact rock)	16	MPa
GSI scaling using RocLab	GSI index	60	
	<i>m</i> <sub>i</sub>	34	
	Tensile strength (rock mass)	-0.14	MPa
	Deformation modulus (rock mass)	17.5	GPa
	Friction angle	46	
	Cohesion	7	MPa

\* = derived by Mohr-Coulomb fit

For the elasto-plastic models, the bulk modulus of the A-gneisses was set to 4 GPa, and 10 GPa for the B-gneisses; a shear modulus of 4 GPa was chosen for the A-gneisses and 9 GPa for B-gneisses. Intact block cohesion, tensile strength and the internal friction were lowered from the values obtained from the GSI estimate until internal block damage by tensile and/or shear failure was obtained. Table 4-4 shows the range of values used to model the elastic and elasto-plastic blocks.

A detailed overview of the joint and block parameters for each run is provided in Table 4-5 a,b.

Table 4-4: Overview of block parameters for modelling.

<i>Block properties</i>	<i>Group A</i>	<i>Group B</i>	<i>Unit</i>
<i>Density</i>	2700	2700	$kg\ m^{-3}$
<i>Bulk modulus K</i>	$10\ e^9$	$18\ e^9$	<i>Pa</i>
<i>Shear modulus G</i>	$9\ e^9$	$13\ e^9$	<i>Pa</i>
<i>Cohesion</i>	$3\ e6 - 1\ e5$	$7\ e6 - 1\ e6$	<i>Pa</i>
<i>Friction</i>	40-30	46-40	°
<i>Tensile strength</i>	$5\ e6 - 1e4$	$1\ e6 - 1e5$	<i>Pa</i>
<i>Dilation</i>	0	0	°

*Group A = fine grained, chloritic gneisses, Group B = fine-medium grained gneisses with porphyroblasts*

Table 4-5: Parameters for the presented models.

a) Models with planar and circular sliding surface

<i>Model</i>	<i>Planar sliding surface</i>			<i>Circular sliding surface</i>		
	<i>I a</i>	<i>I b</i>	<i>I c</i>	<i>II a</i>	<i>II b</i>	<i>II c</i>
<i>Fractures</i>						
<i>φ sliding surface [°]</i>	35	35	42	23	25	25
<i>φ steep fractures [°]</i>	35	30	30	30	30	30
<i>φ foliation fractures [°]</i>	-	25	-	-	20	-
<i>Joint shear stiffness [Pa/m]</i>	$1e9$	$1e9$	$1e9$	$1e9$	$1e9$	$1e9$
<i>Joint normal stiffness [Pa/m]</i>	$1e9$	$1e9$	$1e9$	$1e9$	$1e9$	$1e9$
<i>Gneisses A</i>						
<i>bulk modulus [MPa]</i>	10	10	4	10	10	4
<i>shear modulus [MPa]</i>	9	9	4	9	9	4
<i>internal friction angle [°]</i>	-	-	35	-	-	30
<i>cohesion [Pa]</i>	-	-	$1e6$	-	-	$5e5$
<i>tensile strength [Pa]</i>	-	-	$5e5$	-	-	$1e5$
<i>Gneisses B</i>						
<i>bulk modulus [MPa]</i>	18	18	10	18	18	10
<i>shear modulus [MPa]</i>	13	13	7	13	13	7
<i>internal friction angle [°]</i>	-	-	40	-	-	40
<i>cohesion [Pa]</i>	-	-	$1e6$	-	-	$1e6$
<i>tensile strength [Pa]</i>	-	-	$5e5$	-	-	$1e5$
<i>Cycles [ ]</i>	50'000	50'000	70'000	50'000	50'000	70'000

## b) Models with bilinear and stepped sliding surface

Model	Bilinear sliding surface			Stepped sliding surface		
	III a	III b	III c	IV a	IV b	IV c
<i>Fractures</i>						
$\phi$ sliding surface [°]	30	25	30	25	25	25
$\phi$ steep fractures [°]	30	30	30	30	25	30
$\phi$ foliation fractures [°]	-	25	-	15	15	15
Joint shear stiffness [Pa/m]	1e9	1e9	1e9	1e9	1e9	1e9
Joint normal stiffness [Pa/m]	1e9	1e9	1e9	1e9	1e9	1e9
<i>Gneisses A</i>						
bulk modulus [MPa]	10	10	4	10	10	4
shear modulus [MPa]	9	9	4	9	9	4
internal friction angle [°]	-	-	35	-	-	30
cohesion [Pa]	-	-	1e6	-	-	7e5
tensile strength [Pa]	-	-	5e5	-	-	3e5
<i>Gneisses B</i>						
bulk modulus [MPa]	18	18	10	18	18	10
shear modulus [MPa]	13	13	7	13	13	7
internal friction angle [°]	-	-	40	-	-	45
cohesion [Pa]	-	-	1e6	-	-	7e6
tensile strength [Pa]	-	-	5e5	-	-	1e6
Cycles [ ]	50'000	50'000	50'000	50'000	50'000	50'000

## 4.4.6 Results and comparison with measured displacement fields

### 4.4.6.1 Case I - Planar sliding surface

For the three block material representations (cases I a-c), a persistent planar sliding surface dipping with 40° from horizontal towards the valley was added to the extrapolated mapped active fractures. The displacement patterns associated with this geometry are of interest, even though the presence of such an extensive planar feature was rendered doubtful by the mapping results.

#### *Case I a - Elastic blocks*

The block displacements obtained for elastic blocks on a planar sliding surface are plotted in Figure 4-10a. The most important characteristic is that only certain sections of the complete rock mass are displaced along the sliding surface, even though the strength parameters along the surface are constant. Three types of block behaviour could be distinguished: The front blocks (area A on Figure 4-10a) exhibit pure translational sliding with displacement vectors parallel to the sliding surface and constant displacement magnitudes within the sliding blocks. Behind these front blocks a gap is opening. The adjacent blocks of area B show an increased vertical displacement as they slide/sink into this gap. This movement is mirrored in the steepened surface displacement vectors. In area C toppling dominates the displacements of the blocks.

#### *Case I b - Elastic blocks with foliation fractures*

In model Case I b the elastic blocks are dissected by sub-horizontal foliation fractures. The results (Figure 4-10b) show that like in model I-a, the front blocks show translational sliding with displacements parallel to the sliding surface (area A on Figure 4-10b). Unlike in case I a, the blocks show toppling (area B) directly behind the fracture delineating area A. Hence the surface displacement

vectors have similar dips along both area A and B. Compared to case I-a, the strength of the steep fractures was reduced to  $30^\circ$ . However, this showed no effects on the displacement patterns, and only a small increase of the maximum displacements from 2.03 to 2.35 m. Likewise, tests of reducing the friction angle of the steep fractures in model I a led only to a small increase in the maximum displacements.

#### *Case I-c - Elasto-plastic blocks*

Model Case I c includes displacement patterns relating to both the sliding of intact blocks and the elasto-plastic deformation of yielding blocks above the planar sliding surface (Figure 4-11). Intact rock cohesion and internal friction angle for the blocks were lowered, with respect to the laboratory-derived values, to favour internal damage and yielding of the blocks. No plastic failure happened when the rock mass parameters according to the GSI scaling were used. Therefore, the strength properties of both gneiss types were lowered. Likewise, the joint friction angle along the sliding surface was increased to  $42^\circ$ . Test models showed that at lower friction angles the blocks were sliding without significant internal damage. In consequence, the front block slides less and displacements within the block decrease along the sliding surface and with increasing distance from the ground surface. According to the model results, (stopped after 50'000 time steps), internal block failure in tension (indicated by grey circles around the failed elements) leads to the internal deformation of the front block (labelled A in Figure 4-11). Most blocks in area B are less subjected to internal deformation and show toppling as a rigid body movement. The surface displacement vectors at in this model case vary between  $30$  and  $40^\circ$  and are not always parallel to the sliding surface

#### *Modelled inclinometer-/extensometer data*

Figure 4-12 shows simulated inclinometer-/extensometer plots for model I a, derived from the modelled axial and horizontal displacement profiles in comparison to the measured displacement patterns in SB 120. The slope of the modelled cumulative horizontal displacement curve indicates block toppling down to depths of approximately 80 m. Below this depth, translational sliding is indicated in the vertical inclination change curve. Between 90 and 110 m a block is crossed by the model borehole that shows almost no displacements (marked in Figure 4-10a). Therefore, displacements towards the valley increase drastically at 110 m, where blocks of the moving rock mass are intersected. The bottom of the simulated borehole is moving towards the valley with respect to the borehole top as is indicated by cumulative horizontal displacement profile ending with a positive value. The modelled cumulative vertical displacement curve indicates extension at two locations (75 and 90 m) whereas only shortening along the borehole axis was measured in SB 120.

In Figure 4-12 c-d the measured and predicted 3-D displacement vectors are plotted against each other. It should be noted that the modelled displacement vectors can only lie in the plane of the section and have values of either  $140^\circ$  or  $320^\circ$ . As the trajectory of SB 120 is curved and the modelled 120 m borehole straight, the positions of the fractures along the depth axes of the plots agree only partly, thus the modelled dislocation zone at 80 m corresponds to the fracture intersecting SB 120 at 85 m depth. As at this position and at 110 m depth the modelled displacement vectors are influenced by the intersection of the almost stable block, the comparability with the measured displacement vectors is limited. The comparison of the measured and predicted displacement vectors shows that they do not correspond either in magnitude or in dip, although the sense of movement is largely correct.



To summarise, the predicted and measured displacements show agreement only for some of the displacement patterns which can be deduced from the cumulative horizontal displacement profiles. The profiles agree in: i) the blocks in upper part of the borehole show toppling; ii) the following borehole section is characterised by translational sliding without rotation of the blocks; and iii) the bottom of the real and modelled borehole are both displaced towards the valley with respect to the top of the borehole. The rotation of blocks towards the valley that was measured in SB 120 could not be reproduced with the chosen geometry of the sliding surface.

#### *Summary - Comparison with measured displacement fields*

The three modelled cases show that complex displacement patterns can occur for “simple” translational sliding on a planar surface if the rock mass is fractured and not moving as a single coherent mass. As well the surface displacement vectors under such conditions are not always parallel to the dip of the sliding surface. The predicted displacement patterns show more or less translational sliding of the front blocks, accompanied by a mixture of sliding with different vertical components and toppling closer to the back-scarp. In the blocks behind the coherently moving blocks, the modelled displacement patterns correspond only partially to those derived from the inclinometer-/extensometer surveys in SB 120. Nevertheless, it must be remembered that the key discrepancy between the model and investigation results relates to the lack of field evidence for a highly persistence planar sliding surface, especially with respect to the current instability.

#### **4.4.6.2 Case II - Circular sliding surface**

The sliding surface for the three models of Case II is approximately circular. This geometry is usually considered typical for weak, intensely fractured rock masses and soils. Nevertheless the apparent rotational movements of the lower blocks intersected by the borehole SB 120 suggested insights may be gained by modelling a rotational failure surface as well. The circular sliding surface existing of several fractures was implemented instead of lowering the block strength to the initiation of block failure, since the rigid body rotations were the focus of these model runs. In order to allow the internal deformation of the unstable rock mass, additional steep fractures dipping away from the valley were added to the model. Significant displacements >1m could only be obtained by decreasing the friction angle on the fractures forming the sliding surface to 23° in case II a, and to 25° in the cases II b and c.

##### *Case II a - Elastic blocks*

As Figure 4-13a shows, the blocks generally exhibit homogeneous translational sliding with displacement vectors parallel to the dip of sliding surface limiting the sliding block. These movements are favoured by the steep fractures dipping away from the valley that were added to dissect the unstable rock mass. Toppling motions or rotations of block bottoms with respect to their tops are slight. The surface displacement vectors mirror the displacement patterns at depth and increase from near horizontal at the front blocks to almost vertical close to the back scarp.

##### *Case II b - Elastic blocks with foliation fractures*

In model Case II b, the elastic blocks on the circular sliding surface are dissected into smaller blocks by foliation fractures (Figure 4-13b). Despite these changes, the displacement patterns do not change with respect to case II a, and block assemblages are coherently sliding parallel to the inclination of the underlying sliding surface segment.

### *Case II c – Elasto-plastic blocks*

The results for the elasto-plastic (II c) block constitutive models in combination with a circular sliding surface are shown in Figure 4-14. The strength properties of the blocks had to be lowered with respect to those used in model case I c in order to obtain plastic deformation within the blocks. Compared against the cases II a-b, the displacement fields changed such that displacements in the front blocks decrease from the surface to depth as plastic deformation occurs. The displacement patterns in the upper blocks however remain unchanged.

#### *Modelled inclinometer-/extensometer data*

The cumulative horizontal displacement profile (Figure 4-15) shows that in the upper 40 m of the borehole no incremental horizontal displacements can be inferred; hence the toppling measured in the upper 40 m of SB 120 was not predicted. Below 40 m depth, only minor rotations of the block bottoms with respect to their tops occur. As in Case I a, the bottom of the borehole is displaced towards the valley with respect to the borehole top, in accord with the measurements in SB 120. The axial strain in the borehole indicates shortening across the active fractures, which is in agreement to the measured axial strains. As both the bottom and top of the simulated borehole are located in blocks which move coherently downwards, the cumulative vertical displacement profile shows only small axial strain. The combination of modelled axial strain and horizontal displacement data shown in Figure 4-15d, illustrates that only two fractures accommodate the internal deformation along the borehole. In both cases the modelled displacement vectors across the fractures is inclined upward (lower block wrt upper) at higher angles than measured in SB 120.

#### *Summary - Comparison with measured displacement fields*

The degree of correlation between the modelled displacement fields associated with the circular-sliding-surface scenario and the measured displacement fields is only small. The modelled displacement patterns are dominated by translational sliding of large blocks and block assemblies. The circular sliding surface models evoke displacement fields without combined sliding and toppling blocks in the upper sections of the unstable rock mass that the models should predict. Likewise, rotational block movements are only minor under the chosen kinematic conditions and only partly correspond to the rotational movements indicated by the inclinometer survey data for the bottom of SB 120. Another important difference between modelled and measured displacement patterns is the inclination of surface displacement vectors; at the study site the displacement vectors are less inclined than the modelled ones.

### **4.4.6.3 Case III - Bilinear sliding surface**

One steep (80°) and one shallow (20°) dipping persistent fracture delineate the bilinear sliding surface in the model for Case III. The rock mass was dissected by steep fractures dipping away from the valley, almost perpendicular to the basal sliding surface. The friction angle on the sliding surfaces was set to 30° and only decreased to 25° in case III b to achieve a higher signal to noise ratio on the predicted inclinometer data.

#### *Case III a - Elastic blocks*

The modelled displacement patterns for model III a with elastic blocks are given in Figure 4-16a. Translational block movements parallel to either the moderately inclined or steeply dipping

slide surface dominate. Therefore two areas with different displacement vectors (area A and B) could be distinguished, which are separated by the steep fracture in the hinge of the bilinear sliding surface. At this fracture the internal deformation of the unstable rock mass is concentrated. Apart from the front block, most blocks exhibit a minor toppling displacement component. Similarly to the displacement patterns at depth, only two inclinations of the displacement vectors occur at the surface.

#### *Case III b - Elastic blocks with foliation fractures*

The displacement fields for the model III b (bilinear sliding surface with elastic blocks with foliation fractures) are plotted in Figure 4-16b. The presence of the sub-horizontal foliation fractures apparently has only a small effect on the internal deformation of the rock mass. Nevertheless, not all internal deformation is concentrated on the steep fracture in the hinge of the bilinear sliding surface, but is distributed on two fractures (labelled 1 and 2 in Figure 4-16b). An additional model run with a friction angle of 30° on the sliding surfaces (comparable to case III a) showed that this change disappears for higher friction angles and smaller displacement magnitudes. As well, the rotational toppling movements are slightly larger than in model III a with elastic blocks. As more fractures accommodate the internal deformation of the rock mass, the surface displacement vectors in the front blocks (area A) show a higher variability, especially close to the hinge region.

#### *Case III c - Elasto-plastic blocks*

As in the cases III a and b, the front block (area A) in case III c with elasto-plastic blocks is subjected to translational sliding along the sliding surface (Figure 4-17). In area B, the displacement patterns exhibit increased toppling in areas where internal damage occurs. Due to the decreased strength of the lower gneisses (gneiss-type A) relative to those in the upper part of the slope, internal damage by tensile failure is concentrated in this lithology. Due to the internal damage in area B the internal deformation of the rock mass is distributed on most of the steep fractures within this area. In area C steep displacement vectors can be observed which are comparable to those of the cases III a and b.

#### *Modelled inclinometer-/extensometer data*

The simulated inclinometer-/ extensometer measurements for the scenario Case III b (Figure 4-18) depict the toppling component within the sub-vertical displacements in the wedge behind the hinge of the two sliding surfaces better than the block displacement plot. From the top of the borehole to a depth of 110 m toppling movements are revealed by the slope of the cumulative horizontal displacement profile; nevertheless between the top of the borehole and 110 m no significant displacements of the borehole bottom with respect to top accrued. The lowermost part of the inclination change curve should not be considered for interpretation due to the presence of a so called 'artefact' (see section 4.4.3).

#### *Summary - Comparison with measured displacement fields*

The modelled displacement patterns for the three bilinear slide surface models are mainly characterised by translational sliding parallel to the lower sliding surface and sub-vertical displacements of the wedge above the hinge of the two sliding surfaces. This applies to the surface displacement vectors as well as to the displacements at depth. At the surface, displacement vectors have dip angles of 20 or 80°. Only the small part above the hinge zone is associated with surface displacement vectors with dips of 40°; thus these predicted values correspond only partly to the measured vectors which

vary between 20 and 50°. The modelled displacement patterns in the simulated borehole correspond only to those measured in the upper sections of SB 120 showing toppling. In the middle and lower sections of the simulated borehole, toppling occurs, whereas in SB 120 translational and rotational movements (bottom with respect to top) were measured.

#### 4.4.6.4 Case IV - Stepped sliding surface

In this model no sliding surface was explicitly defined but a network of fractures defined by three joint sets allows for the formation of a stepped sliding surface. As such, the gaps between the fractures dipping with  $45 \pm 5$  towards the valley force the sliding surface to step through a combination of sub-horizontal and/or sub-vertical fractures. This model represents the most complex representation of the rock mass and possible geometries of the sliding surface. To favour displacements on the fractures with dip towards the valley, their strength properties were reduced in all three presented cases (friction angle = 25°).

##### *Case IV a - Elastic blocks*

The modelled fracture network for case IV a and the resulting displacement patterns are illustrated in Figure 4-19a. Due to the complex intersection of the fractures, no through-going basal sliding surface was formed. The modelled displacement patterns show only regional localised shear displacements on the fractures. The predicted surface displacement vectors dip with small to intermediate angles, with slightly larger dips in the immediate vicinity of the inclinometer. In most regions of the slope the displacements decrease continuously with depth. Nevertheless the upper 200 m of the slope are subjected to sliding of different sized block assemblies; in addition to translational sliding, block toppling is predicted by the model.

##### *Case IV b - Elastic blocks with foliation fractures*

In the model Case IV-b foliation fractures dissect the upper part of the slope. The addition of these fractures slightly altered the location of fractures dipping towards the valley (Figure 4-19b). Because the displacements were not much above the threshold of 1 m when the same parameters as in case III a were used, the friction angle on the steep fractures was reduced to 25°. The predicted displacements after this change were found to be significantly larger (Figure 4-19b). This model result shows a different sensitivity to the friction angle on the steep fractures than in the other model cases. There, the displacement magnitudes were rather independent of this property. However, the general displacement patterns in model case IV b do not significantly differ from those of the case IV a, and are apparently not influenced by the additional foliation fractures.

##### *Case IV c - Elasto-plastic blocks*

Case IV c includes elasto-plastic block behaviour, such that the location of block yielding can be modelled. This case of stepped sliding surfaces provides the best insights as to whether block failure could be involved in the formation of a failure surface. In the model presented (Figure 4-20), especially the strength parameters of the gneisses below 1200 m were reduced, whereas the strength parameters of the gneisses in the hanging wall correspond to those determined from the GSI rock mass classification. Internal damage after 50'000 time steps is hence concentrated in the lower gneisses. Along the intermittent fractures with dip towards the valley a zone of tensile damage and yielding can be observed. This zone also separates the blocks with higher displacements from those with smaller or no

displacements. This indicates that by progressive failure a persistent failure surface dipping towards the valley could be formed even though no highly persistent fractures with corresponding directions were present in the slope. Nevertheless, the model results show comparable displacement patterns as those shown in model IV b (elastic blocks with foliation fractures).

#### *Modelled inclinometer-/extensometer data*

The simulated borehole displacement patterns for model IV b are plotted in Figure 4-21. The predicted cumulative horizontal displacement profile shows that toppling dominates in the upper 90 m. Below this, the lower blocks are towards the valley by sliding and have smaller toppling components. Again the bottom of the modelled borehole can be seen to move towards the valley with respect to the top of the borehole, although the sense of block rotation in the lower borehole section is opposite to the observed. Taking into account the presence of artefacts in the upper 20 m of the predicted inclinometer profile, the predicted and measured horizontal displacements can be considered to agree for the upper 40-50m. Below this depth, the toppling component predicted by the model is larger than measured. The predicted vertical displacement profile indicates that all active fractures contribute to shortening along the borehole axis, whereas observations show that only two fractures contribute.

#### *Comparison with measured displacement fields*

The rather complex fracture pattern due to the intersection of three fracture sets with limited persistence generates rather complex displacement patterns. The three models predict significant displacements that are confined to the upper 200-250 m of the slope, but extend further back from the slope than observations support, although they diminish. The comparison of predicted and measured inclinometer-/extensometer data shows agreements for the upper sections of the borehole (i.e. those in relation to toppling). However, in the simulated borehole, only the lowermost blocks are located in sliding blocks with diminished toppling. As in each of the previous models, no blocks were either intersected by the simulated borehole or found in the modelled slope that suggest a rotational sliding component (i.e. the bottom rotating towards the valley with respect to top) measured in the field. The predicted surface displacement vectors have small to moderate dip angles and varying magnitude which corresponds to the measured surface displacements.

### **4.4.7 Discussion**

#### ***4.4.7.1 Implications of the modelling results for the investigated slope instability***

The comparison of the modelled and measured displacement patterns at the surface and in the 120 m deep borehole is summarised in the model result matrix shown in Table 4-6. With respect to identifying the best suited model to explain the measured displacement fields three rankings were considered: i) the agreement of predicted and measured displacement fields for the complete model, ii) the agreement of predicted and measured displacement fields in the borehole, and iii) the agreement of the model structure and the geological investigations performed at the study site. The modelling results revealed that a comparably good prediction of the measured displacements can be obtained with a sliding surface stepping through several fracture sets; this model also represents the fracture geometry closest to the geological model of the slope. Fairly good agreement of the modelled and measured displacement fields could be found for the simple planar sliding surface model, especially with respect to the modelled inclinometer-/extensometer data in the borehole. However, the

highly persistent discontinuity as sliding surface is not in accord with the mapping data. The bilinear and circular sliding surface models both show major discrepancies to the measured surface displacement directions. Both models were found to predict the measured borehole displacement patterns only to a limited extent.

Table 4-6: Model result matrix.

	<i>Agreement of predicted and measured displacements for the complete model</i>		<i>Agreement of predicted and measured displacements in the simulated borehole</i>		<i>Agreement of the model structure and the results of the geological investigations</i>
<i>I</i>	<i>surface displacements:</i>	$\pm$	<i>toppling :</i>	+	<i>no observations of a large</i>
<i>Planar sliding surface</i>	<i>complex block displacements:</i>	+	<i>sliding :</i>	+	<i>through-going sliding surface</i>
			<i>rotation towards the valley:</i>	-	
			<i>bottom of borehole displaced</i>		
			<i>towards the valley wrt the top:</i>	+	
<i>II</i>	<i>surface displacements:</i>	-	<i>toppling :</i>	-	<i>unlikely sliding surface</i>
<i>Circular sliding surface</i>	<i>complex block displacements:</i>	-	<i>sliding :</i>	-	<i>geometry in massive crystal-</i>
			<i>rotation towards the valley:</i>	-	<i>line rock</i>
			<i>bottom of borehole displaced</i>		
			<i>towards the valley wrt the top:</i>	+	
<i>II</i>	<i>surface displacements:</i>	-	<i>toppling :</i>	+	<i>no observations of a large</i>
<i>Bilinear sliding surface</i>	<i>complex block displacements:</i>	-	<i>sliding :</i>	-	<i>sliding surface with a dip of</i>
			<i>rotation towards the valley:</i>	-	<i>20°</i>
			<i>bottom of borehole displaced</i>		
			<i>towards the valley wrt the top:</i>	$\pm$	
<i>IV</i>	<i>surface displacements:</i>	+	<i>toppling :</i>	+	<i>only few fractures with</i>
<i>Stepped sliding surface</i>	<i>complex block displacements:</i>	+	<i>sliding :</i>	-	<i>moderate dip towards the</i>
			<i>rotation towards the valley:</i>	-	<i>valley mapped</i>
			<i>bottom of borehole displaced</i>		
			<i>towards the valley wrt the top:</i>	+	

$\pm$  = partly in agreement

+

- = no agreement

Through further study, insights may be gained to help explain the rotational movements at the bottom of SB 120 and the observations that not all active fractures are activated in shear but in pure extension as well. The source of this discrepancy may be related to several factors. Firstly, the amount of rotational block movements may be influenced by systematic errors as pointed out in Chapter 3 and the assumptions made in correcting these errors might have led to an overestimation of the rotational block movements at the bottom of SB 120. Better agreement between modelled and measured displacement fields may be possible as further inclinometer and surface displacement measurements are made over time. Secondly, more complicated fracture networks with fractures dipping with varying dip angles towards the valley may result in models producing localised block rotations; similarly these movements could indicate localised damage and yielding within a weaker gneiss layer below the boreholes (comparable to the Prandtl prism suggested by Kvapil & Clews 1979). Thirdly, discrepancies between the modelled and measured displacements may be related to the 2-D assumption used for the models. This applies especially to the representation of foliation fractures as sub-horizontal, even though they dip perpendicular to the model section, and to neglecting the N-S striking faults and fracture zones in the modelled scenarios.

In conclusion, the modelling revealed that translational sliding along intermittent planar sliding surfaces can explain the many of the measured displacement patterns, based on the fits achieved by the corresponding models relative to the measured displacement data. The results of the step-path sliding surface scenario also suggests that only a few fractures dipping towards the valley in combination with other fracture sets are required to accommodate translational displacements. These results are also interesting with regard to the interpretation of the large failure surface of the second 1991 rockslide. Modelling results of this model case suggest that this large plane does not necessarily imply the presence of highly persistent, pre-existing fractures before the initiation of the slope instability. As such, more realistic models can be constructed that account for the limited occurrence of the fractures dipping towards the valley. Together, these results have provided key first estimates that can be used to direct further modelling in order to better predict the kinematic stability state present in the rock slope.

In the context of improving the prediction by increasing the complexity of the model, consideration should be given to the fact that many important constraints for modelling the displacement patterns are unknown. These include: i) the lower boundary of the unstable rock mass and thus the location of the sliding surface, ii) the orientation of the sliding surface and the number of faults and fracture sets contributing to it, and iii) their static and dynamic strength properties. To overcome these deficiencies, the performance of additional field measurements should be considered (e.g. ground based radar interferometry or differential GPS measurements).

#### **4.4.7.2 *Implications for modelling complex rockslides***

The modelling study clearly demonstrated that the prediction of displacement patterns is a difficult task when dealing with fractured rock masses. Results show that the displacement patterns measured in boreholes will strongly depend on the location of the borehole in the unstable rock mass. As such the prediction of borehole displacement patterns as suggested by Kovari (1990) based on the geometry of the sliding surface and intact block translation and rotation can not be transferred to fractured rock masses. Their blocky nature will introduce a high variability of movement modes (e.g. toppling, rotation, sliding).

The presented study, the displacement patterns for the twelve models were found to depend strongly on the geometry of the sliding surface and only to a limited extent with the different material block representations of the rock mass (i.e. elastic *vs.* elasto-plastic). This emphasises the importance of properly assessing the internal structure of an unstable rock mass for the development of representative model geometries. As demonstrated in this thesis, an adequate model should be constrained by the integrated geological and geophysical investigation of the rock mass structure and the measurement of displacement fields at the surface and at depth.

## 4.5 Figures

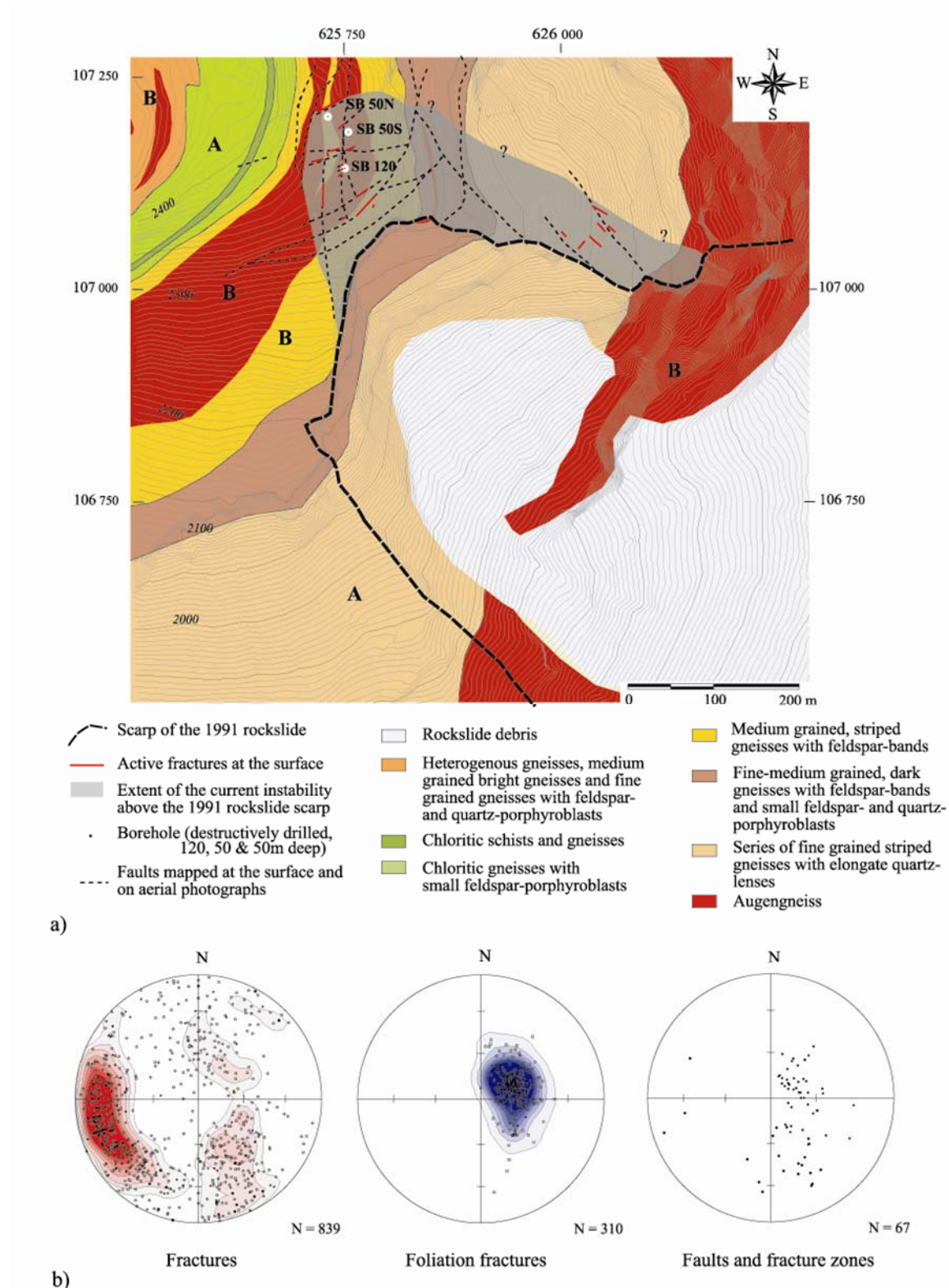


Figure 4-1: a) Geological map of the study area showing the mapped lithologies, the fault and fracture zone network and the assumed extent of the unstable rock mass. The lithological units are labelled A and B according to their mechanical behaviour. b) Stereonets for the fractures, foliation fractures and faults for elevations 2000-2350 m.



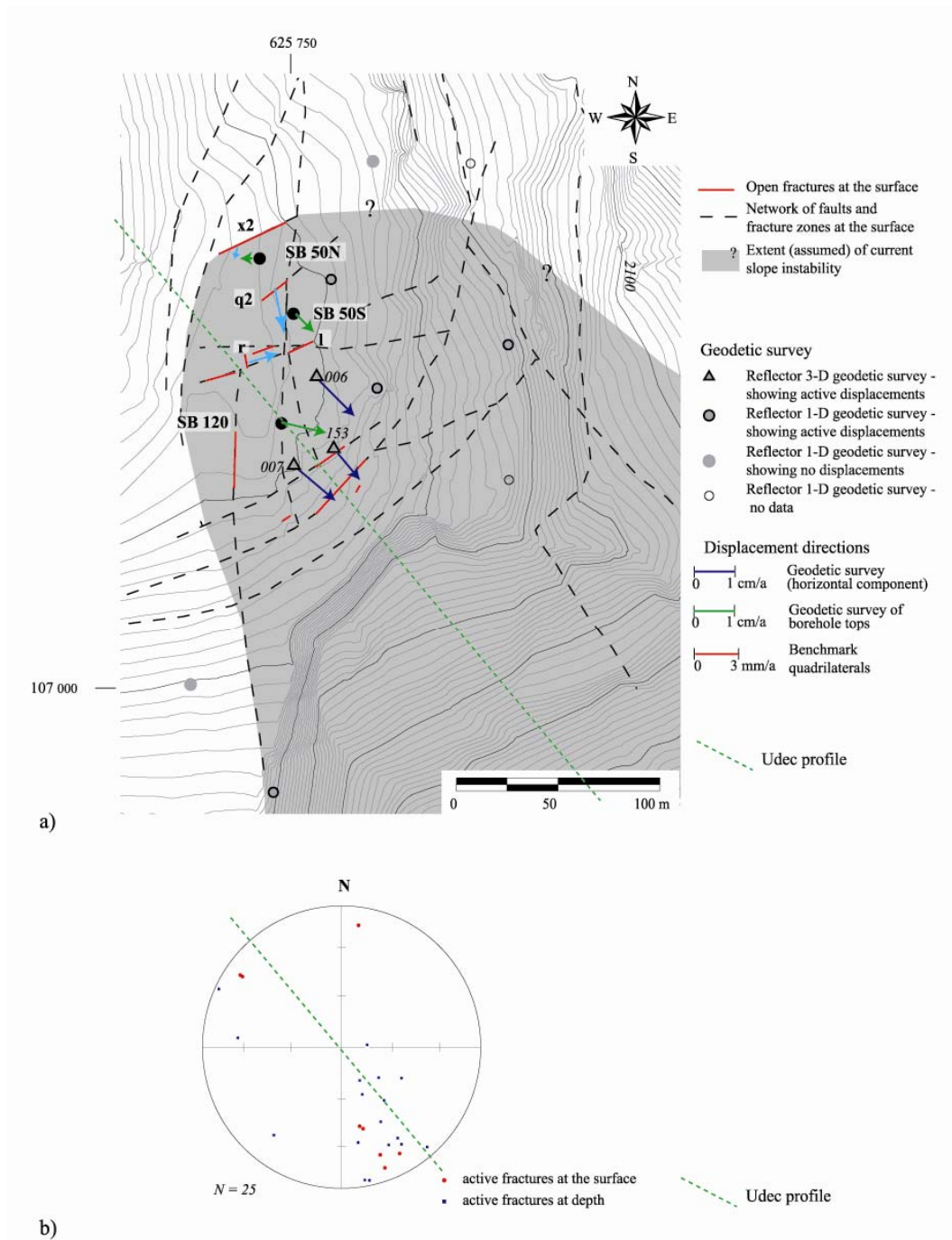


Figure 4-2: a) Horizontal surface displacement vectors (relative, i.e. one side of the active fracture with respect to the other: fracture opening in cyan; absolute, i.e. with respect to external reference frame: geodetic survey of reflectors and borehole tops in blue and green). Red segments of the fault and fracture zone network represent active opening surface fractures. b) Stereoplot showing the orientation of active fractures at the surface and at depth. The chosen direction for the modelling profile is approximately parallel to both the orientation of the active fractures and the direction of displacement.

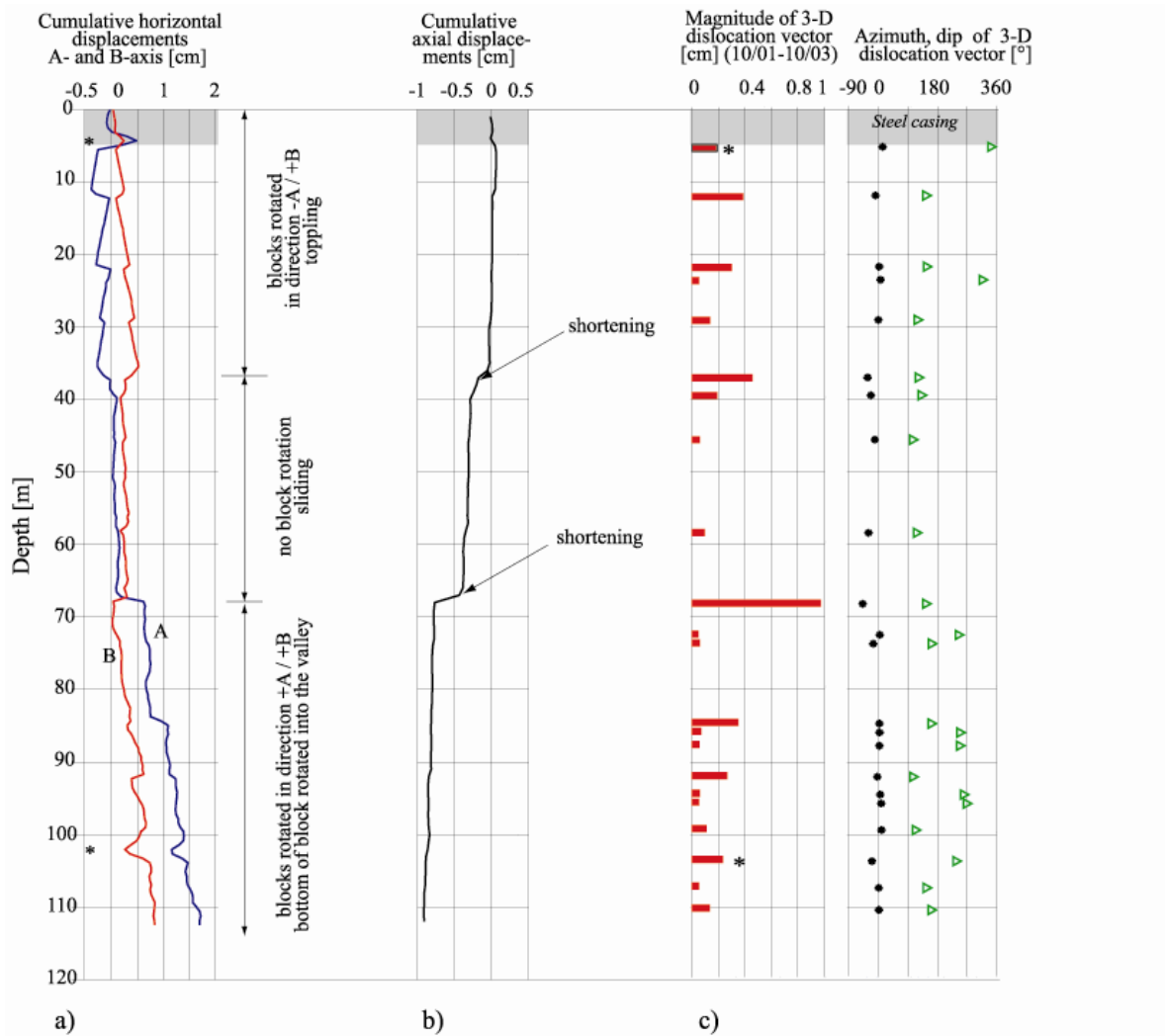


Figure 4-3: a) Profile of cumulative inclination changes for a two year period in SB 120 and inferred block rotations. b) Profile of cumulative vertical displacements showing two zones of shortening. c) Derived incremental displacement vector with incremental magnitude, azimuth and dip across dislocation zones are plotted to the right. The reference frame is bottom of the borehole with respect to the top.

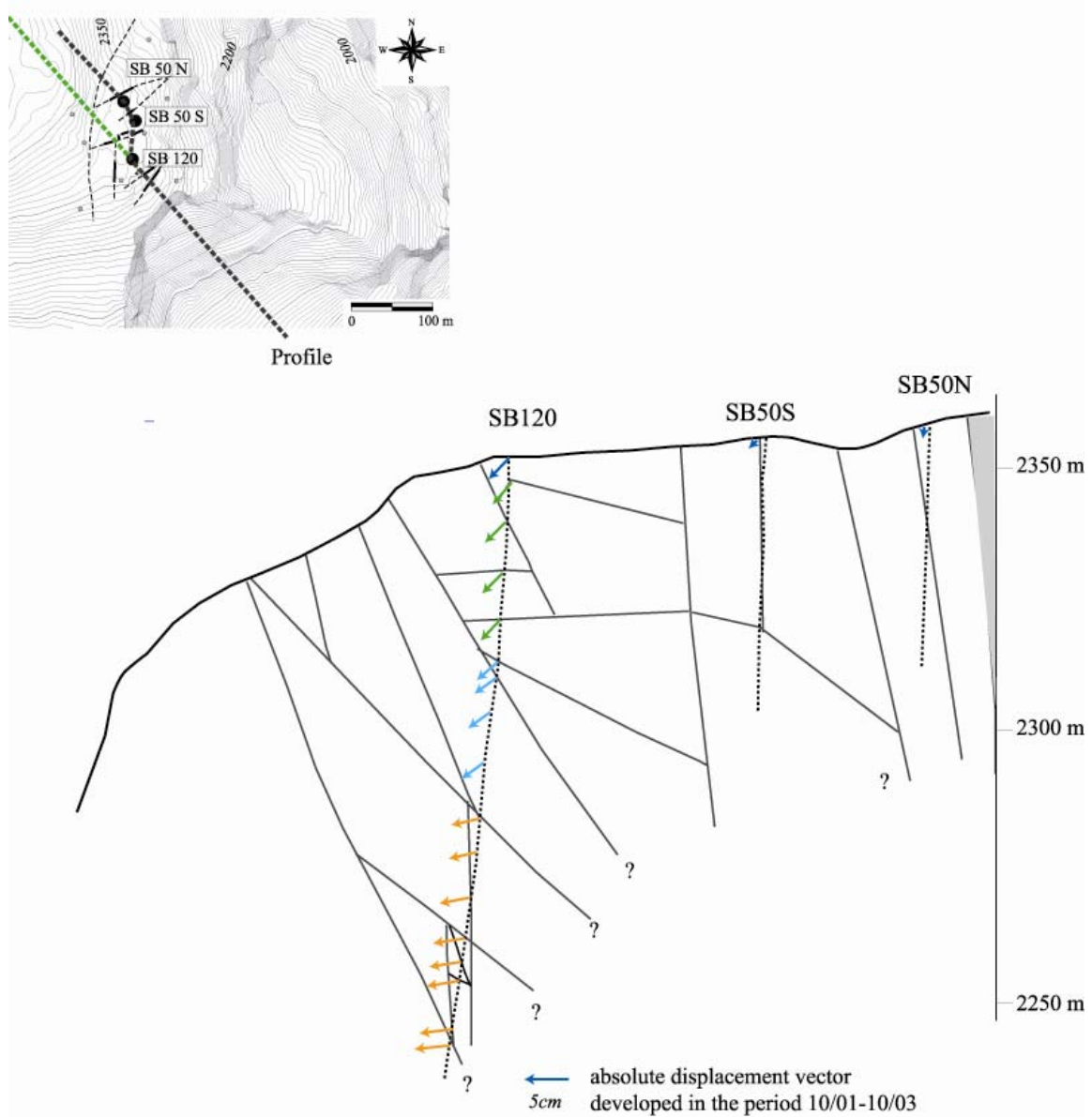


Figure 4-4: Block model along the boreholes showing displacements at the borehole tops; also shown are absolute displacements along SB 120 obtained by the integration of the borehole displacements with geodetic displacement vectors. In the upper part (green arrows) inclinometer surveys indicate toppling, in the middle part (light blue arrows) sliding without block rotations was inferred and in the lowermost part (orange arrows) the bottom of the blocks is rotated towards the valley wrt the top.

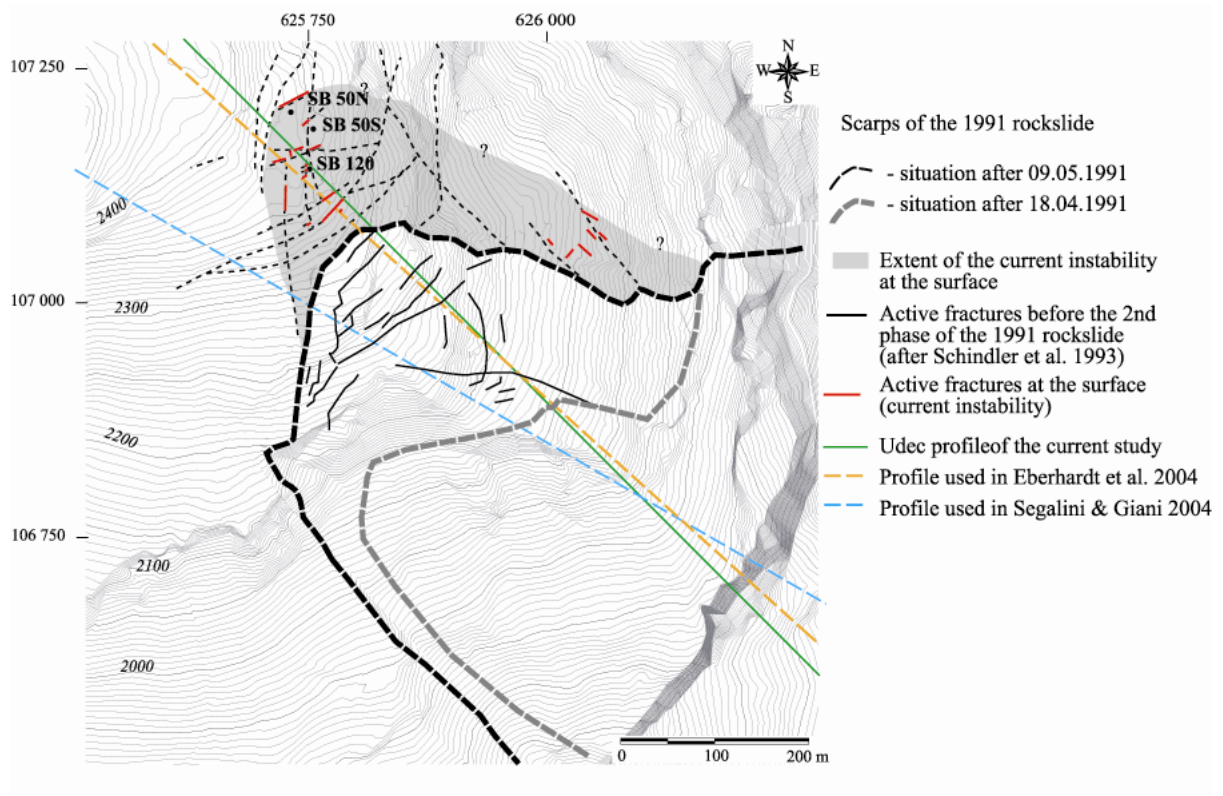
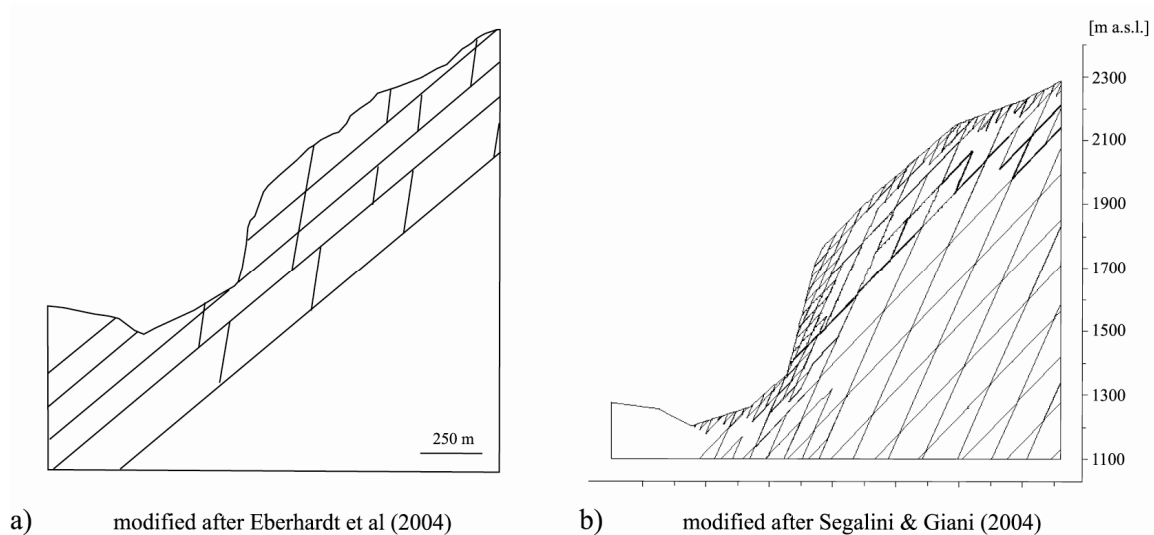


Figure 4-5: Map showing the pre-rockslide topography before 1991 with orientations of active fractures before the second phase of the 1991 rockslide (after Schindler et al. 1993) and active fractures of the current instability. Also plotted are the inferred directions of sections for numerical modeling.



a) modified after Eberhardt et al (2004)

b) modified after Segalini & Gianni (2004)

Figure 4-6: a) Discontinuum model used in Eberhardt et al. (2004). b) Discontinuum model used in Segalini & Gianni (2004). Both models involve moderately inclined, through-going fractures dipping towards the valley as well as steep fractures dipping towards the valley.

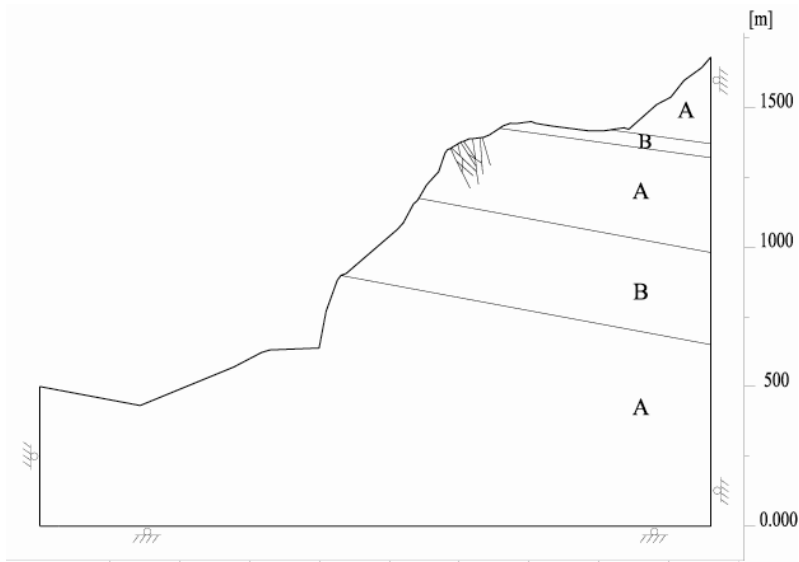


Figure 4-7: General model geometry with lithological units of the two gneiss-types A and B together with the active fractures intersected by the boreholes. The model height zero refers to 970 m altitude.

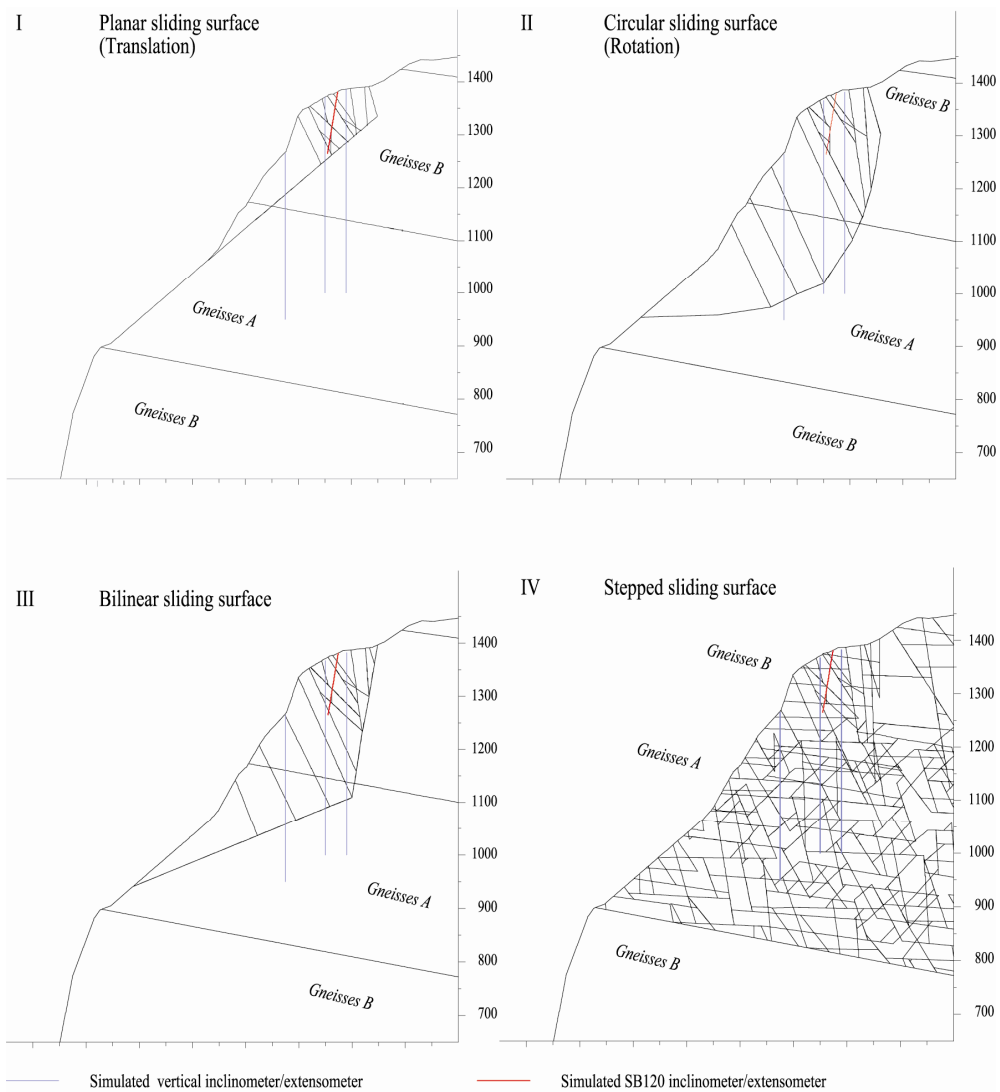


Figure 4-8: Model geometries for the four kinematic models considered in the parametric study.

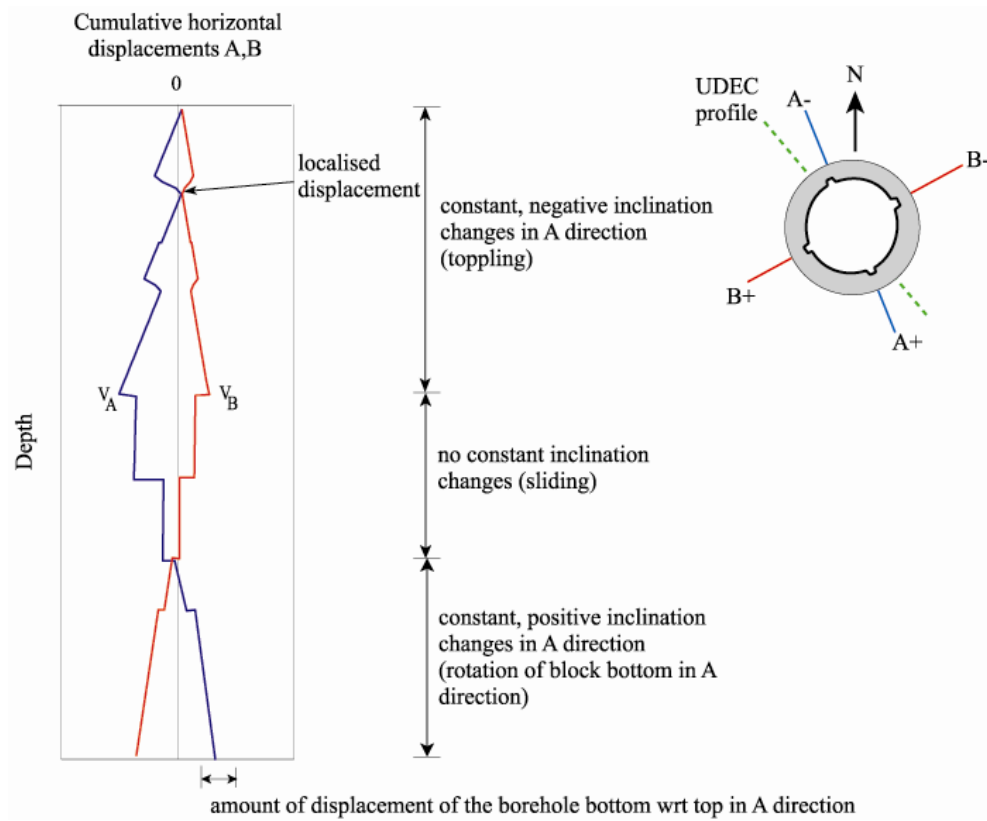


Figure 4-9: Conventions for the interpretation of measured and predicted cumulative horizontal displacement profiles in SB 120. Note that displacements are expressed with respect to the borehole top (positive displacements on the A axis indicate movements to the SSE). Steps in the cumulative displacement profile are interpreted as localised displacements on active fractures. In the upper part of the curves, constantly decreasing (A) and increasing (B) cumulative displacements indicate that the lower part of the blocks between the active fractures is rotated to NW which is identical with a toppling movement to the SW. In the middle part both cumulative displacement profiles are vertical which is interpreted as a sign for the absence of block rotations. In the lowermost section increasing (A) and decreasing (B) cumulative displacements indicate that the lower part of the blocks rotates towards SW.

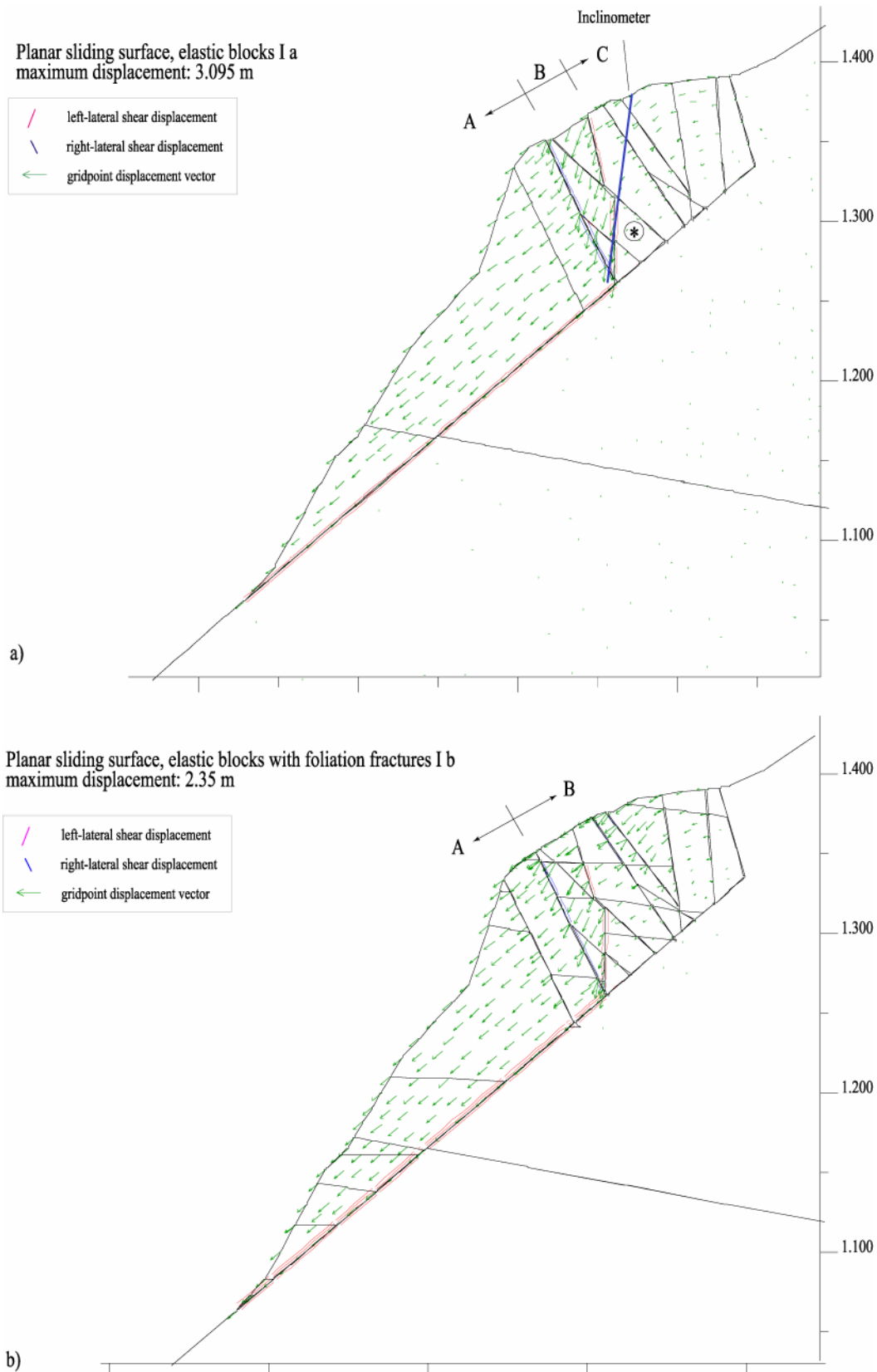


Figure 4-10: a) Model I a - planar sliding surface with elastic blocks (a). Three areas A-C with different displacement patterns were distinguished. The \* highlights a block with small displacements intersected by the borehole. Predicted borehole displacement profiles are given in Figure 4-12. b) Model I b - planar sliding surface with elastic blocks with foliation fractures. Only two areas A-B with different displacement patterns were distinguished.



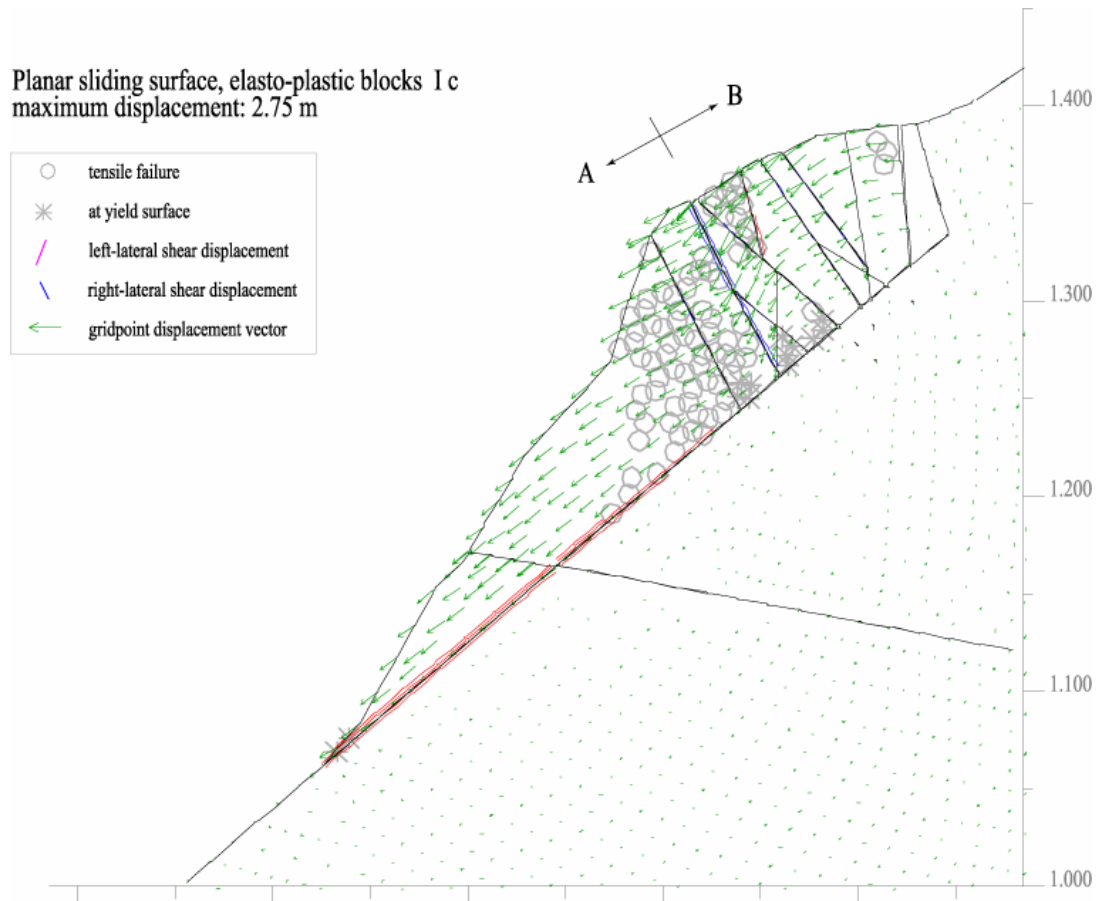


Figure 4-11: Model I c - planar sliding surface with elasto-plastic blocks. Grey circles indicate that internal damage by tensile failure occurs mainly in the large blocks of area A; in area B only some blocks show internal damage.



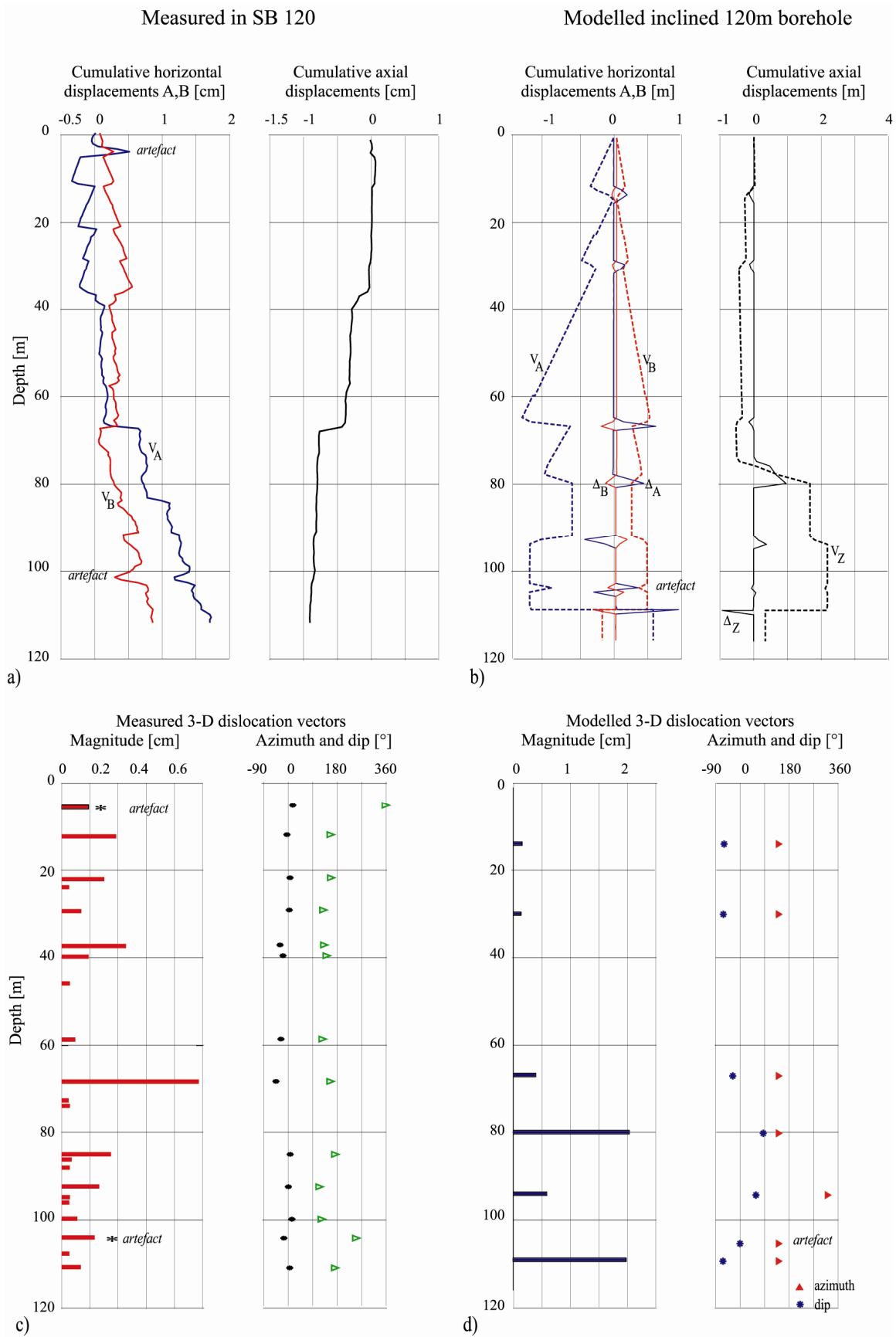


Figure 4-12: Comparison of measured displacement profiles from SB 120 (a,c) and predicted displacement profiles for model I a - planar sliding surface with elastic blocks (b,d). The displacements are expressed with respect to the borehole top and cannot be directly compared against the absolute block displacements shown in Figure 4-10a.

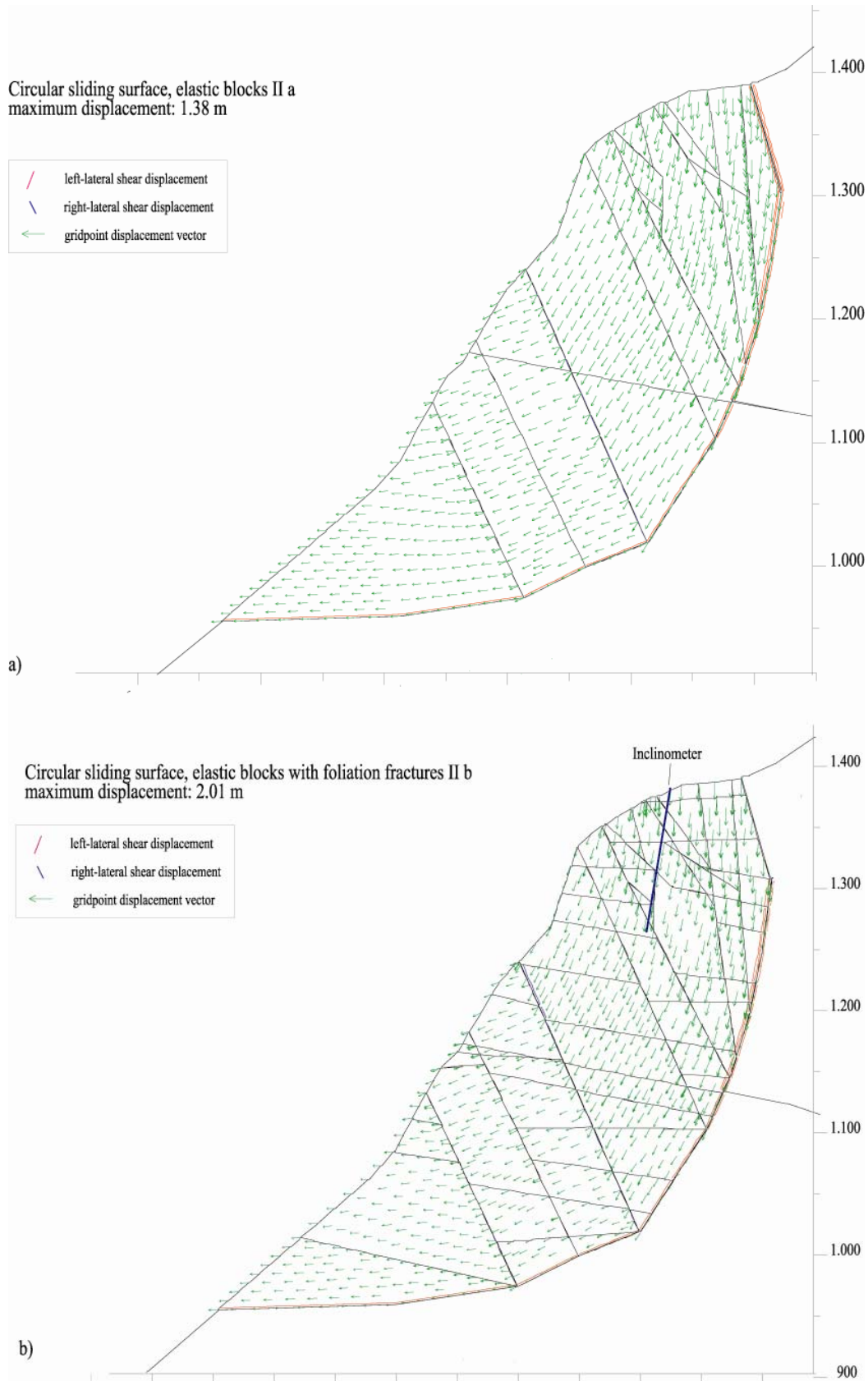


Figure 4-13: Model II a and II b - circular sliding surface with elastic blocks (a) and circular sliding surface with elastic blocks with foliation fractures (b). Next to the circular sliding surface steep fractures dipping away from the valley were added to the model. Predicted borehole displacement profiles for case II b are given in Figure 4-15.

Circular sliding surface, elasto-plastic blocks II c  
maximum displacement: 3.63 m

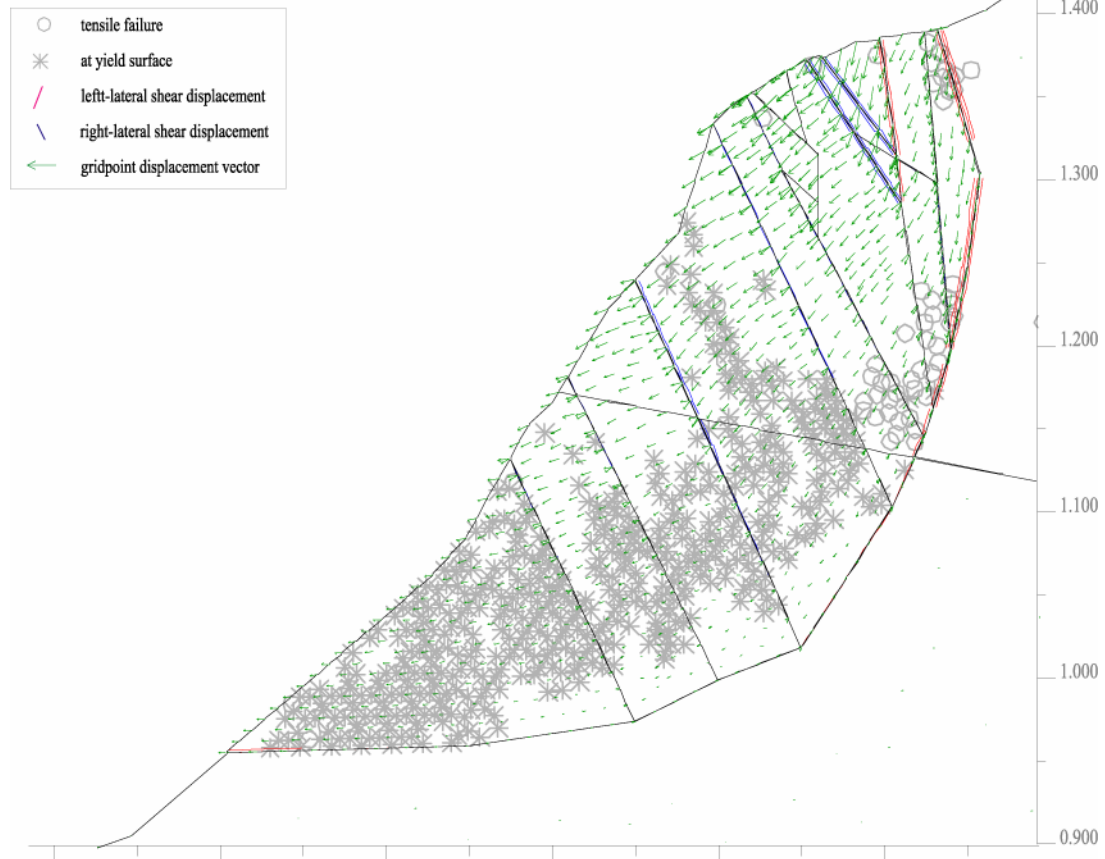


Figure 4-14: Model II c - circular sliding surface with elasto-plastic blocks.

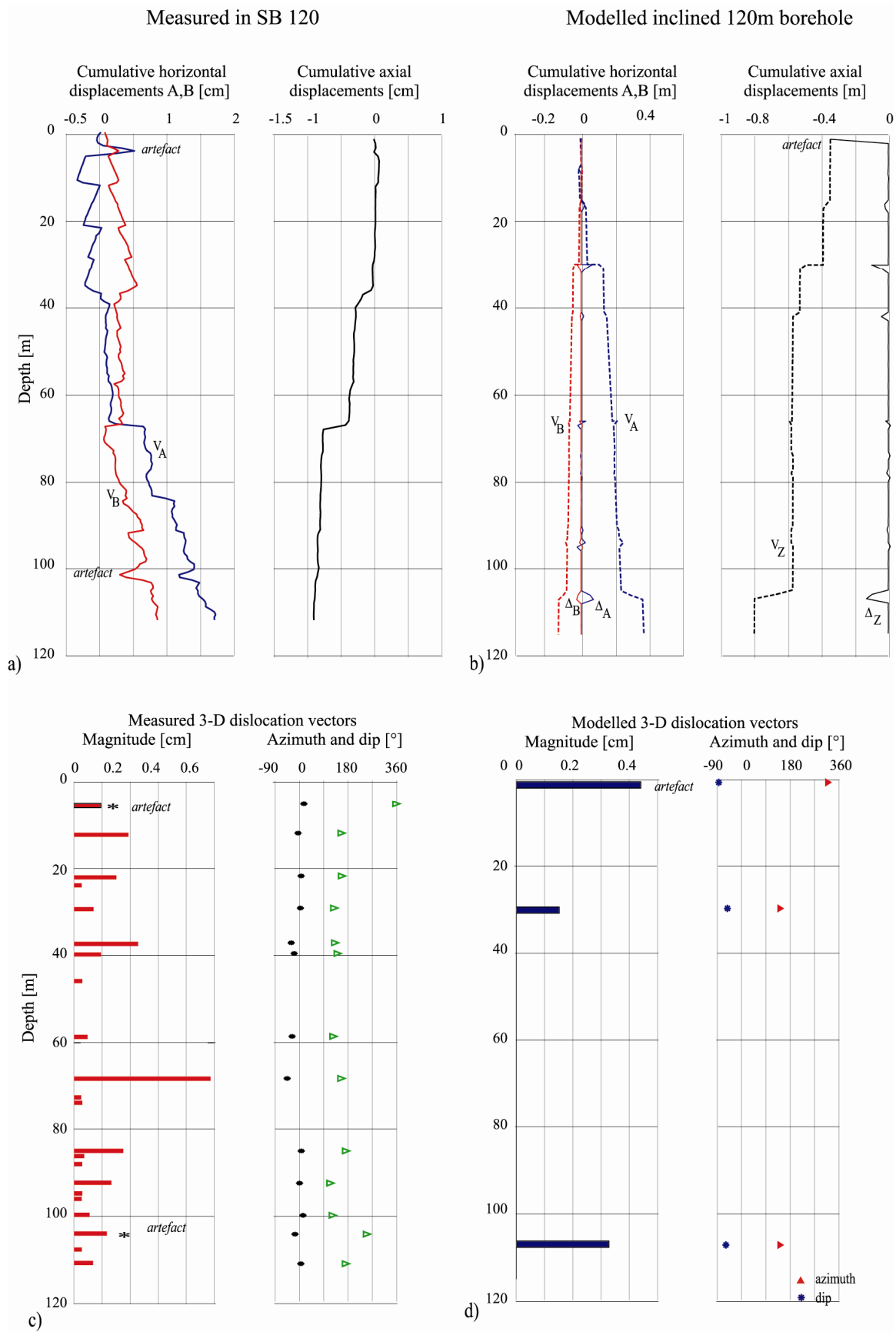


Figure 4-15: Comparison of measured displacement profiles from SB 120 (a,c) and predicted displacement profiles for model II b circular sliding surface with elastic blocks and foliation fractures (b,d). The displacements are expressed with respect to the borehole top and cannot be directly compared against the absolute block displacements shown in Figure 4-13b.

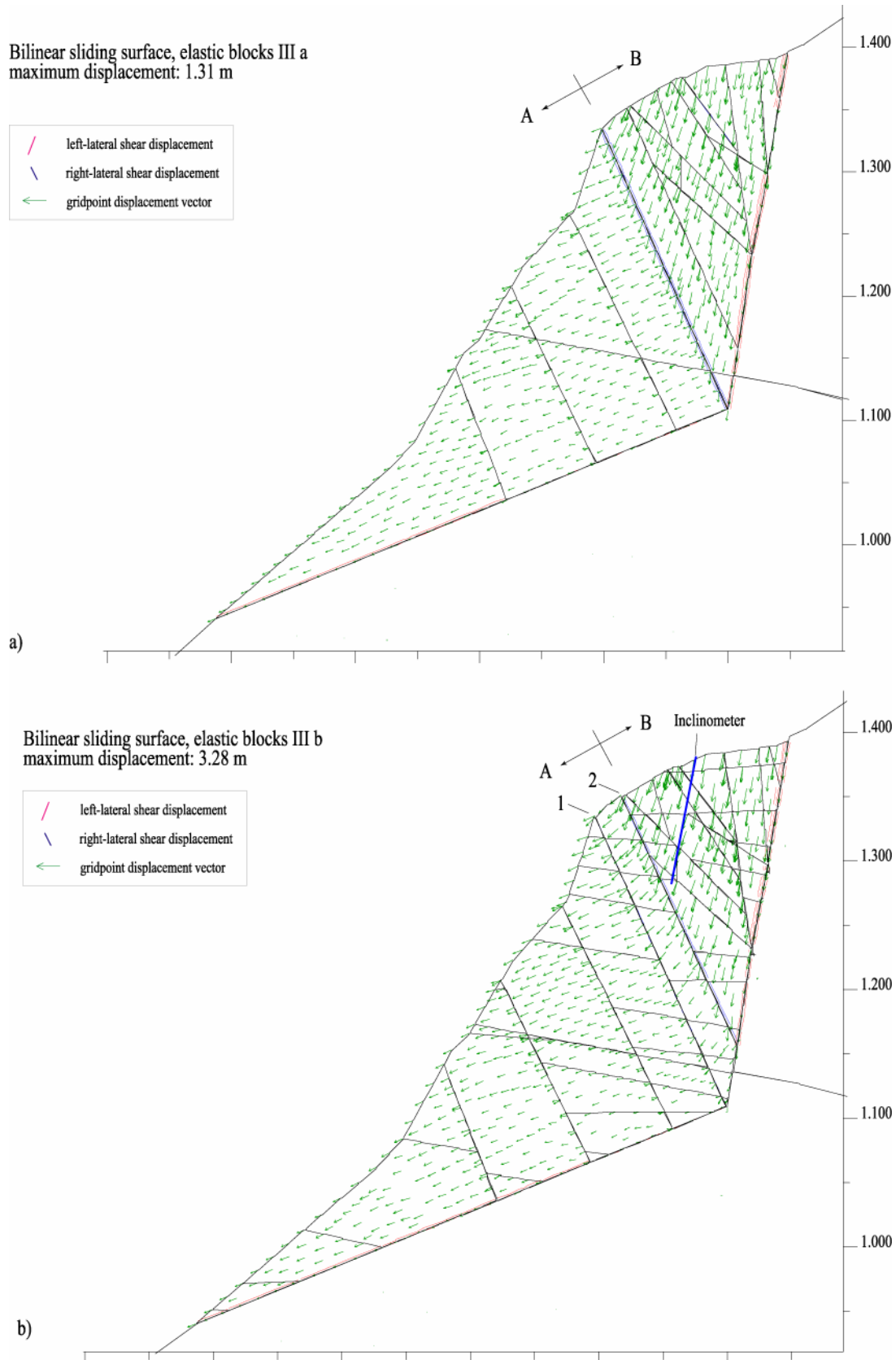


Figure 4-16: a) Model III a and III b - bilinear sliding surface with elastic blocks. In area A the displacement vectors are parallel to the lower sliding surface, in area B parallel to the steep back limitation of the unstable rock mass b) Model III b - bilinear sliding surface with elastic blocks with foliation fractures. Two fractures (1-2) accommodate the internal deformation of the block assembly. Predicted borehole displacement profiles are shown in Figure 4-18.

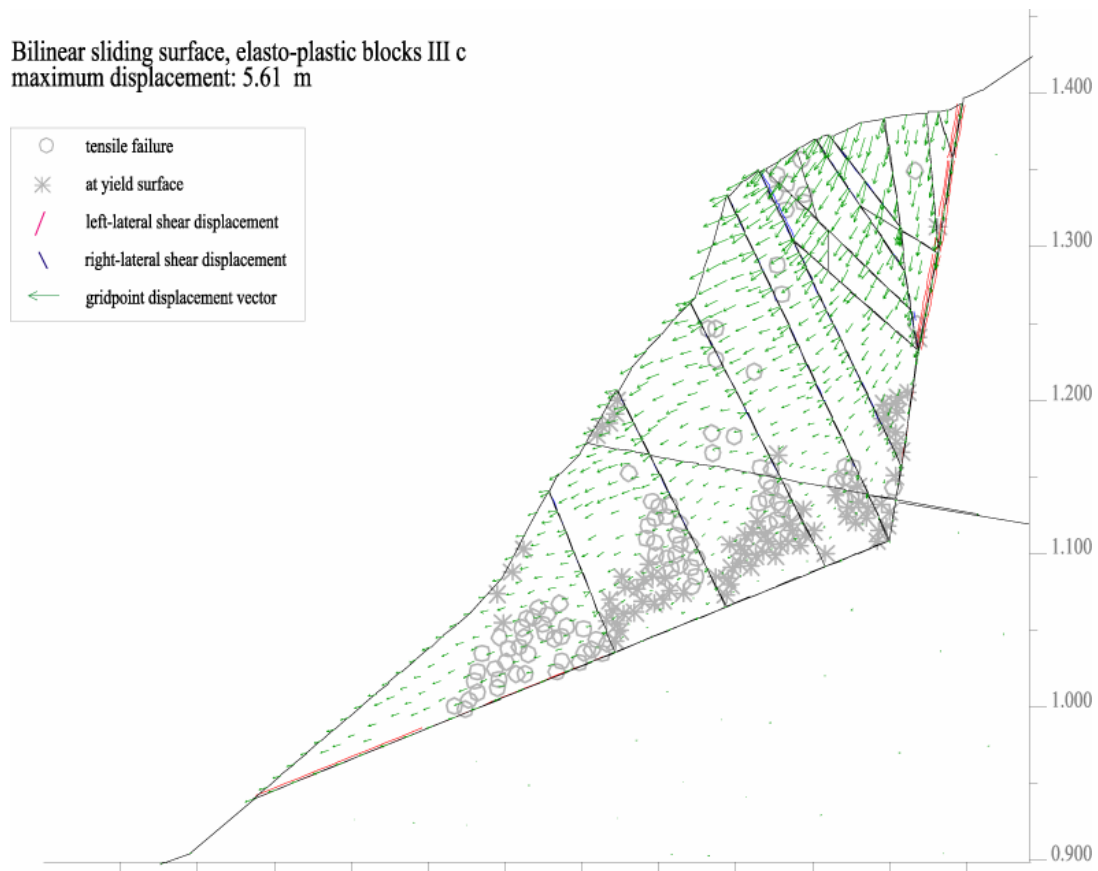


Figure 4-17: Model III c - bilinear sliding surface with elasto-plastic blocks.

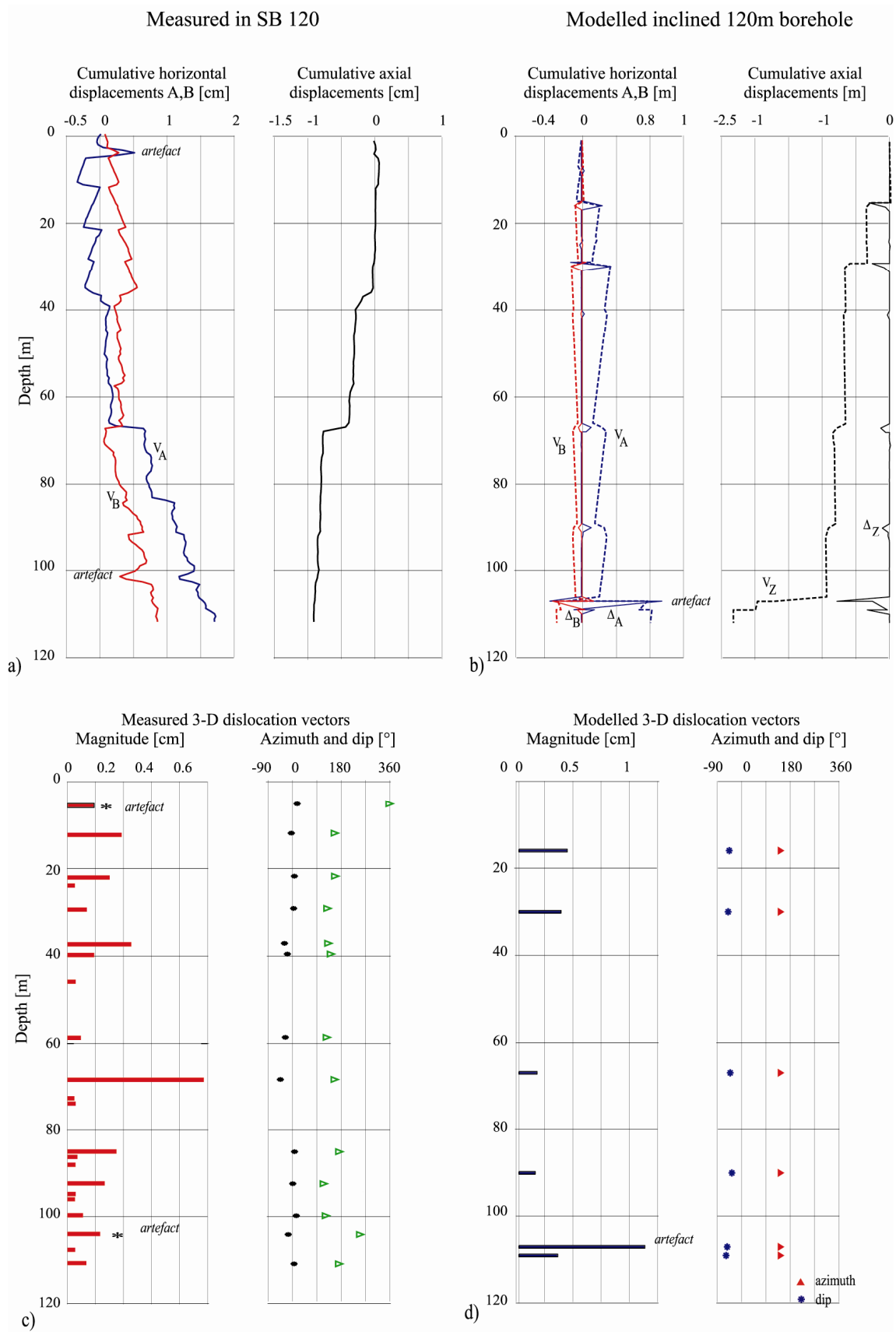
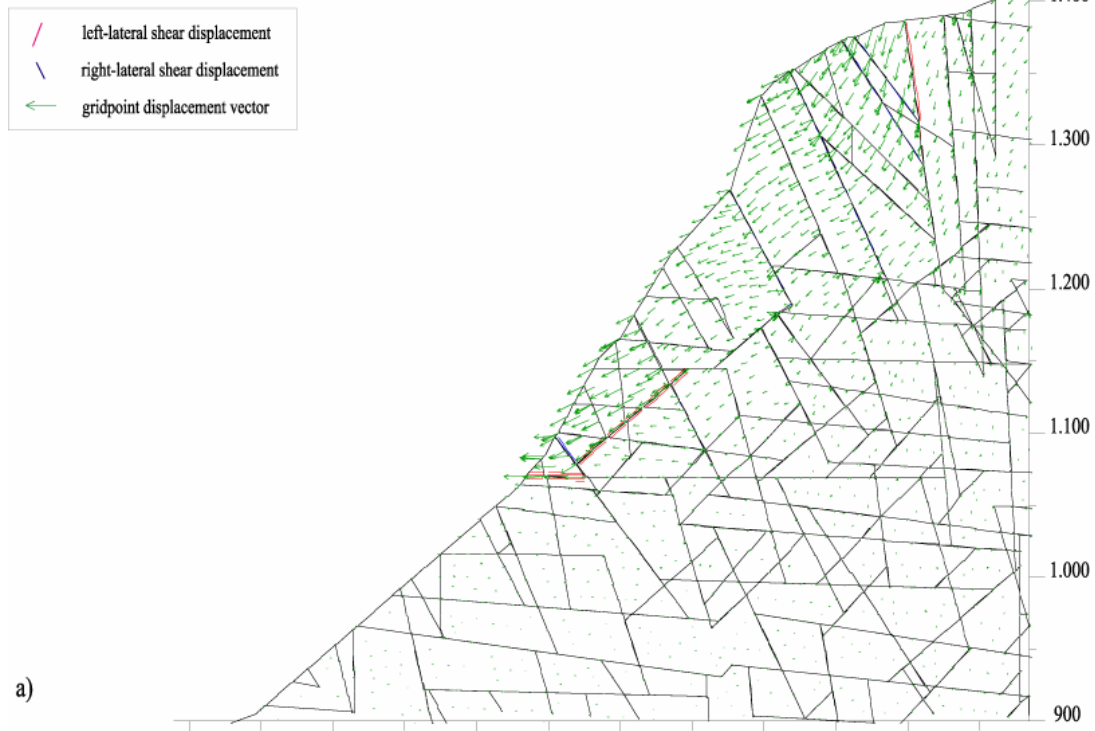


Figure 4-18: Comparison of measured displacement profiles from SB 120 (a,c) and predicted displacement profiles for model III b - bilinear sliding surface with elastic blocks with foliation fractures (b,d). The displacements are expressed with respect to the borehole top and cannot be directly compared against the absolute block displacements shown in Figure 4-16.

Stepped sliding surface, elastic blocks IV a  
maximum displacement: 1.79 m



Stepped sliding surface, elastic blocks with foliation fractures IV b  
maximum displacement: 2.78 m

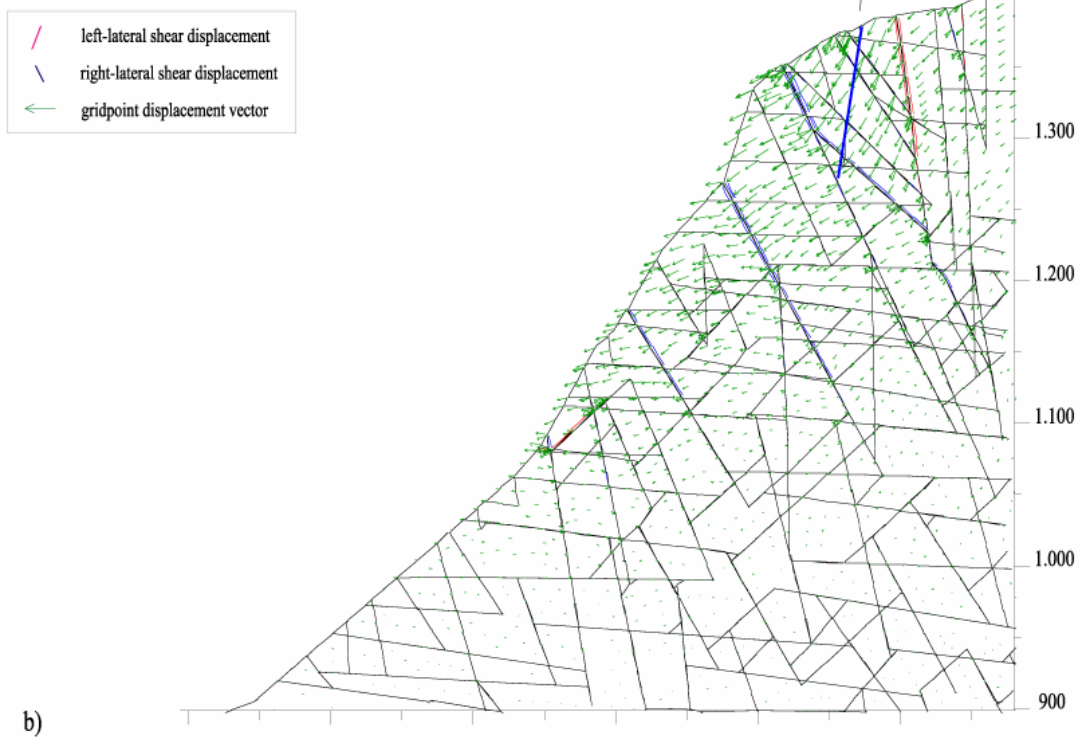


Figure 4-19: a) Model IV a and IV b - stepped sliding surface with elastic blocks. Foliation fractures were only added below the investigated part of the rock mass. b) Model IV b - stepped sliding surface with elastic blocks with foliation fractures. Predicted borehole displacement profiles are given in Figure 4-21.



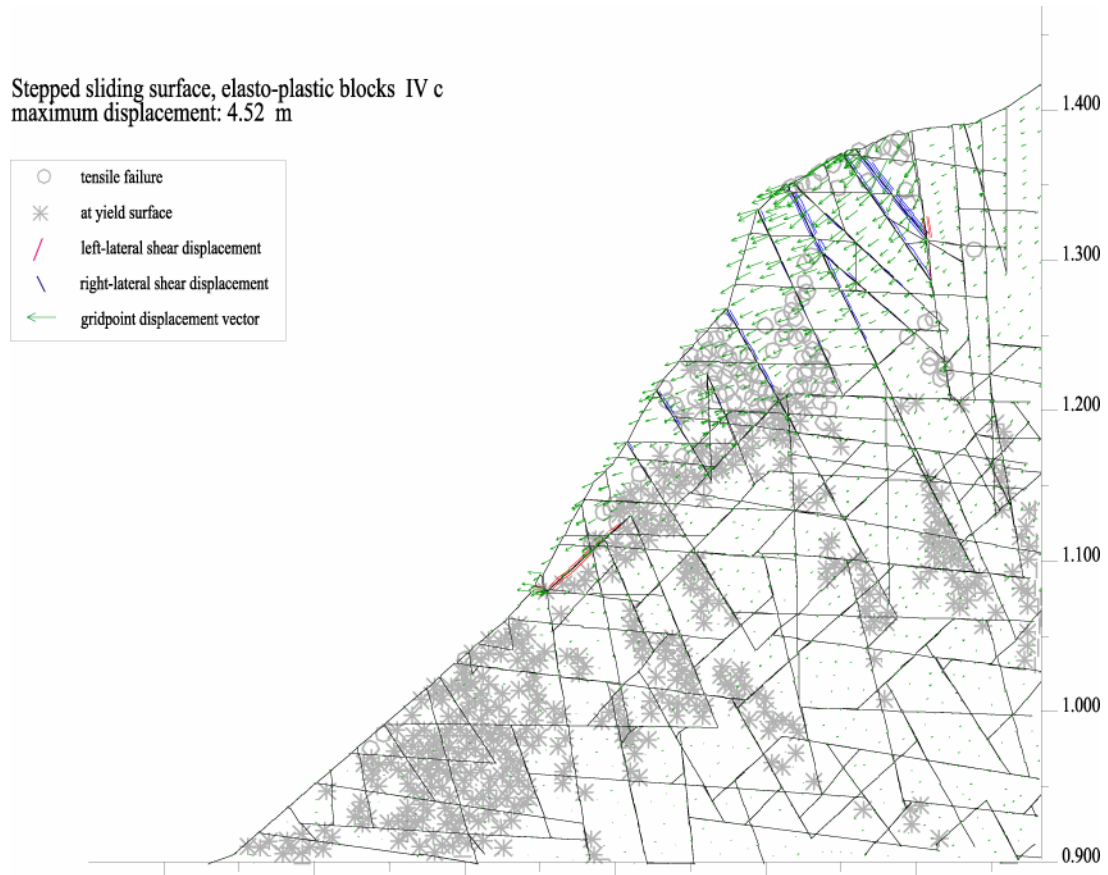


Figure 4-20: Model IV c - stepped sliding surface with elasto-plastic blocks with foliation fractures. Internal damage by tensile failure and yielding connects the intermittent fractures dipping towards the valley. In the lower part of the figure (<1100 m model height), internal damage is controlled by yielding.

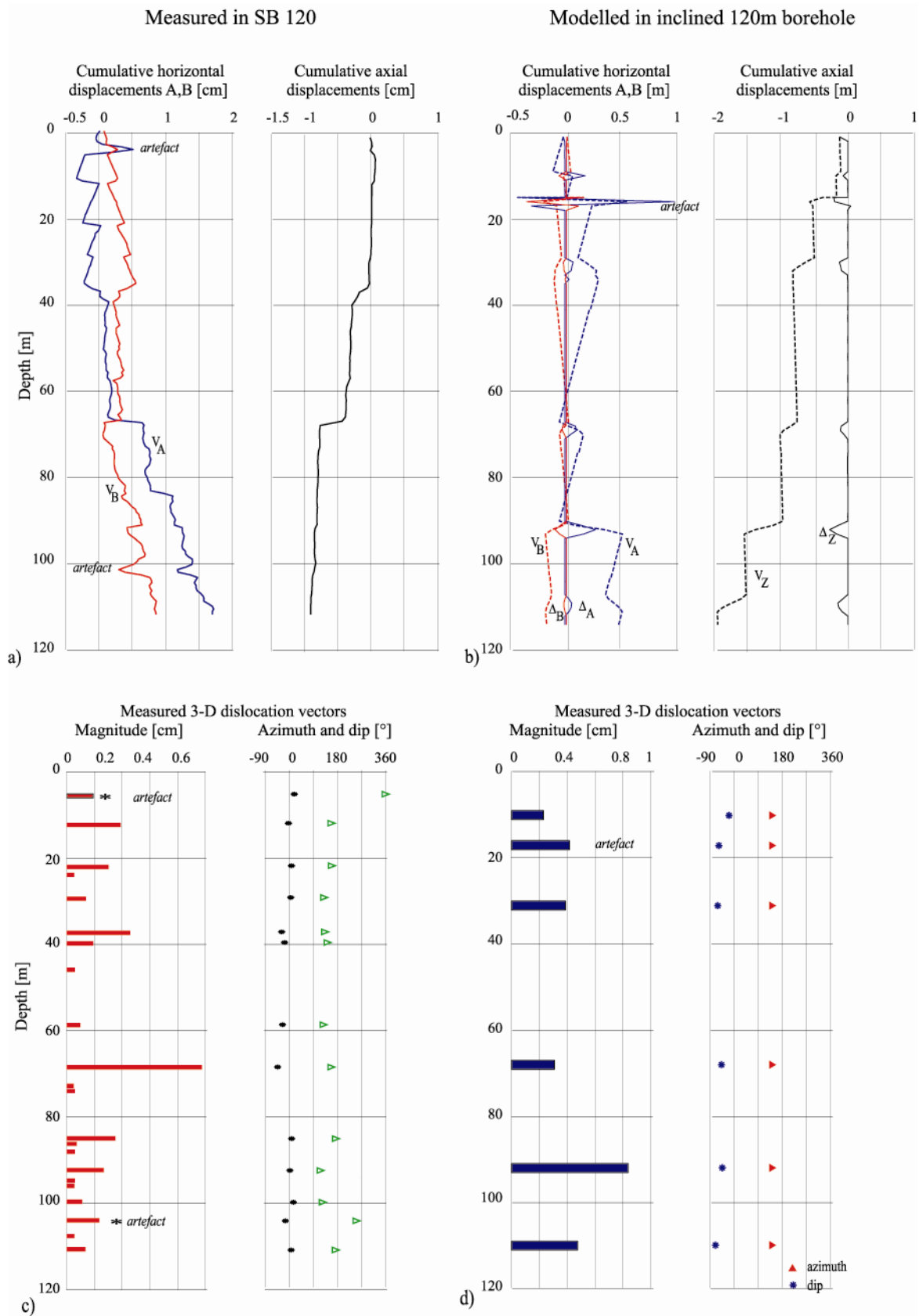


Figure 4-21: Comparison of measured displacement profiles from SB 120 (a,c) and predicted displacement profiles for model IV b - stepped sliding surface with elastic blocks with foliation fractures (b,d). The displacements are expressed with respect to the borehole top and cannot be directly compared against the absolute block displacements shown in Figure 4-19b.

## **5 Conclusions and perspectives**

## 5.1 Conclusions

The work and results presented in this thesis provide detailed insights into the internal structure and kinematics of an unstable slope in massive crystalline rock. The investigations were performed on an unstable rock mass located next to the scarp of a large rockslide that occurred in 1991 above the village Randa (Valais, Switzerland). The local geology is characterised by gneisses and some schists with foliation dipping away from the valley. Under such conditions, the underlying instability mechanism depends strongly on the internal structure of the rock mass. With the aid of three deep boreholes drilled into the unstable rock mass to depths of up to 120 m, a 3-D geological model for the slope was developed and compared against the results of geophysical borehole and surface experiments. The boreholes also allowed for extending the displacement fields measured at the surface into depth. As such the internal structure and the displacement patterns of the unstable rock mass could be assessed and subsequently compared against modelled displacements to constrain the instability scenario of the study site. These revealed the complex nature of the present-day rockslide most notably with respect to the heterogeneity of the displacement patterns. These arise from the intersection of various fault and fracture zones that dissect the rock mass into blocks. The integration of the 3-D geological model, the displacement data and the insights gained through numerical modelling used to study how displacement patterns relate to the geological structure of a rock slope, pointed to the conclusion that the displacement patterns measured at the investigated slope instability can be explained without assuming the presence of highly persistent pre-existing discontinuities. Instead, several auxiliary fracture- and fault sets can allow for a stepped sliding surface to accommodate the displacements. Under such conditions, progressive failure mechanisms can lead to the formation of a through-going failure surface with time.

The following sections summarise the findings of the mapping, monitoring and modelling studies. Based on these, several implications with respect to the slope stability assessment in massive rocks are given.

### 5.1.1 Integrating geological and geophysical investigations towards a 3-D engineering geological model of an unstable slope in crystalline rock

The mapping area is situated within a sequence of polymetamorphic paragneisses together with intercalations of orthogneisses from a metamorphosed Permian granitic intrusion. Geological outcrop and scanline mapping, aerial photograph analysis and the results of geophysical borehole and surface experiments (i.e. georadar and seismics) were used in to investigate the internal structure of the rock slope. Rock mechanics laboratory testing was performed to derive estimates of intact rock strength and other key material properties required for numerical modelling. The following main findings were made:

- Based on intact rock strength two gneissic rock units could be differentiated from the seven lithologies accounted for within the mapping area by field mapping. These lithologies were grouped in mostly fine grained chloritic gneisses that are relatively more ductile and often deformed by small-scale folding (A) and feldspar-rich, homogeneous or porphyritic gneisses and the quartz-rich dark gneisses which represent massive, brittle rocks (B). Intact rock strength parameters for samples from these two lithology groups reveal that these groups can be distin-

guished as well by different strength properties ( $\sigma_{UCS} = 63\text{MPa}$  for group A gneisses instead of  $\sigma_{UCS} = 88\text{MPa}$  for group B gneisses).

- The discontinuity network consists of a large-scale fault and fracture zone and a small-scale fracture network with a trace-length threshold of 5 m. The fault and fracture zone network is dominated by two steep sets with dip directions to the NW and E, and one fault set parallel to foliation, dipping  $20^\circ$  W. As such, the major faults with NW dip directions and the foliation features dip away from the valley. The small-scale fracture network was found to involve steep fractures with a variety of dip directions and two moderately inclined sets dipping to NE and NW, which is perpendicular and opposite respectively to the direction of geodetically determined surface displacements.
- Statistical properties of the small-scale fracture network could be assessed by scanline mapping. Large-scale faults and fracture zones mapped on the surface and in the boreholes were described as a network of discrete fractures and extrapolated using results of geophysical experiments. Analysis of single-hole georadar reflection profiles proved capable of imaging active fractures seen on the optical televiewer images and allowed their minimum extension from the borehole to be estimated. Most of the mapped fractures with persistences greater than 30 m were found to be active. The geological data from borehole and surface mapping were also compared against 3-D surface georadar, which allowed moderately inclined faults and fracture zones identified on the surface to be traced at depth. The integration of the lithological and fracture data with a 2-D grid of active seismic refraction tomography profiles provided only limited input for delineating discrete faults and fracture zones.
- Within the unstable rock mass where the boreholes are located, the faults and fracture zones were found to dissect the rock mass into blocks with dimensions ranging from 10 to 20 m.
- With respect to identifying possible sliding surfaces, only few fractures or faults dipping towards the valley (i.e. to the SE) could be identified, their occurrence being apparently linked to the foliation-parallel faults.

### **5.1.2 Establishing a block kinematic model for the study site using a multi-component geotechnical monitoring system**

Geodetic measurements of surface displacements provided by CREALP indicate that surface displacement vectors dip  $20\text{-}50^\circ$  to the SE and show displacement rates of  $1.5\text{-}2$  cm/year. To further improve the network of surface displacement measurements, continuously recording crackmeters and benchmark quadrilaterals were installed across opening fractures. The monitoring systems in the three deep boreholes (i.e. 120, 50 and 50 m) were installed to record displacements, water pressures and microseismicity. Based on monitoring results from the surface and in the boreholes the following insights into the kinematic behaviour of the unstable rock mass could be gained:

- The surface displacement field is heterogeneous with displacements decreasing from the scarp of the 1991 rockslide to the NW. The differential movements are accommodated by the large-scale fault and fracture zone network. Surface fracture opening rates were monitored as having a constant trend (up to 4 mm/year) with an overprint of annual fluctuations of possibly thermo-elastic origin.

- 
- The measured displacement data from the inclinometer-/extensometer surveys were analysed with the focus being directed towards improving the signal quality by carefully correcting for systematic errors. This was necessary because the signals were relatively small. Three sources of errors that are manifest in inclined boreholes with contorted inclinometer casings were corrected for by applying: i) an empirical torsion correction, ii) depth matching of measurement intervals, and iii) correction of sensor rotation errors. After applying these corrections, resulting displacement profiles revealed on-going internal deformation of the sliding mass accommodated along major fractures and faults dipping NW (i.e. away from the valley). The most active fractures accommodate dislocations of up to 5 mm/year with a tendency for blocks in the footwall to be displaced towards the valley with respect to those in the hangingwall. The dislocations largely involve shear movement in a normal faulting sense (i.e. footwall moves up-dip with respect to hanging wall); however, several fractures at depth also show a significant component of opening. The cumulative horizontal displacement profiles measured in SB 120 suggested that the upper 40-50 m of the rock mass are subjected to toppling, followed by a 30 m section of translational sliding; the lowermost blocks were found to exhibit sliding with rotation of the block bottom towards the valley.
  - The bottom of SB 120 was found to be moving towards the valley with respect to the borehole top, which indicates that the boreholes drilled into the unstable rock mass did not reach stable ground. Thus the measured displacement fields characterised only the internal block displacements within the unstable rock mass. These displacement patterns exhibit a high degree of complexity and are probably influenced, if not governed, by the geometry of the basal sliding surface(s).
  - Within the deep boreholes, localised perched ground water tables were encountered a few meters above the borehole bottoms. The records of piezometric pressures in the boreholes show annual fluctuations of 1-2 m.
  - To date, the continuously recorded surface fracture opening series showed only small and steady displacement rates without indicators for an influence of precipitation or water table changes in the boreholes. Given that the monitoring period to date spans only two years, further monitoring is required to gain insights into the behaviour of the instability with respect to strong precipitation or snow melt events.

### **5.1.3 Modelling the internal kinematics and deformation of a complex rockslide based on field data constraints**

Numerical modelling was performed in order to identify and constrain possible sliding surface scenarios that would cause displacement patterns similar to those measured at the study site. This involved comparing modelled and measured displacement patterns. The displacement patterns on the surface and at depth were modelled using simplified 2-D distinct element models which incorporated the active structures identified by mapping and geotechnical monitoring. Of particular importance to the modelling was the reproduction of modes of deformation along explicitly modelled inclinometer-/extensometer data in the 120 m deep borehole (i.e. toppling, translation and back-rotation of blocks). Four failure modes relating to the slide surface geometry were considered: i) planar sliding surface, ii) circular sliding surface, iii) bilinear sliding surface, and iv) step-path sliding surface.

- 
- The predicted displacement patterns for most models were highly complex. The blocky nature of the fractured rock mass was found to introduce a high variability in deformation modes (e.g. toppling, rotation, sliding), even for simple sliding surface geometries.
  - The different model results depended strongly on the geometry of the sliding surface, but only to a limited extent on the different constitutive material representations assumed for the intact blocks (i.e. elastic *vs.* elasto-plastic).
  - Modelling results showed fairly good agreement between the measured and modelled displacement patterns for the step-path sliding surface models. Good agreement between the simulated and measured borehole displacements was also obtained for a persistent planar sliding surface. However, the model with non-persistent sliding surfaces is more in accord with the mapped fracture network geometry. Predicted tensile block failure at the end points of the non-persistent fractures dipping towards the valley suggested the possible formation of a through-going failure surface by means of progressive failure.
  - Further modelling is needed to understand the rotations measured in the lowermost blocks intersected by the borehole; within the described study only the combination of toppling and translational sliding could be modelled.

#### **5.1.4 Implications for the slope stability assessment of the present day instability**

In order to provide a standard slope stability assessment of the present-day instability above the village of Randa, the volume of the unstable rock mass and the degree to which potential failure surface(s) have developed are crucial parameters. As the location and geometry of basal sliding surface(s) and the lower lateral limitation of the unstable rock mass could not be assessed by mapping or monitoring, these parameters remained unconstrained. Nevertheless, the displacement measurements at the surface and at depth suggest that the unstable rock mass is dissected into various blocks that move incoherently. As such, similarities with the 1991 rockslides can be suggested. For the 1991 events, the long duration and relatively small travel distances were explained by the blocky structure of the rock mass and the absence of a highly-persistent, pre-existing sliding surface. Whether a future rockslide from the present-day instability will have the same behaviour concerning duration and travel distance, will strongly depend on the circumstances under which failure occurs, and on whether these could control the triggering of any secondary mass movements from mobilised debris or valley infill.

## **5.2 Perspectives and recommendations for further studies**

This study clearly demonstrates that the understanding of complex rockslides can be significantly improved by combining mapping, geophysical experiments, displacement monitoring at the surface and in boreholes, and numerical modelling. Still, suggestions for further investigations can be made. Of importance would be the delineation of the extent of the unstable rock mass, especially at depth (i.e. the basal sliding surface), which was not feasible within the framework of this thesis.

Given that data from the geophysical experiments (i.e. crosshole and surface georadar and seismics, 3-D georadar reflection data of the third investigation area around SB 120, 3-D refraction

tomography) are still in different stages of processing, it is suggested that the geological model for the upper part of the unstable slope should be refined as new results come to light. Another important improvement can be expected with respect to the displacement data, since longer time series of periodic and continuous measurements will lead to an improvement in the signal to noise ratio.

Further investigations into the internal structure of the unstable rock mass should be directed towards the lower area between 1900 and 2200 m elevation and towards the 1991 rockslide scarp. As these regions are difficult to access, it is suggested to assess the fracture patterns of the steep flanks and the scarps using photogrammetric techniques. These investigations should also provide input for better constraining the basal and lateral boundaries of the present-day instability. In this context it is also suggested that further displacement monitoring should also focus on determining the transition from the stable to the unstable rock mass across the slide body. This could be achieved by means of a denser network of geodetic retro-reflectors extending into the scarp region or by remote sensing techniques (e.g. ground based radar interferometry or differential GPS measurements).

Based on these new insights the modelling study should then be extended into 3 dimensions to improve the fracture network representation in the distinct element models. For example, an improved grid search modelling study could be initiated for systematically comparing modelled and measured displacement fields once the location of the basal sliding surface is known. These 3-D models could also be extended to model the 1991 rockslide events in order to address the open question as to how the proposed failure surface for the first 1991 rockslide with a dip towards the NE contributed to the slope failure.



## References

- Aargand, E. 1916. Sur l'arc des Alpes Occidentales. *Eclogae Geologicae Helvetiae* 14: 145-204.
- Agliardi, F., Crosta, G. B. & Zanchi, A. 2001. Structural constraints on deep-seated slope deformation kinematics. *Engineering Geology* 59: 83-102.
- Amstad, C., Koeppel, J. & Kovari, K. 1988. TRIVÉC - measurements in geotechnical engineering. In: *2nd International Symposium on Field Measurements in Geomechanics*: 17-32.
- Barton, N. 1973. Review of a new shear-strength criterion for rock joints. *Engineering Geology* 7(4): 287-332.
- Baum, R. L., Johnson, A. M. & Fleming, R. W. 1988. Measurement of slope deformation using quadrilaterals. *US Geological Survey Bulletin* 1842: b1-b23.
- Bearth, P. 1964. Geologischer Atlas der Schweiz - Blatt: Randa. 1:25000.
- Bearth, P. 1964. Geologischer Atlas der Schweiz - Erläuterungen zum Blatt Randa. Bern, Kümmerly & Frey. 27.
- Bhasin, R. & Kaynia, A. M. 2004. Static and dynamic simulation of a 700-m high rock slope in western Norway. *Engineering Geology* 71(3-4): 213-226.
- Bloetzer, W. & Stoffel, M. 1998. Klimawandel als Herausforderung für die Raumplanung der Vispertäler. In: Bloetzer, W., et al. (ed). *Synthesebericht NFP 31 - Klimaänderungen und Naturgefahren in der Raumplanung*: 127-187. Zürich, vdf Hochschulverlag.
- Bogaard, T. A., Antoine, P., Desvarreux, P., Giraud, A. & van Asch, T. W. J. 2000. The slope movements within the Mondorès graben (Drôme, France); the interaction between geology, hydrology and typology. *Engineering Geology* 55: 297-312.
- Brasser, J. P. & Gruner, U. 2002. Behebung der Felssturzgefahr bei Innertkirchen durch zwei Grosssprengungen. *Felsbau* 20(5): 195-202.
- Bussy, F., Sartori, M. & Thélin, P. 1996. U-Pb zircon dating in the middle Penninic basement of the Western Alps (Valais, Switzerland). *Schweizerische Mineralogische und Petrographische Mitteilungen* 76: 81-84.
- Canuti, P., Casagli, N., Moretti, S., Leva, D., Sieber, A. J. & Tarchi, D. 2002. Landslide monitoring by using ground-based radar differential interferometry. In: *Landslides - First European Conference on Landslides, Prague*: 523-528.
- Cappa, F., Guglielmi, Y., Soukatchoff, V. M., Mudry, J., Bertrand, C. & Charmoille, A. 2004. Hydromechanical modeling of a large moving rock slope inferred from slope levelling coupled to spring long-term hydrochemical monitoring: example of the La Clapiere landslide (Southern Alps, France). *Journal of Hydrology* 291(1-2): 67-90.
- Chowdhury, R. 1992. Progressive failure considerations in slope stability analysis. In: *6th International Symposium on Landslides, Christchurch*: 1659-1663.
- Coggan, J. S. & Pine, R. J. 1996. Application of distinct-element modelling to assess slope stability at Delabole slate quarry, Cornwall, England. *Transactions of the Institution of Mining and Metallurgy (Section A, Mining industry)* 105: A22-A30.
- Cosma, C., Olsson, O., Keskinen, J. & Heikkinen, P. 2001. Seismic characterization of fracturing at the Aspö Hard Rock Laboratory, Sweden, from the kilometer scale to the meter scale. *International Journal of Rock Mechanics and Mining Sciences* 38(6): 859-865.
- Crosta, G. B. & Agliardi, F. 2002. How to obtain alert velocity thresholds for large rockslides. *Physics and Chemistry of the Earth* 27: 1557-1565.

- Cruden, D. & Varnes, D. J. 1996. Landslide types and processes. In: Turner, A. K. & Schuster, R. L. (ed). *Landslides: investigation and mitigation*: 36-75. Washington, National Academy Press.
- Cundall, P. A. & Hart, R. D. 1993. Numerical modeling of discontinua. In: Hudson, J. A. (ed). *Comprehensive rock engineering: principles, practice, and projects*: 231-343, Pergamon Press Ltd.
- Ding, X., Ren, D., Montgomery, B. & Swindells, C. 2000. Automatic monitoring of slope deformations using geotechnical instruments. *Journal of Surveying Engineering May 2000*: 57-68.
- Dowding, C. H. & O'Connor, K. M. 2000. Comparison of TDR and inclinometers for slope monitoring. In: *Geo-Denver 2000, Denver, Colorado*: 80-90.
- Dunnicliff, J. 1988. *Geotechnical instrumentation for monitoring field performance*. New York, John Wiley & Sons Inc. 577.
- Duzgun, H. S. B., Yucemen, M. S. & Karpuz, C. 2002. A probabilistic model for the assessment of uncertainties in the shear strength of rock discontinuities. *International Journal of Rock Mechanics and Mining Sciences* 39(6): 743-754.
- Eberhardt, E., Spillmann, T., Maurer, H. R., Willenberg, H., Loew, S. & Stead, D. 2004. The Randa Rockslide Laboratory: Establishing brittle and ductile instability mechanisms using numerical modelling and microseismicity. In: *International Symposium on Landslides, Rio de Janeiro*: 481-487.
- Eberhardt, E., Stead, D. & Coggan, J. S. 2004. Numerical analysis of initiation and progressive failure in natural rock slopes - the 1991 Randa rockslide. *International Journal of Rock Mechanics and Mining Sciences*(41): 68-87.
- Eberhardt, E., Willenberg, H., Loew, S. & Maurer, H. R. 2001. Active rockslides in Switzerland - understanding mechanisms and processes. In: *International Conference on Landslides - Causes, Impacts and Countermeasures, Davos*: 25-34.
- Einstein, H. H. 1993. Modern developments in discontinuity analysis - the persistence-connectivity problem. In: Hudson, J. A. (ed). *Comprehensive rock engineering*: 193-213. Oxford, Pergamon Press.
- Einstein, H. H. & Lee, J. S. 1995. Topological slope stability analysis using a stochastic fracture geometry model. In: *Fractured and Jointed Rock Masses, Lake Tahoe, California*.
- Einstein, H. H. & Stephansson, O. 2000. Fracture systems, fracture propagation and coalescence. In: *GeoEng 2000: An International Conference on Geotechnical & Geological Engineering, Melbourne*.
- Einstein, H. H., Veneziano, D., Baecher, G. B. & O'Reilly, K. J. 1983. The effect of discontinuity persistence on rock slope stability. *International Journal of Rock Mechanics and Mining Sciences* 20(1): 227-236.
- Ellis, A. C., Barnicoat, A. C. & Fry, N. 1989. Structural and metamorphic constraints on the tectonic evolution of the upper Pennine Alps. In: Coward, M. P., et al. (ed). *Alpine Tectonics*: 173-188.
- Epard, J.-L. & Escher, A. 1996. Transition from basement to cover: a geometrical model. *Journal of Structural Geology* 18(5): 533-548.
- Escher, A. 1988. *Structure de la nappe du Grand-Saint-Bernard entre le val de Bagnes et les Mischabel*. Landeshydrologie und -geologie, Bern
- Escuder Viruete, J., Carbonell, R., Marti, D., Jurado, M. J. & Perez-Estaun, A. 2003. Architecture of fault zones determined from outcrop, cores, 3-D seismic tomography and geostatistical modeling: example from the Albalá Granitic Pluton, SW Iberian Variscan Massif. *Tectonophysics* 361(1-2): 97-120.
- Eyer, W., Gubler, H. U., Keusen, H. R. & Naef, O. 1998. Frühwarndienste - Stand der Erkenntnisse und Anwendungsbeispiele. Rageth, T., Forstliche Arbeitsgruppe Naturgefahren.
- Fraefel, M. 2002. *Geologische und ingenieurgeologische Untersuchungen am Lago di Poschiavo (Val Poschiavo, Graubünden)*. Diploma thesis, Ingenieurgeologie, Swiss Federal Institute of Technology: 103.

- Fruneau, B., Achache, J. & Delacourt, C. 1996. Observation and modelling of the Saint-Etienne-de-Tinee landslide using SAR interferometry. *Tectonophysics* 265(3-4): 181-190.
- Gehle, C. & Kutter, H. K. 2003. Breakage and shear behaviour of intermittent rock joints. *International Journal of Rock Mechanics and Mining Sciences* 40: 687-700.
- Gili, J. A., Corominas, J. & Rius, J. 2000. Using Global Positioning System techniques in landslide monitoring. *Engineering Geology* 55: 167-192.
- Girod, F. 1999. Altération météorique de roche granitique en milieu alpin: le cas de l'othogneiss associé à l'éboulement de Randa (Mattertal, Valais, Suisse). Thèse de doctorat, Faculté de Sciences de l'Université de Lausanne, Université de Lausanne: 207.
- Girod, F. & Thélin, P. 1998. Weathering of granitic rock in the Alps: preliminary results from orthogneiss associated with the Randa rockfall (Matter Valley, Valais, Switzerland). *Schweizerische Mineralogische und Petrographische Mitteilungen* 78: 179-184.
- Goodman, R. E. & Shi, G. H. 1985. Block theory and its application in rock engineering. Englewood Cliffs, New Jersey, Prentice-Hall. 338.
- Grasmück, M. 1996. 3-D georadar mapping, looking into the subsurface. *Environmental and Engineering Geoscience* 2: 195-200.
- Green, A., Gross, R., Holliger, K., Horstmeyer, H. & Baldwin, J. 2003. Results of 3-D georadar surveying and trenching the San Andreas fault near its northern landward limit. *Tectonophysics* 368(1-4): 7-23.
- Gruber, S. & Hoelzle, M. 2001. Statistical modelling of mountain permafrost distribution: local calibration and incorporation of remotely sensed data. *Permafrost and Periglacial Processes* 12: 69-77.
- Harrison, J. C. & Herbst, K. 1977. Thermoelastic strains and tilts revisited. *Geophysical Research Letters* 4(11): 535-537.
- Hart, R. D. 1993. An introduction to distinct element modeling for rock engineering. In: Hudson, J. A. (ed). *Comprehensive rock engineering: principles, practice, and projects*: 245-261, Pergamon Press Ltd.
- Heincke, B., Green, A. G., van der Kruk, J. & Horstmeyer, H. 2004. Acquisition and processing strategies for 3-D georadar surveying a region characterized by rugged topography. *submitted to Geophysics*.
- Heincke, B., Horstmeyer, H., Meier, U. & Green, A. 2003. Investigation of fracture zones with GPR and seismic refraction tomography on an active landslide. In: *EGS-AGU-EUG Joint Assembly, Nice*: 5107.
- Heincke, B., Spillmann, T., Horstmeyer, H. & Green, A. 2002. 3-D georadar surveying in areas of moderate topographic relief. In: *Ninth International Conference on Ground-Penetrating Georadar, Santa Barbara*: 223-226.
- Helmstetter, A., Sornette, D., Grasso, J.-R., Andersen, J. V., Gluzman, S. & Pisarenko, V. 2004. Slider block friction model for landslides: Application to Vaiont and La Clapière landslides. *Journal of Geophysical Research* 109(B2).
- Hencher, S. R., Liao, Q.-H. & Monaghan, B. G. 1996. Modelling slope behaviour of open-pits. *Transactions of the Institution of Mining and Metallurgy (Section A, Mining industry)* 105: A37-A47.
- Hoek, E. & Brown, E. T. 1997. Practical estimates of rock mass strength. *International Journal of Rock Mechanics and Mining Sciences* 8: 1165-1186.
- Holloway, A. L. & Mugford, J. C. 1990. Fracture characterization in granite using ground probing radar. *Canadian Mining and Metallurgical Bulletin* 83: 61-70.
- Huber, A. 1992. Der Val Pola Bergsturz im oberen Veltlin vom 28. Juli 1987. *Eclogae Geologicae Helveticae* 85(2): 307-325.

- Hungr, O. & Evans, S. G. 2004. The occurrence and classification of massive rock slope failure. *Felsbau* 22(2).
- Imrie, A. S. & Moore, D. P. 1993. The use of rock engineering to overcome adverse geology at Revelstoke Dam. In: Hudson, J. A. (ed). *Comprehensive rock engineering: 701-725*, Pergamon Press.
- Ingraffea, A. R. 1987. Theory of crack initiation and propagation in rock. In: Atkinson, B. K. (ed). *Fracture mechanics of rocks: 71-166*. London, Academic Press Inc.
- Ischi, H., Keusen, H. R. & Scheller, E. 1991. Randa, Kt. Wallis, Bergsturz Grossgufer vom April/Mai 1991 - Zusammenfassender Bericht über die Aktivitäten der Geotest AG. Geotest AG, Martigny: 20.
- ITASCA 2000. UDEC - Universal Distinct Element Code. Minneapolis, Itasca Consulting Group, Inc.
- Jaboyedoff, M., Ornstein, P. & Rouiller, J. D. 2004. Design of a geodetic database and associated tools for monitoring rock-slope movements: the example of the top of Randa rockfall scar. *Natural Hazards and Earth System Sciences* 204(4): 187-196.
- Jäckli, H. 1962. Die Vergletscherung der Schweiz im Würmmaximum. *Eclogae Geologicae Helvetiae* 55: 285-294.
- Jing, L. 2003. A review of techniques, advances and outstanding issues in numerical modelling for rock mechanics and rock engineering. *International Journal of Rock Mechanics and Mining Sciences* 40: 283-353.
- Joris, C. L. 1995. Der Bergsturz, ein Zufallsereignis unter vielen. In: Naturforschende Gesellschaft Oberwallis (ed). *Der Bergsturz von Randa 1991 - eine Dokumentation: 43-48*, Naturforschende Gesellschaft Oberwallis.
- Karasaki, K., Freifeld, B., Cohen, A., Grossenbacher, K., Cook, P. & Vasco, D. 2000. A multidisciplinary fractured rock characterization study at Raymond field site, Raymond, CA. *Journal of Hydrology* 236: 17-34.
- Kawamoto, T. & Takeda, N. 1979. An analysis of progressive failure in rock slopes. In: *3rd International Conference on Numerical Methods in Geomechanics, Aachen: 797-808*.
- Kemeny, J. M. 1993. The micromechanisms of deformation and failure in rocks. In: *Assessment and Prevention of Failure Phenomena in Rock Engineering, Istanbul: 23-33*.
- Kennedy, B. A. & Niermeyer, K. E. 1970. Slope monitoring systems in the prediction of a major slope failure at the Chuquicamata Mine, Chile. In: *Planning Open Pit Mines, Johannesburg: 215-225*.
- Keusen, H. R. 2000. Schynige Platte, Jungfrauengebiet - Langzeitbeobachtungen an einer grossen Felsbewegung. *Felsbau* 18(3): 56-62.
- Keusen, H. R. 2002. Infrastrukturanlagen in instabilen felsigen Gebirgen - Werkzeuge für das Risikomanagement. *Felsbau* 20(5).
- Keusen, H. R. & Graf, K. 2000. A29 Berninastrasse Abschnitt Poschiavo - Campocologno Ponte Scalascia, Felsstabilität. Geotest AG, Zollikofen: 14.
- Kilburn, C. R. J. & Petley, D. N. 2003. Forecasting giant, catastrophic slope collapses: lessons from Vajont, Northern Italy. *Geomorphology* 1342: 1-12.
- Kovari, K. 1990. General report: Methods of monitoring landslides. In: *5th International Symposium on Landslides, Lausanne: 1421-1433*.
- Krähenbühl, R. 2004. Temperatur und Kluftwasser als Ursachen von Felssturz. *Bulletin Angewandte Geologie* 9(1): 19-35.
- Kvapil, R. & Clews, K. M. 1979. An examination of the Prandtl mechanism in large-dimension slope failures. *Transactions of the Institution of Mining and Metallurgy ( Section A, Mining industry )* 88: A1-A5.

- Ladner, F., Rovina, H., Pointner, E., Dräyer, B. & Sambeth, U. 2004. Geologische Überwachung und Instrumentierung des Felssturzes "Medji" (St. Niklaus/ Schweiz). *Felsbau* 22: 37-45.
- LaFonta, J.-G. & Beth, M. 2001. Laboratory testing of in-place inclinometers - part1: 10.
- Landeshydrologie (Bundesamt für Wasser und Geologie) 1992. Hydrologischer Atlas der Schweiz. varying scales.
- Lane, J. W., Haeni, F. P. & Williams, J. H. 1994. Detection of bedrock fractures and lithologic changes using borehole radar at selected sites. In: *5th International Conference on Ground Penetrating Radar GPR'94*, Kitchener: 557-591.
- Lavisolo, M., Ghirotto, S., Scardia, C. & Battaglio, M. 2003. The use of Differential Monitoring Stability (DMS) for remote monitoring of excavation and landslide movements. In: *Sixth International Symposium on Field Measurements in Geomechanics, Oslo*: 519-524.
- Leahey, M. 2003. Reflexionsseismik & Laufzeit-tomographie oberhalb des Felssturzes von Randa. Diploma thesis, Institut für Geophysik, Swiss Federal Institute of Technology: 101.
- MacLaughlin, M., Sitar, N., Doolin, D. & Abbot, T. 2001. Investigation of slope-stability kinematics using discontinuous deformation analysis. *International Journal of Rock Mechanics and Mining Sciences* 38: 753-762.
- Markley, M., Teyssier, C. & Caby, R. 1999. Re-examining Aargand's view of the Siviez-Mischabel nappe. *Journal of Structural Geology* 21: 1119-1124.
- Markley, M., Teyssier, C., Cosca, M. A., Caby, R., Hunziker, J. C. & Sartori, M. 1998. Alpine deformation and  $^{40}\text{Ar}/^{39}\text{Ar}$  geochronology of synkinematic white mica in the Siviez-Mischabel Nappe, western Pennine Alps, Switzerland. *Tectonics* 17(3): 407-425.
- Martel, S. J. & Peterson, J. E. 1991. Interdisciplinary characterization of fracture systems at the US/BK site, Grimsel Laboratory, Switzerland. *International Journal of Rock Mechanics and Mining Sciences & Geomechanics Abstracts* 28(4): 295-323.
- Marti, D., Carbonell, R., Tryggvason, A., Escuder, J. & Perez-Estaun, A. 2002. Mapping brittle fracture zones in three dimensions; high resolution travelttime seismic tomography in a granitic pluton. *Geophysical Journal International* 149: 95-105.
- Mathab, A., Xu, S., Grasso, P. & Kendorski, F. S. 1995. Use of alternative distributions for characterizing joint extend and spacing. In: *Fractured and Jointed Rock Masses, Lake Tahoe, California*.
- Mauldon, M. & Goodman, R. E. 1990. Rotational kinematics and equilibrium of blocks in a rock mass. *International Journal of Rock Mechanics and Mining Sciences & Geomechanics Abstracts* 27(4): 291-301.
- Mikkelsen, P. E. 2003. Advances in inclinometer analysis. In: *Field Measurements in Geomechanics, Oslo*: 555-567.
- Mikkelsen, P. E. & Wilson, S. D. 1983. Field instrumentation: Accuracy performance, automation and procurement. In: *International Symposium on Field Measurements in Geomechanics, Zürich*: 251-272.
- Milnes, A. G., Grellier, M. & Müller, R. 1981. Sequence and style of major post-nappe structures, Simplon - Pennine Alps. *Journal of Structural Geology* 3(4): 411-420.
- Moormann, C. 2003. A new study on the reliability and quality assurance of inclinometer measurements. In: *Sixth International Symposium on Field Measurements in Geomechanics, Oslo*: 575-583.
- Moos, D. & Zoback, M. D. 1983. In situ velocity in fractured crystalline rock. *Journal of Geophysical Research* 88(B3): 2345-2358.
- Müller, E. R. & Bonanomi, Y. 1996. N13C Abschnitt Mesocco Süd - Pian San Giacomo, Galerie Gorda Süd. Beurteilung der Felsbewegungen. Büchi + Müller AG, Chur: 8.
- Müller, R. 1983. Die Struktur der Mischabelfalte (Penninische Alpen). *Eclogae Geologicae Helvetiae* 76(2): 391-416.

- Norrish, N. I. & Wyllie, D. C. 1996. Rock slope stability analysis. In: Turner, A. K. & Schuster, R. L. (ed). Landslides: investigation and mitigation. Washington, National Academy Press.
- O'Connor, K. M. & Dowding, C. H. 1999. Geomeasurements by pulsing TDR cables and probes, CRC Press. 402.
- Olsson, O., Falk, L., Forslund, O., Lundmark, L. & Sandberg, E. 1992. Borehole radar applied to the characterization of hydraulically conductive fracture zones. *Geophysical Prospecting* 40: 109-142.
- Oppizzi, P. 1995. Commune di Airolo, Misure inclinometriche nella zona de I Dragoni, Rapporto No. 1. Studio di Consulenza Geologica e Ambientale, Camorino: 7.
- Ornstein, P., Jaboyedoff, M. & Rouiller, J. D. 2001. Surveillance géodésique du site de Randa (VS): gestion des mesures 1-D et 3-D. In: *Herbsttagung der Schweizerischen Gesellschaft für Boden- und Felsmechanik*: 82-91.
- Passchier, C. W. & Trouw, R. A. J. 1996. Microtectonics. Berlin, Springer-Verlag. 289.
- Priest, S. D. 1993. Discontinuity analysis for rock engineering. London, Chapman & Hall.
- Ramsay, J. G. & Huber, M. I. 1987. The techniques of modern structural geology - Folds and fractures. London, Academic Press Limited. 700.
- Reyes, O. & Einstein, H. H. 1991. Failure mechanisms of fractured rock - a fracture coalescence model. In: *7th International Congress on Rock Mechanics, Aachen*: 333-340.
- ROCSCIENCE 2002. RocLab. Toronto.
- Sandersen, F., Bakkehoi, S., Hestnes, E. & Lied, K. 1996. The influence of meteorological factors on the initiation of debris flows, rockfalls, rockslides and rockmass instability. In: *7th International Symposium on Landslides, Trondheim*: 97-114.
- Sartori, M., Baillifard, F., Jaboyedoff, M. & Rouiller, J. D. 2003. Kinematics of the 1991 Randa rockslides (Valais, Switzerland). *Natural Hazards and Earth System Sciences* 3: 423-433.
- Schepers, R., Rafat, G., Gelbke, C. & Lehmann, B. 2001. Application of borehole logging, core imaging and tomography to geotechnical exploration. *International Journal of Rock Mechanics and Mining Sciences* 38: 867-876.
- Schindler, C., Cuénod, Y., Eisenlohr, T. & Joris, C. L. 1993. Die Ereignisse vom 18. April und 9. Mai 1991 bei Randa (VS) - ein atypischer Bergsturz in Raten. *Eclogae Geologicae Helvetiae* 86(3): 643-665.
- Schindler, C. & Eisenlohr, T. 1992. Bergsturz Grossgufer bei Randa: Geologisch-geotechnische Expertise. Geologisches Institut ETH, Ingenieurgeologie, Zürich: 83.
- Segalini, A. & Giani, G. P. 2004. Numerical model for the analysis of the evolution mechanisms of the Grossgufer rock slide. *Rock Mechanics and Rock Engineering* 37(2): 151-168.
- Senn, P. 2002. Massenbewegungen am Grätli, Schynige Platte. Diploma thesis, Ingenieurgeologie, Swiss Federal Institute of Technology: 81.
- Seno, S. 1996. Commune di Preonzo: valutazione della stabilità dell' Alpe di Rosciuro. Cantone Ticino, Dipartimento Del Territorio, Cadenazzo: 26.
- Serzu, M. H., Kozak, E. T., Lodha, G. S., Everitt, R. A. & Woodcock, D. R. 2004. Use of borehole radar techniques to characterize fractured granitic bedrock at AECL's Underground Research Laboratory\*1. *Journal of Applied Geophysics* 55(1-2): 137-150.
- Shea, W. T., Kronenberg, J. R. & Kronenberg, A. K. 1993. Strength and anisotropy of foliated rocks with varied mica contents. *Journal of Structural Geology* 15(9/10): 1097-1121.
- Simeoni, L. & Mongiovi, L. 2003. The problematic management of the displacement monitoring system of a landslide. In: *Sixth International Symposium on Field Measurements in Geomechanics, Oslo*: 673-680.

- Sonmez, H., Ulusay, R. & Gokceoglu, C. 1998. A practical procedure for the back analysis of slope failures in closely jointed rock masses. *International Journal of Rock Mechanics and Mining Sciences* 35(2): 219-233.
- Sorriso-Valvo, M., Gulla, G., Antrocino, L., Tansi, C. & Amelio, M. 1999. Mass-movement, geologic structure and morphologic evolution of the Pizzotto-Greci slope (Calabria, Italy). *Geomorphology* 30: 147-163.
- Spillmann, T. 2001. Tomographische Auswertung von Bohrlochradar mit fat rays. Diploma thesis, Institut für Geophysik, Swiss Federal Institute of Technology: 83.
- Steck, A., Bigioggero, B., Dal Piaz, G. V., Escher, A., Marchant, R., Martinotti, G. & Payot, S. 1999. Carte tectonique des Alpes de Suisse occidentale, feuille 47 Monte Rosa. 1:100000.
- Steck, A., Epard, J.-L., Escher, A., Lehner, P., Marchant, R. & Masson, H. 1997. Geological interpretation of the seismic profiles through Western Switzerland: Rawil (W1), Val d'Anniviers (W2), Mattertal (W3), Zmutt-Zermatt-Findelen (W4) and Val de Bagnes (W5). In: Pfiffner, O. A., et al. (ed). Results of NRP20: 380. Basel, Birkhäuser Verlag.
- Tanaka, Y. 1998. Rock slope stability assessment incorporating fissure effects. In: *8th International IAEG Congress, Vancouver*: 3005-3009.
- Voight, B. 1989. Relation to describe rate-dependent material failure. *Science* 243(4888): 200-203.
- Wagner, A. 1991. Bergsturz Grossgufer Randa - Etude structurale et géomécanique. Centre de Recherches Scientifiques Fondamentales et Appliquées de Sion, Sion: 15.
- Watson, A. D., Moore, D. P. & Stewart, T. W. 2004. Temperature influence on rock slope movements at Checkerboard Creek. In: *International Symposium on Landslides, Rio de Janeiro*: 1293-1298.
- Willenberg, H., Spillmann, T., Eberhardt, E., Evans, K. F., Loew, S. & Maurer, H. R. 2002. Multidisciplinary monitoring of progressive failure processes in brittle rock slopes - concepts and system design. In: *Landslides - First European Conference on Landslides, Prague*: 477-483.
- Willenberg, H., Spillmann, T., Evans, K. F., Maurer, H. R., Eberhardt, E. & Loew, S. 2004. Geological, geophysical and geotechnical investigations into the internal structure and kinematics of an unstable, complex sliding mass in crystalline rock. In: *International Symposium on Landslides, Rio de Janeiro*: 489-494.
- Winistorfer, J. 1978. Paléogéographie des stades glaciaires des vallées de la rive gauche du Rhone entre Viège et Aproz. Université de Lausanne, Sion
- Yilmaz, Ö. 2001. Seismic data analysis - processing, inversion and interpretation of seismic data. Tulsa, Society of Exploration Geophysicists.
- Yoon, W. S., Jeong, U. J. & Kim, J. H. 2002. Kinematic analysis for sliding failure of multi-faced rock slopes. *Engineering Geology* 67: 51-61.
- Zangerl, C. J. 2003. Analysis of surface subsidence in crystalline rocks above the Gotthard Highway Tunnel, Switzerland, Earth Science Department, Swiss Federal Institute of Technology: 190.
- Zwahlen, P. 1999. Steinschlag- und Felssturzgefährdung Val del Infern - Cauco, Maladers: 13.





## **A-1 Appendix**

## A-1.1 Borehole logging

### A- 1.1.1 SB 120

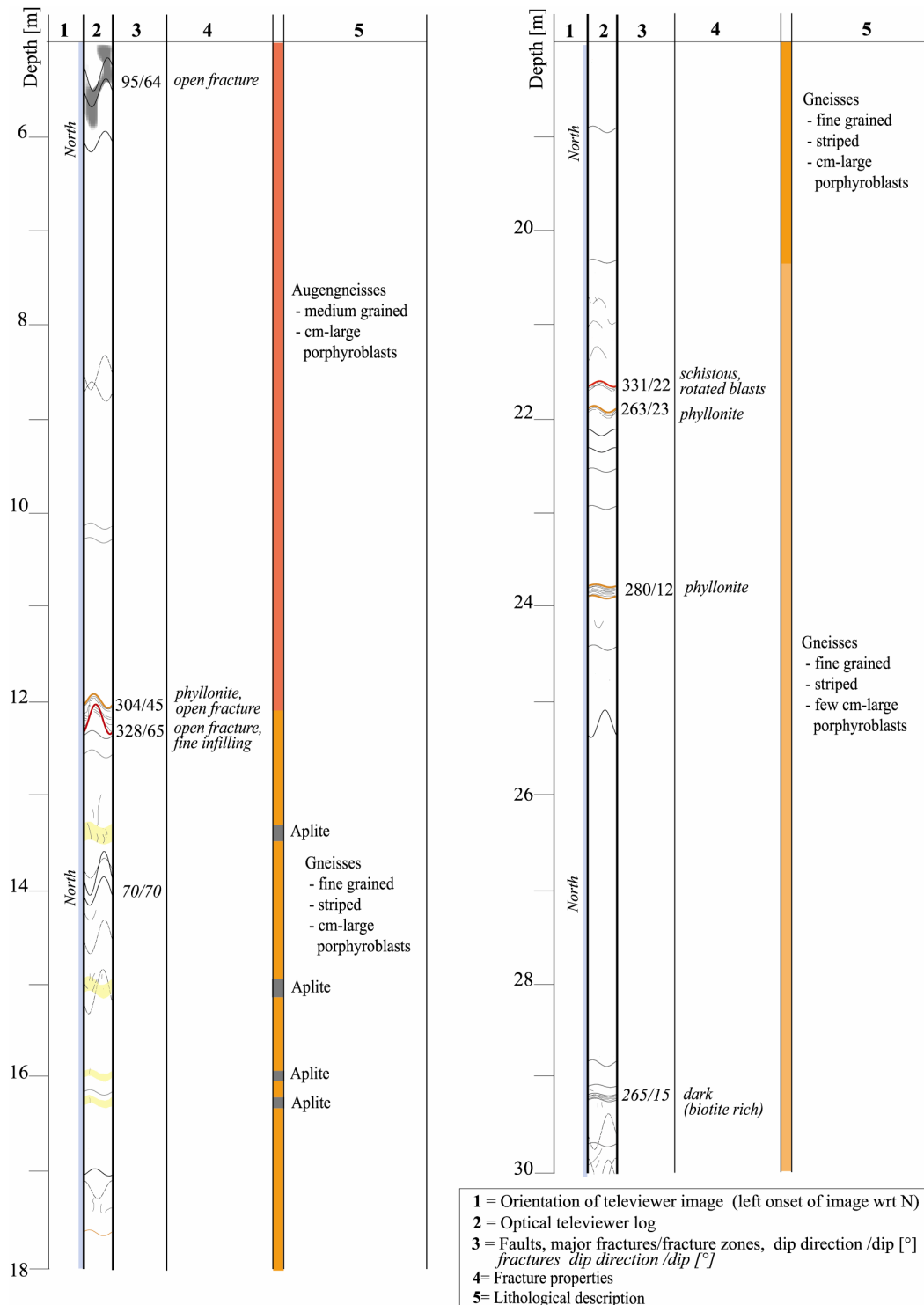


Figure A- 1: SB 120 optical televiewer log 0-30m showing digitised fractures, calculated dip directions and dip and lithological descriptions.

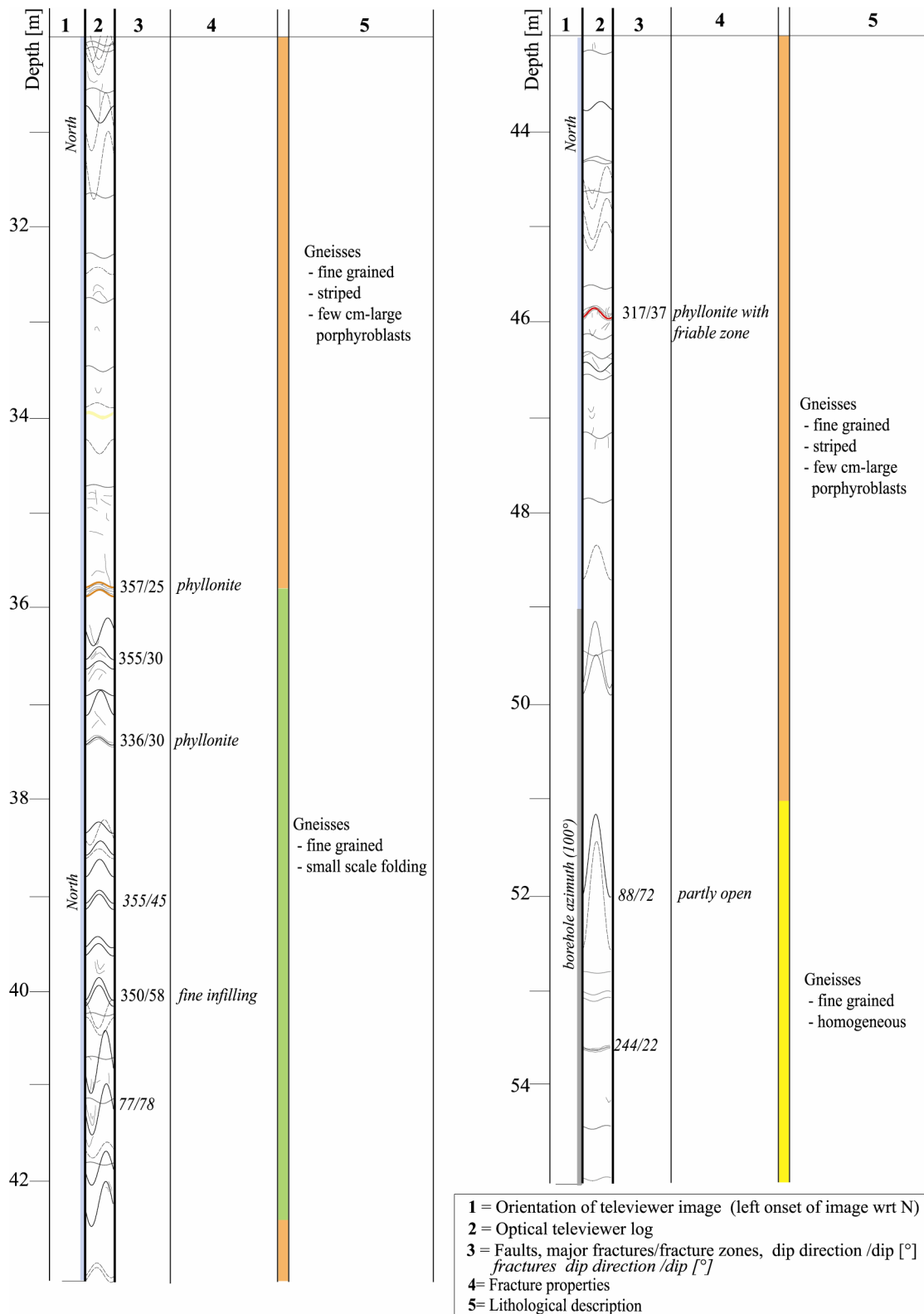


Figure A- 2: SB 120 optical televiewer log 30-55 m showing digitised fractures, calculated dip directions and dip and lithological descriptions.

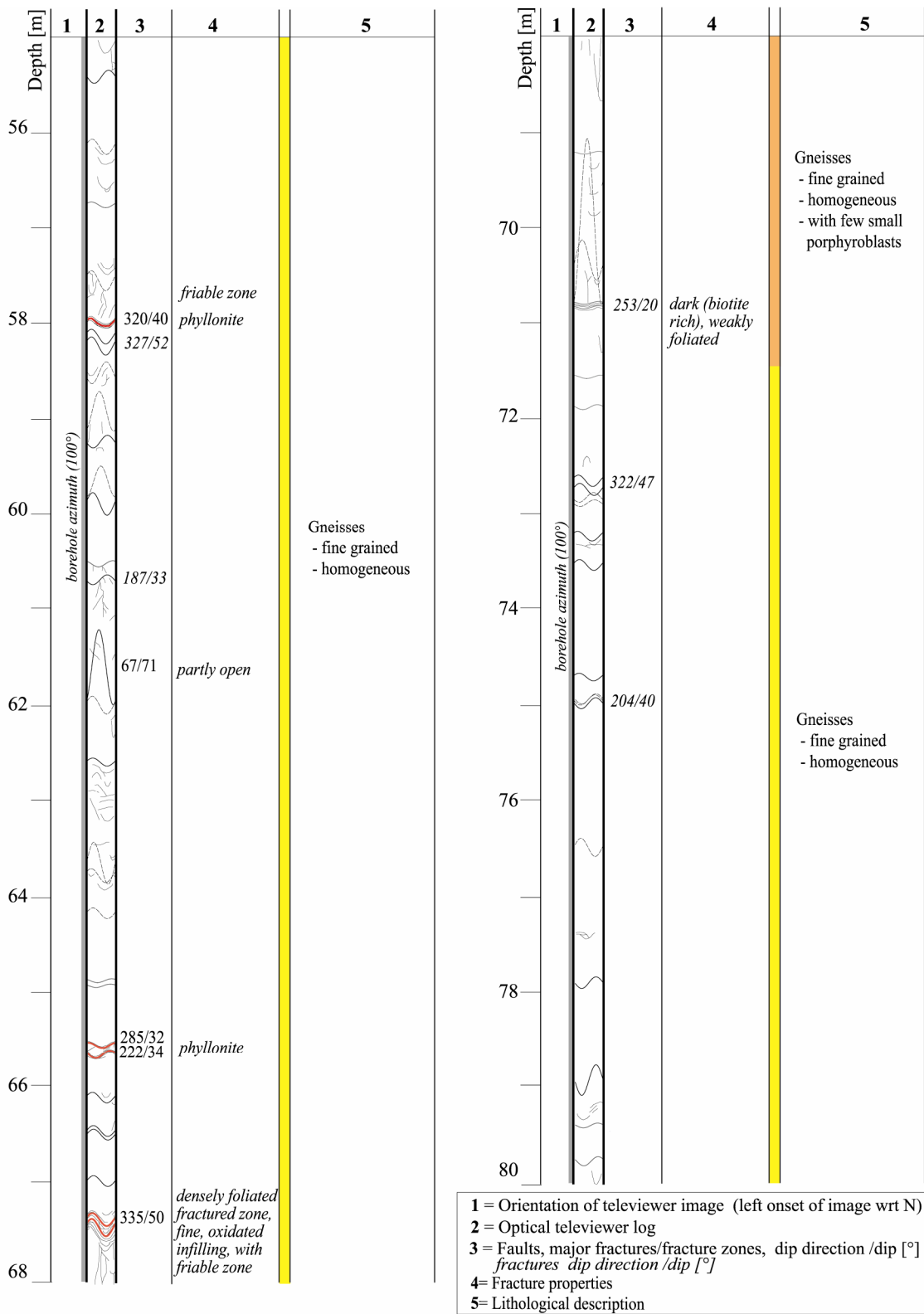


Figure A- 3: SB 120 optical televiewer log 55-80 m showing digitised fractures, calculated dip directions and dip and lithological descriptions.

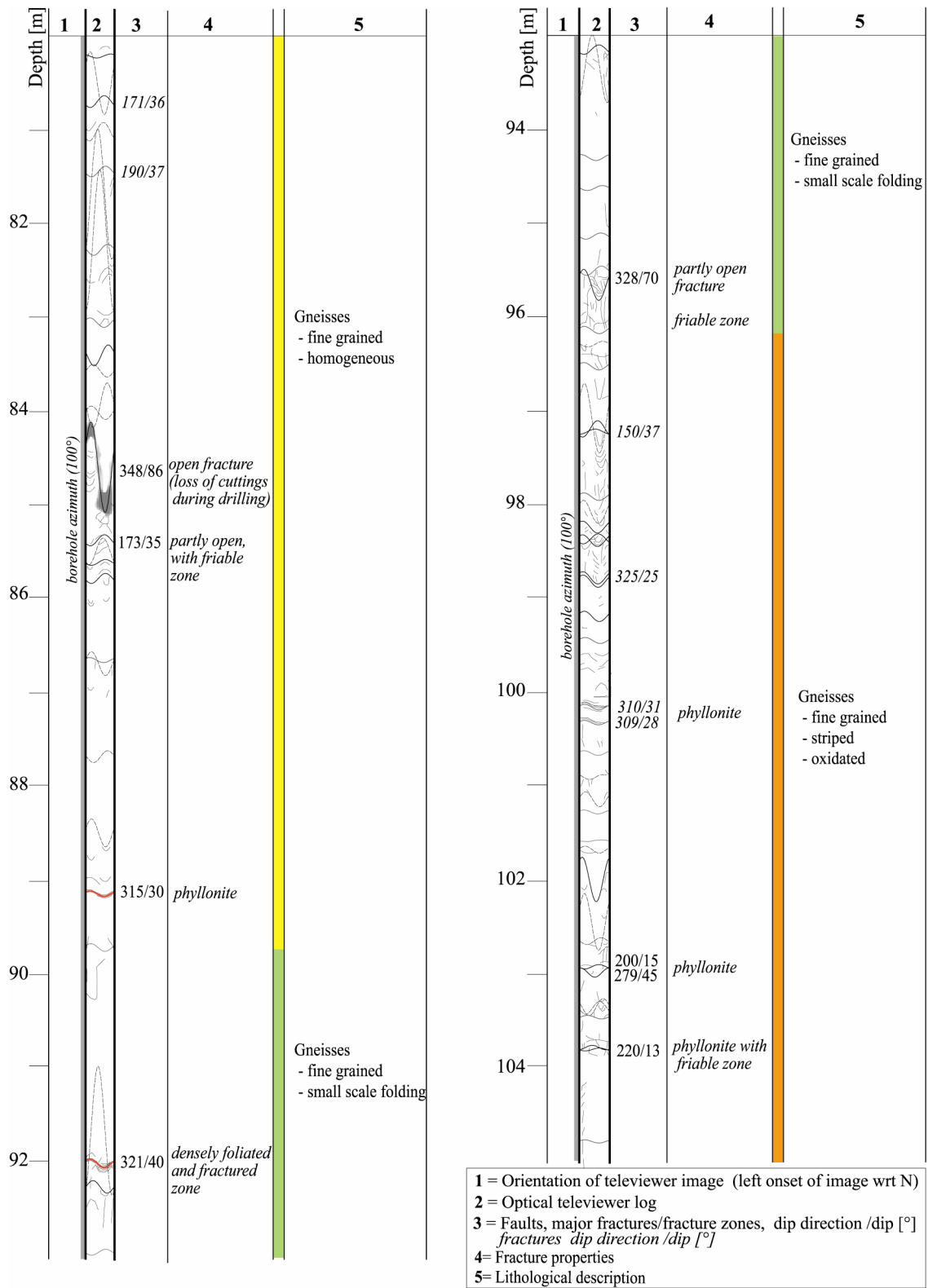


Figure A- 4: SB 120 optical televiewer log 80-105 m showing digitised fractures, calculated dip directions and dip and lithological descriptions.

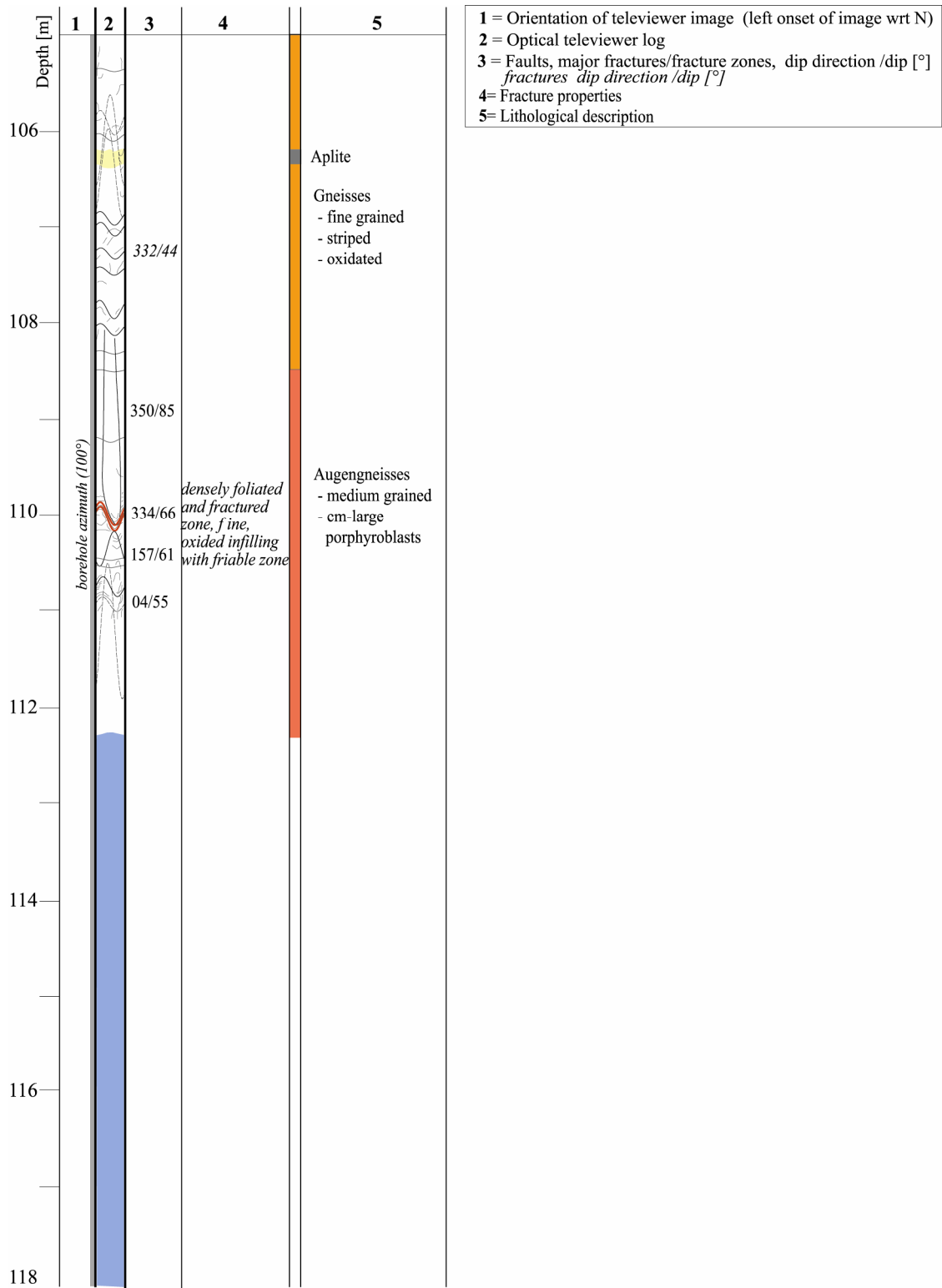


Figure A- 5: SB 120 optical televiewer log 105-118 m showing digitised fractures, calculated dip directions and dip and lithological descriptions.

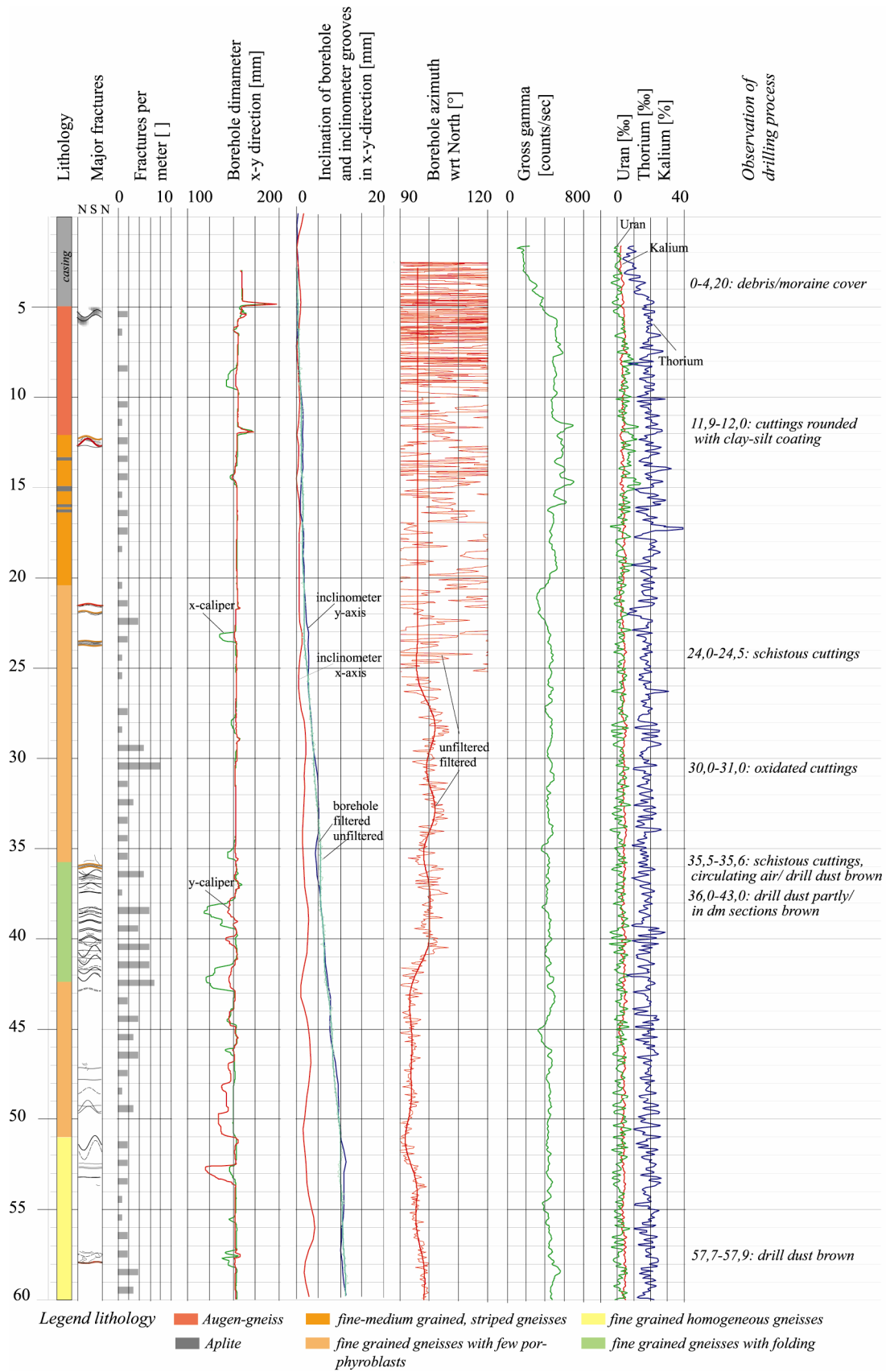


Figure A- 6: SB 120 well logs 0-60 m: Lithology, major fractures, fractures per meter, 4-arm caliper, borehole and inclinometer casing inclination, borehole azimuth, spectral gamma (gross gamma), K-U-Th content derived from spectral gamma log and observations during drilling.

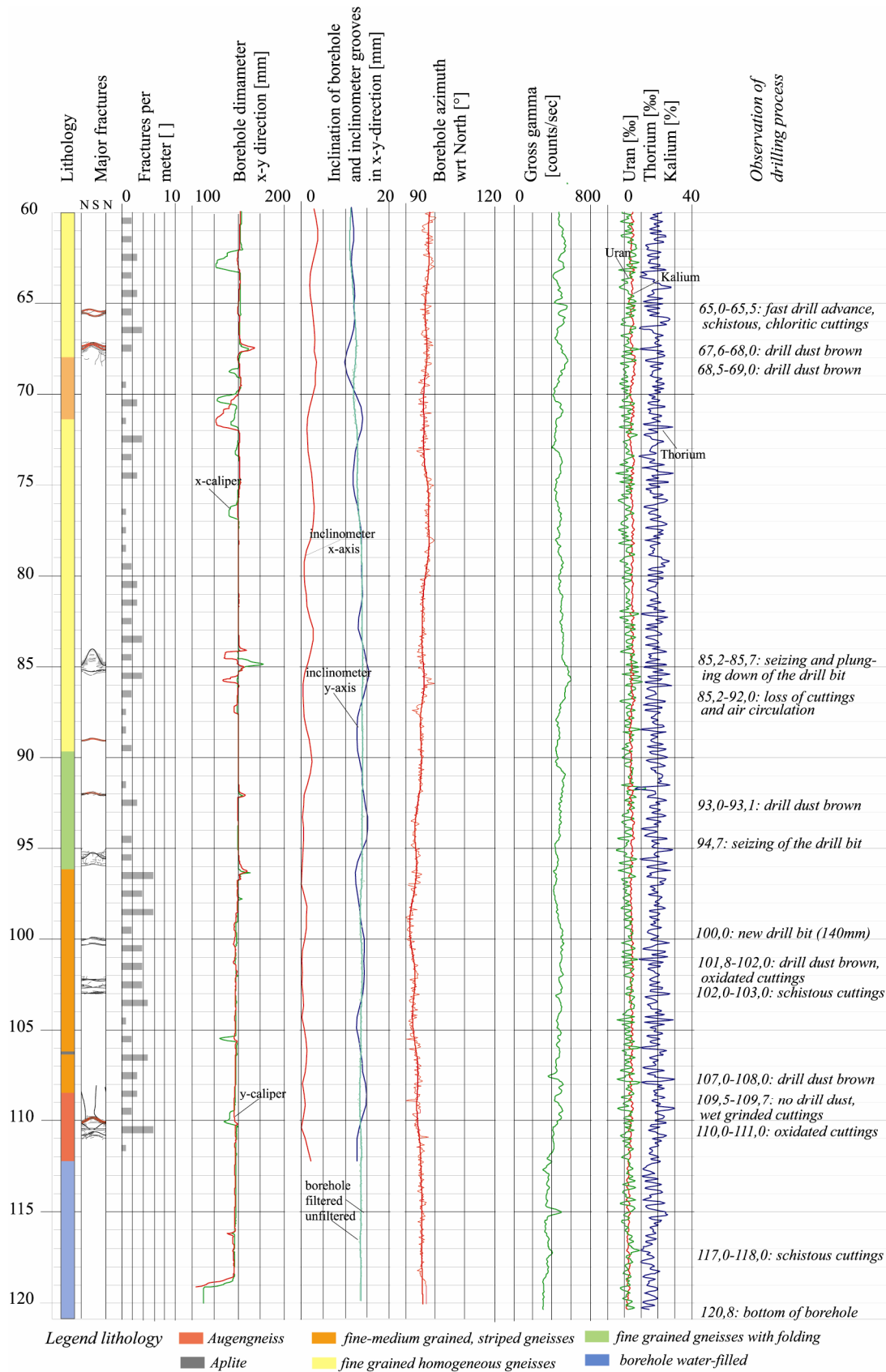


Figure A- 7: SB 120 well logs 60-120 m: Lithology, major fractures, fractures per meter, 4-arm caliper, borehole and inclinometer casing inclination, borehole azimuth, spectral gamma (gross gamma), K-U-The content derived from spectral gamma log and observations during drilling.



## A- 1.1.2 SB 50N

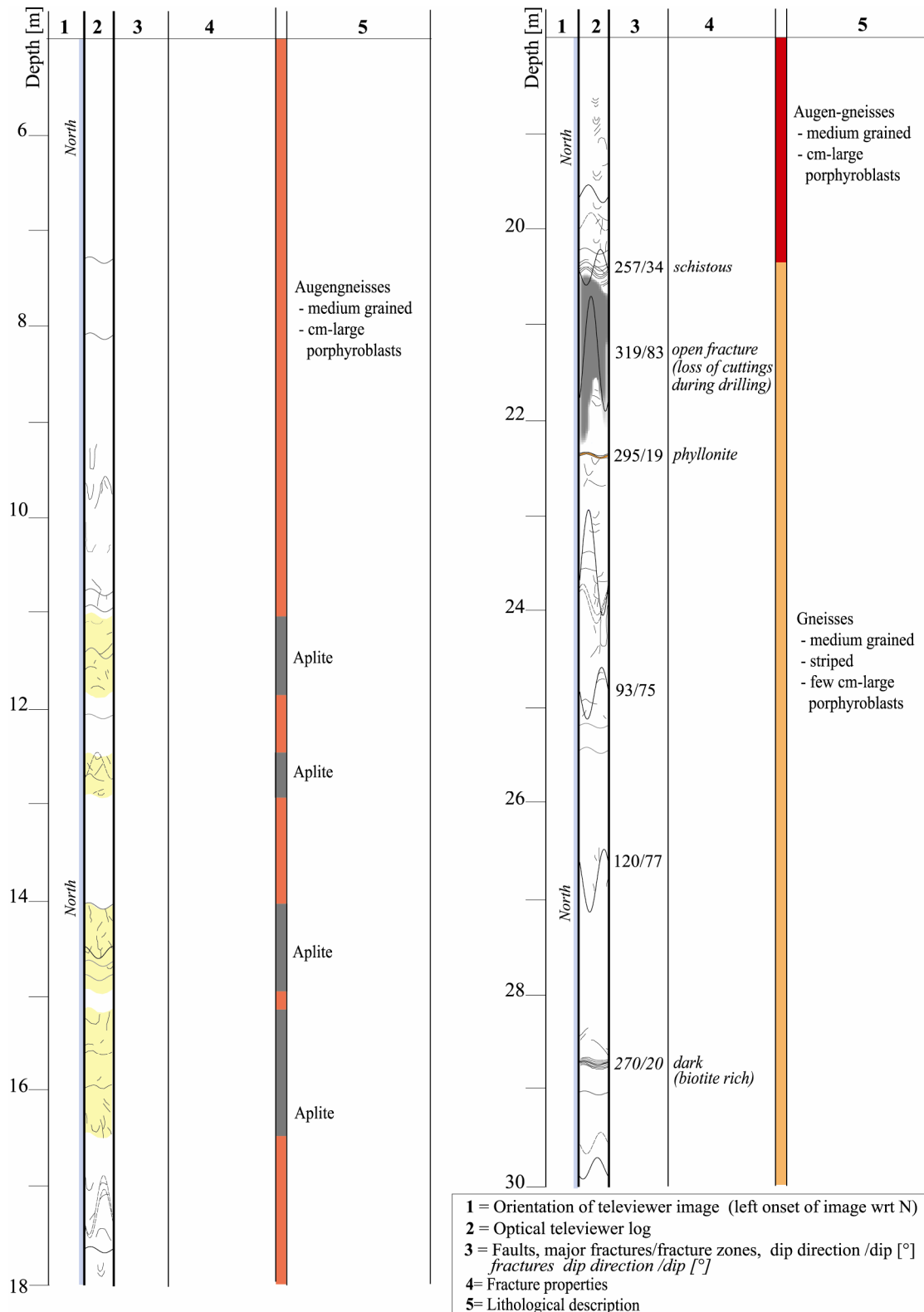


Figure A- 8: SB 50N optical televiewer log 0-30m showing digitised fractures, calculated dip directions and dip and lithological descriptions.

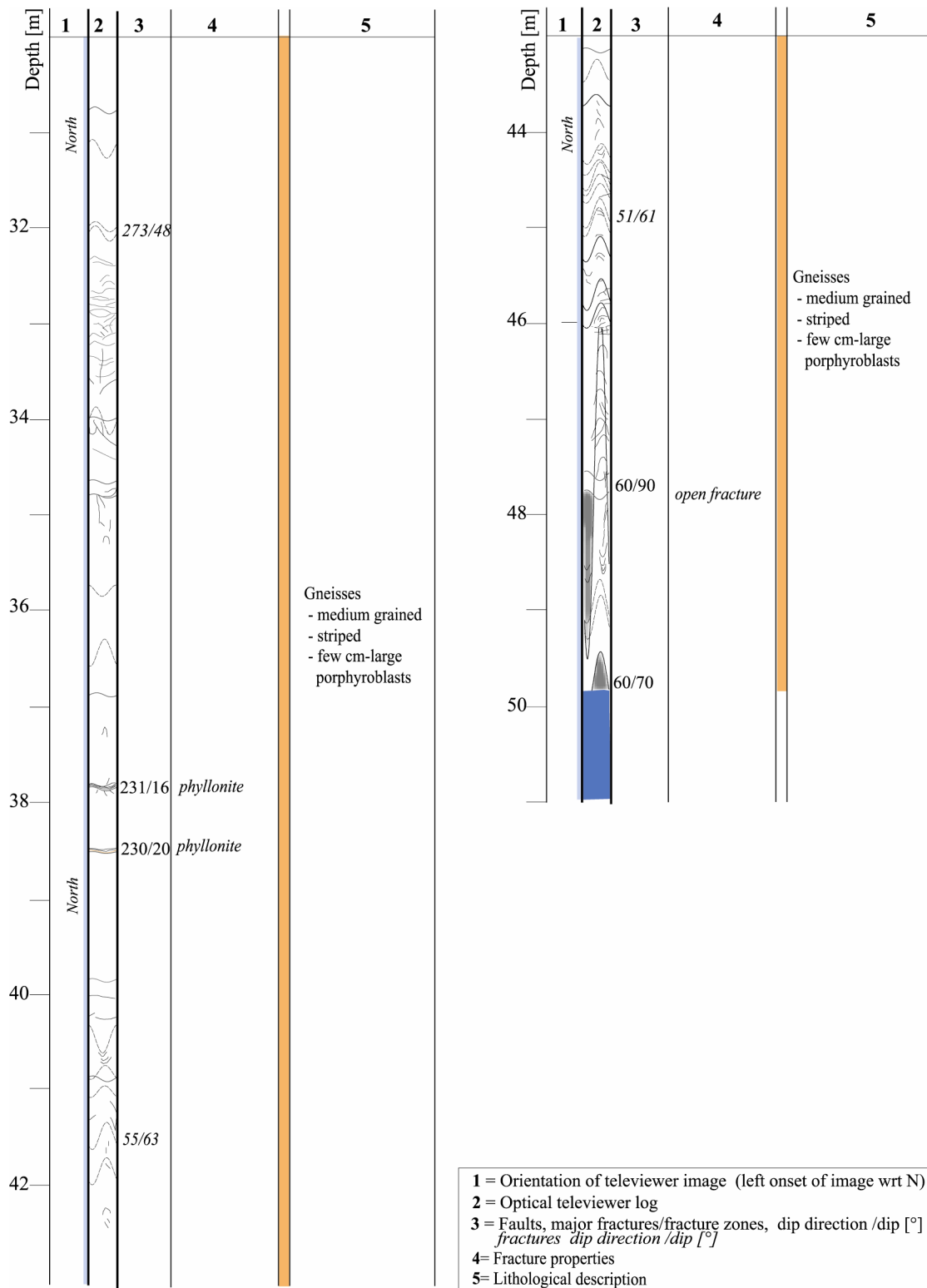


Figure A- 9: SB 50N optical televiewer log 30-51 m showing digitised fractures, calculated dip directions and dip and lithological descriptions.

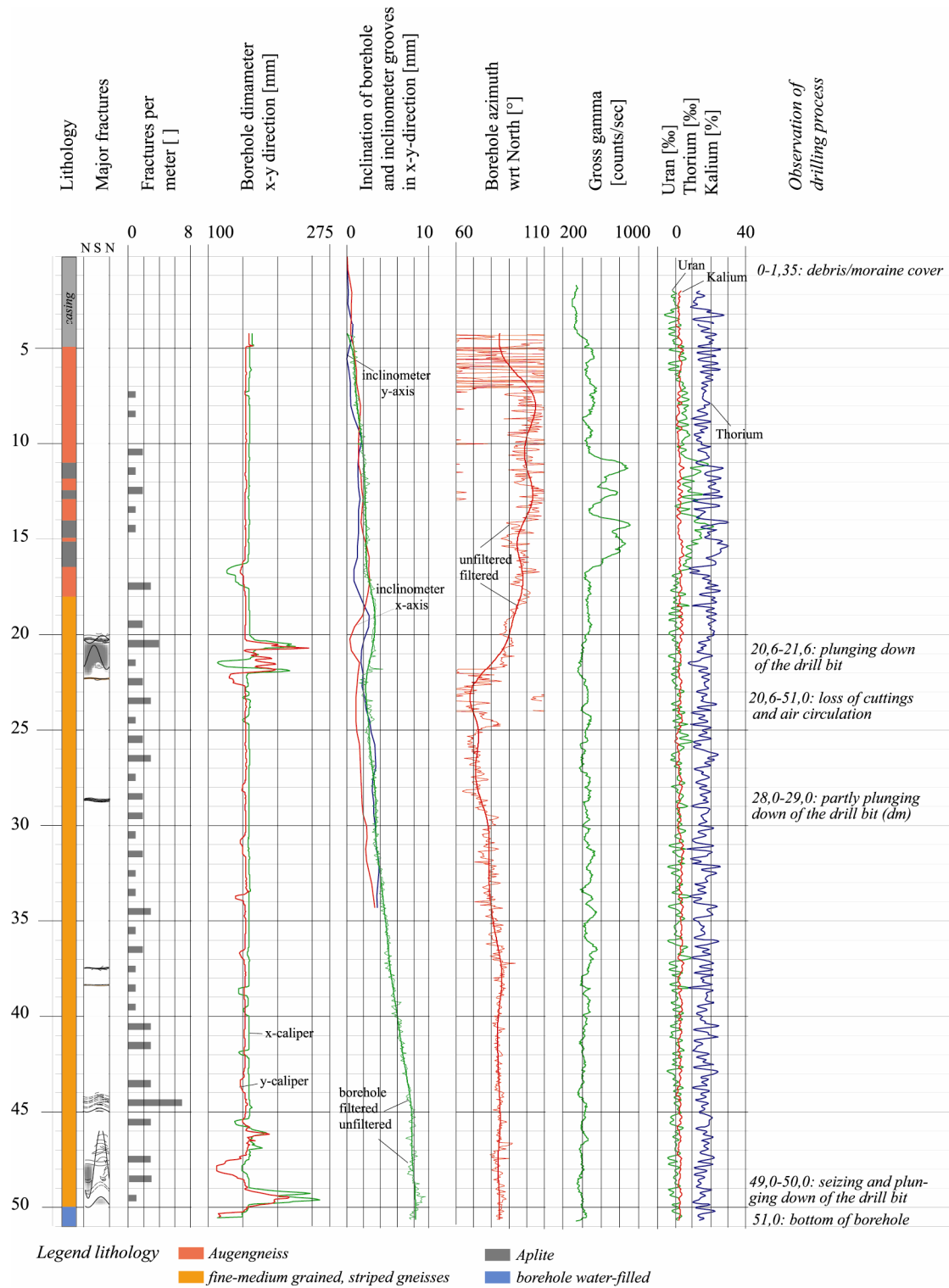


Figure A- 10: SB 50N well logs: Lithology, major fractures, fractures per meter, 4-arm caliper, borehole and inclinometer casing inclination, borehole azimuth, spectral gamma (gross gamma), K-U-Th content derived from spectral gamma log and observations during drilling.

A- 1.1.3 SB 50S

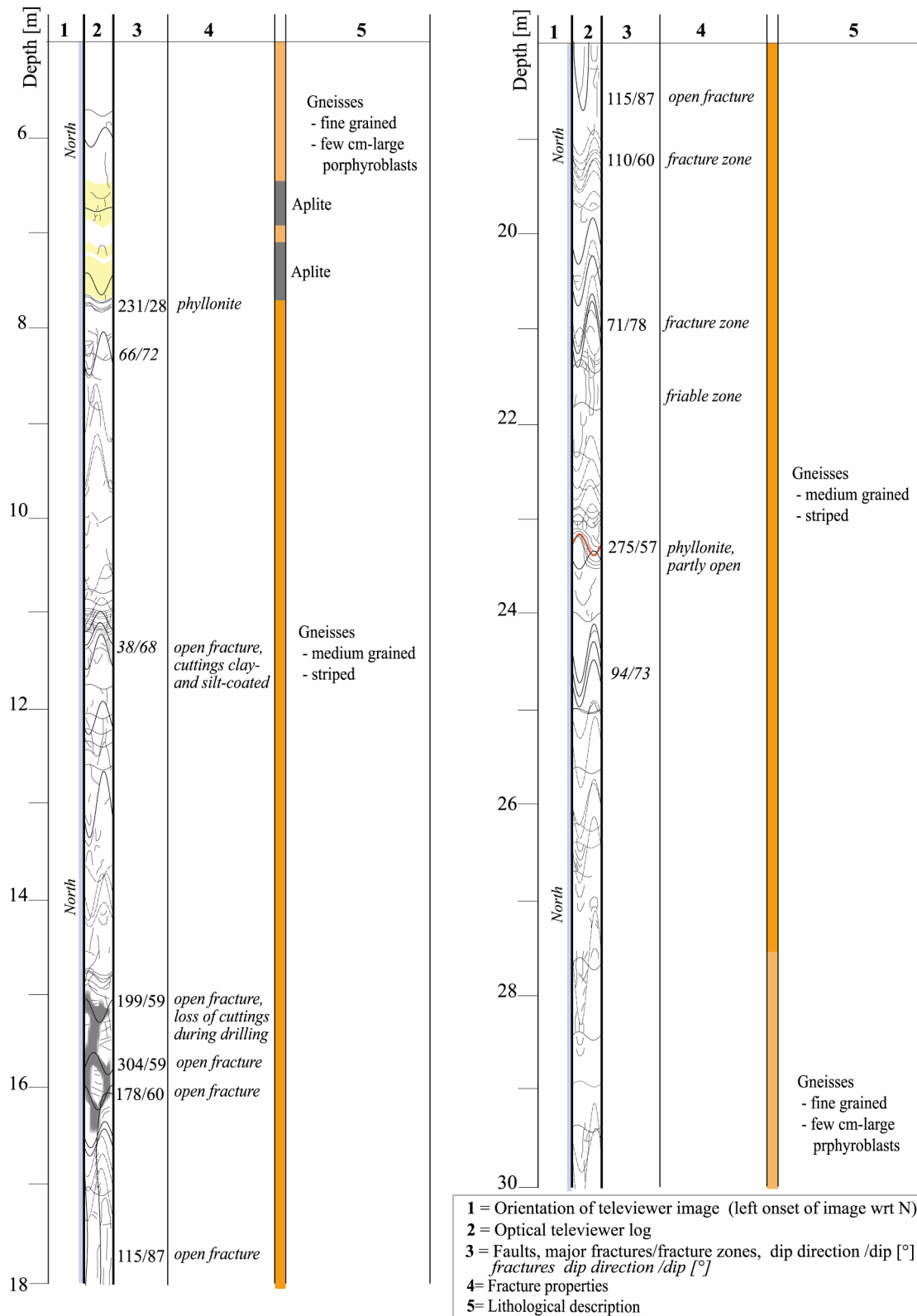


Figure A- 11: SB 50S optical televiewer log 0-30m showing digitised fractures, calculated dip directions and dip and lithological descriptions.

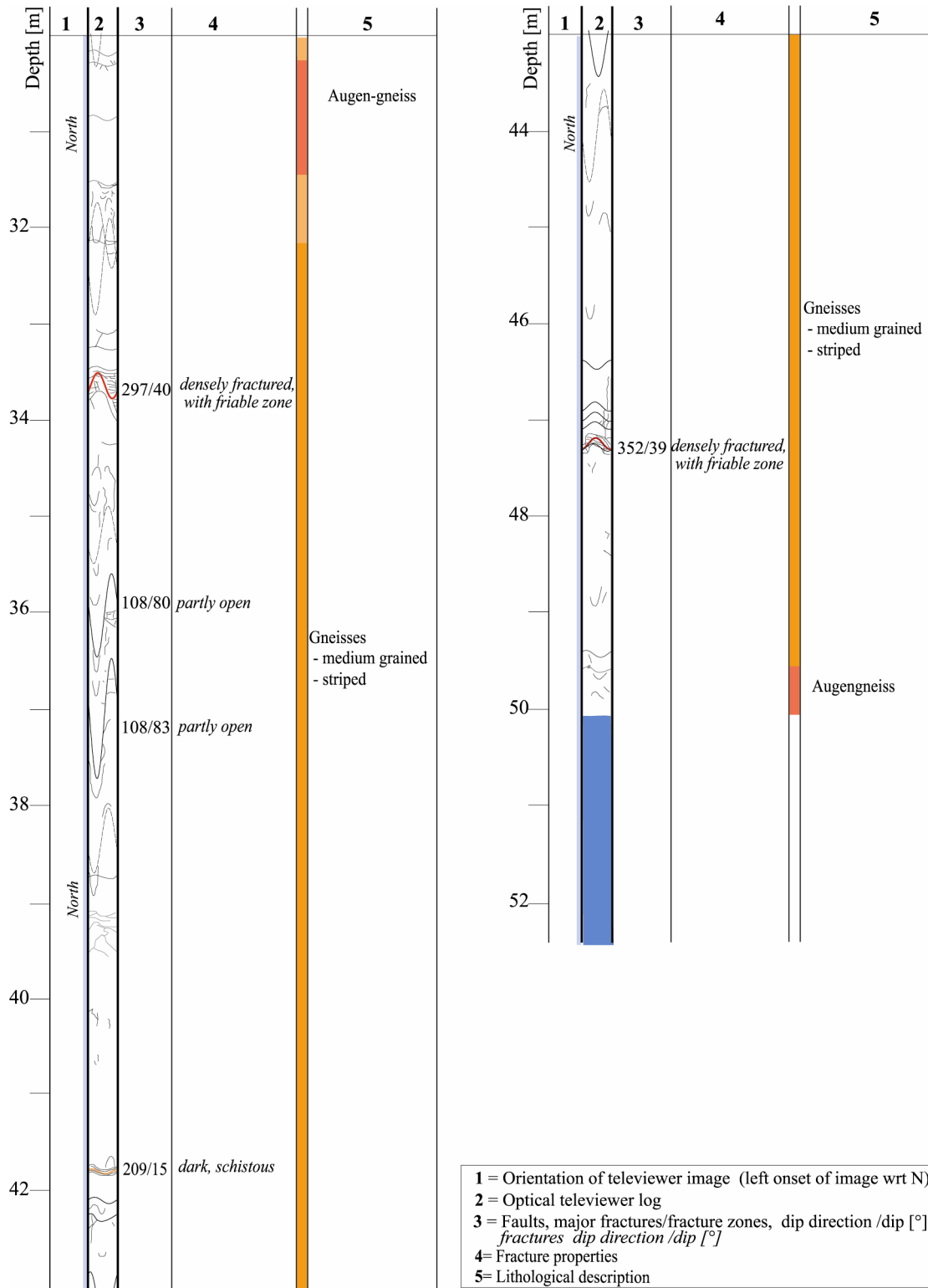


Figure A- 12: SB 50S optical televiewer log 30-52.5m showing digitised fractures, calculated dip directions and dip and lithological descriptions.

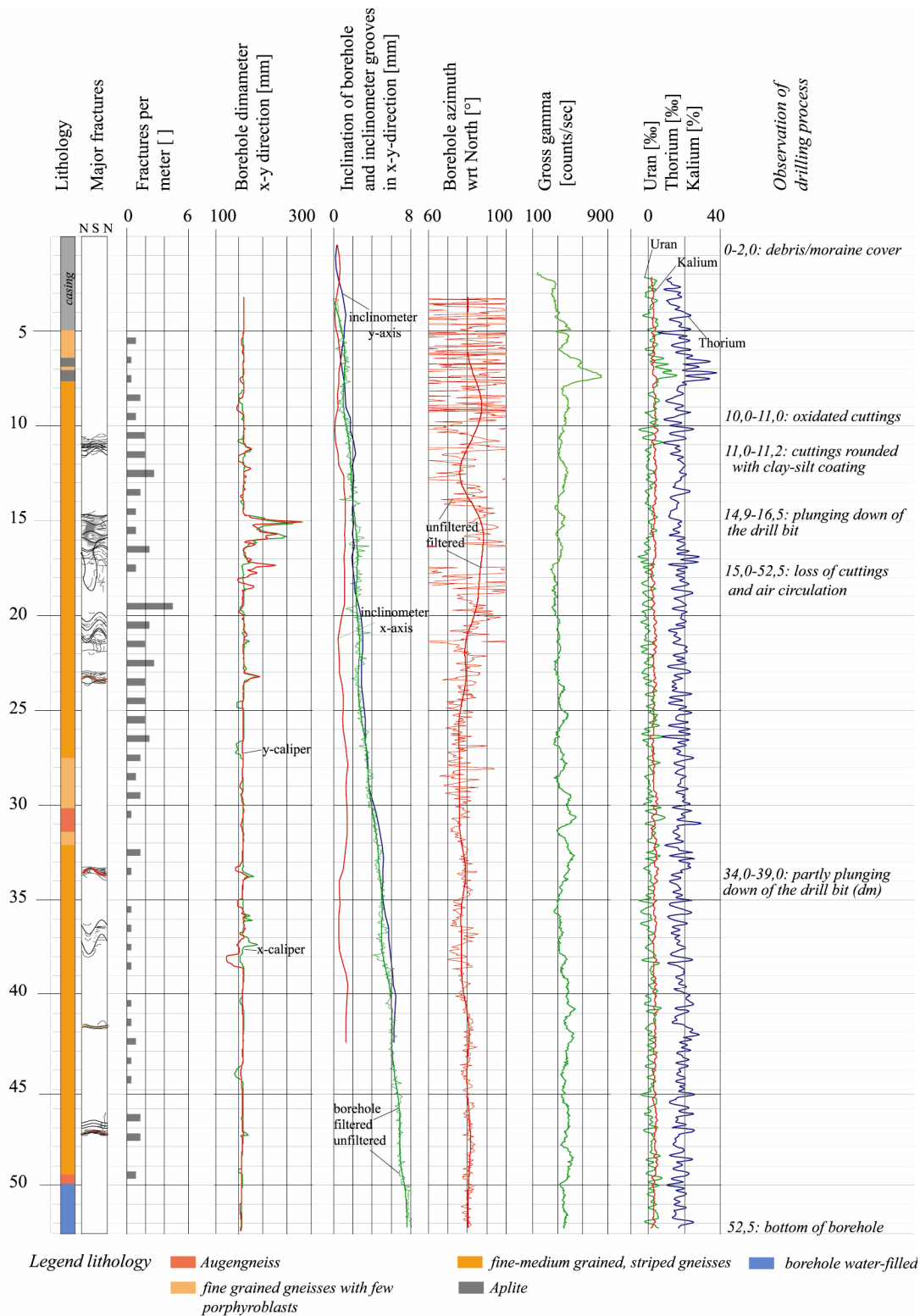


Figure A- 13: SB 50S well logs: Lithology, major fractures, fractures per meter, 4-arm caliper, borehole and inclinometer casing inclination, borehole azimuth, spectral gamma (gross gamma), K-U-Th content derived from spectral gamma log and observations during drilling.

## A-1.2 Scanline mapping

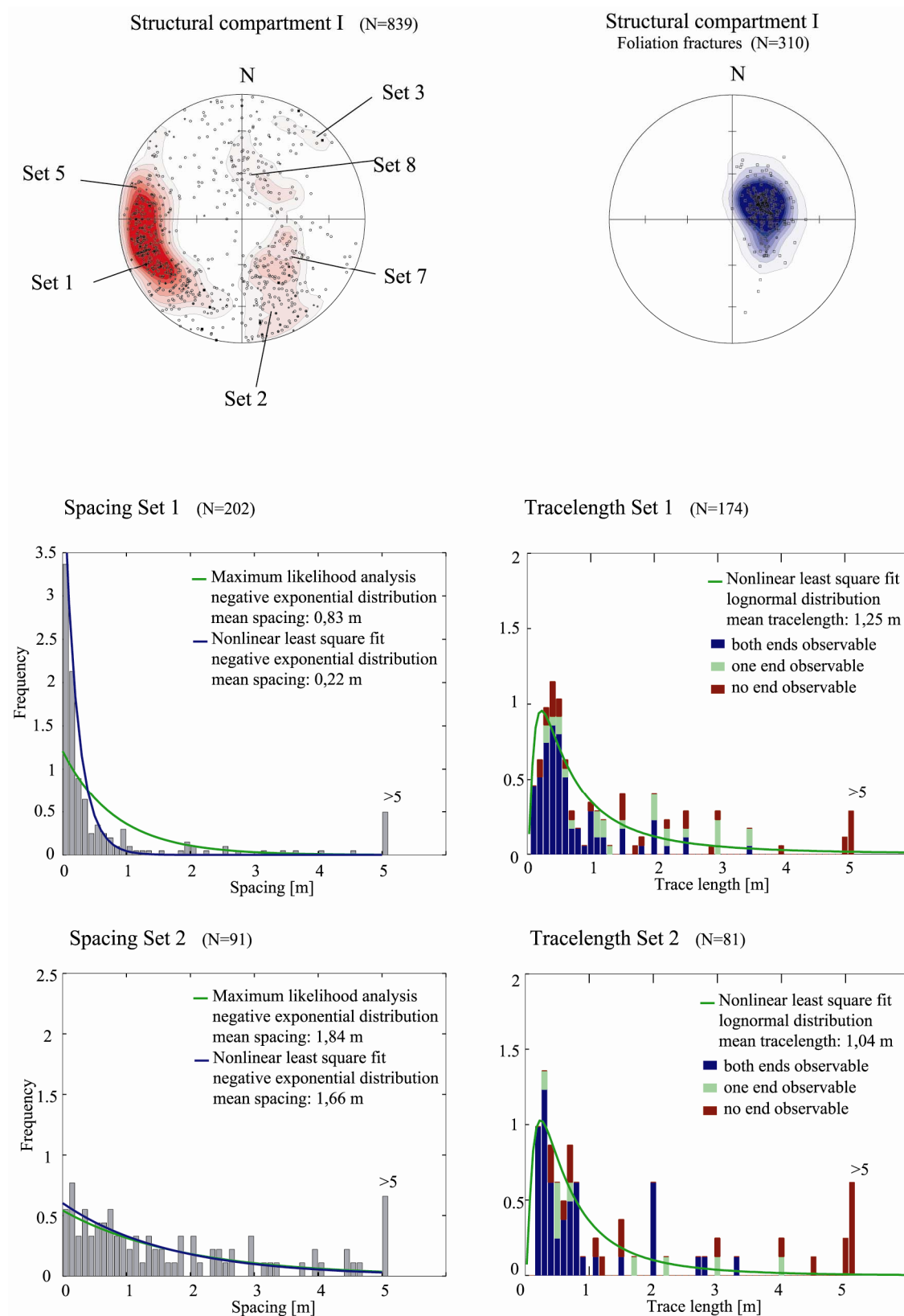


Figure A- 14: Histograms of normal-set spacing (left) and trace length (right) with fitted distributions and distribution means for fracture sets of the structural compartment I. Part1.

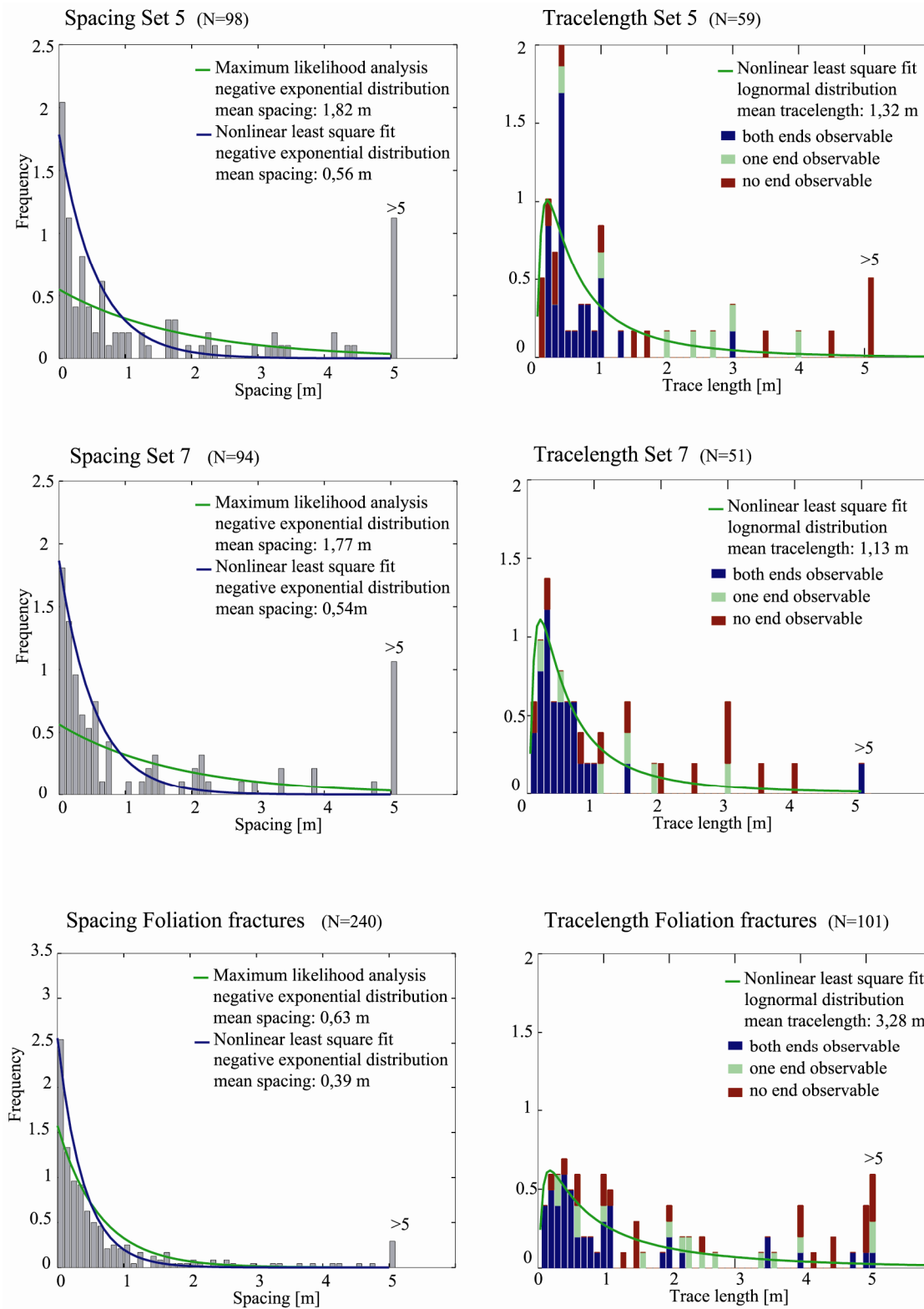


Figure A- 15: Histograms of normal-set spacing (left) and trace length (right) with fitted distributions and distribution means for fracture sets of the structural compartment I. Part2.



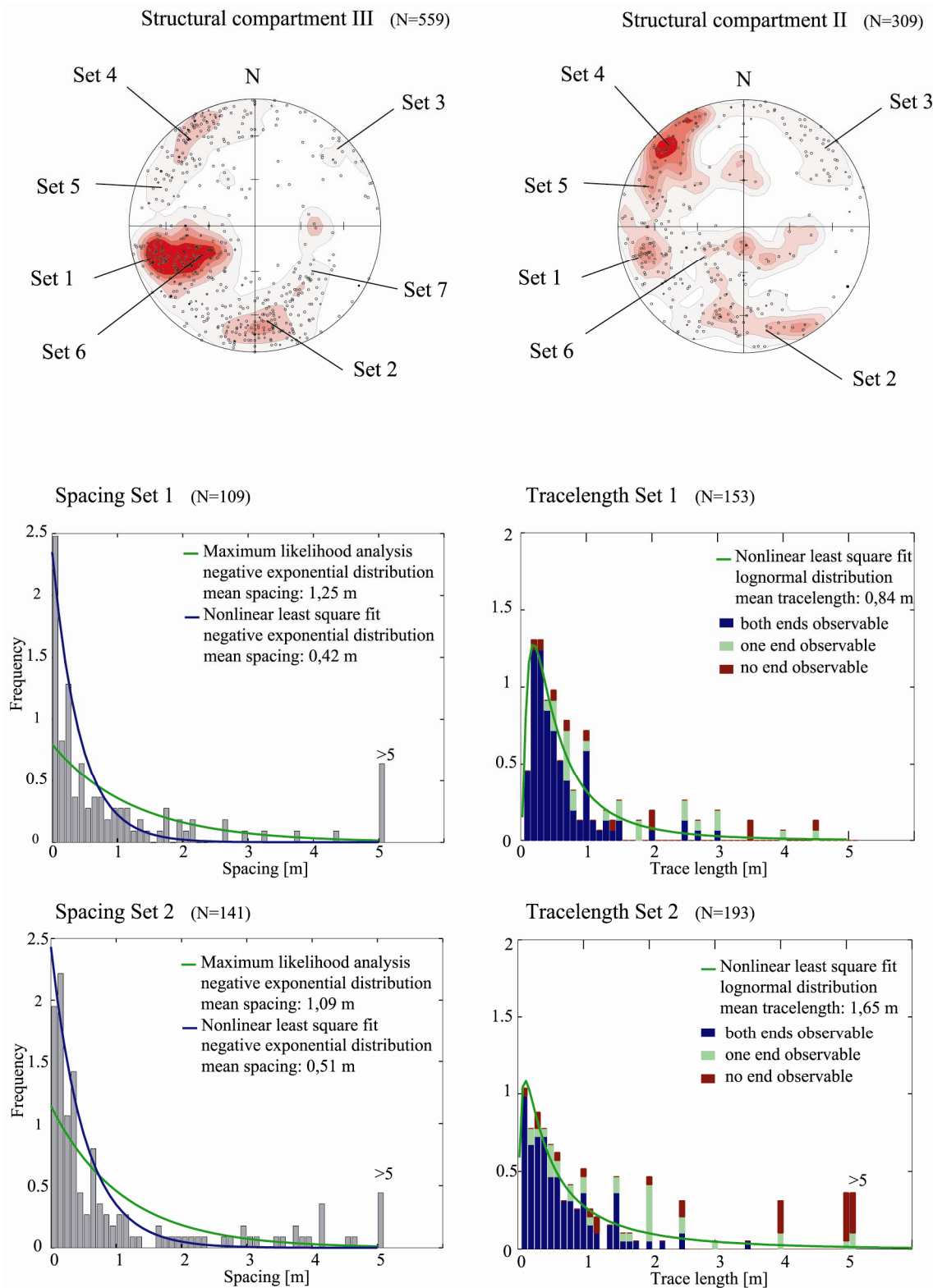


Figure A- 16: Histograms of normal-set spacing (left) and trace length (right) with fitted distributions and distribution means for fracture sets of the structural compartment II & III. Part1.

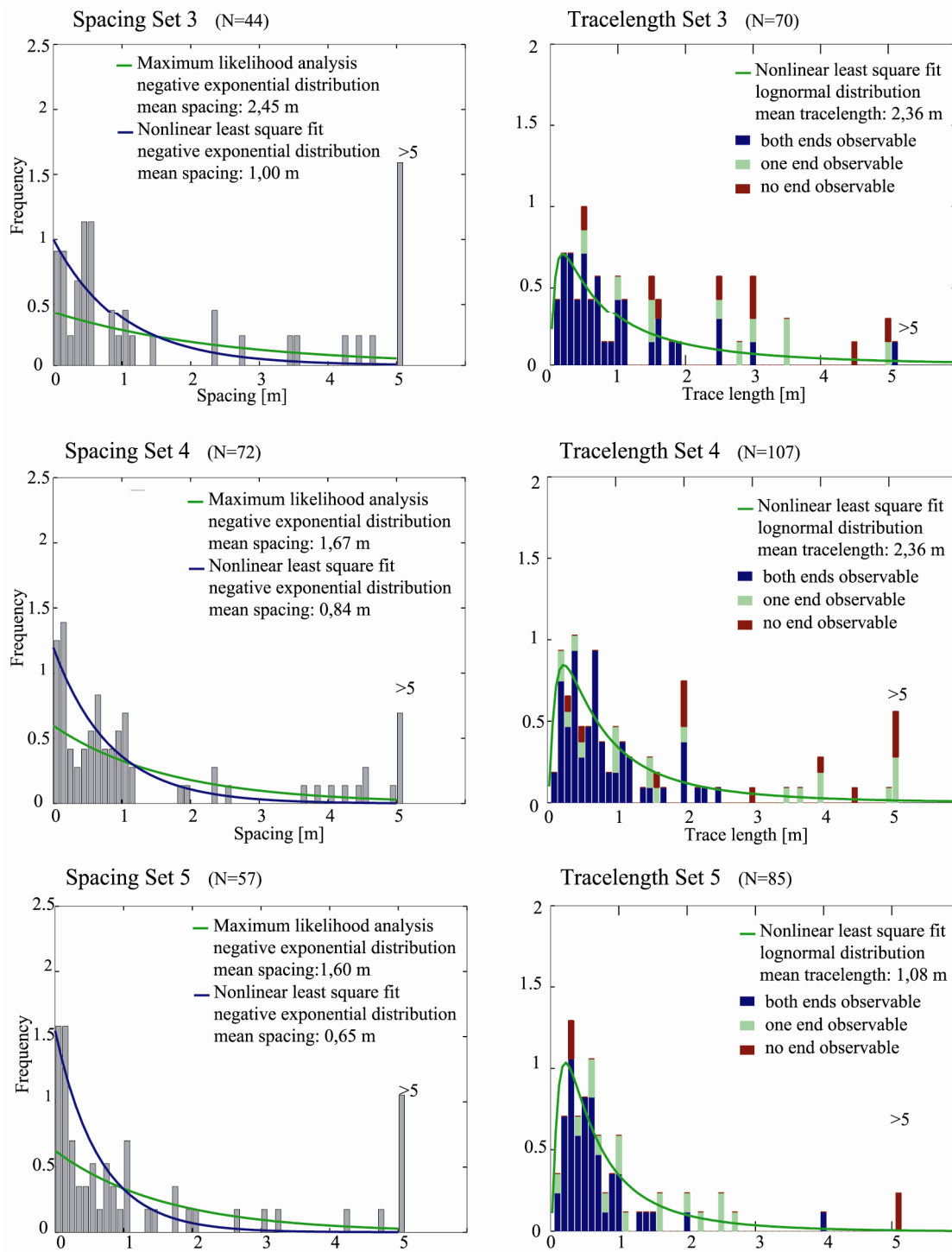


Figure A- 17: Histograms of normal-set spacing (left) and trace length (right) with fitted distributions and distribution means for fracture sets of the structural compartment II & III. Part2.

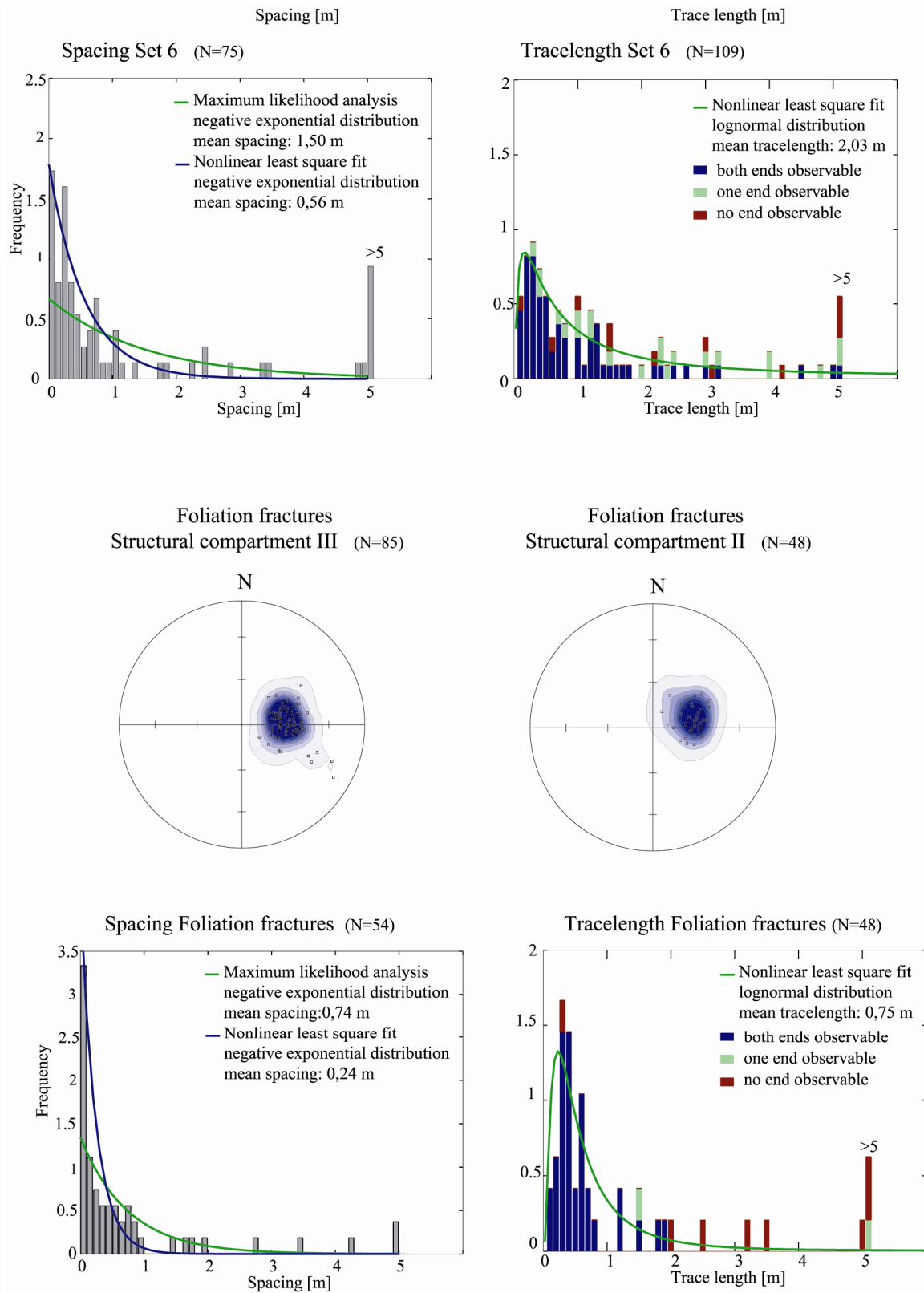


Figure A- 18: Histograms of normal-set spacing (left) and trace length (right) with fitted distributions and distribution means for fracture sets of the structural compartment II & III. Part3.

### A-1.3 Rock mechanical testing

Table A- 1: Rock mechanical testing results. a) Results of the uniaxial tests. b) Results of the triaxial tests; the friction angle and cohesion were derived using the Coulomb-failure criterion.

*a) Uniaxial tests.*

<i>Lithological unit</i>	<i>Test Group</i>	<i>Sample</i>	<i>Density [g/cm<sup>3</sup>]</i>	<i>E<sub>tangential</sub> [GPa]</i>	<i>v [ ]</i>	<i>σ<sub>UCS</sub> [MPa]</i>
GS III a	A	A 5a	2.673	18	0.14	65
GS III a	A	A 7a	2.721	22	0.07	80
GS III a	A	A 7b	2.683	20	0.2	77
GS III a	A	A 7c	2.673	20	0.16	60
GS III a	A	A 7d	2.678	23	0.12	37
GS II a	B	B 1	2.632	33	0.23	92
GS II a	B	B 2	2.607	31	0.16	77
GS II b	B	B 11	2.602	29	0.12	92
GS II b	B	B 12	2.643	45	0.18	135
GS II b	B	B 13a	2.630	22	0.24	46 *
GS II b	B	B 13b	2.635	33	0.3	100
GS II b	B	B 15b	2.662	31	0.19	77

\* values from sample B 13a were ignored

*b) Triaxial tests.*

<i>Lithological unit</i>	<i>Test Group</i>	<i>Sample</i>	<i>Density [g/cm<sup>3</sup>]</i>	<i>σ<sub>2,3</sub> [MPa]</i>	<i>σ<sub>1max</sub> [MPa]</i>	<i>φ [°]</i>	<i>c [MPa]</i>
GS III a	A	A 1	2.703	2.5	95		
GS III a	A	A 2a	2.699	5	120	32	19
GS III a	A	A 2b	2.740	10	110		
GS III a	A	A 5b	2.733	20	130		
GS II a	B	B 14	2.641	10	238		
GS II b	B	B 4	2.665	2.5	105	55	16
GS II b	B	B 9	2.662	5	175		
GS II b	B	B 15a	2.646	20	285		

## A- 1.3.1 Uniaxial tests

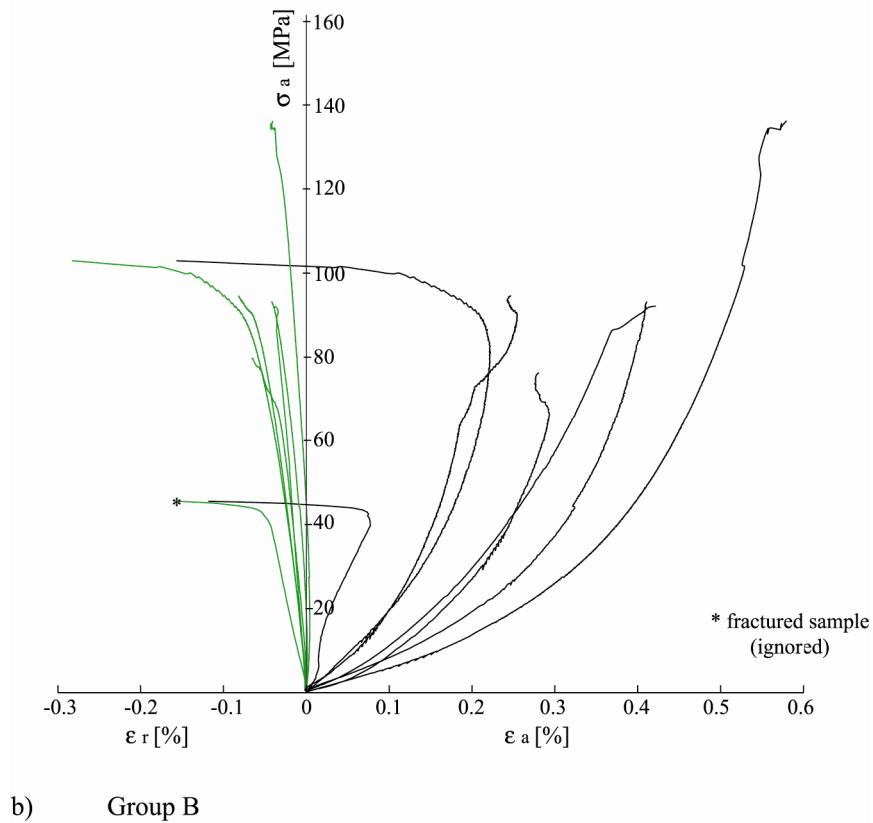
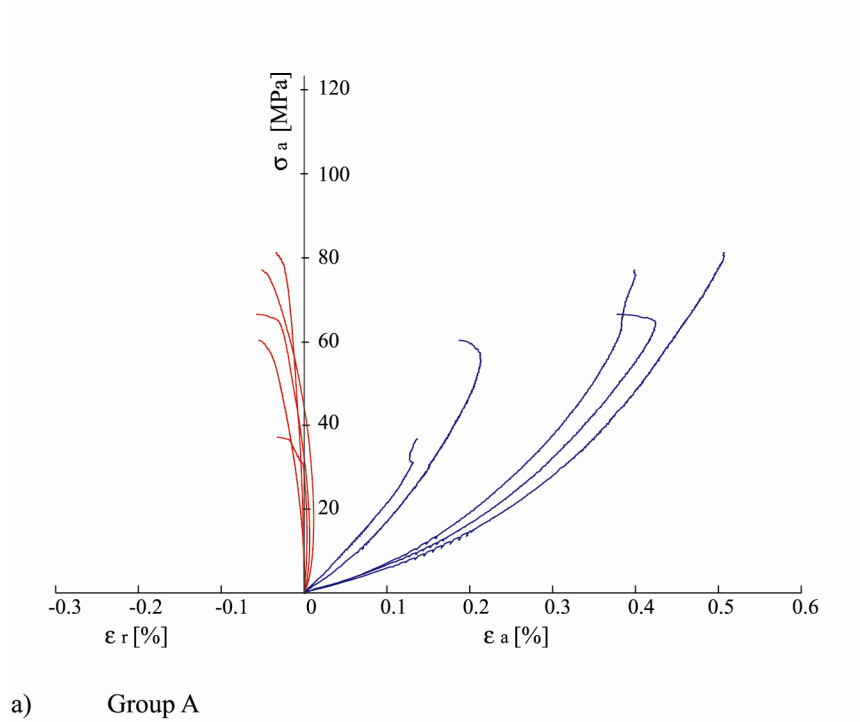
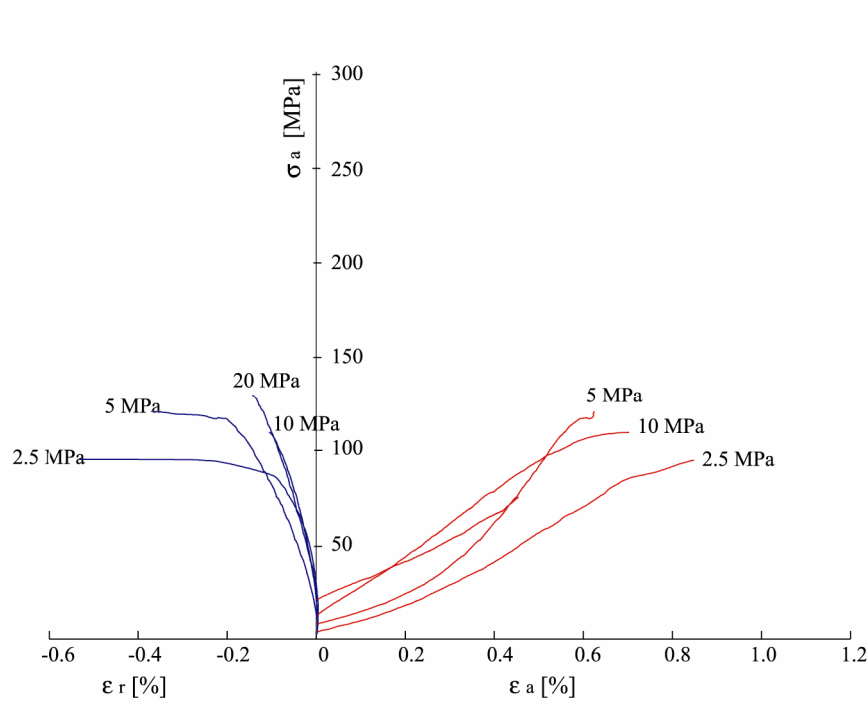
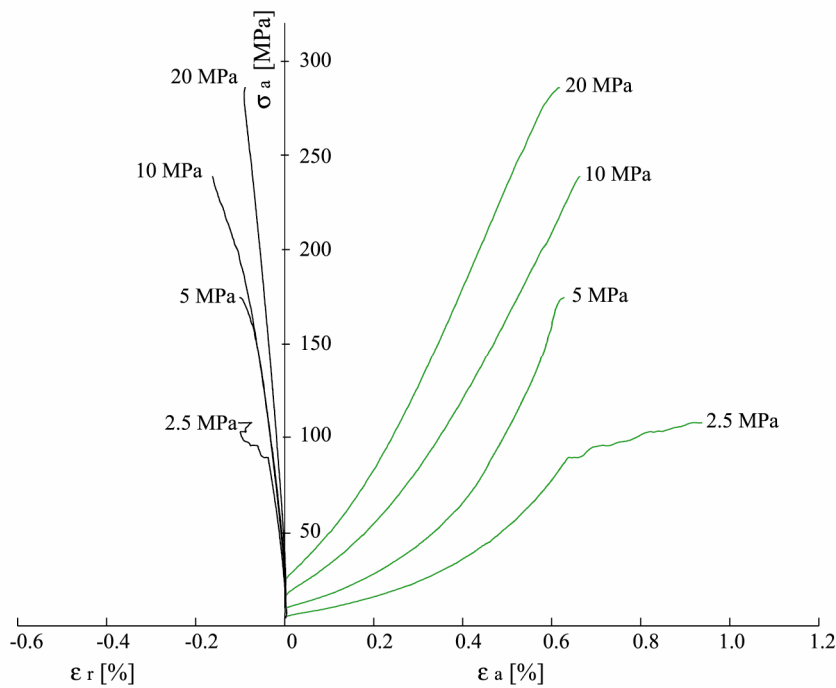


Figure A- 19: Stress-strain curves of uniaxial tests.

## A- 1.3.2 Triaxial tests



a) Group A



b) Group B

Figure A- 20: Stress-strain curves of triaxial tests. Confining pressures are plotted at the end of stress-strain curves.

# Acknowledgments

I would like to thank Prof. Simon Löw for supervising my thesis and giving me the opportunity to work on this challenging and interesting project. I am likewise thankful to Dr. Erik Eberhardt who initiated this multidisciplinary research project on the processes and mechanisms of rockslides. Simon Löw and Erik Eberhardt are also acknowledged for their work and input into the planning of the installation campaign and their very helpful comments on the development of this thesis and the subsequent analyses.

Dr. Keith Evans became a member of the Engineering geology group just in time to take part in the project and for my thesis to benefit from his experience. Keith's valuable input for the design of the monitoring network and the borehole logging campaign is greatly appreciated. I am very grateful that he agreed to co-supervise the thesis and on bearing the load of helping me to interpret the logging and monitoring data and expressing the results in proper English.

I also want to acknowledge Prof. Herbert Einstein, the external co-referent of this thesis, for his helpful corrections and constructive criticism.

A big thankyou goes to Tom Spillmann (Institute of Geophysics, ETH Zürich), not only a co-PhD student on this project, for the collaboration in the field work, analysis of the data, numerous discussions, co-authorship on the publications and for reading the first drafts of this thesis with his hard but justified criticism. Björn Heincke (Institute of Geophysics, ETH Zürich) likewise was a good helper during the field campaign, a nice colleague, and allowed me to use his results on surface georadar and seismic refraction tomography in this thesis. The time we three spent on this mountain is mostly un-reportable but perhaps the most fascinating phase of the project. Dr. Hansruedi Maurer (Institute of Geophysics, ETH Zürich) is acknowledged last but not least in this section for his helpful comments on interpreting the results of his PhD students.

This thesis also benefited from the help and thoughts of many people outside my supervisory committee; they are acknowledged in the order of appearance in the next sections.

- First of all I would like to thank Stephan Husen, Prof. Kurt Schetelig, Hartmut Taubmann and my parents for encouraging me to start this thesis and the Swiss National Fond for funding it.
- In the first phase of the research project the choice of the study site was only possible due to the support of Dr. Hansruedi Keusen (Geotest), Dr. Bernhard Krummenacher (Geotest), Dr. Ruedi Krähenbühl (Strassenbauamt Graubünden), Giorgio Valenti (Dipartimento del Territorio, Ticino), Jean-Daniel Rouiller (Département des transports, de l'équipement et de l'environnement, CREALP), Charles-Louis Joris (Büro Odilo Schmid, Brig) and Thomas Rageth (Amt für Umweltschutz, Glarus) who all allowed insight into reports and data on unstable rock slopes. I also want to acknowledge the contributions of Sarah Signorelli (even though she decided to leave the project after the first months). The mountain guide of Randa, Yann Dupertuis, helped in solving logistical and accessibility problems and Lina Summermatter was as cordial a landlady in Randa as could be.

- The drilling and installation campaign was only possible with the enthusiastic drill work performed by the Arge ISR Injectobohr SA & SIF Groutbor SA and the installation efforts of Stump Foratec AG. Optical televiewer logs were run by Terratec GmbH and I would like to express my gratitude to Dr. Klaus Brauch for providing the opportunity to analyse the data in Heitersheim. The data acquisition system was designed and set up by Beat Rinderknecht and Christoph Bärlocher (both Institute of Geophysics, ETH Zürich), who were highly appreciated technical specialists and guaranteed most entertaining field days. From the Engineering Geology group Dr. Kurosch Thuro, Benoit Valley, David Estoppey and Franz Gönner supported the field work. Matthieu Dussud (Northwestern University, Evanson, USA) travelled to Randa to help us to perform the first TDR measurements. The transportation work was performed by the Swiss Air Force and AirZermatt; the latter were most collaborative and innovative in solving all transportation problems.
- Dr. Kurosch Thuro helped me with field mapping and Dr. Bas den Brok was so kind to have the first look at the results and provided valuable criticism on the drafts of the geological map.
- The borehole displacement measurements were performed by Florentin Ladner (Stump Foratec AG), who proved to be reliable, professional and especially patient in explaining the data analysis and in helping to improve the data quality.
- I want to thank Peter Giger (Solexperts AG) for designing the benchmark survey tool and Marcel Mettler (Geological Institute, ETH Zürich) for maintaining it.
- The thin sections were prepared by Frowin Pirovino (Geological Institute, ETH Zürich) and his team and Urs Gerber was very helpful in photographing them. The rock mechanical testing was performed by Zig Szczepanik at the University of Saskatchewan.
- Jana and Markus Niederöst and Jochen Willneff (Institute of Geodesy and Photogrammetry, ETH Zürich) are acknowledged for their first attempts to derive a photogrammetric model of the investigated slope.

Bettina Roth-Galamb, Rita Gysin, Bernadette Würsch and Thomas Löffler deserve gratitude for their administrative support.

I would like to express my gratitude to all my colleagues in the Engineering geology group. Especially I want to acknowledge Delphine Fitzenz, Christian Zangerl, Volker Lützenkirchen, Susanne Laws, Nathalie van Meir, David Estoppey, Andrew Kos and Benoit Valley for their help, moral support and interesting discussions.

This final thanksgiving section is reserved for my family and all the precious, helpful and loving friends who accompanied me during the thesis. They know who they are and I am decided not to forget to express my gratitude personally.



# Curriculum vitae

## Personal details:

Name: Heike Willenberg  
Date and place of birth: 20.12.1972, Gross-Gerau , Germany  
Nationality: German

## Doctorate

since 05/2000 Ph.D. position at the Geological Institute, Engineering geology group, ETH Zürich

## Employment

02/1999 - 04/2000 Technical employee at WBI (Prof. Wittke Beratende Ingenieure für Grundbau und Felsbau GmbH), Aachen

## University studies

10/1995 – 02/1999 Diploma in Geology at the Rheinisch Westfälische Technische Hochschule RWTH Aachen.

Diploma thesis „Dokumentation der Baugrundverhältnisse beim Süd-vortrieb des Limburger Tunnels und der Hebungsinjektionen unter dem Hochregallager der Firma TetraPak“, supervised by Prof. Dr. K. Schetelig and Prof. Dr. W. Wittke.

Diploma mapping project „Das Altpaläozoikum zwischen Condades und Rodomouls–Ostabschnitt (Montagne Noire, Frankreich)“, supervised by Prof. Dr. G. Flajs and Dr. U. Glasmacher.

10/1992 – 09/1995 Pre-diploma in Geology at the Christian-Albrechts-Universität zu Kiel.

## Education

07/1983 – 05/1992 Ludwig-Georgs Gymnasium in Darmstadt, final degree: Abitur.

07/1979 – 07/1983 Erich-Kästner elementary school in Darmstadt.